Vanadium-based and Manganese-based Cathode Material for Rechargeable Aqueous Zinc-ion Batteries

by

Mei Han

A thesis
presented to the University of Waterloo
in fulfilment of the
thesis requirement for the degree of
Doctor of Philosophy
in
Chemical Engineering

Waterloo, Ontario, Canada, 2024

© Mei Han 2024

Examining Committee Membership

The following served on the Examining Committee for this thesis. The decision of the Examining Committee is by majority vote.

External Examiner:	Prof. Xiaoxiao Huang Professor Department of Materials Science, Harbin Institute for Technology
Supervisor:	Prof. Pu Chen Professor Department of Chemical Engineering, University of Waterloo
Internal Member:	Prof. Eric Croiset Professor Department of Chemical Engineering, University of Waterloo
Internal Member:	Prof. Boxin Zhao Professor Department of Chemical Engineering, University of Waterloo
Internal-External Member:	Prof. Xiaoyu Wu Assistant Professor Department of Mechanical and Mechatronics Engineering, University of Waterloo

Author's Declaration

This thesis consists of material all of which I authored or co-authored: see Statement of Contributions included in the thesis. This is a true copy of the thesis, including any required final revisions, as accepted by my examiners.

I understand that my thesis may be made electronically available to the public.

Statement of Contributions

This thesis consists in a combination of published and unpublished works.

Parts of **Chapter 4** is adapted with permission from: **Han, M.**, Zhi, J., Huang, J., Zhao, W., Wu, Y., & Chen, P. (2023). Ultra-stable aqueous zinc-ion battery enabled by highly reversible Zn^{2+}/Na^{+} co-intercalation chemistry. *Cell Rep. Phys. Sci*. **4**, 101242 (2023). DOI: 10.1016/j.xcrp.2022.101242. Copyright © 2023 Elsevier B.V.

I am the first author of this paper, and was responsible for all experimental planning, methodology, data collection and analysis, and draft writing and editing. Yan Wu, Dr. Jing Huang and Dr. Weinan Zhao assisted in performing initial experiments. Dr. Jian Zhi assisted in part of the experimental planning and data analysis. Dr. Pu Chen assisted in supervision, experimental planning, and reviewing and editing the manuscript. Two patents for these works have also been filed.

Han, M., Chen, P. "The synthesis method and application of dual-ion doped vanadium oxide as the cathode material in rechargeable aqueous zinc-ion batteries," patent number: ZL 2019 1 0619367.4 (2023).

Han, M., Zhi, J., Chen, P. "Rechargeable aqueous Zn-ion batteries with dual-ion system," patent application number.: CN115312880A or CN202110496889.7 (2021)

Chapter 5 and **Chapter 6** are adapted from: **Han, M.**, Zhi, J., Li, S., Liu, Z., Zhao, W., Ren, K., Chen, P. Unveiling the ionic crosstalk in aqueous zinc-ion batteries. The manuscript has been submitted to *Joule* and is under review. A patent application is in preparation.

I am the first author of this work, and was responsible for all experimental planning, methodology, data collection and analysis, and draft writing and editing. Dr. Shaopeng Li, Dr. Zhongyi Liu and Dr. Weinan Zhao assisted in performing initial experiments. Keily Ren assisted in carrying out experiments under my direction. Dr.

Jian Zhi assisted in part of the experimental planning and data analysis. Dr. Jian Zhi and Dr. Pu Chen assisted in supervision, experimental planning, and reviewing and editing the manuscript. A patent for these works has also been filed.

Chapter 7 is adapted from: **Han, M.**, Sun, Z., Zhu, R., Zhi, J., Zhou, M., Chen, P. Manuscript in preparation.

I am the co-first author of this work, and was responsible for experimental planning, methodology, data collection and analysis, and draft writing and editing. Dr. Zhixin Sun was the other first author of this work, and was responsible for analyzing the computational and simulation results, and draft writing and editing. Ray Zhu assisted in carrying out experiments under my direction. Dr. Jian Zhi and Dr. Min Zhou assisted in experimental planning and reviewing and editing the manuscript. Dr. Min Zhou assisted with the computational modelling. Dr. Pu Chen assisted in supervision, experimental planning, and reviewing and editing the manuscript.

Other published works beyond the scope of this thesis:

Han, M., Zhi, J., Hoang, T. K., Li, Y., Li, L., & Chen, P. Artificial solid electrolyte interphase for thermally stable rechargeable aqueous zinc batteries. *J. Power Sources* **441**, 227171 (2019). DOI: 10.1016/j.jpowsour.2019.227171

A patent for this work has also been filed.

Han, M., Chen, P. "A synthesis method of artificial solid electrolyte interphase for rechargeable aqueous zinc-ion batteries," patent number: ZL 2019 1 0379771.9 (2022).

Abstract

Rechargeable batteries offer a feasible solution to storing the intermittent energy supplies associated with renewable energy production. Despite the dominance of lithium-ion batteries (LIBs) in the current battery market, their application is hindered by the scarcity of lithium resources, unaffordable costs, and safety concerns. Consequently, rechargeable aqueous zinc-ion batteries (RAZBs) with mildly acidic electrolytes have garnered attention due to their cost-effectiveness, high safety and environmental friendliness. However, identifying suitable zinc ion intercalation-type cathode materials that meet commercial standards remains a significant challenge, impeding the widespread adoption of RAZBs. Vanadium- and manganese-based compounds, recognized for their unique structures and substantial theoretical capacities, are among the foremost cathode materials for RAZBs. Nonetheless, these materials often suffer from structural degradation during cycling, limited electrical conductivity, and severe side reactions, substantially restricting their practical applications.

In this thesis, we introduce strategies to improve the electrochemical performance of vanadium-based and manganese-based cathodes in RAZBs through ionic pre-intercalation techniques and the integration of cathode-electrolyte interface layers, respectively. In particular, the RAZB with an improved vanadium-based cathode maintains 90% capacity after 4000 cycles and achieves a discharge specific capacity of 209 mAh g^{-1} at 5 C. Furthermore, our in-depth analysis of the reaction mechanisms in vanadium-based cathodes with pre-intercalated ions uncovered a reversible dual-cation (Zn^{2+} and Na^{+}) intercalation chemistry. This not only stabilizes the vanadium-based material structure, but also facilitates the free access of ions from the electrolyte to the cathode, thus mitigating structural collapse or failure due to ion insertion during cycling.

In the study of MnO_2 cathodes, we have prioritized the exploration of the intrinsic failure mechanism and disclosed the phenomenon of "ionic crosstalk" between electrodes for the first time. The release of a significant amount of Mn^{2+} ions from the MnO_2 cathode

detrimentally impacts the ion concentration on the Zn anode surface, which is detrimental to the uniform deposition of zinc metal and exacerbates the growth of dendrites as well as anode corrosion; simultaneously, the stripping of Zn^{2+} ions from the zinc anode results in the formation of by-products on the cathode and triggers irreversible phase transitions in the cathode material. These ionic crosstalk effects exacerbate electrode deterioration, culminating in the failure of the Zn-MnO_2 battery system. To address this, we apply a hierarchical porous membrane on the MnO_2 cathode surface to mitigate ionic crosstalk and promote reversible dissolution/deposition reactions. As a result, the cell demonstrates an exceptional capacity retention of 97% after 1000 cycles at 2 C and an operational lifespan exceeding 500 hours, markedly outperforming previously reported aqueous Zn-MnO_2 batteries by over 1.5 times.

Furthermore, to explore the commercial potential of MnO_2 cathode materials, we combine the liquid-phase in situ encapsulation method with a straightforward heat treatment to cover a Bi_2O_3 layer on the MnO_2 material surface. This approach facilitates a significant increase in the mass loading of the cathode material to 16 mg cm^{-2}. Our findings reveal that these cathodes exhibit exceptional cycling stability and Coulombic efficiency in larger battery configurations, with an exceptional capacity retention of 72.7% over 330 cycles (equivalent to a calendar life of 60 days), showcasing its superior performance and reliability for high-energy-density battery applications. These results not only underscore the significant potential of Bi_2O_3 coating technology to advance the development of aqueous Zn-MnO_2 batteries but also lay a solid foundation for the commercialization of aqueous batteries.

Keywords: vanadium oxide, manganese oxide, reversible dual-ion de-/intercalation, ionic crosstalk, high mass-loading, rechargeable aqueous zinc-ion batteries.

Acknowledgements

First and foremost, I would like to express my deepest and most heartfelt gratitude to my supervisor, Dr. Pu Chen. Since our first meeting in 2017, you have been a constant source of guidance, support, and encouragement. Your unwavering belief in my abilities and potential has been a significant driving force in my academic and personal growth. From the early days of uncertainty to the confident steps I take today, you have witnessed and nurtured my development. Your dedication to my academic skills and genuine concern for my overall well-being have left an indelible mark on my life. As I approach the completion of this significant stage, I look back with immense appreciation for your mentorship and support.

I would also like to express my sincere thanks to all my committee members- Dr. Eric Croiset, Dr. Boxin Zhao, Dr. Xiaoyu Wu and Dr. Xiaoxiao Huang-for taking the time to read my thesis and provide their valuable feedback. Your critical insights are crucial in refining my research and broadening my perspectives. The encouragement and guidance I received from each of you have been instrumental in navigating the complexities of my research and have fostered a richer, more nuanced understanding of the subject matter.

I also want to thank Dr. Tong Leung and Charles Dal Castel for the use of their lab facilities. Thank you to Judy Caron for her help on many occasions throughout my PhD.

The accomplishments encapsulated in this thesis are a testament to the invaluable collaborations I've been fortunate to have over the recent years. I want to extend my sincere thanks to my colleagues Zhongyi Liu, Shaopeng Li, Yan Wu and Sara Shi, your insightful contributions and engaging discussions on the cathode works have been pivotal to this project. I am deeply grateful to each of you for your expertise and the vibrant exchanges we've shared. A heartfelt thanks to my co-op students Kaiyang Ren, Ray Zhu, Eric Zhou and Meixuan Li, whose commitment and enthusiasm in the experimental projects made mentoring an immensely rewarding experience. My

gratitude also extends Dr. Jian Zhi, your guidance and insightful feedback during the manuscript writing have been pivotal in shaping this thesis. Your expertise and constructive discussions have not only enriched the content but also profoundly influenced my approach to research.

To my dear friends, whose unwavering support and companionship have been the backbone of my journey. A special note of thanks goes to my friends Pax, Alice, and Miao. Your care and concern for my well-being in everyday life have been a source of comfort and joy. Whether it was a late-night chat to de-stress, a laugh to break the monotony of study, or just being there when I needed a shoulder, your everyday support and care, even in the smallest things, have meant the world to me.

To my family, especially my parents, who are an entire ocean away but never out of my heart – thank you doesn't even begin to cover it. Your endless encouragement, those late-night calls filled with laughter and sometimes tears, and your "you can do it" messages have kept me going. It's like you've been right beside me, every step of the way, even though we're miles apart. Your belief in me has been a constant source of motivation and has helped me persevere through every barrier.

Lastly, I would like to acknowledge any funding bodies or organizations that have supported my research. Their financial assistance has been essential in facilitating my research endeavors.

This thesis is not just a reflection of my work, but a testament to the collaborative effort and support of all the individuals mentioned above and many others who have contributed in various capacities. I am deeply thankful to each one of you.

Dedication

Dedicated to my family –

to my parents, for their patience, support, and unconditional love.

Table of Contents

Examining Committee Membership ..... **ii**

Author's Declaration ..... **iii**

Statement of Contributions ..... **iv**

Abstract ..... **vi**

Acknowledgements ..... **viii**

Dedication ..... **x**

List of Figures ..... **xvi**

List of Tables ..... **xxix**

List of Abbreviations ..... **xxx**

Chapter 1. Introduction **1**

1.1. Background 1

1.2. Rechargeable Batteries 2

1.3. Rechargeable Aqueous Zinc-ion Batteries 5

Chapter 2. Literature Review **9**

2.1. Cathode Materials for the RAZB System 9

2.1.1. Vanadium-based materials 10

2.1.2. Manganese-based materials 16

2.2. Electrolyte Optimization for More Reliable RAZBs 21

2.2.1. Electrolytes and their basic characteristics 22

2.2.1.1. Ionic conductivity 22

2.2.1.2. Ion transference number 23

2.2.1.3. Electrochemical stability window 25

2.2.2. Electrolyte optimization strategies 27

2.2.2.1. Species of zinc salts 27

2.2.2.2. Concentration of zinc salts 29

2.2.2.3. Functional additives in electrolytes 31

2.3. Zinc Anode 33

2.3.1. Issues for Zn anodes 33

2.3.1.1. Zinc dendrite formation 33
2.3.1.2. Hydrogen evolution reaction 34
2.3.1.3. Zinc corrosion and by-products generation 35
2.3.2. Interface modification of Zn anodes 36
2.3.2.1. Redistribution of concentration field 37
2.3.2.2. Redistribution of electric field 38
2.3.3. Controlling Zn texture orientation 39
2.3.4. Structural Zn anodes 42
2.3.5. Electrolyte optimization and design 43
2.4. Energy Storage Mechanisms of RAZBs 46
2.4.1. Zn^{2+} insertion/extraction mechanism 47
2.4.2. H^{+}/Zn^{2+} co-insertion/extraction mechanism 48
2.4.3. H_2O/Zn^{2+} co-insertion/extraction mechanism 49
2.4.4. Conversion reaction mechanism (manganese-based cathode) 51
2.4.5. Deposition and dissolution reaction mechanism (manganese-based cathode) 52
2.4.6. Pseudocapacitive Faradaic process 54
2.5. Project Objectives 57
2.6. Thesis Outline 58
Chapter 3. Experimental Methods 59
3.1. Cathode Fabrication 59
3.2. Battery Assembly 59
3.2.1. Coin cell assembly 59
3.2.2. Swagelok-type battery assembly 60
3.2.3. Iron plate battery assembly 60
3.3. Material Characterization Techniques 61
3.3.1. X-ray diffraction technique 61
3.3.2. Scanning electron microscopy and energy-dispersive X-ray 61
3.3.3. X-ray photoelectron spectroscopy 61
3.3.4. Brunauer-Emmett-Teller 61
3.3.5. Fourier transform infrared spectroscopy 62

3.3.6. Inductively coupled plasma optical emission spectrometry 62
3.4. Electrochemical Characterization Techniques.....62
3.4.1. Cyclic voltammetry.....62
3.4.2. Electrochemical impedance spectroscopy 63
3.4.3. Linear polarization.....64
3.4.4. Linear sweep voltammetry.....64
3.4.5. Battery testing.....65
3.4.5.1. Full cell testing.....65
3.4.5.2. Zn symmetric cell testing.....65
3.4.6. Self-discharge 66
3.5. Battery Performance Evaluation Metrics.....67
Chapter 4. High Performance RAZB Enabled by Reversible Zn^{2+}/Na^{+} Co-Intercalation Chemistry 70
4.1. Introduction.....70
4.2. Experimental Methods.....72
4.2.1. Cathode material synthesis 72
4.2.2. Other experimental methods.....73
4.3. Results and Discussion 74
4.3.1. Cathode material fabrication.....74
4.3.2. Electrochemical performance of ZNVO cathode 76
4.3.3. Electrolyte modification.....78
4.3.4. Energy storage mechanism 87
4.4. Conclusion 103
Chapter 5. Unveiling the Ionic Crosstalk in Aqueous Zn-MnO_2 Batteries 106
5.1. Introduction.....106
5.2. Experimental Methods.....109
5.2.1. Material synthesis 109
5.2.2. Other experimental methods.....109
5.3. Results and Discussion 110
5.3.1. The ionic crosstalk effect of Mn^{2+} on Zn anodes.....110

5.3.2. The ionic crosstalk of Zn^{2+} on MnO_2 cathodes 116
5.4. Conclusion 123
Chapter 6. An Effective Method for Mitigating Zn^{2+}/Mn^{2+} Ionic Crosstalk ... 125
6.1. Introduction 125
6.2. Experimental Methods 126
6.2.1. PM fabrication 126
6.2.2. Other experimental methods 127
6.3. Results and Discussion 127
6.3.1. PM fabrication and characterization 127
6.3.2. The inhibitory effect of the PM on Mn^{2+} ionic crosstalk 131
6.3.3. The inhibitory effect of the PM on Zn^{2+} ionic crosstalk 134
6.3.4. Electrochemical performance evaluation 139
6.4. Conclusion 146
Chapter 7. Unlocking High-capacity Aqueous Zn-MnO_2 Batteries with Bismuth Oxide Surface Modification 148
7.1. Introduction 148
7.2. Experimental Methods 150
7.2.1. Cathode material synthesis 150
7.2.2. Cathode fabrication and battery assembly 151
7.3. Results and Discussion 152
7.3.1. Cathode material characterization 152
7.3.2. Coin-type cell electrochemical performance 154
7.3.3. Large cell electrochemical performance 160
7.4. Conclusion 165
Chapter 8. Conclusion and Future Work 167
8.1. Conclusion 167
8.2. Future Work 169
8.2.1. Vanadium-based cathode materials 170
8.2.2. Manganese-based cathode materials 174
References 179

Appendices.....225
Appendix A: Supplementary Information for Chapter 4 225
Appendix B: Supplementary Information for Chapter 5 232
Appendix C: Supplementary Information for Chapter 6 234
Appendix D: Supplementary Information for Chapter 7 240

List of Figures

Figure 1.1. a) Year-on-year percent change in electricity demand in selected regions, 2019-2026[1]. b) Total electricity demand in China, European Union, and the United States, 1990-2026[1]. c) Recent cost developments for selected clean energy technologies, 2014-2022[2]. d) Estimated market size for selected clean energy technologies by technology and region, 2020-2050[3]. STEPS: Stated Policies Scenario; NEZ: Net Zero Emissions by 2050 Scenario. 2

Figure 1.2. a) Schematic illustration of representative rechargeable batteries and their applications in traditional and emerging portable electronic devices[5]. b) Ragone plot of various energy storage systems. The times marked on the blue axes represent reaction kinetics[8]. 4

Figure 1.3. a) Ragone plot of energy storage systems in mild aqueous electrolyte system with different energy carriers[24]. b) Radar diagram of Zn property regimes: compared with other metals, Zn shows capacity advantages, high stability, and good reversibility in aqueous electrolyte[25]. c) Timeline of the Zn-based batteries development history[28,30,33–44]. 7

Figure 2.1. a) Schematic illustration of RAZBs[68]. b) Operating voltage vs. specific capacity for various cathode materials presently used for RAZBs[50]. 10

Figure 2.2. The crystal structures of typical vanadium oxides: V_2O_3, VO_2, V_6O_{13}, $H_2V_3O_8$ ($V_3O_7{\bullet}H_2O$), and V_2O_5[70]. In the blue box is a schematic illustration of V_2O_5 crystal structure with VO_5 square pyramids[21] 11

Figure 2.3. V_2O_5 cathode materials with different types of nanostructures: (a) nanofibers[75], (b) nanorods[76], (c) hollow nanospheres[78], (d) porous V_2O_5 yolk-shell microspheres[79] 13

Figure 2.4. a) Cycling stability of the NVO at 0.1 and 0.5 A g^{-1} [85]. b) SEM images of the effects of different K^+ intercalation amounts[88]. Schematic illustration of c) Zn^{2+} storage mechanism of $Zn_{0.1}V_2O_5{\bullet}nH_2O$ cathode[99], d) reversible H_2O molecules intercalation into $Zn_{0.25}V_2O_5{\bullet}nH_2O$ cathode in aqueous electrolyte, and the H_2O deintercalation accompanying Zn^{2+} intercalation during discharge process[22], e)

hydrated Zn^{2+} ($Zn(H_2O)_6^{2+}$) intercalation process into NHVO cathode[105], f) synthesis process of the PANI/V_2O_5 composite[108]. 15

Figure 2.5. a) Cycle performance of V_2O_5@CNTs and pure V_2O_5 electrodes at 5 A g^{-1}, inset is the morphology of V_2O_5@CNTs sample[116]. b) Cycle performance of C@V_2O_5 at 0.5 A g^{-1}, inset is the morphology of C@V_2O_5 sample[117]. 16

Figure 2.6. Schematic diagram of the order of thermal stability of MnO_2 polymorphs. Ranking as $\beta > \alpha > \gamma > \delta \cong \lambda$[131]. 17

Figure 2.7. a) XRD patterns of β-MnO_2 electrode at selected states during first and second cycles[132]. b) Schematic illustration of the Zn-MnO_2 battery with $CF_3SO_3^-$-based aqueous electrolyte[132]. c) Cycle capacity evolution of the β-MnO_2 nanorod cathode using $MnSO_4$/$ZnSO_4$ electrolyte[124] 19

Figure 2.8. a) Schematic illustration of Zn^{2+} adsorption/desorption for perfect MnO_2 and MnO_2 with oxygen vacancies[144]. b) Cyclic performance at current densities of 2 A g^{-1}. Inset: schematic of defect-engineered Mn_3O_4/CNTs composites[146]. c) Schematic illustration of interactive forces between CH and Mn^{2+}/Zn^{2+} ions, respectively. Cyclic performance at a current density of 0.02 A g^{-1} [149]. 21

Figure 2.9. a) Raman spectra of $ZnCl_2$ solutions of different concentrations. b) The transference number of Zn^{2+} at 21℃ for dilute (5 m) and concentrated (30 m) $ZnCl_2$ electrolytes[164]. Enlarged regions near c) anodic and d) cathodic extremes of the electrochemical windows on nonactive titanium mesh electrodes. e) Overall electrochemical windows of bi-cation and mono-cation electrolytes were evaluated with CV at a scanning rate of 10 mV s^{-1} [177]. 26

Figure 2.10. a) Problems of metal Zn contact with aqueous electrolytes with varying pH values[180]. b) Micrographs of polished Zn electrode, and Zn electrode placed in acetate electrolyte ($ZnSO_4$/$(NH_4)_2SO_4$/$(CH_3COO)_2Pb$), sulfate electrolyte ($ZnSO_4$/$(NH_4)_2SO_4$) and chloride electrolyte ($ZnCl_2$/NH_4Cl) for 30 days, respectively[183]. c) Cycling performance of Zn-V_2O_5 battery with *x* M $ZnSO_4$ electrolyte[185]. d) Comparison of cycling performances between batteries in 0.3 M $Zn(TFSI)_2$ electrolyte and in 1 M $ZnSO_4$ electrolyte[186]. 29

Figure 2.11. Characterization of aqueous $Zn(CF_3SO_3)_2$ electrolyte with different concentrations (1–4 M): a) Coulombic efficiency of $ZnMn_2O_4$ electrode at current rate of 0.05 A g^{-1} within 0.8–1.9 V, b) viscosity and ionic conductivity. c) Schematic of mitigating active substance dissolution[57]. d) Schematic for Zn^{2+}-solvation structures in the electrolytes with 1 m $Zn(TFSI)_2$ and other concentrations of LiTFSI (5 m, 10 m and 20 m)[187]. e) The charge/discharge curves of Zn-V_2O_5 batteries at 0.1 A g^{-1} [192]. f) Cycling performance of V_2O_5 in 1 m $Zn(CF_3SO_3)_2$ and 21 m LiTFSI+1 m $Zn(CF_3SO_3)_2$ electrolytes at 0.5 A g^{-1} [192].....31

Figure 2.12. a) Schematic illustration of the function of pre-added Mn^{2+} in Zn-MnO_2 battery. b) Cycling performance of the two samples over 100 cycles[197]. c) Schematic illustration of Na salt additive inhibited the dissolution of NVO cathode and Zn dendrites formation. d) Cycling performance of NVO cathode in Zn^{2+}/Na^+ electrolyte at 4 A g^{-1} [26].....32

Figure 2.13. a) Schematic diagram of the zinc deposition process on the surface of bare Zn anode[206]. b) Defects on Zn anodes such as roughened surface, surface scratches or folds, and newly exposed unpolished edges, all of which can predispose to the creation of dendritic grains during electrochemical cycling[208]. c) Deposition products morphology of the Zn (100) and Zn (002) planes[209]. d) The morphology of the bare Zn foil and the Zn foil after soaking in 1 M $ZnSO_4$ electrolyte for 7 days[218].
.....36

Figure 2.14. a) Schematic illustration of the synthesis of HsGDY. b) Electric and concentration field simulation with protuberances of bare Zn and coated Zn[224]. c) Schematic diagram of the mechanism of cyanoacrylate for suppressing zinc dendrite[233]. d) Schematic diagram of Zn@ZnF_2 electrode regulating Zn^{2+} ion flux[237]. e) Illustration of synchronously reducing and assembling MXene layer on the surface of Zn foil and zinc plating behavior of MXene-coated Zn (top right) and pure Zn (bottom left)[249]. SEM images of cycled MXene-coated Zn and pure Zn. f) Schematic illustration of zinc plating on bare Zn electrode (upper) and NGO@Zn electrode (lower)[250].....40

Figure 2.15. a) Crystal structure of the metallic Zn[251]. Surface atomic arrangement and electron equipotential plane of Zn (002) and Zn (100)[209]. b) Schematic illustration

of zinc plating on the commercial Zn anode and the Zn anode with preferred (002) plane[251]. c) Schematic of preferential growth of (002) plane induced by $BMIm^+$ ion during cycling. Morphologies of cycled Zn anodes in Blank and 0.02 M $BMIm^+$ [255]. d) Morphologies of Zn (002) plane after cycling in 2 M $Zn(OTf)_2$ electrolyte and the Zn (101) plane in 2 M $ZnSO_4$ electrolyte[256]. 41

Figure 2.16. a) Schematic illustrations of CM@CuO@Zn. SEM images of Zn anode using reduced CM@CuO as the host[259]. b) Schematic illustration of zinc deposition on the 3D nickel (Ni) substrate[260]. c) Schematic illustration of the preparation of npZn electrode. d) Nanoporous Zn electrode with interface-localized concentrated electrolyte[262].....43

Figure 2.17. a) Schematic of electrostatic shield mechanism applied in Zn^{2+}/Na^+ electrolyte. b) Morphology of Zn anode surfaces cycled in $ZnSO_4$ and $ZnSO_4/Na_2SO_4$ electrolytes, respectively[26]. c) Schematics of the step-by-step zinc reduction and deposition process in control and PEG200 electrolytes under negative potential bias on the Zn anode[271].....45

Figure 2.18. General classification and schematic diagram of energy storage mechanisms of RAZBs[71].....46

Figure 2.19. a) Schematic illustration of expected mechanism of Zn^{2+} intercalation in VO_2[287]. Investigation of reaction mechanism of the MnO_2@CFP cathode during discharge: b) Discharge GITT profiles of the Zn-MnO_2@CFP cell, and c) *ex situ* XRD patterns of the MnO_2@CFP cathode at depth of discharge at 1.3 V and 1.0 V, respectively[291]. d) Schematic illustration of crystal structures of pristine V_2O_5, V_2O_5 after charging to 1.3 V and discharging to 0.2 V[60]. 50

Figure 2.20. a) HRTEM images of MnO_2 discharged to 1 V during the first cycle, and energy dispersive X-ray spectroscopy in scanning transmission electron microscopy (STEM-EDS) mappings of the elemental distributions of Mn, O, and Zn in the MnO_2 electrode. The lattice fringes of 0.33 and 0.26 nm from the discharged products are consistent with the d spaces from the (210) and (020) planes in monoclinic MnOOH[42]. b) The schematic for different reaction mechanisms in D1, D2 and D3 stages[174]. c)

The schematic diagram of the proposed charge storage mechanism of β-MnO_2 cathode[304]. 53

Figure 2.21. a) Power law dependence of the peak current on sweep rate for capacitive materials (b=1) and typical battery-type materials (b=0.5). The "transition" area between capacitive and battery-type materials area is located in the range of b=0.5-1[309]. b) The capacitive contributions at different scan rates in Zn-NVO battery[26]. c) Schematic CVs and corresponding electrochemical charge/discharge curves for various energy storage materials[310]..... 56

Figure 3.1. Schematic illustration of cathode fabrication process. 59

Figure 3.2. External view and internal composition of the a) CR2025 coin-type cell, b) T-type cell (Swagelok), and c) large battery..... 61

Figure 3.3. An example of Nyquist plot and its equivalent circuit[311]. 63

Figure 3.4. Schematic of three-electrode beaker type cell. WE: working electrode, CE: counter electrode, RE: reference electrode. 64

Figure 4.1. Schematic of reversible Zn^{2+}/Na^{+} co-intercalation in vanadium cathode. 72

Figure 4.2. Schematic illustrating the experimental procedure of synthesizing ZNVO material. 73

Figure 4.3. a) Morphology of commercial V_2O_5 powder and synthesized ZNVO nanowires. Element mapping of ZNVO material. Scale bar: 2 μm. b) XPS survey spectra of ZNVO sample. XRD patterns of c) commercial V_2O_5 and d) ZNVO-2 sample and schematic diagrams of their corresponding crystal structures. Shcherbinaite (V_2O_5, PDF#97-008-2151), $Na_{3.25}(OH)_{0.25}(H_2O)_{12}(VO_4)$ (PDF#01-070-2496), $Zn_{0.25}V_2O_5(H_2O)$ (PDF#01-086-1238), $Zn_3(VO_4)_2(H_2O)_{2.93}$ (PDF#01-074-2959). 75

Figure 4.4. a) Cycling performance of HVO and ZNVO electrodes in 2 M $ZnSO_4$ electrolyte at 1 C. b) Cycling performance of ZNVO electrodes with various cations insertion amounts in 2 M $ZnSO_4$ electrolyte. c) Comparison of specific capacity and voltage platform of ZNVO-2 with other reported cathode materials[33,43,44,57,59,63,65,83,269,279,325–330]. CV profiles of ZNVO cathode in 2 M $ZnSO_4$

electrolyte at a scan rate of d) 0.1 mV s^{-1} and e) 1 mV s^{-1} at selected cycle numbers. f) Nyquist plots of ZNVO cathode in 2 M $ZnSO_4$ electrolyte over the frequency range of 100 mHz-1 MHz at selected cycles. Inset is the equivalent circuit diagram. 78

Figure 4.5. a) Cycling performance of a) ZNVO electrodes with various cations insertion amounts in 2 M $ZnSO_4$ electrolyte. b) ESW of different electrolytes in three electrode configuration. Scan rate 10 mV s^{-1}. Magnified view of the regions outlined near anodic (hydrogen evolution reaction, HER) and cathodic (oxygen evolution reaction, OER) extremes. c) Morphology of ZNVO cathode in different electrolytes at 50th cycles. Scale bar: 1 μm. d) Long-term galvanostatic cycling of Zn-Zn symmetric cells at a current density of 0.1 mA cm^{-2} with an areal capacity of 1.0 mAh cm^{-2}. Morphogy of cycled Zn anode in e) 2 M $ZnSO_4$ electrolyte and f) 1 M $ZnSO_4$/1 M Na_2SO_4 electrolyte at the selected cycles. Scale bar: 2 μm.....81

Figure 4.6. Cycling performance of a) HVO and b) ZNVO cathodes in 2 M $ZnSO_4$ and 1 M $ZnSO_4$/1 M Na_2SO_4 electrolytes at 5 C. c) Initial cycles of ZNVO cathode in 1 M $ZnSO_4$/1 M Na_2SO_4 electrolyte at 5 C. d) Long-term cycling performance of HVO and ZNVO cathodes in 1 M $ZnSO_4$/1 M Na_2SO_4 electrolytes at 5 C. The Coulombic efficiency for a narrow y-axis scale is shown in **Figure A6**c. e) GCD profiles of ZNVO cathode in 1 M $ZnSO_4$/1 M Na_2SO_4 electrolyte at 5 C. The average charge voltage is around 1.0 V, and average discharge voltage is around 0.8 V. f) Long-term cycling performance of HVO and ZNVO cathodes in 1 M $ZnSO_4$/1 M Na_2SO_4 electrolytes at 10 C. 83

Figure 4.7. Rate performance of a) HVO and b) ZNVO cathodes in different electrolytes. Morphology of c) HVO cathodes and e) ZNVO cathodes after cycling in different electrolytes at various small current densities. Scale bar: 1 μm. Images of the obtained separators from the d) Zn-HVO cells and f) Zn-ZNVO cells after 10th cycle in different electrolytes at 1 C.....85

Figure 4.8. a) Cycling performance of ZNVO in 1 M $ZnSO_4$/1 M Na_2SO_4 electrolyte at 5 C. b) Cycling performance and c) Coulombic efficiency plots with standard deviations calculated from three cells for HVO, ZNVO and NVO cathodes at 5 C. d) Cycling performance of ZNVO cathode in 1 M $ZnSO_4$/1 M Na_2SO_4 electrolyte in 9 mAh batteries at 2.5 C. 87

Figure 4.9. CV profiles of a-c) HVO cathode, d-f) NVO cathode and g-i) ZNVO cathode in different electrolytes. The scan rate is 0.1 mV s^{-1}. HVO/NVO/ZNVO electrode was used as the working electrode, AgCl/Ag as the reference electrode and graphite rod as the counter electrode in T-type batteries. 90

Figure 4.10. a) GCD curve of cycled HVO cathode in 1 M $ZnSO_4$/1 M Na_2SO_4 electrolyte at 2nd cycle. Current rate is 1 C. b) *Ex situ* XRD pattern of cycled HVO electrode in 1 M $ZnSO_4$/1 M Na_2SO_4 electrolyte at determined voltages. $Zn_{0.25}V_2O_5 \cdot H_2O$, PDF# 01-086-1238, ZnV_3O_8, PDF# 04-011-2142, NaV_2O_5, PDF# 04-010-2339. c) and d) are *Ex situ* XRD patterns of the yellow areas after magnification. e) Contour map of the corresponding areas in the upper *ex situ* XRD pattern. f) Contour map of HVO reflection peaks migration with varying voltages. The inset scale represents the peak intensity, with 600 for high-intensity and 240 for low-intensity. 92

Figure 4.11. The molar ratio of a) Na and b) Zn normalized to V in 1 M $ZnSO_4$/1 M Na_2SO_4 electrolyte at various charge/discharge states. c) The molar ratio of Zn in different electrolytes at various charge/discharge states. XPS spectra of d) Zn 2p and e) Na 1s with their content percentages on the cycled HVO cathode under varying voltages. XPS spectra of V $2p_{3/2}$ at fully discharged (0.2 V) and fully charged (1.6 V) states in f) 1 M $ZnSO_4$/1 M Na_2SO_4 and g) 2 M $ZnSO_4$ electrolytes. Inset pie charts are the respective percentages of V^{4+} and V^{5+}. 93

Figure 4.12. Schematic illustration of Zn^{2+} and Na^+ de-/intercalation mechanism in HVO cathode. 96

Figure 4.13. *Ex situ* XRD patterns of a) and b) HVO cathodes, c) and d) ZNVO cathodes in different electrolyte at selected cycle numbers. e) Nyquist plots of ZNVO cathode in 1 M $ZnSO_4$/1 M Na_2SO_4 electrolyte over the frequency range of 100 mHz-1 MHz. Inset is the equivalent circuit diagrams. CV profiles of f) ZNVO cathode and g) HVO cathode in 1 M $ZnSO_4$/1 M Na_2SO_4 electrolyte at selected cycle numbers. .. 98

Figure 4.14. CV profiles of ZNVO cathode in 1 M $ZnSO_4$/1 M Na_2SO_4 electrolyte at its a) 50th cycle, b) 200th cycle and c) 500th cycle. Yellow: total capacity; mint: capacity contribution of Zn^{2+} de-/intercalation; rouge: capacity contribution of Na^+

de-/intercalation. d) Capacity contribution of Na^+ ion (rouge) and Zn^{2+} ion (mint) from ZNVO cathode in 1 M $ZnSO_4$/1 M Na_2SO_4 electrolyte at different cycles (averaged over three samples), with respective standard deviations of ±7.06% (Na^+ at 50th cycle), ±0.08% (Zn^{2+} at 50th cycle), ±5.65% (Na^+ at 200th cycle), ±7.70% (Zn^{2+} at 200th cycle), ±2.09% (Na^+ at 500th cycle) and ±3.40% (Zn^{2+} at 500th cycle). 99

Figure 4.15. CV curves of a) HVO cathode in 2 M $ZnSO_4$ electrolyte, b) 1 M $ZnSO_4$/1 M Na_2SO_4 electrolyte, and c) ZNVO cathode in 1 M $ZnSO_4$/1 M Na_2SO_4 electrolyte. The range of scan rate is 0.1-1 mV s^{-1}. d) The corresponding plots of log(*i*) vs. log(*v*) for HVO and ZNVO cathodes in different electrolytes. 102

Figure 4.16. The capacitive contribution percentage at different scan rates of a) HVO cathode in 2 M $ZnSO_4$ electrolyte, b) 1 M $ZnSO_4$/1 M Na_2SO_4 electrolyte, and c) ZNVO cathode in 1 M $ZnSO_4$/1 M Na_2SO_4 electrolyte. 103

Figure 5.1. a) Schematic diagram of the *in situ* optical visualization observation device. b) Actual image of the *in situ* optical visualization observation setup. c) Schematic of a symmetric transparent electrochemical cell. *In situ* optical visualization observations of zinc deposition in d) 2.2 M $ZnSO_4$ electrolyte and e) 2 M $ZnSO_4$/0.2 M $MnSO_4$ electrolyte at various deposition times. Scale bar: 200 μm. 111

Figure 5.2. a) LP curves of Zn-Zn symmetrical cells using $ZnSO_4$ electrolytes with different Mn^{2+} additions, with a scan rate of 0.1 mV s^{-1}. b) The corresponding Zn corrosion potential in $ZnSO_4$ electrolyte with different Mn^{2+} additions. c) Galvanostatic cycling performance of Zn-Zn symmetric cells in different electrolytes at a current density of 0.5 mA cm^{-2} and an areal capacity of 0.5 mAh cm^{-2}. Insets: detailed voltage profiles at specific cycling times. 112

Figure 5.3. a) *Ex situ* XRD patterns of Zn electrodes after plating/stripping in $ZnSO_4$ electrolyte with different Mn^{2+} additions for 100 hours at 0.5 mA cm^{-2} and 0.5 mAh cm^{-2}. b) The RTC of Zn electrodes cycled in different electrolytes. c) Morphology of pristine Zn electrode surface, and Zn electrode surface in $ZnSO_4$/0 M Mn^{2+}, $ZnSO_4$/0.1 M Mn^{2+}, $ZnSO_4$/0.2 M Mn^{2+}, $ZnSO_4$/0.5 M Mn^{2+} electrolytes after cycling for 100 hours at 0.5 mA cm^{-2} and 0.5 mAh cm^{-2}. Scale bar: 2 μm. Inset in c) is the

enlarged view, scale bar: 1 μm. d) Long-term galvanostatic cycling performance of Zn-Zn symmetric cells in different electrolytes at a current density of 1 mA cm^{-2} and an areal capacity of 0.5 mAh cm^{-2}.....114

Figure 5.4. a) The obtained LP curves as the Mn^{2+} variation rate in the $ZnSO_4$ electrolyte increases. The scan rate is 0.5 mV s^{-1}. b) The corresponding change in Zn corrosion potential with the Mn^{2+} variation rate. The error band is obtained from three trials.....116

Figure 5.5. a) Morphology evolution of the MnO_2 cathode in the discharged state at selected cycle numbers in 2 M $ZnSO_4$ electrolyte. b) Elemental mapping images of MnO_2 cathode in 2 M $ZnSO_4$ electrolyte at 10th discharge and 300th discharge. Scale bar: 2 μm.....117

Figure 5.6. a) *Ex situ* XRD patterns of MnO_2 cathodes in H_2SO_4 electrolyte at 5th discharge. *Ex situ* XRD patterns of MnO_2 cathodes in the discharged state in b) 2 M $ZnSO_4$ electrolyte and c) 2 M $ZnSO_4$/0.2 M $MnSO_4$ electrolyte at selected cycle numbers. ZSH ($Zn_4SO_4(OH)_6 \cdot 4H_2O$, PDF# 00-044-0673), MnOOH Groutite (PDF# 99-000-1423), ZMO Woodruffite ($(Zn,Mn)_2Mn_5O_{12} \cdot 4H_2O$, PDF# 99-000-4329), β-$MnO_2$ (PDF# 04-005-4881). d) XPS spectra of Mn 2p from the discharged MnO_2 cathodes.....119

Figure 5.7. a) GCD curve and *in situ* XRD counter map of MnO_2 cathode in 2 M $ZnSO_4$ electrolyte at determined voltages. The applied current density is 2 C. GIXRD patterns of the MnO_2 cathode corresponding to b) the first discharge and c) the second discharge of the GCD curves in a).....120

Figure 5.8. Schematic illustration of the Zn^{2+} ionic crosstalk effect (upper) and Mn^{2+} ionic crosstalk effect (lower) in the aqueous Zn-MnO_2 battery.....122

Figure 6.1. Schematic of the PM function in the aqueous Zn-MnO_2 battery. 126

Figure 6.2. a) Schematic diagram of the PM fabrication process. b) PM surface morphology based on various mass ratios (H_2O:PVDF-HFP=0.2:1, 0.5:1, 0.7:1, 1:1 , 1:1.5 and 2:1). Scale bar: 2 μm.....129

Figure 6.3. a) Cross-sectional SEM images of the PM (H_2O:PVDF-HFP=0.5:1). Scale bar: 2 μm. b) Side view schematic of a PM with a hierarchical porous structure. Green arrows represent long migration paths of ions in the PM. c) FT-IR spectra of the PM. d) Nitrogen adsorption/desorption curve of PM. The inset shows the BJH pore size distribution of PM. 131

Figure 6.4. *In situ* optical visualization observations of Zn anodes paired with a) bare MnO_2 and b) PM-MnO_2 cathodes in 2 M $ZnSO_4$ electrolyte within transparent electrochemical cells at various deposition times. Scale bar: 200 μm. Morphology of cycled Zn anode surface paired with c) bare MnO_2 and d) PM-MnO_2 cathodes in 2 M $ZnSO_4$ electrolyte. Scale bar: 20 μm. 132

Figure 6.5. a) *Ex situ* XRD patterns of Zn anodes paired with bare and PM-MnO_2 cathodes after 300 cycles in 2 M $ZnSO_4$ electrolyte. Inset: the RTC of Zn anodes paired with bare and PM-MnO_2 cathodes (300 cycles). The Mn concentration in 2 M $ZnSO_4$ electrolyte at a b) fully discharged state and c) fully charged state for different cycle numbers. d) Schematic diagram of Mn^{2+} ions passing through the PM. 134

Figure 6.6. a) *Ex situ* XRD patterns of MnO_2 cathodes in H_2SO_4 electrolyte at 5th discharge. b) *Ex situ* XRD patterns of MnO_2 cathodes in the discharged state in 2 M $ZnSO_4$ electrolyte at selected cycle numbers. ZSH ($Zn_4SO_4(OH)_6 \cdot 4H_2O$, PDF# 00-044-0673), MnOOH Groutite (PDF# 99-000-1423), ZMO Woodruffite ($(Zn,Mn)_2Mn_5O_{12} \cdot 4H_2O$, PDF# 99-000-4329), β-$MnO_2$ (PDF# 04-005-4881). c) XPS spectra of Mn 2p from the discharged PM-MnO_2 cathodes. d) Percentage contents of Mn^{3+} and Mn^{4+} on bare and PM-MnO_2 cathodes based on XPS results. 136

Figure 6.7. a) GCD curve and *in situ* XRD counter map of PM-MnO_2 cathode in 2 M $ZnSO_4$ electrolyte at determined voltages after 24 hours activation. The applied current density is 2 C. GIXRD patterns of the PM-MnO_2 cathode corresponding to b) the first discharge and c) the second discharge of the GCD curves 137

Figure 6.8. a) Morphology evolution of the PM-MnO_2 cathode in the discharged state at selected cycle numbers in 2 M $ZnSO_4$ electrolyte. Scale bars: 2 μm and 1 μm. Elemental mapping images of PM-MnO_2 cathode in 2 M $ZnSO_4$ electrolyte after b) 10th discharge and c) 300th discharge. Scale bar: 2 μm. 138

Figure 6.9. Current-time curves at the bias potential of 10 mV and Nyquist plots before and after polarization of a) bare Zn-Zn, b) PM Zn-Zn c) PP Zn-Zn symmetric cells in 2 M $ZnSO_4$ electrolyte. Inset: the morphology of PP film (Celgard 2340). Scale bar: 1 μm. Current-time curve at the bias potential of 10 mV and Nyquist plots before and after polarization of b) bare Zn-Zn and c) PM Zn-Zn symmetric cells in 2 M $MnSO_4$ electrolyte. 139

Figure 6.10. a) Cycling performance of bare MnO_2 and PM-MnO_2 electrodes in 2 M $ZnSO_4$/0.2 M $MnSO_4$ electrolytes at 1 C and b) Coulombic efficiency with a narrow y-axis scale. c) Long-term cycling stability of bare MnO_2 and PM-MnO_2 cathodes in 2 M $ZnSO_4$/0.2 M $MnSO_4$ electrolyte at 2 C and d) Coulombic efficiency with a narrow y-axis scale. GCD profiles of e) bare cathode and f) PM-cathode in 2 M $ZnSO_4$/0.2 M $MnSO_4$ electrolyte at 2 C. The average charge voltage of PM-equipped battery is around 1.61 V, and average discharge voltage is around 1.30 V. g) The comparison of cycle number, operation time and cell capacity with previously reported aqueous Zn-MnO_2 batteries. More details are listed in **Table C1**. 141

Figure 6.11. a) Cycling performance of PM-coated battery in 2 M $ZnSO_4$/0.2 M $MnSO_4$ electrolyte at 2 C. b) The cycling performance and c) Coulombic efficiency plots with standard deviations calculated from three cells. 142

Figure 6.12. a) CV profiles of bare MnO_2 and PM-MnO_2 cathodes in 2 M $ZnSO_4$/0.2 M $MnSO_4$ electrolyte at 3rd cycle. CV profiles of b) bare MnO_2 and c) PM-MnO_2 cathode in 2 M $ZnSO_4$/0.2 M $MnSO_4$ electrolyte at selected cycle numbers. Nyquist plots of d) bare MnO_2 cathode and e) PM-MnO_2 cathode in 2 M $ZnSO_4$/0.2 M $MnSO_4$ electrolyte over the frequency range of 10 mHz-1 MHz. Insets are the enlarged profiles and equivalent circuit diagrams. f) Rate performance of bare MnO_2 and PM-MnO_2 cathodes in 2 M $ZnSO_4$/0.2 M $MnSO_4$ electrolyte..... 144

Figure 6.13. Schematic illustration of the PM function in the aqueous Zn-MnO_2 battery. 145

Figure 7.1. a) Morphology and EDS elemental mapping of Bi-coated MnO_2 nanowires. Scale bar: 5 μm. b) XRD patterns of Bi-coated MnO_2 nanowires. Bismuth

trioxide (Bi_2O_3, PDF#97-003-8436), β-MnO_2 (PDF# 04-005-4881). XPS spectra of the BMO sample: c) a survey spectrum, d) Bi 4f and e) O 1s. 154

Figure 7.2. Cycling performance of β-MnO_2 and BMO cathodes in 2 M $ZnSO_4$/0.2 M $MnSO_4$ electrolyte at a) 0.2 C and b) 1 C. The active material mass loading is around 9 mg cm^{-2}. The charging/discharging plateaus of c) β-MnO_2 cathode and d) BMO cathode in 2 M $ZnSO_4$/0.2 M $MnSO_4$ electrolyte at 0.2 C. 156

Figure 7.3. CV profiles of a) β-MnO_2 and b) BMO cathodes at determined cycle numbers, with a scan rate of 0.5 mV s^{-1}. Nyquist plots of c) β-MnO_2 and d) BMO cathodes in 2 M $ZnSO_4$/0.2 M $MnSO_4$ electrolyte over the frequency range of 100 mHz-1 MHz at selected cycles. Inset is the corresponding equivalent circuit diagram. 158

Figure 7.4. Cycling performance of BMO cathode in 2 M $ZnSO_4$/0.2 M $MnSO_4$ electrolyte at a) 1 C and b) 2 C. The standard deviations in these plots are calculated based on three cells. c) The comparison of cell cycle number, active material mass loading with recently reported coin-type Zn-MnO_2 batteries. More details are listed in **Table D3**. 160

Figure 7.5. a) Internal view of the large battery. b) Cycling performance of β-MnO_2 and BMO cathodes in 2 M $ZnSO_4$/0.2 M $MnSO_4$ electrolyte at 0.2 C. The active material mass loading >9 mg cm^{-2}. c) The corresponding charging/discharging plateaus. d) Cycling performance of the BMO cathode in 2 M $ZnSO_4$/0.2 M $MnSO_4$ electrolyte at 0.2 C. The active material mass loading >16 mg cm^{-2}. e) The comparison of cell calendar life, active material mass loading and cell capacity with recently reported zinc-ion batteries. More details are listed in **Table D4**. 162

Figure 7.6. The standard deviations of a) cycling performance and b) Coulombic efficiency of BMO cathodes in 2 M $ZnSO_4$/0.2 M $MnSO_4$ electrolyte at 0.2 C. The active material mass loading >16 mg cm^{-2}. These plots are calculated based on three cells. 163

Figure 7.7. a) The standard deviations of cycling performance of BMO (ε) cathodes in coin-type batteries at 0.5 C. The active material mass loading >9 mg cm^{-2}. The standard deviation in this plot is calculated based on three cells. Cycling performance

of ε-MnO_2 and BMO (ε) cathodes in large batteries with 2 M $ZnSO_4$/0.2 M $MnSO_4$ electrolyte at the current densities of b) 0.5 C, c) 2 C and d) 5 C. The active material mass loading >20 mg cm^{-2}. 164

List of Tables

Table 1.1. The performance comparison of different battery systems[9–12]. 4

Table 1.2. Properties comparison of LIBs and RAZBs.....8

Table 3.1. Element detection limit for ICP-OES. 62

Table 4.1. pH level and ion conductivity of three electrolytes (at room temperature). 74

Table 4.2. Molar ratio of Zn:Na for each ZNVO material. 75

List of Abbreviations

AC	Alternating current
ARBs	Aqueous rechargeable batteries
BET	Brunauer-Emmett-Teller analysis
CNTs	Carbon nanotubes
CV	Cyclic voltammetry
EDS	Energy-dispersive X-ray
EIS	Electrochemical impedance spectroscopy
ESW	Electrochemical stability window
EV	Electric vehicle
FT-IR	Fourier transform infrared spectroscopy
GCD	Galvanostatic charge-discharge
GITT	Galvanostatic intermittent titration technique
GIXRD	2D synchrotron grazing-incidence X-ray diffraction
HER	Hydrogen evolution reaction
HRTEM	High-resolution transmission electron microscopy
HVO	Hydrated vanadate
ICP-OES	Inductively coupled plasma optical emission spectrometry
LIBs	Lithium-ion batteries
LP	Linear polarization
LSV	Linear sweep voltammetry
NHVO	Ammonium vanadate
Ni-Cd	Nickel-cadmium batteries

Ni-MH	Nickel-metal hydride batteries
NVO	Sodium vanadate
OER	Oxygen evolution reaction
PANI	Polyaniline
RAZBs	Rechargeable aqueous zinc-ion batteries
R_{ct}	Charge transfer resistance
R_i	Interfacial resistance
R_s	Equivalent serial resistance
SDS	Sodium dodecyl sulfate
SEI	Solid electrolyte interface
SEM	Scanning electron microscopy
SHE	Standard hydrogen electrode
STEM-EDS	Energy dispersive X-ray spectroscopy in scanning transmission electron microscopy
XPS	X-ray photoelectron spectroscopy
XRD	X-ray diffraction
ZIBs	Zinc-ion batteries
ZSH	Zinc sulfate hydroxide
ZVO	Zinc vanadate

Chapter 1. Introduction

1.1. Background

Since the dawn of the industrial revolution, the extensive development and utilization of fossil fuels have been pivotal in advancing human civilization. However, this progress has come at a cost: depletion of resources, environmental pollution, and climate change, posing serious challenges to sustainable development. In response, there is a global shift towards an ecological civilization, marking a significant transformation in energy use and innovation. This transformation is essential for nations worldwide to overcome these challenges and achieve sustainable growth. A key aspect of this transformation is the evolving role of hydrocarbon fuels, such as oil and natural gas. While they remain an integral part of the energy system, particularly in large energy demand centers, a gradual decline in their demand is evident[1]. In contrast, electricity is emerging as a central player in the energy landscape and is becoming increasingly vital for everyday needs-mobility, cooking, lighting, heating, and cooling-due to its efficiency and reliability. The 2024 Electricity Report highlights a surge in global electricity demand, projecting an increase from 2.2% in 2023 to an average of 3.4% in 2026[1] (**Figure 1.1**a). It is estimated that by 2026, China's electricity demand will grow significantly to exceed 50% of the European Union's current total annual electricity consumption (**Figure 1.1**b).

This increased demand for electricity is propelling clean energy technologies to the forefront, with a sustained thrust from their indisputable economic merits. The price index for clean energy equipment, including battery storage and electric vehicle (EV) batteries, has shown a significant downward trajectory, with costs significantly reducing from 2014 to 2022[2] (**Figure 1.1**c). This trend reaffirms the critical position of battery technology in the transition to a clean energy economy. The World Energy Outlook 2023 underscores the meteoric rise of the battery sector, forecasting its market dominance by 2050[2,3] (**Figure 1.1**d). This forecast has sparked a surge in battery-centric research and development, establishing the

battery technology not merely as a fleeting trend but as a cornerstone of our clean energy future. The sector's competitive pricing and cutting-edge developments are setting the stage for a world where sustainable energy is not just aspirational but a tangible reality.

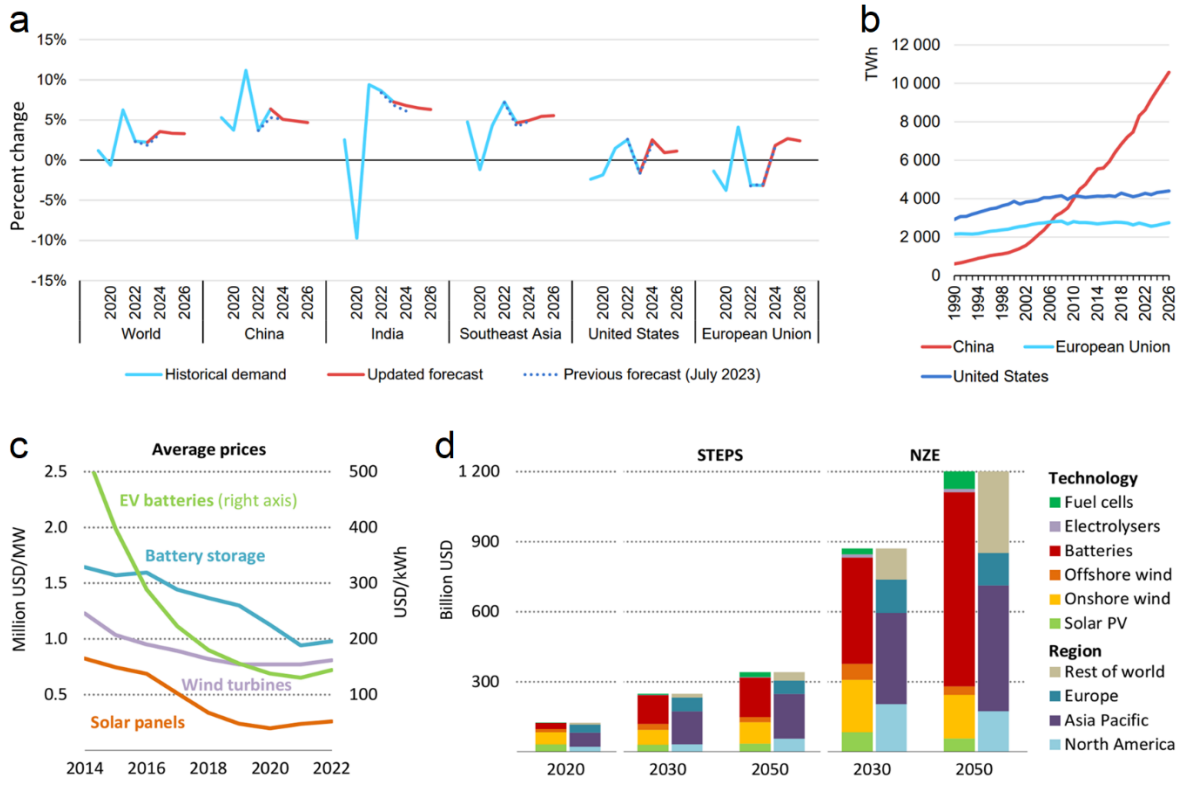


Figure 1.1. a) Year-on-year percent change in electricity demand in selected regions, 2019-2026[1]. b) Total electricity demand in China, European Union, and the United States, 1990-2026[1]. c) Recent cost developments for selected clean energy technologies, 2014-2022[2]. d) Estimated market size for selected clean energy technologies by technology and region, 2020-2050[3]. STEPS: Stated Policies Scenario; NEZ: Net Zero Emissions by 2050 Scenario.

1.2. Rechargeable Batteries

A rechargeable battery, also called secondary battery, is a device that reversibly converts electrical energy into chemical energy and stores the resulting energy in a cell[4]. A typical rechargeable battery consists of a positive electrode (cathode), a negative electrode (anode), and an electrolyte. Nestled between the cathode and anode is a porous membrane separator, which is crucial in preventing direct electrical contact between two electrodes while permitting the flow of electrolytes[4]. Thus, when a rechargeable battery is connected to an output electrical device, it sets off a series of redox reactions at each electrode, releasing the

stored energy. Rechargeable battery system has become an essential development direction for today's energy storage technologies. An array of these battery systems—ranging from Nickel-cadmium (Ni-Cd) and Nickel-metal hydride (Ni-MH) to Lead-acid and the more advanced Lithium-ion batteries (LIBs)—has been extensively adopted across various sectors, including EVs, portable electronics, and broader energy storage infrastructures (**Figure 1.2**a)[5–7]. Despite their widespread use, current electrochemical energy storage solutions face challenges in meeting market demands, particularly when it comes to longevity, energy density, environmental impact, and safety. As shown in **Figure 1.2**b and **Table 1.1**, Ni-Cd, Ni-MH, and Lead-acid batteries grapple with inherent limitations such as low power density, limited operational lifespans, and serious environmental hazards, that have hindered their development[5–7]. Conversely, LIBs, which boast high energy density and extended cycle life, are regarded as the frontrunners of electrochemical energy storage, especially used in EVs. Conventional vehicles are powered by internal combustion engines (ICEs), which rely on the combustion of fossil fuels such as gasoline or diesel. This combustion process results in the emission of greenhouse gases and pollutants, including carbon dioxide (CO_2), nitrogen oxides (NO_x), and particulate matter (PM). These emissions significantly exacerbate air pollution and contribute to climate change, presenting substantial environmental and public health challenges. In contrast, EVs are driven by electric motors and utilize energy stored in batteries. EVs offer a significant advantage in terms of emissions, as they produce zero tailpipe emissions. This capability substantially reduces local air pollution and contributes to a decrease in overall greenhouse gases emissions. The environmental benefits of EVs underscore the importance of advancing battery technology to maximize these advantages.

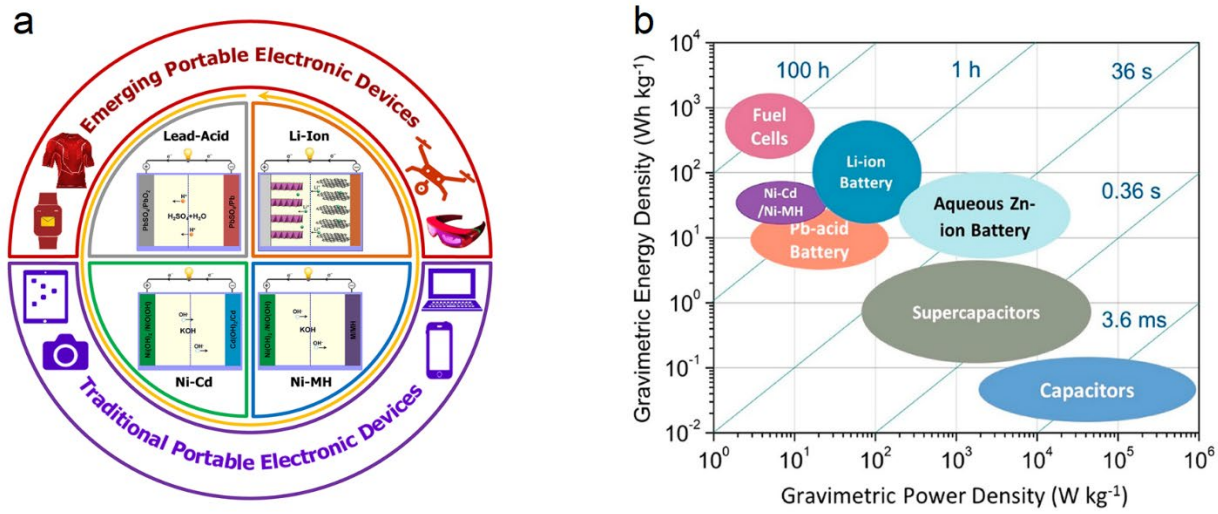


Figure 1.2. a) Schematic illustration of representative rechargeable batteries and their applications in traditional and emerging portable electronic devices[5]. b) Ragone plot of various energy storage systems. The times marked on the blue axes represent reaction kinetics[8].

Table 1.1. The performance comparison of different battery systems[9–12].

Battery systems	Energy density (Wh kg^{-1})	Lifespan (cycles)	Voltage (V)
Ni-Cd	45-80	300-2000	1.2
Ni-MH	60-120	180-2000	1.25
Lead-acid	33-42	200-300	2.1
Li-ion	200-300	400-1200	3.2-5.0

However, despite these benefits, there are some significant risks associated with LIBs commonly used in EVs. One of the primary concerns is the potential for fire hazards. This risk primarily arises from the phenomenon of thermal runaway, where a self-sustaining reaction causes a rapid and uncontrollable increase in temperature and pressure[13–15]. Such reactions can be triggered by physical damage, overheating, or internal short circuits. The presence of flammable electrolytes and the exothermic nature of the chemical reactions further exacerbate the fire risks associated with LIBs. In addition to fire risks, LIBs contain hazardous materials such as lithium and cobalt. These materials, while essential for battery performance, pose health risks during both battery use and disposal[16]. The environmental

impact of LIBs is also a critical concern. The extraction and processing of lithium and cobalt are linked to substantial ecological damage. Furthermore, the disposal of LIBs poses significant environmental challenges. Improper disposal can result in the leaching of toxic substances into soil and water systems, compounding environmental degradation[17,18]. Moreover, the economic implications of LIBs are non-negligible. The high cost of raw materials, combined with the complex and resource-intensive manufacturing processes, contribute to the elevated cost of LIBs. These economic factors, coupled with the financial burden associated with safe disposal, impact the overall cost-effectiveness and sustainability of LIB technology[19,20]. Therefore, exploring alternative battery systems that can mitigate these drawbacks is essential for the future of energy storage. Newer technologies, such as aqueous rechargeable batteries, offer promising solutions. These batteries not only have the potential to reduce production costs and significantly enhance safety but also may provide energy densities that rival or exceed those of current energy storage systems. By addressing the key hazards of LIBs, these advanced battery systems pave the way for a safer and more efficient generation of energy storage technology.

1.3. Rechargeable Aqueous Zinc-ion Batteries

Compared to LIBs that utilize organic electrolytes, aqueous rechargeable batteries (ARBs) offer several notable advantages. Primarily, ARBs are inherently safer due to their use of water-based electrolytes, which significantly reduces the risk of flammability and chemical hazards associated with organic solvents. Additionally, ARBs are more environmentally friendly, as water is a benign solvent and often results in less environmental impact during production and disposal. Moreover, the ionic conductivity (10^{-1}–6 S cm^{-1}) of aqueous electrolyte soars at a rate two orders of magnitude higher than the organic electrolytes (10^{-3}–10^{-2} S cm^{-1})[21–23]. In terms of cost, ARBs offer a substantial advantage; they utilize inexpensive and abundant materials, reducing the overall production costs compared to lithium-ion batteries, which require more expensive raw materials and complex manufacturing processes. ARBs that utilize multivalent ions are theoretically capable of

delivering higher specific capacities and energy densities, which is attributed to the multi-electron transfer characteristic of their redox processes[21]. Therefore, rechargeable batteries with aqueous electrolytes are increasingly applied in various fields, characterized by their safety, environmental sustainability and cost-effectiveness[21,23,24]. These include large-scale energy storage systems, which benefit from the unrestricted space and construction scope and economical materials of aqueous batteries for grid stabilization purposes. Their utility extends to renewable energy integration, where they efficiently store surplus energy from intermittent sources such as solar and wind power. Furthermore, ARBs will be promising in portable electronics and electric vehicles due to their potentially for high energy density and rapid charging capabilities.

Within the category of ARBs, rechargeable aqueous zinc-ion batteries (RAZBs) are particularly notable for research and development. As illustrated in **Figure 1.3**a, Zn^{2+} ions offer power and energy densities comparable to those of Li^{+} ions, making RAZBs a compelling subject in battery technology. Additionally, due to a lower redox potential (-0.763 V vs. standard hydrogen electrode (SHE))[25,26], zinc metal demonstrates high stability in aqueous environment, surpassing both lithium and sodium. Although magnesium and aluminum metals have attractive specific capacities, their reversibility in aqueous solutions is limited, as illustrated in **Figure 1.3**b. The historical development of zinc-based primary batteries, such as Zn-Air, Zn-NiOOH, and Zn-MnO_2, underscores the maturity and commercial viability of zinc technology (**Figure 1.3**c). Specifically, alkaline Zn-MnO_2 batteries have dominated the primary battery (non-rechargeable battery) market due to their reliability[27,28]. However, early attempts to develop rechargeable alkaline Zn-MnO_2 batteries faced challenges, including poor cycling performance and limited charge/discharge depth due to issues like zinc dendrite formation and irreversible by-products[28–31]. A breakthrough occurred in 1988 when Shoji et al. reported a rechargeable aqueous Zn-MnO_2 battery using a neutral or mildly acidic electrolyte, paving the way for future RAZB advancements[32].

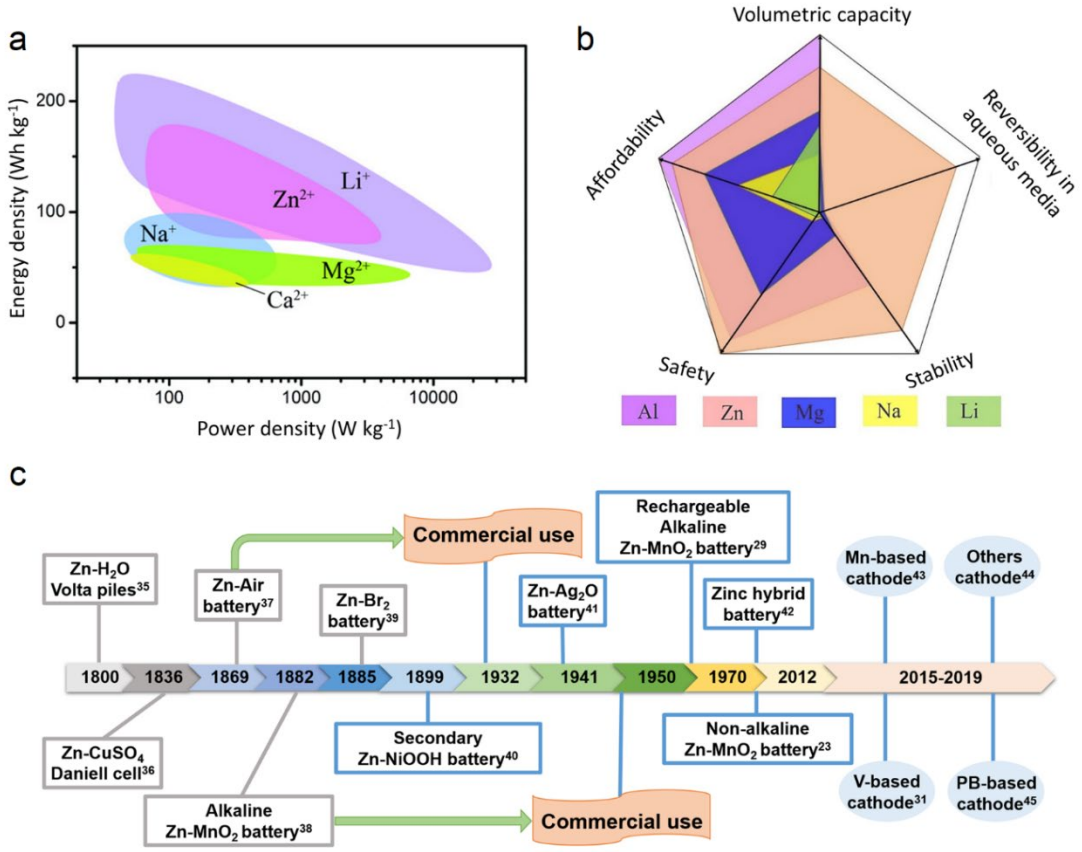


Figure 1.3. a) Ragone plot of energy storage systems in mild aqueous electrolyte system with different energy carriers[24]. b) Radar diagram of Zn property regimes: compared with other metals, Zn shows capacity advantages, high stability, and good reversibility in aqueous electrolyte[25]. c) Timeline of the Zn-based batteries development history[28,30,33–44].

Furthermore, economically, RAZBs are more advantageous due to their lower production costs, with estimates ranging from 25-135 USD kWh^{-1}, compared to LIBs, which cost between \$150-300 USD kWh^{-1} (**Table 1.2**). Moreover, commonly used cathode materials for LIBs include lithium cobalt oxide ($LiCoO_2$) and nickel-cobalt-manganese (NCM) oxides, with prices ranging from 50-100 USD kg^{-1} and 40-80 USD kg^{-1}, respectively. In contrast, RAZBs typically use manganese dioxide (MnO_2) and vanadium pentoxide (V_2O_5), with costs around 2-10 USD kg^{-1} and 30-60 USD kg^{-1}, respectively. Although RAZBs generally have a lower energy density (70-140 Wh kg^{-1}) compared to LIBs (200-300 Wh kg^{-1}), their favorable properties, including longer cycle life (2000-3000 cycles for RAZBs vs. 400-1200 cycles for LIBs) and environmental benefits, position them as a promising and sustainable alternative to traditional lithium-ion technology.

Table 1.2. Properties comparison of LIBs and RAZBs.

Property	LIBs	RAZBs	Ref
Cost	Higher (150-300 USD kWh^{-1})	Lower (25-135 USD kWh^{-1})	45,46
Cathode Materials	$LiFePO_4$ (10-20 USD kg^{-1}) NCM (40-80 USD kg^{-1}) $LiCoO_2$ (50-100 USD kg^{-1})	MnO_2 (2-10 USD kg^{-1}) V_2O_5 (30-60 USD kg^{-1})	47–49
Safety	Flammable organic solvents; thermal runaway risk	Non-flammable; aqueous electrolytes	20,50
Environmental Impact	High hazards due to extraction and disposal of harmful materials	Low hazards due to abundant materials and benign electrolytes	16,50
Energy Density	200-300 Wh kg^{-1}	70-140 Wh kg^{-1}	47,51,52
Cycle Life	400-1200 cycles	2000-3000 cycles *(more stable in aqueous environments)*	53,54

Chapter 2. Literature Review

The charge storage mechanism of RAZBs is predominantly dependent on the shuttling of Zn^{2+} ions back and forth between the cathode and anode. Within the electrolyte, Zn^{2+} ions migrate to the cathode, which serves as a host for their insertion and extraction. Simultaneously, the zinc anode facilitates the reversible deposition and dissolution of zinc, a process commonly referred to as plating/stripping, as depicted in **Figure 2.1**a. Contemporary research and development efforts for RAZBs have been mainly focused on innovations of cathode and anode materials, improvements in electrolyte compositions, and studies of battery mechanisms. This chapter aims to comprehensively present the most significant and recent advancements in these pivotal areas.

2.1. Cathode Materials for the RAZB System

The journey toward the practical application of RAZBs is fraught with significant obstacles, the foremost one is to find a cathode material that can deliver a high capacity and maintain structural stability during Zn^{2+} ion storage. The quest is complicated by the relatively small radius of Zn^{2+} ion (0.74 Å), which intensifies the electrostatic interactions with the crystal lattice of the cathode material, and such interactions are markedly stronger than those involving monovalent ions[55,56]. Despite these complexities, the pursuit of suitable cathode materials has made significant progress through relentless research. Promising candidates have emerged, predominantly among manganese-based oxides[57–59], vanadium-based oxides[60–63], Prussian blue analogs[44,64], and polyanion compounds[65–67]. These materials have not only proven to be cost-effective but also suitable for RAZBs. Furthermore, both manganese-based and vanadium-based materials have exhibited superior operating voltages and specific capacities compared to other cathode materials (**Figure 2.1**b). Therefore, I chose to study vanadium-based and manganese-based materials for my PhD research topic and I will detail the recent research advances in these two cathode materials in this chapter.

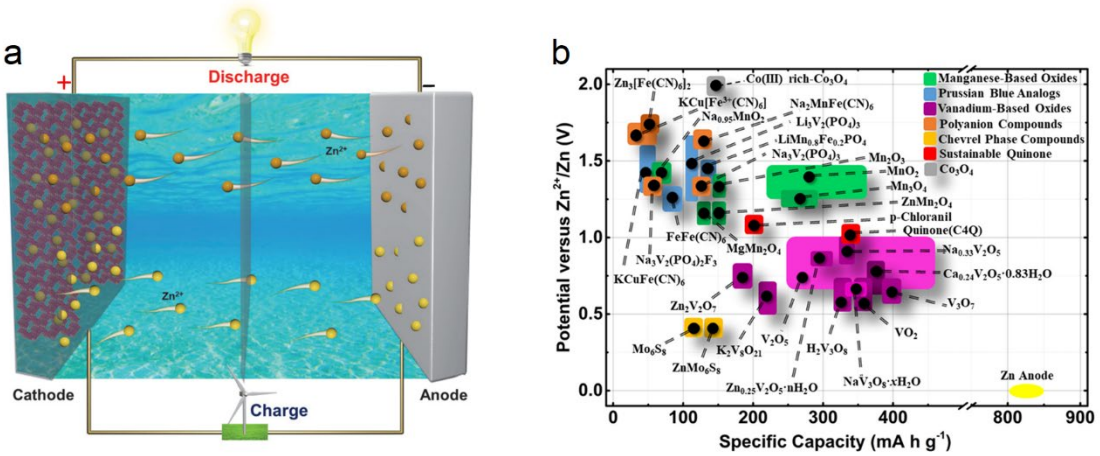


Figure 2.1. a) Schematic illustration of RAZBs[68]. b) Operating voltage vs. specific capacity for various cathode materials presently used for RAZBs[50].

2.1.1. Vanadium-based materials

Vanadium-based compounds have long been the subject of research as prospective cathode materials for diverse battery systems. With its abundant resources, vanadium has four oxidation states (V^{2+}, V^{3+}, V^{4+} and V^{5+}), which correspond to a series of oxides (VO, V_2O_3, VO_2 and V_2O_5), as well as a variety of mixed valence oxides such as V_6O_{13}, V_4O_9, V_3O_7[69,70]. The vanadium pentoxide (V_2O_5) is of particular interest due to its unique layered structure and superior electrochemical properties (**Figure 2.2**). The crystal structure of V_2O_5 reveals VO_5 square pyramids composed of vanadium and oxygen atoms interconnected via V-O bonds that are shared across edges and corners, thus forming V_4O_{10} layers[69]. These layers are held together by Van der Waals forces, which contribute to the unique layered structure of V_2O_5[71,72]. The generous interlayer spacing within this open framework is 4.4 Å, significantly larger than the 0.74 Å radius of Zn^{2+} ion, thus facilitating the Zn^{2+} insertion and extraction[71–73]. However, the structural integrity of V_2O_5 faces challenges during the repeated insertion and extraction of Zn^{2+} ions. The Van der Waals forces, responsible for maintaining the layered architecture, weaken over time, which adversely impacts the battery cycling stability. Furthermore, the inherent low electronic conductivity of V_2O_5, the structural instability under cycling conditions, and the pronounced solubility in acidic aqueous electrolytes present additional barriers for its application in RAZBs. Therefore, it is paramount to engage in the

meticulous design and optimization of V_2O_5 material to improve its electrochemical performance. In the forthcoming sections, I will delve into several typical modification approaches, including morphological and structural engineering, interlayer spacing enhancement, and composite material construction, each of which can contribute to the advancement of V_2O_5 cathode material for RAZBs.

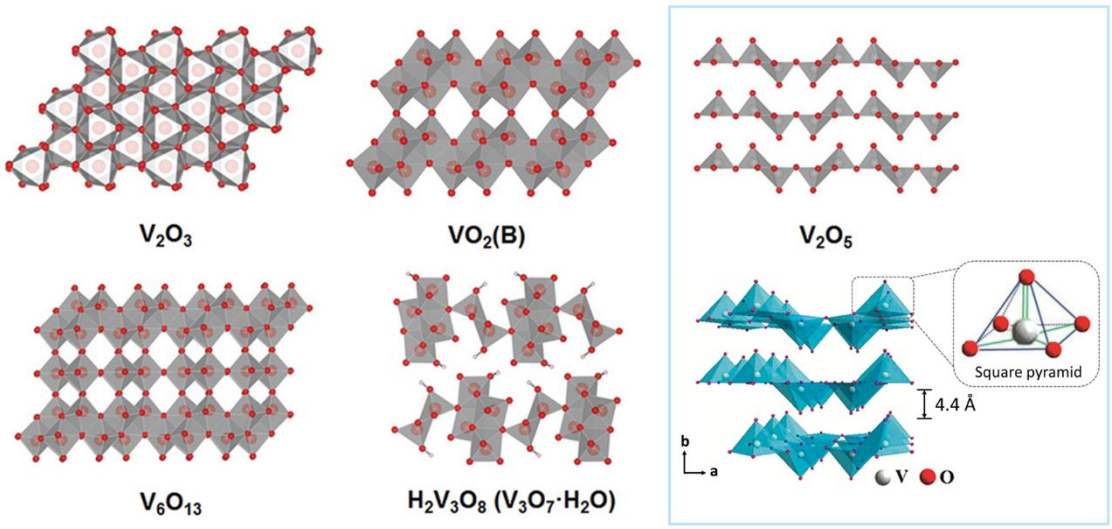


Figure 2.2. The crystal structures of typical vanadium oxides: V_2O_3, VO_2, V_6O_{13}, $H_2V_3O_8$ (V_3O_7•H_2O), and V_2O_5[70]. In the blue box is a schematic illustration of V_2O_5 crystal structure with VO_5 square pyramids[21].

2.1.1.1. Morphological and structural engineering

The exploration of diverse V_2O_5 nanostructures is warranted, given that the size and morphology of electrode materials are critical determinants of battery performance. Nanostructured materials, such as fibers, rods, sheets, flowers, and hollow spheres, possess increased specific surface areas. This increase enhances the contact between the electrode materials and electrolytes, subsequently shortening the diffusion path for ions/electrons and providing a greater number of active sites for ion insertion. Moreover, these structures can mitigate the volumetric changes associated with Zn^{2+} insertion and extraction[74–78]. Chen et al. synthesized porous V_2O_5 nanofibers (**Figure 2.3**a), delivering a high reversible capacity of 319 mAh g^{-1} at a current density of 0.02 A g^{-1}, with a capacity retention of 81% after 500 cycles in 1 M $Zn(CF_3SO_3)_2$ electrolyte. The porous structure, with a substantial specific

surface area of 27.08 m^2 g^{-1}, enabled effective electrolyte infiltration[75]. Another one-dimensional (1D) material, a rod-like anhydrous V_2O_5 material with an expansive surface area of 218 m^2 g^{-1} (**Figure 2.3**b), was fabricated by Wong and his colleagues by using tiny nanosheets. This material demonstrated exceptional reversible capacity (449.8 mAh g^{-1} at 0.1 A g^{-1}), sustained cyclability (86.8% capacity retention after 2000 cycles at 2 A g^{-1}) and high rate performance (314.3 mAh g^{-1} at 2 A g^{-1}) with a 3 M $Zn(CF_3SO_3)_2$ electrolyte. Its electrochemical excellence was attributed to the high Zn^{2+} ion diffusion coefficient, the significant capacity contribution of pseudocapacitance, and the swift electrochemical kinetic due to its structural composition[76]. However, the utilization of costly electrolytes escalates the overall production costs, impacting the cost-efficiency of the battery systems. For a 10 mL solution, for example, a 1 M or 3 M $Zn(CF_3SO_3)_2$ electrolyte would cost 25-75 CAD, while a 2 M $ZnSO_4$ electrolyte would only cost 0.7 CAD or less (reference price from Sigma-Aldrich).

Three-dimensional (3D) V_2O_5 materials can be crafted with core-shell or hollow structures through solvothermal methods under certain conditions. Notably, the hollow spheres (**Figure 2.3**c) and porous yolk–shell microspheres (**Figure 2.3**d) developed by Yang's and Li's groups, respectively, have showed substantial improvements in both reversible capacity and rate performance. These spherical materials outperformed commercial V_2O_5 by exhibiting reduced Zn^{2+} transfer resistance and maintaining structural integrity through the cycling process. The hollow spherical architecture offers multifaceted advantages: it enriches Zn^{2+} intercalation sites, expedites electrolyte permeation, an thus, fosters reaction kinetics[78]. In addition, it alleviates structural stress during Zn^{2+} insertion, preventing structural collapse. Li's group discerned that the yolk-shell microsphere could induce a phase transition (from V_2O_5 to V_2O_5•nH_2O) that expands the layer spacing from 4.4 Å to 13.45 Å, which is attributed to the co-insertion of H^+/Zn^{2+} ions during the material activation process (i.e., activating the material with a small current density)[79]. Consequently, the enhanced battery performance may also depend on material phase transitions during cycling. Nevertheless, a caveat emerges: an excessive specific surface area could accelerate the dissolution of V_2O_5 material, suggesting that an unyielding focus on maximizing surface area is imprudent. Future

research should pivot towards alternative methodologies to develop advanced vanadium-based materials, avoiding the pitfalls associated with an overemphasis on surface area enhancement.

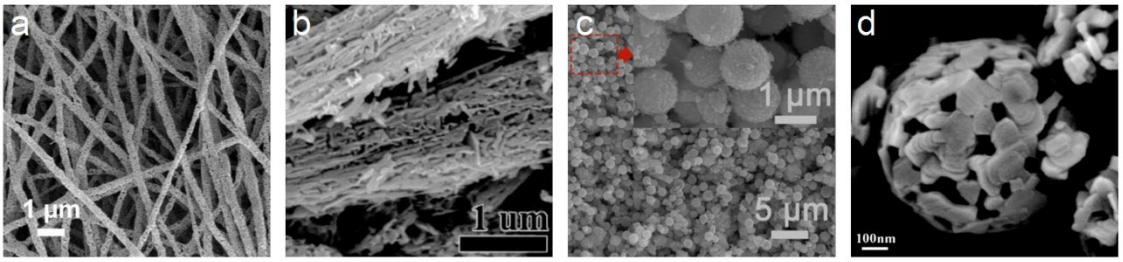


Figure 2.3. V_2O_5 cathode materials with different types of nanostructures: (a) nanofibers[75], (b) nanorods[76], (c) hollow nanospheres[78], (d) porous V_2O_5 yolk-shell microspheres[79].

2.1.1.2. Interlayer spacing enhancement

In the V_2O_5 cathode material, the weakening of Van der Waals forces that maintain the layered structure upon repeated ion intercalation necessitates an intervention through intercalation chemistry. This approach involves the incorporation of various guest ions or molecules into the V_2O_5 interlayer space as "pillars" to enhance its structural integrity through coordination, electrostatic repulsion, or binding interactions[80–82]. The pre-intercalation strategy has emerged as a pivotal technique to augment the physicochemical properties of layered materials. Current research classifies guest species for pre-intercalation into categories such as metal ions, non-metal ions, organic molecules, and structured water, each contributing uniquely to the enhancement of the host material properties.

A multitude of studies have investigated the pre-insertion of monovalent ions like Li^+, K^+, Na^+, Ag^+ into layered V_2O_5[61,83–92]. Among these, Na^+ ion, with its lower relative molecular mass, is preferred for bolstering specific capacity. Ling et al. engineered $Na_{0.56}V_2O_5$ (NVO) with a nanobelt morphology, achieving a high initial discharge capacity of 317 mAh g^{-1} at 0.1 A g^{-1} and subsequently increased the current density to 0.5 A g^{-1}, attaining 84% capacity retention after 200 cycles (**Figure 2.4**a). This material benefitted from the chemical pre-insertion of Na^+ ions, which induced an expansion of the layer spacing and heightened electrical conductivity[85]. Chen's group assessed the impact of K^+ ion pre-insertion levels on

electrochemical behavior, discovering that optimal K^+ ion doping inhibited cathode dissolution. However, an excessive K^+ ion content (x>0.5 in $K_xV_2O_5$) could disrupt the nanowire structure, detrimentally affecting the battery performance (**Figure 2.4**b)[88]. In contrast to monovalent cations, cations with more charges, i.e. divalent alkaline earth cations (Mg^{2+}, Ca^{2+} and Ba^{2+}), trivalent Al^{3+} ions and tetravalent Sn^{4+} ion, introduce stronger ionic bonds with the O atoms of the host structure, enhancing structural robustness[62,63,93–98]. Transition metal cations such as Zn^{2+}, Co^{2+}, Fe^{2+}, Ni^{2+}, Mn^{2+} and Cu^{2+} have also been incorporated into layered V_2O_5 to improve the reversibility of Zn^{2+} de-/intercalation[22,99–104]. As shown in **Figure 2.4**c, Huang's group demonstrated a vanadium oxide bronze cathode material enriched with intercalated water molecules (H_2O) and Zn^{2+} ions, which addressed the inherent defects of the material, targeting slow diffusion kinetics, low electrical conductivity, and structural instability to achieve superior cyclability and improved capacity retention[99]. The inclusion of H_2O molecules within the host matrix also exhibited beneficial effects on Zn^{2+} ion diffusion, where intercalated H_2O in $Zn_{0.25}V_2O_5•nH_2O$ (ZnVO) (**Figure 2.4**d) reduced charge transfer activation energy at the electrode interface and mitigated strong electrostatic interactions between the framework and Zn^{2+} ions[22]. Besides metal ions, non-metal cations (e.g. NH_4^+) and organic molecules (e.g. conductive polyaniline, THF, PEDOT, etc.) have also served as guest species for V_2O_5 intercalation[105–110]. Fu's team reported on $(NH_4)_{0.58}V_2O_5•0.98H_2O$ (NHVO) nanobelts, achieving an expanded interlayer spacing conducive to hydrated Zn^{2+} intercalation (**Figure 2.4**e)[105]. Subsequently, Zhang et al. fine-tuned the quantity of polyaniline (PANI) in PANI/V_2O_5 (**Figure 2.4**f) composites, attaining a significant interlayer spacing of 13.82 Å and an enhanced specific capacity of 353.6 mAh g^{-1} at 0.1 A g^{-1} [108]. Despite these advancements, the challenge of achieving a higher working voltage persists, with many Zn//vanadium-based oxide cells operating below the desired 1.0 V threshold.

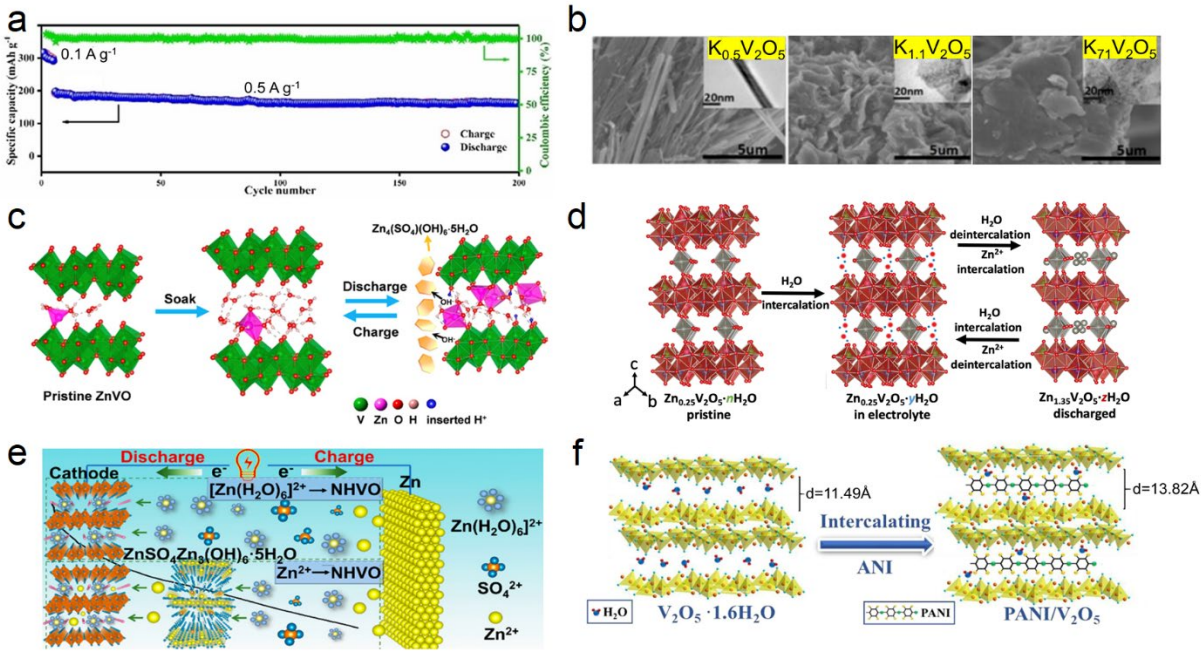


Figure 2.4. a) Cycling stability of the NVO at 0.1 and 0.5 A g^{-1} [85]. b) SEM images of the effects of different K^+ intercalation amounts[88]. Schematic illustration of c) Zn^{2+} storage mechanism of $Zn_{0.1}V_2O_5$•$n$$H_2O$ cathode[99], d) reversible H_2O molecules intercalation into $Zn_{0.25}V_2O_5$•$n$$H_2O$ cathode in aqueous electrolyte, and the H_2O deintercalation accompanying Zn^{2+} intercalation during discharge process[22], e) hydrated Zn^{2+} ($Zn(H_2O)_6^{2+}$) intercalation process into NHVO cathode[105], f) synthesis process of the PANI/V_2O_5 composite[108].

2.1.1.3. Composite material construction

The de-/intercalation kinetics of divalent Zn^{2+} ions within the crystal lattice of cathode materials such as V_2O_5 are inherently hindered by strong electrostatic interactions. This sluggishness is compounded by its relatively low electronic conductivity, leading to substantial resistive polarization and compromised rate performance in RAZBs[71,111]. To surmount these obstacles, the integration of carbon materials with V_2O_5 to construct composite materials has been explored, leveraging the exceptional electrical conductivity, chemical robustness, and structural versatility of carbon[112–115]. Yang's team employed a straightforward solvothermal approach to synthesize a V_2O_5@carbon nanotubes (V_2O_5@CNTs) composite (as depicted in **Figure 2.5**a), achieving an 72% capacity retention over 6000 cycles at a high current density of 5 A g^{-1}. The embedded CNTs within this composite facilitate the formation of electron conduction networks, markedly diminishing

charge transfer resistance and polarization[116]. Nonetheless, the fabrication of such composites, often through the blending of carbon nanoparticles or via phase separation, is predominantly surface-level work. This method may result in uneven modifications and presents challenges in achieving uniform enhancements. Chen et al., capitalizing on the benefits of a carbon network infrastructure, implemented a mild chitosan-assisted hydrothermal method to fabricate a carbon@V_2O_5 (C@V_2O_5) network (illustrated in **Figure 2.5**b). The cathode material of the resultant RAZB exhibited a specific capacity of 361 mAh g^{-1} at a current density of 0.5 A g^{-1} [117]. Beyond optimizing the electrical conductivity, the carbon network structure effectively shortened the diffusion pathway for Zn^{2+} ions, thus expediting the storage of Zn^{2+} ions within the electrode matrix. This innovation in material engineering showcases the potential for advanced composite cathode materials to enhance the efficacy and longevity of RAZBs.

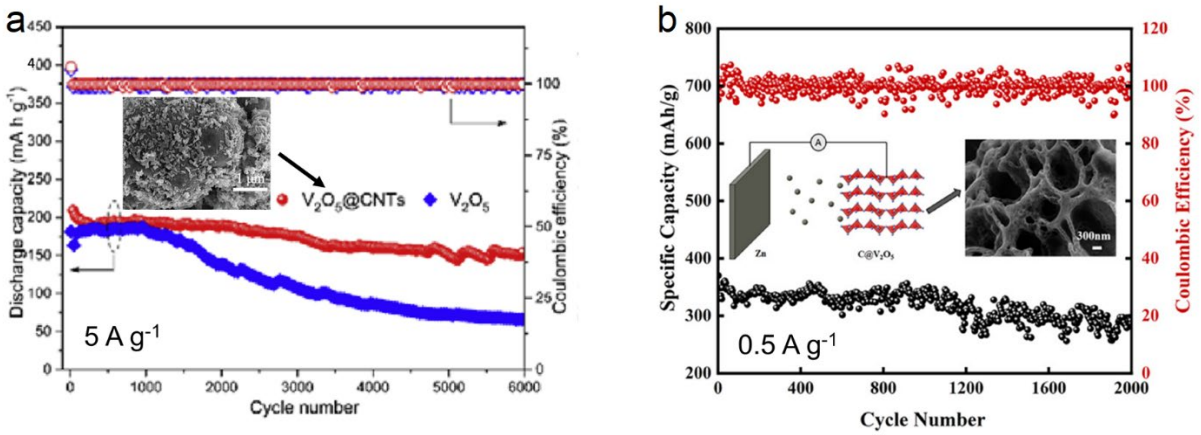


Figure 2.5. a) Cycle performance of V_2O_5@CNTs and pure V_2O_5 electrodes at 5 A g^{-1}, inset is the morphology of V_2O_5@CNTs sample[116]. b) Cycle performance of C@V_2O_5 at 0.5 A g^{-1}, inset is the morphology of C@V_2O_5 sample[117].

2.1.2. Manganese-based materials

In the realm of RAZBs research, manganese-based materials are increasingly being acknowledged as an exemplary cathode choice alongside vanadium-based materials. Manganese oxides, endowed with a high theoretical capacity of 308 mAh g^{-1} stemming from the single electron transition between Mn^{4+} and Mn^{3+}, offer operational voltages in the range

of 0.8–1.8 V. Their low-cost, non-toxicity, abundant availability and multivalent states (Mn^x, x = 0, 2+, 3+, 4+, and 7+) further bolster their appeal[118–121]. To date, extensive investigations into RAZBs have focused on MnO_2, Mn_2O_3, and Mn_3O_4 as promising cathode materials. Moreover, various polymorphic forms of MnO_2, such as α-MnO_2, β-MnO_2, γ- MnO_2, λ-MnO_2, δ-MnO_2, and todorokite-type MnO_2, have been explored for their Zn^{2+} ion storage capabilities[28,122–128]. As delineated in **Figure 2.6**, at the core of MnO_2 polymorphs lies the [MnO_6] octahedral unit, comprising a central Mn^{4+} ion encircled by six O atoms. The α, β, and γ polymorphs exhibit 1D tunnel-like structures of varying sizes, 2×2 (4.6× 4.6 $Å^2$), 1×1 (2.3×2.3 $Å^2$), and randomly arranged 1×1 and 1×2 tunnels, respectively. The λ-MnO_2 variant presents a 3D spinel structure, while δ-MnO_2 is distinguished by its two-dimensional (2D) interlayered composition with larger interlayer spacing (about 7 Å)[48,129,130]. The interconnected hexagonal oxide ions within these [MnO_6] octahedra can accommodate Zn^{2+} ions within their tunnel-like or layered structures. Given the direct impact of crystal structure on material properties, the MnO_2 polymorphs exhibit distinct reaction mechanisms and electrochemical behaviors within RAZBs. Empirical studies have verified that the β-MnO_2 (1×1 tunnel, rutile structure) is the most thermal stable form of MnO_2 polymorph, and its crystalline form can be maintained up to 500°C[131]. For the purposes of this study, β-MnO_2 has been selected for an in-depth analysis, which will be expounded upon in subsequent sections.

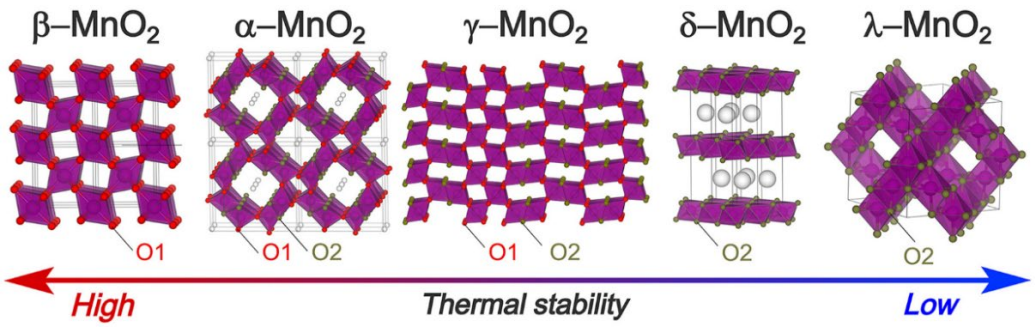


Figure 2.6. Schematic diagram of the order of thermal stability of MnO_2 polymorphs. Ranking as β > α > γ > δ ≅ λ[131].

2.1.2.1. Crystal phase control

β-MnO_2, with its distinctive 1×1 tunnel structure formed by vertex-sharing octahedral [MnO_6] chains, is acknowledged as the most thermodynamically stable polymorph of MnO_2. Nevertheless, the restricted size of these tunnels imposes limitations on the material capacity for Zn^{2+} ion storage, resulting in a discharge capacity that is inferior to some other polymorph (e.g., α-MnO_2)[33]. Chen et al. have observed that during the initial discharge, β-MnO_2 undergoes a structural transformation into a layered phase, which then accommodates reversible Zn^{2+} insertion/extraction[132]. This transformation is evidenced by *ex situ* X-ray diffraction (XRD) patterns, which reveal the reduction of characteristic β-MnO_2 peaks and the emergence of a new Zn-buserite phase during the first discharge, as shown in **Figure 2.7**a. The mechanism for the Zn-MnO_2 cell employing a $CF_3SO_3^-$-based aqueous electrolyte is schematically depicted in **Figure 2.7**b. Here, the initial discharge induces the transition of tunneled β-MnO_2 to a layered Zn-buserite structure, enabling the subsequent reversible intercalation and de-intercalation of Zn^{2+} ions within the water-incorporating Zn-buserite framework. Moreover, Islam S et al. have pioneered the use of β-MnO_2 nanorods as a cathode material for zinc-ion batteries (ZIBs), synthesized via a microwave-assisted hydrothermal method[124]. After 200 cycles, the cathode retains a discharge capacity of 135 mAh g^{-1}, indicating a capacity retention of three-quarters while maintaining a Coulombic efficiency of 100% (**Figure 2.7**c). This research underscores the dynamic structural behavior of β-MnO_2 in ZIBs and its potential for high-efficiency energy storage when subjected to a suitable electrochemical environment.

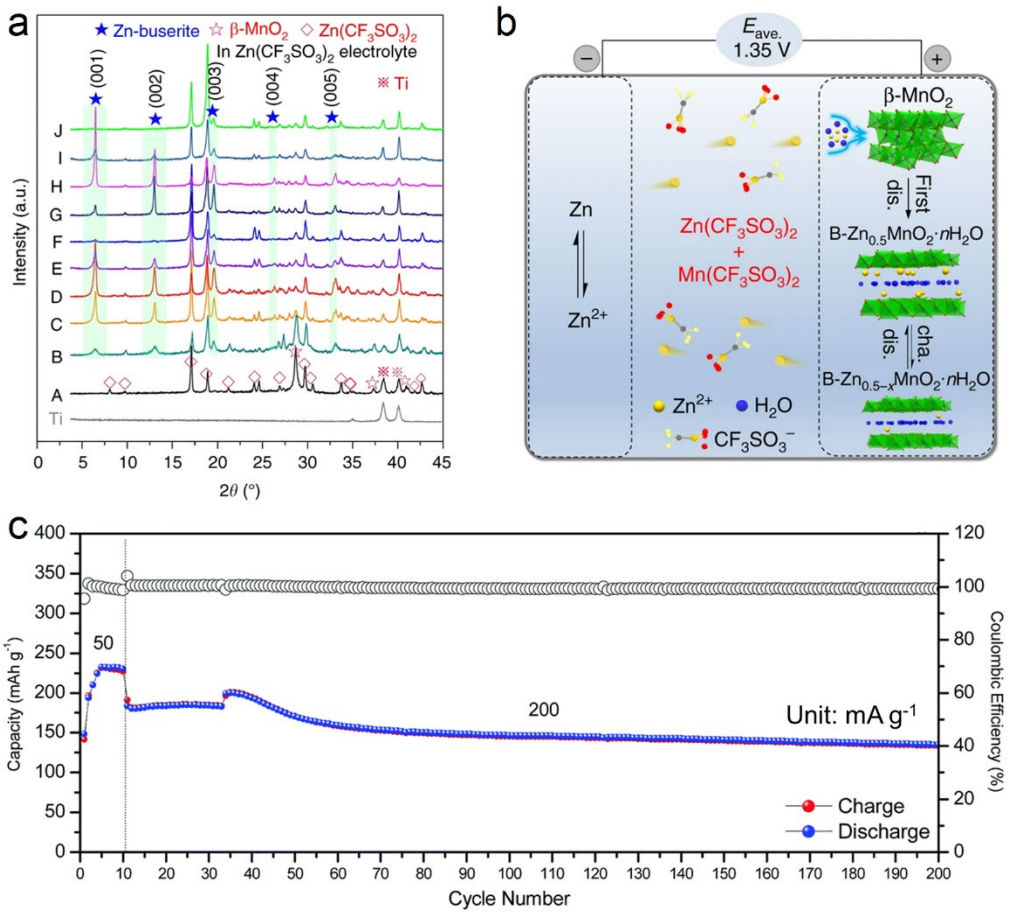


Figure 2.7. a) XRD patterns of β-MnO_2 electrode at selected states during first and second cycles[132]. b) Schematic illustration of the Zn-MnO_2 battery with $CF_3SO_3^-$-based aqueous electrolyte[132]. c) Cycle capacity evolution of the β-MnO_2 nanorod cathode using $MnSO_4$/$ZnSO_4$ electrolyte[124].

2.1.2.2. Enhancing structural stability

The integrity of MnO_2 as a cathode material in RAZBs can be compromised over prolonged cycling due to the repetitive intercalation and de-intercalation of Zn^{2+} ions. This dynamic can induce irreversible phase changes or volumetric expansion within the MnO_2, leading to a substantial alteration in the electrode material structure and potentially triggering a collapse. Such degradation severely hampers the cyclic stability and rate capability of RAZBs. In response, researchers have innovated several methods to bolster material stability, including but not limited to pillar engineering, heteroatom doping, defect engineering, surface engineering, and the design of controlled nanostructures[133–141]. While the former two

techniques have been introduced in the context of vanadium-based materials, the subsequent discussion will focus on the latter array of sophisticated methods.

Defect engineering can imbue materials with exceptional properties, notably enhancing the electrochemically active surface area and significantly boosting electrochemical performance[142,143]. Xiong et al. fabricated MnO_2 enriched with oxygen vacancies (Od-MnO_2) within its lattice, thereby facilitating a more reversible adsorption/desorption process for Zn^{2+} ions compared to pristine MnO_2[144], as demonstrated in **Figure 2.8**a. This approach yielded a higher active surface area and, by introducing oxygen defects, reduced the electron requirement for Zn-O bond formation. Consequently, more electrons become delocalized into the electrode, amplifying its specific capacity. The introduction of defects, whether in Mn or other elements, has been shown to significantly enhance the structural stability of cathode materials[145]. In **Figure 2.8**b, Guo et al. prepared Mn_3O_4 nanoparticles replete with Mn defects, which regulated the surface electronic properties and provided additional active sites for electrochemical reactions, thereby accelerating the kinetics and ensuring structural fidelity during cycling[146].

Surface engineering exploits the synergistic effects of covering MnO_2 cathode surface with protective layers—either organic or inorganic. The formation of heterogeneous interfaces through this strategy can effectively alleviate the dissolution of active materials and significantly improve the cathode performance[147,148]. Our group previously introduced a biomimetic electrode microskin (EMS) composed of collagen hydrolysate, which effectively converts irreversible side reactions into reversible ones[149]. As depicted in **Figure 2.8**c, this innovative EMS adeptly adsorbs and confines Mn^{2+} ions in proximity to the cathode through Van der Waals forces, hydrogen bonds, and ionic interactions, thus reversing reactions previously deemed irreversible. Consequently, the aqueous Zn-MnO_2 cell equipped with EMS exhibited an extraordinary discharge capacity of 415 mAh g^{-1} at a current density of 0.02 A g^{-1}, surpassing the theoretical capacity limit of 308 mAh g^{-1} associated with the Zn^{2+} intercalation mechanism.

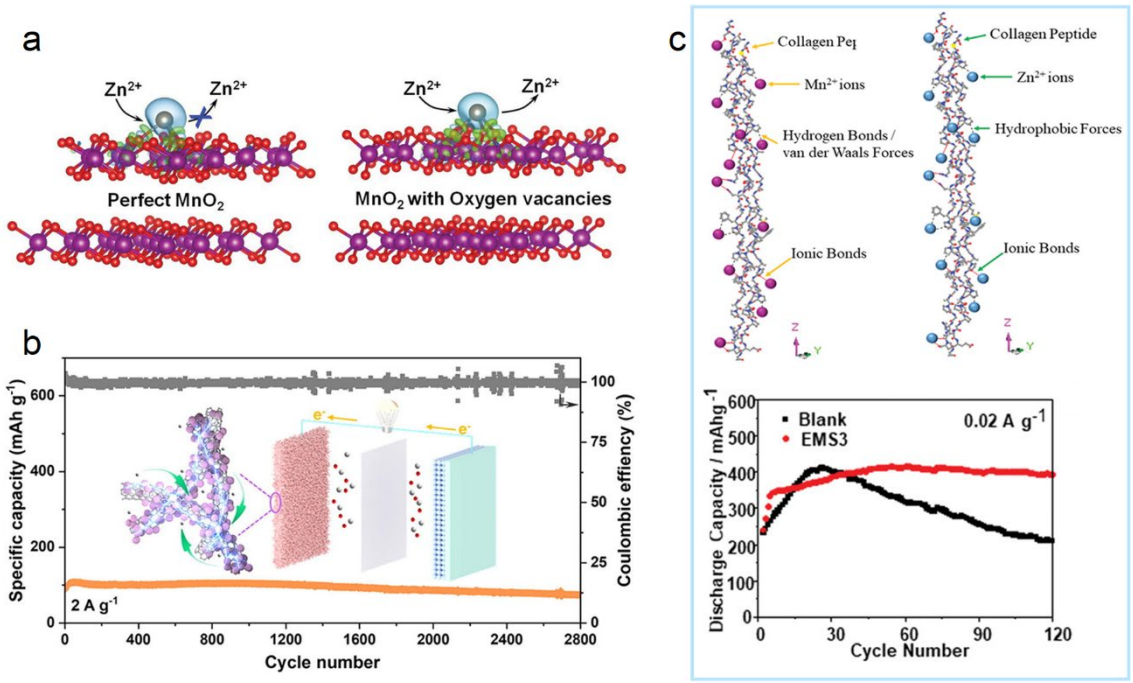


Figure 2.8. a) Schematic illustration of Zn^{2+} adsorption/desorption for perfect MnO_2 and MnO_2 with oxygen vacancies[144]. b) Cyclic performance at current densities of 2 A g^{-1}. Inset: schematic of defect-engineered Mn_3O_4/CNTs composites[146]. c) Schematic illustration of interactive forces between CH and Mn^{2+}/Zn^{2+} ions, respectively. Cyclic performance at a current density of 0.02 A g^{-1} [149].

2.2. Electrolyte Optimization for More Reliable RAZBs

The research focus on RAZBs has recently broadened beyond cathode material development to include rigorous investigations into electrolyte composition—spanning the spectrum of electrolyte species, their concentrations, and the strategic use of additives. The electrolyte, as an integral battery component, is primarily to supply space for ion diffusion and charge ions for reversible chemical reactions, as well as to connect the entire circuit. Dissolving the zinc salt in aqueous solutions are the conventional choice for RAZB electrolyte solutions. As mentioned in the **Introduction** chapter, aqueous electrolytes are preferred for their inherent safety, affordability, ease of preparation, and superior ion transport capabilities. Nonetheless, these electrolytes are not without their challenges: firstly, the mildly acidic electrolyte can induce the undesirable dissolution of cathode materials; secondly, the inherent high reactivity of water, coupled with a constrained electrochemical voltage window of approximately 1.23 V, precipitates gas evolution and other undesirable side reactions at the

electrodes; thirdly, the predilection of Zn^{2+} ions to be solvated by H_2O molecules hinders the kinetics of Zn^{2+} insertion and extraction[111,150–152]. The optimization of electrolytes, therefore, does not merely mitigate these issues but is also of paramount importance in augmenting the electrochemical performance and reliability of RAZBs.

2.2.1. Electrolytes and their basic characteristics

At present, the electrolyte systems for ZIBs are mainly divided into three major aspects including solid state electrolyte, gel state electrolyte, and fluid state electrolyte. Among the fluid state electrolyte, it is subdivided into aqueous system and organic system. Since all of my research projects are based on aqueous electrolytes, all discussions of electrolytes in this section are based on aqueous electrolytes unless otherwise noted. The electrolyte is an important component of a battery, and its physical and chemical properties can significantly affect the electrochemical performance and energy storage mechanism of the battery. Therefore, the basic properties of Zn^{2+} electrolytes, i.e., ionic conductivity, ion transference number, and electrochemical stability window, which are often governed by electrolyte composition and structural factors, will be comprehensively presented and evaluated here. After this I will present recent optimization strategies proposed for electrolyte studies.

2.2.1.1. Ionic conductivity

Ionic conductivity, a fundamental characteristic of electrolytes, is crucial in determining the rate performance of batteries[23,153]. It reflects the ability of ions to transport within the electrolyte[151]. Liquid electrolytes typically exhibit superior ionic conductivity relative to other electrolyte forms, primarily due to their enhanced fluidity which facilitates rapid Zn^{2+} ion migration[150,151]. Notably, aqueous electrolytes outperform organic counterparts in terms of ionic conductivity, attributed to their lower viscosity and solvation energy, often being two orders of magnitude higher[22]. Moreover, the ionic conductivity of an electrolyte is significantly influenced by the type of zinc salt used. Various zinc salts, including ZnF_2, $ZnCl_2$, $Zn(ClO_4)_2$, $ZnSO_4$, $Zn(NO_3)_2$, $Zn(CH_3COO)_2$, $Zn(BF_4)_2{\bullet}xH_2O$, $Zn(CF_3SO_3)_2$ and $Zn(N(CF_3SO_2)_2)_2$ (denoted as $Zn(TFSI)_2$), have been explored for preparing Zn^{2+} electrolytes,

each conferring distinct electrochemical properties. Among these, $ZnSO_4$, $Zn(CF_3SO_3)_2$, and $Zn(TFSI)_2$ are predominantly utilized due to their stable anions and compatibility[23,150,154,155]. Moreover, improving ionic conductivity can be effectively achieved through the incorporation of ionic additives such as Mn^{2+}, which increase the number of conducting ions[150,151]. For instance, a study by Chen et al. demonstrated that adding $Mn(CF_3SO_3)_2$ to a 3 M $Zn(CF_3SO_3)_2$ electrolyte and increasing the concentration of Mn^{2+} from 0 to 0.1 M resulted in elevating the conductivity from 4 S m^{-1} to 6 S m^{-1} [132]. Generally, additives that enhance ion richness and solubility, such as Na^+, Mg^{2+}, Cl^-, ClO_4^-, can also significantly improve electrolyte ionic conductivity[26,156].

In the realm of organic electrolytes, which typically suffer from low ionic conductivity, the introduction of ionic additives emerges as a practicable strategy to enhance diffusion ability[151]. Similarly, in solid electrolytes, doping with additives can increase defect and vacancy concentration of the solid electrolyte, thus boosting the ionic conductivity[157,158]. However, it is essential to recognize that not all ion combinations positively affect conductivity. Certain ions, like the co-deposition of Ca^{2+} and SO_4^{2-}, can reduce conductivity. Therefore, understanding the interaction criterion between different ions is critical in developing new electrolytes. However, the issue of suboptimal ionic conductivity remains a significant challenge in organic, gel, and solid state electrolytes[122,159,160]. To advance ZIB electrolyte development, there is an imperative need for comprehensive research into their unique features and mechanisms.

2.2.1.2. Ion transference number

The ion transference number is another crucial metric for evaluating electrolyte properties. In general, the higher the ion transference number, the better for optimal electrolyte performance. Since it minimizes concentration polarization and mitigates side reactions at the zinc anode (e.g., zinc dendrite formation), it enhances the electrochemical performance of batteries[161]. During the charge and discharge processes, cations and anions migrate across the electrolyte under the electric field between the cathode and anode. For instance, positively

charged Zn^{2+} ions migrate towards the anode, while negatively charged anions (e.g., SO_4^{2-}) move towards the cathode. However, for ZIB, it is the migration of the working ions (e.g., Zn^{2+}) that is of interest. The ion transference number, denoted as $t_{Zn^{2+}}$, quantifies the proportion of Zn^{2+} ion migration relative to the total ion migration in the electrolyte. This can be expressed as[162]:

$$t_{Zn^{2+}} = \frac{\mu_+}{\mu_+ + \mu_-} \quad (1)$$

where μ_+ and μ_- represent the current carried by cations (Zn^{2+}) and anions, respectively. Therefore, a $t_{Zn^{2+}}$ value closer to 1 indicates a higher proportion of Zn^{2+} ion migration, leading to increased charge transfer efficiency between the cathode and anode[163]. Addressing the challenge of increasing the ion transference number in liquid electrolytes is a key concern for ZIBs. According to the above equation, limiting anion movement and reducing the coordination number of Zn^{2+} can partially address this issue. For instance, Ji's group experimentally demonstrated a structural transition in Zn^{2+} coordination from octahedral $[Zn(OH_2)_2Cl_4]_2$ (peak: 287 cm^{-1}) to tetrahedral $[ZnCl_4]^{2-}$ (peak: 243 cm^{-1}) with increasing $ZnCl_2$ concentration, indicating a reduction in the solvation effect of Zn^{2+} ion[164] (**Figure 2.9**a). Consequently, in **Figure 2.9**b, a higher ion transference number was observed in a 30 m $ZnCl_2$ electrolyte compared to a 5 m $ZnCl_2$ electrolyte. Despite limited research in this area, it is evident that developing liquid electrolytes with high $t_{Zn^{2+}}$, possibly through soluble, polymeric, anionic zinc salts, is a promising avenue deserving further exploration.

While my research does not directly propose a solution for improving ion transference numbers, it includes analysis of this parameter. I conducted the experiments using the steady-state current approach within Zn/electrolyte/Zn symmetric cells, the ion transference number can be calculated as follows[165,166]:

$$t_{Zn^{2+}} = \frac{I_s(\Delta V - I_i R_i)}{I_i(\Delta V - I_s R_s)} \quad (2)$$

where ΔV is the polarization potential, I_i and I_s are the initial and steady current values, R_i and R_s are the charge transfer resistances before and after polarization, respectively.

2.2.1.3. Electrochemical stability window

RAZBs currently face challenges in meeting the high-energy-density requirements for large-scale energy storage, primarily due to the constraints imposed by their electrochemical stability window (ESW). The inherently low ESW of aqueous electrolytes restricts the operational voltage, consequently limiting the achievable energy density[167–169]. The theoretical ESW of water, limited to 1.23 V, introduces problems such as the hydrogen evolution reaction (HER) and oxygen evolution reaction (OER), which compromise battery through water depletion and reduced efficiency[25]. In simple terms, the ESW refers to a specific range on the cyclic voltammetry (CV) curve characterized by the absence of electrochemical reactions, typically represented by a nearly flat line. Within this range, the electrode is essentially in a charging state, neither reduction reactions (e.g., HER) nor oxidation reactions (e.g., OER) take place. Consequently, in the field of electrochemical research, the redox potential of the subject under study must be within the ESW of the selected electrolyte and electrode to avoid any detrimental effects. Recent research endeavors aim to extend the ESW (i.e., increasing OER potential and reducing HER potential) of aqueous electrolytes, thereby enhancing the voltage window of RAZBs. Approaches to optimize electrolyte performance encompass the isolation of water from the electrode, for instance, by introducing hydrophobic interfacial agents that impede water contact with the electrode[170,171]. In addition, modifying the solvation structure of H_2O molecules, similar to the effects observed in high-concentration electrolytes[172,173], and incorporating competitive reactions to mitigate H_2O-related side effects, such as the Mn^{2+} deposition reaction, have been explored[174].

An exemplary modification involves the addition of the sodium dodecyl sulfate (SDS) additive to a 1 M Na_2SO_4/1 M $ZnSO_4$ aqueous electrolyte, achieving an ESW expansion to 2.5 V[175]. The SDS additive creates a hydrophobic layer at the electrode/electrolyte interface,

imposing a significant energy barrier to water dissociation and thus preventing O_2 evolution. This mechanism not only restricts H_2O access to the electrode, enhancing electrochemical stability, but also facilitates Zn^{2+} desolvation, which helps prevent the side reactions, thereby improving Coulombic efficiency[170,171,176]. Furthermore, the introduction of ionic additives such as Al^{3+} has been shown to broaden the electrochemical window. As shown in **Figure 2.9**c-e, an electrolyte enriched with Al^{3+} additive can lower the HER potential from 0.8 V to 0.61 V and elevate the OER potential from 2.31 V to 2.51 V, effectively widening the ESW by nearly 0.4 V[177].

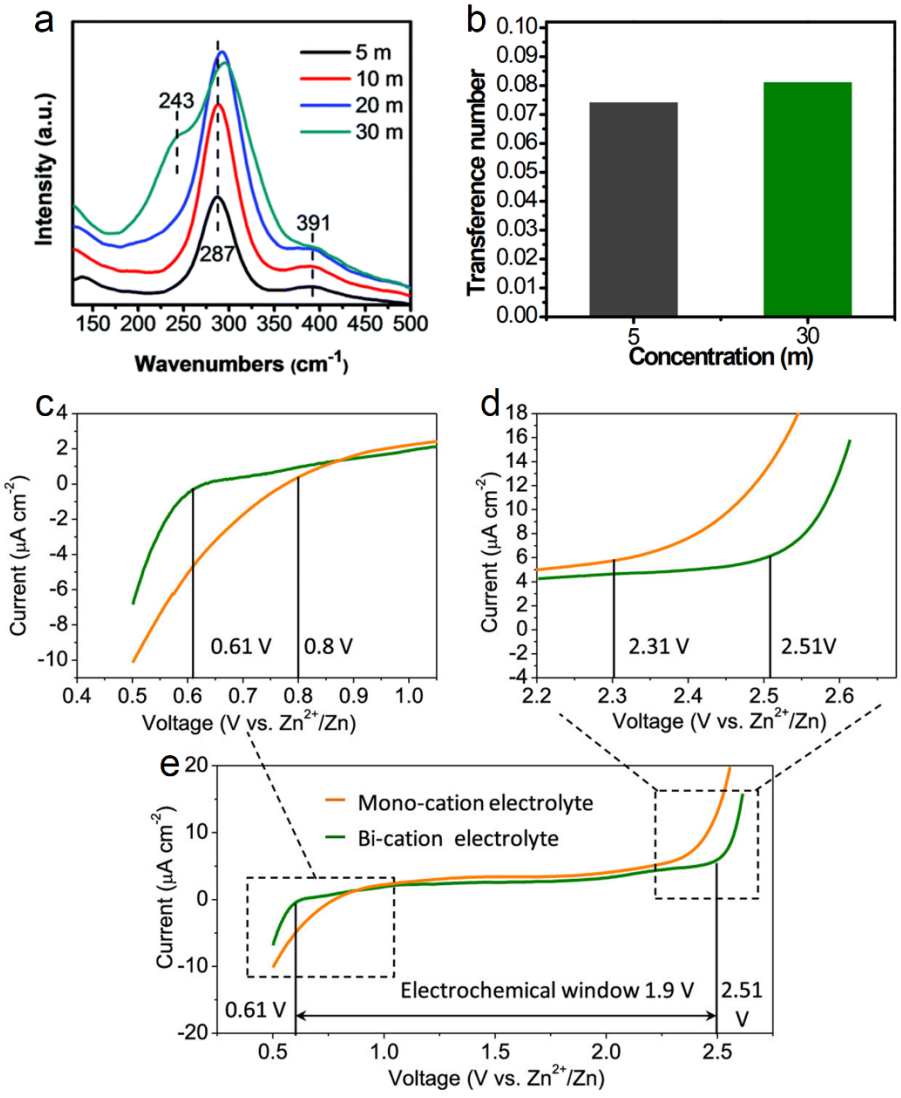


Figure 2.9. a) Raman spectra of $ZnCl_2$ solutions of different concentrations. b) The transference number of Zn^{2+} at 21°C for dilute (5 m) and concentrated (30 m) $ZnCl_2$ electrolytes[164]. Enlarged regions near c) anodic and d) cathodic extremes of the

electrochemical windows on nonactive titanium mesh electrodes. e) Overall electrochemical windows of bi-cation and mono-cation electrolytes were evaluated with CV at a scanning rate of 10 mV s^{-1} [177].

2.2.2. Electrolyte optimization strategies

In the above, we introduced three basic properties of electrolytes and talked lightly about several ways to improve them. In this section, we will discuss aspects of electrolyte optimization, starting with the species of zinc salts, and progressing to the development of highly concentrated electrolytes and the use of electrolyte additives.

2.2.2.1. Species of zinc salts

Neutral to mildly acidic electrolytes, with pH values between 4.0 and 8.0, offer a favorable environment for battery operation. Alkaline electrolytes (pH>8.0), despite their high ionic conductivity and zinc salt solubility, suffer from zinc passivation, undesirable morphological alterations, and carbonate precipitation due to CO_2 interaction from air[178–180]. These issues, illustrated in **Figure 2.10**a, have prompted a pivot towards employing near-neutral electrolytes. Within the spectrum of near-neutral electrolytes, various salts have been explored, including chlorine-based salts (e.g., NH_4Cl, NaCl, $ZnCl_2$, etc.), other inorganic soluble salts (e.g., NO_3^-, SO_4^{2-}, ClO_4^-, etc.), and organic-based salts. Notably, NO_3^- anions are strong oxidants which pose a risk of oxidizing zinc metal, thereby exacerbating corrosion and causing a significant pH increase locally or even throughout the electrolyte system[181]. ClO_4^- anions have been observed to reduce the corrosion rates at the zinc anode, however, their interaction with Zn^{2+} ions may lead to the formation of a ZnO passivation layer on the anode surface. This passivation layer acts as a barrier to zinc dissolution/deposition, resulting in sluggish reaction kinetics[181,182]. $ZnCl_2$ has been considered as an electrolyte candidate for RAZBs, primarily due to the low oxidizability of Cl^- ions. Nonetheless, the practical deployment of $ZnCl_2$ in RAZBs is constrained by its narrow anodic potential window, which leads to continuous decomposition of the electrolyte under higher voltages[57].

Hu et al. conducted a comprehensive study on the effects of mildly acidic aqueous electrolytes containing different species on the zinc anode. Among the acetate electrolyte ($ZnSO_4/(NH_4)_2SO_4/(CH_3COO)_2Pb$), sulfate electrolyte ($ZnSO_4/(NH_4)_2SO_4$) and chloride electrolyte ($ZnCl_2/NH_4Cl$), the use of chloride electrolyte offered lower charge transfer resistance and minimize corrosion and dendrite formation[183] (**Figure 2.10**b). However, Cl_2 evolution during charging ($2Cl^- \rightarrow Cl_2 + 2e^-, E_0 = 1.36V$) curtails charging efficiency[183,184]. Consequently, $ZnSO_4$ has been adopted as the preferred electrolyte for contemporary aqueous ZIBs. A comparative study on electrolyte types and concentrations by Liang's team found that $ZnSO_4$ provided the most favorable results for zinc deposition/dissolution reversibility and kinetics, attributed to the destabilizing effects of CH_3COO^-, NO_3^- and Cl^-, anions in comparison to SO_4^{2-} [185]. Afterwards, further analysis of varying concentrations of $ZnSO_4$ electrolytes (ranging from 0.5 M to 3 M) demonstrated optimal performance with a 3 M solution, as depicted in **Figure 2.10**c. The higher concentration diminished the activity of H_2O molecules and enhanced electrolyte viscosity, thus stabilizing ion solvation and promoting cation/anion transport kinetics[7,57,185]. Chen and Mai's research corroborated that mild acid organic salt-based electrolytes, such as $Zn(CF_3SO_3)_2$ and $Zn(TFSI)_2$, shown in **Figure 2.10**d, outperformed $ZnSO_4$ solutions. Their bulky anions effectively reduce H_2O molecules coordination around the Zn^{2+} ion, thereby minimizing solvation and enhancing performance[57,186]. Nevertheless, the adoption of these organic electrolytes comes with a substantial cost premium, which could escalate the overall production expenses, thus running counter to the cost-effectiveness and practical concepts of RAZB technology.

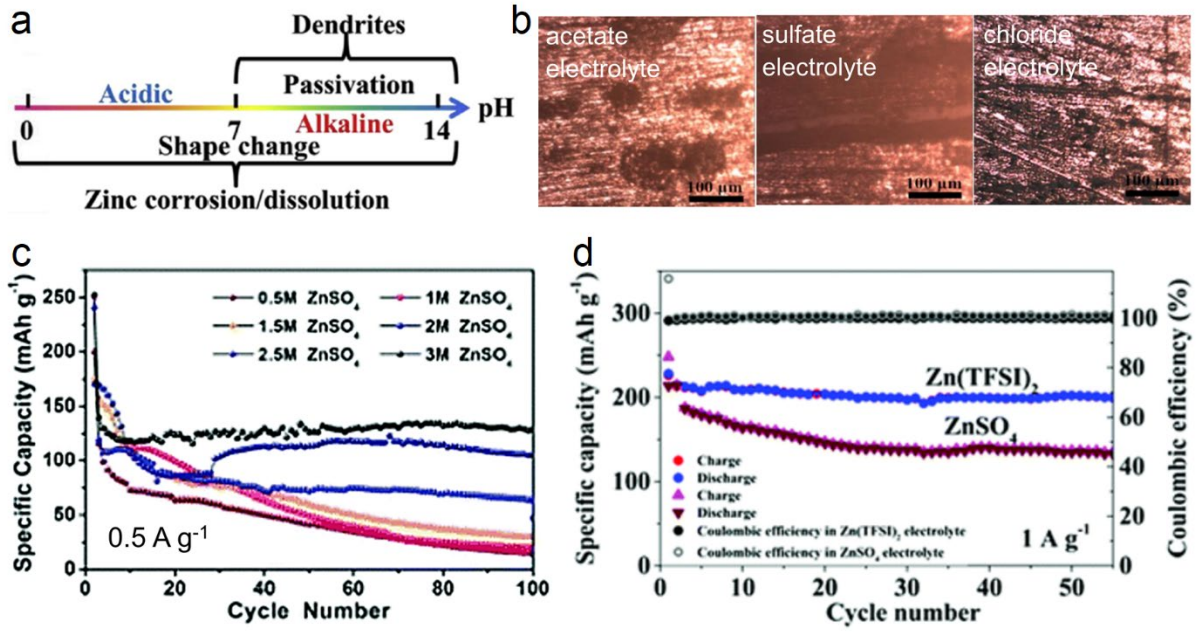


Figure 2.10. a) Problems of metal Zn contact with aqueous electrolytes with varying pH values[180]. b) Micrographs of polished Zn electrode, and Zn electrode placed in acetate electrolyte ($ZnSO_4/(NH_4)_2SO_4/(CH_3COO)_2Pb$), sulfate electrolyte ($ZnSO_4/(NH_4)_2SO_4$) and chloride electrolyte ($ZnCl_2/NH_4Cl$) for 30 days, respectively[183]. c) Cycling performance of Zn-V_2O_5 battery with *x* M $ZnSO_4$ electrolyte[185]. d) Comparison of cycling performances between batteries in 0.3 M $Zn(TFSI)_2$ electrolyte and in 1 M $ZnSO_4$ electrolyte[186].

2.2.2.2. Concentration of zinc salts

According to previous reports, the interaction between Zn^{2+} ions and H_2O molecules, forming a solvation sheath structure typified as $[Zn(H_2O)_6]^{2+}$ [31,187,188]. This structure necessitates a high energy barrier for Zn^{2+} desolvation and deposition, contributing to potential irreversibility issues on anodes[22]. It has been observed that elevating the electrolyte salt concentration can alter the ionic solvation structure and significantly affect the ion transport behavior, thereby imparting beneficial effects on electrodes and overall electrochemical performance of the batteries[189,190]. Notably, research conducted by Chen et al. demonstrated that increasing the concentration of $Zn(CF_3SO_3)_2$ from 1 M to 4 M in a Zn-$ZnMn_2O_4$ battery system could increase the Coulombic efficiency to 100%[57] (**Figure 2.11**a). This effect is attributed to the high-concentration electrolyte's ability to diminish H_2O activity and mitigate H_2O-induced side reactions, as well as reduce the dissolution of active species,

such as Mn from the $ZnMn_2O_4$ spinel structure (**Figure 2.11**b). However, a concentration increase also leads to reduced ionic conductivity and elevated solution viscosity (**Figure 2.11**c), necessitating a balance to achieve optimal electrolyte performance.

Moreover, the "water-in-salt" or highly concentrated electrolyte methodology have been developed as a countermeasure to the limitations of traditional aqueous electrolytes affecting electrode efficiency. This approach involves replacing the hydration shell of -OH or H_2O molecules that typically surrounds the Zn^{2+} ion with alternative anions, thereby reducing common issues such as dendrite growth and zinc corrosion[164,187,191,192]. Experimental evidence has supported the efficacy of this strategy; for instance, Wang's team demonstrated that a 20 m LiTFSI+1 m $Zn(TFSI)_2$ concentrated electrolyte could facilitate dendrite-free zinc plating/stripping processes while maintaining close to 100% Coulombic efficiency and mitigating water consumption[187]. As discussed earlier in **Section 2.2.2.1**, with an increase in electrolyte concentration, a substantial number of $TFSI^-$ anions replace H_2O molecules to preferentially bond with Zn^{2+} ion, forming $(Zn\text{-}TFSI)^+$ complexes and curtailing the solvation of Zn^{2+} ions (i.e., the formation of $[Zn(H_2O)_6]^{2+}$). **Figure 2.11**d illustrates the transition from a dilute electrolyte environment (5 m Li^++1 m Zn^{2+}), where Zn^{2+} ion is predominantly coordinated by six H_2O molecules with minimal $TFSI^-$ present, to a scenario where, at moderate electrolyte concentrations (10 m Li^++1 m Zn^{2+}), $TFSI^-$ begin to occupy the Zn^{2+}-solvation sheath. At a concentration of 20 m LiTFSI, the $TFSI^-$ completely supplant the H_2O molecules, effectively preventing H_2 evolution and enhancing electrode cycling stability[187]. Furthermore, the concentrated electrolyte modality enables an extended ESW and augments energy density relative to standard aqueous electrolytes due to the reduced presence of free H_2O. Mai et al. employed a 21 m LiTFSI+1 m $Zn(CF_3SO_3)_2$ concentrated electrolyte within an aqueous Zn-V_2O_5 battery system, achieving an elevated battery voltage plateau from 0.6 V to 1.0 V and realizing enhanced longevity and energy density[192], as shown in **Figure 2.11**e and f.

This innovative "water-in-salt" electrolyte framework offers fresh perspectives for battery enhancement and a comprehensive understanding of aqueous-based ZIB systems. However, concentrated electrolytes may face challenges such as significant voltage polarization at low current densities and limited plating/stripping capacity, alongside increased viscosity and reduced ionic conductivity[193,194]. Moreover, the higher cost of concentrated electrolytes compared to their dilute counterparts could pose obstacles to their large-scale application.

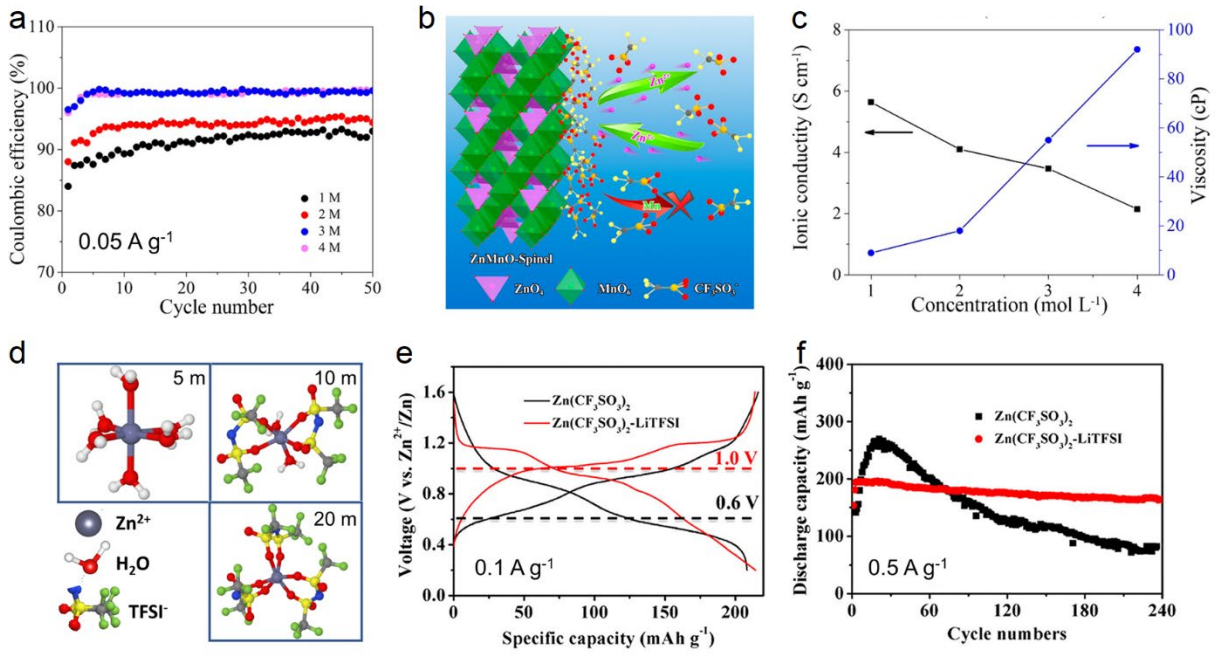


Figure 2.11. Characterization of aqueous $Zn(CF_3SO_3)_2$ electrolyte with different concentrations (1–4 M): a) Coulombic efficiency of $ZnMn_2O_4$ electrode at current rate of 0.05 A g^{-1} within 0.8–1.9 V, b) viscosity and ionic conductivity. c) Schematic of mitigating active substance dissolution[57]. d) Schematic for Zn^{2+}-solvation structures in the electrolytes with 1 m $Zn(TFSI)_2$ and other concentrations of LiTFSI (5 m, 10 m and 20 m)[187]. e) The charge/discharge curves of Zn-V_2O_5 batteries at 0.1 A g^{-1} [192]. f) Cycling performance of V_2O_5 in 1 m $Zn(CF_3SO_3)_2$ and 21 m LiTFSI+1 m $Zn(CF_3SO_3)_2$ electrolytes at 0.5 A g^{-1} [192].

2.2.2.3. Functional additives in electrolytes

The incorporation of electrolyte additives is another sophisticated approach to solve the issues related to the cathode in RAZBs in recent studies. The selection of an appropriate additive is contingent upon the cathode material and zinc salt employed. For instance, to mitigate the dissolution of Mn-based cathodes, Mn^{2+} ions (typically derived from $MnSO_4$ or $Mn(CF_3SO_3)_2$) are introduced into the electrolyte[42,195–197]. This strategy stabilizes the Mn

dissolution equilibrium from the MnO_2 electrode, thereby preserving the integrity of active materials and enhancing its cycling performance, as illustrated in **Figure 2.12**a and b. Furthermore, Pan et al. also highlighted that the addition of $MnSO_4$ did not affect the redox process of the MnO_2 cathode[43]. Building upon this understanding, Qiu et al. conducted further research to elucidate the role of Mn^{2+} ions within the electrolyte. Their findings illuminated that the pre-addition of Mn^{2+} ions to the electrolyte exerts a substantial influence on the battery performance, with approximately 18.9% of the battery capacity being ascribed to the active participation of Mn^{2+} ions present in the electrolyte[195]. Similarly, in RAZB systems utilizing a Co_3O_4 cathode within a mild electrolyte, the dissolution of Co can account for up to 6.4% of the total Co at discharge to 0.8 V, leading to significant initial capacity loss. The pre-addition of Co^{2+} ions can adjust the dissolution equilibrium, resulting in both improved long-term cycling stability and enhanced initial Coulombic efficiency[198]. In addition, Chen et al. discovered that the introduction of sodium salts into $ZnSO_4$ electrolytes could effectively preserve the $NaV_3O_8 \cdot 1.5H_2O$ cathode from dissolution and significantly improve the battery cycle life[26] (as depicted in **Figure 2.12**c and d).

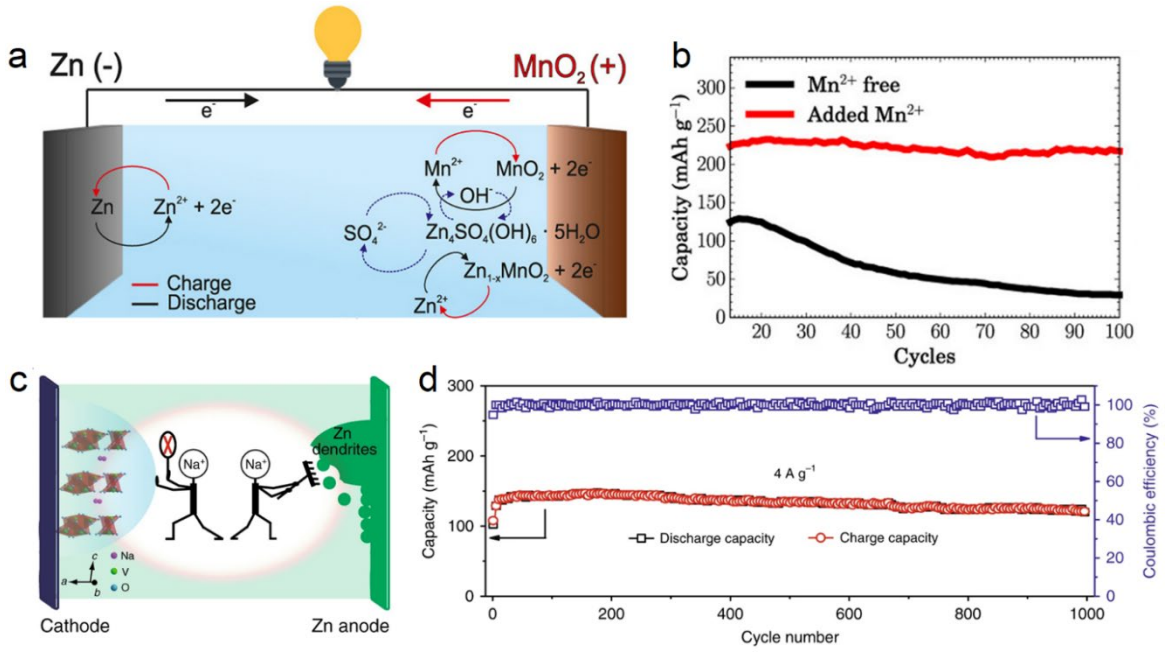


Figure 2.12. a) Schematic illustration of the function of pre-added Mn^{2+} in Zn-MnO_2 battery. b) Cycling performance of the two samples over 100 cycles[197]. c) Schematic illustration of Na salt additive inhibited the dissolution of NVO cathode and Zn dendrites formation. d) Cycling performance of NVO cathode in Zn^{2+}/Na^+ electrolyte at 4 A g^{-1} [26].

2.3. Zinc Anode

Zinc metal, serving as the anode in aqueous battery systems, presents a compelling proposition due to its exceptional compatibility with water-based electrolytes, cost-effectiveness, high safety, abundant availability, low redox potential (−0.763 V vs. SHE), and substantial theoretical capacity (820 mAh g^{-1})[199,200]. These attributes have positioned ZIB as a viable alternative to traditional alkali-ion-based energy storage solutions. In RAZBs, the anode is commonly fabricated from either zinc foil or zinc powder. Regardless of the electrolyte pH, ranging from alkaline to neutral and mildly acidic, energy storage and release mechanisms are predicated on the reversible stripping and plating of Zn^{2+} ions at the zinc (Zn) anode[201,202]. During the charging and discharging process, the Zn anodes undergo two main reactions:

$$\text{Stripping:} \quad Zn \leftrightarrow Zn^{2+} + 2e^{-} \tag{3}$$

$$\text{Plating:} \quad Zn^{2+} + 2e^{-} \leftrightarrow Zn \tag{4}$$

2.3.1. Issues for Zn anodes

Zn anodes in RAZBs encounter several critical issues, such as dendrite growth, electrolyte consumption, hydrogen evolution, and the emergence of by-products (**Figure 2.13**a). These phenomena contribute to significant polarization, diminished capacity, and compromised Coulombic efficiency[203,204]. Addressing these challenges necessitates a comprehensive understanding and the development of strategies for enhancing Zn anode stability and performance.

2.3.1.1. Zinc dendrite formation

Among the challenges, the formation of zinc dendrites stands out as a particularly persistent obstacle impeding the advancement of high performance RAZBs. Dendrites primarily emerge during the zinc plating process, where the electric field intensifies around the protrusions on the Zn anode surface (“tip effect”, as shown in inset of **Figure 2.13**a),

promoting localized Zn^{2+} deposition and the subsequent growth of dendritic structures[205,206]. Unlike alkali metals such as lithium and sodium, higher mechanical strength of zinc does not inherently protect it against the detrimental effects of dendrite formation[202]. Extensive growth of zinc dendrites can pierce the separator, leading to direct anode-cathode contact, which in turn results in short circuits and battery failure. Moreover, factors such as the anode surface condition, substrate structure, electrolyte composition, and current density play significant roles in dendrite formation and growth, highlighting the importance of these parameters in zinc plating optimization[207]. Research by He et al. revealed that surface irregularities, including roughness and microcracks, exacerbate local dendrite growth, thereby reducing cycling stability[208], as shown in **Figure 2.13**b. In addition, the crystallographic orientation of the Zn anode has been identified as a critical factor; zinc deposits presenting (002) crystal planes favor their continuous deposition in the horizontal direction, resulting in dendrite-free growth and extended cycle life[209,210]. In **Figure 2.13**c, Pu and his colleagues further demonstrated that single-crystal (002) Zn anode could effectively mitigate defect formation and vertical zinc plating (i.e., Zn (100) plane), underscoring the importance of anode material selection and preparation in combating dendrite-related issues in RAZBs[211].

2.3.1.2. Hydrogen evolution reaction

In environments where the electrolyte exhibits slight acidity, the standard reduction potential of Zn^{2+}/Zn falls beneath the hydrogen evolution potential, rendering the HER an unavoidable process that typically unfolds in three steps[212]. The initial step, known as the Volmer step (Equation 5), involves the adsorption of H atoms on the electrode surface, necessitating additional overpotential to offset the Gibbs free energy required for HER initiation[213]. Subsequent steps, either through the Tafel step (Equation 6) or the Heyrovsky step (Equation 7), or their concurrent action, expedite HER[214,215]. Hydrogen evolution results in the depletion of electrolyte and electrons that are otherwise allocated for zinc plating during the charging process. This phenomenon not only hastens corrosion rates but also elevates the concentration of OH^- ions, further facilitating the synthesis of zinc sulfate hydroxide (ZSH)[216].

These processes collectively undermine the possibility of achieving 100% Coulombic efficiency in Zn anode cycling. Moreover, H_2 generation at the Zn anode surface may induce battery swelling and elevate safety risks, necessitating strategies to curtail these detrimental side reactions.

$$\text{Volmer step:} \quad H^+ + e^- \leftrightarrow H_{ads} \tag{5}$$

$$\text{Tafel step:} \quad 2H_{ads} \leftrightarrow H_2 \tag{6}$$

$$\text{Heyrovsky step:} \quad H_2O + H_{ads} + e^- \leftrightarrow H_2 + OH^- \tag{7}$$

2.3.1.3. Zinc corrosion and by-products generation

In addition, corrosion phenomena occur concurrently with HER. Specifically, numerous micro-galvanic cells emerge at the phase interface between Zn metal and the electrolyte. At sites of corrosion, Zn metal is dissolved to form Zn^{2+} ions following electron loss during discharge, while H_2O in the acidic or neutral solution gains electrons, leading to the production of H_2 and hydroxide ions (OH^-)[216,217]. It has been established that the accumulation of OH^- ions can further react with the Zn^{2+} ions, leading to the formation of by-products on the anode surface. As illustrated in **Figure 2.13**d, these ions interact with each other to precipitate ZSH (Equations 8 and 9) on the anode surface, which possess a hexagonal structure. This ZSH by-product, unlike the dense solid electrolyte interface (SEI) layers found in LIBs, accumulates in a loose manner on the anode surface, failing to shield against further corrosive reactions[218,219]. The continued corrosion and ZSH formation not only elevate electrode polarization, potentially fostering dendrite formation but also exacerbate electrolyte depletion, detracting from Coulombic efficiency and battery lifespan[220,221]. Addressing zinc corrosion is imperative to enhance metallic Zn anode utilization and bolster the practical applicability of RAZBs.

$$Zn + 2H_2O \leftrightarrow Zn^{2+} + H_2 + 2OH^- \tag{8}$$

$$4Zn^{2+} + 6OH^- + SO_4^{2-} + xH_2O \leftrightarrow Zn_4(OH)_6SO_4 \cdot xH_2O \text{ (ZSH)} \tag{9}$$

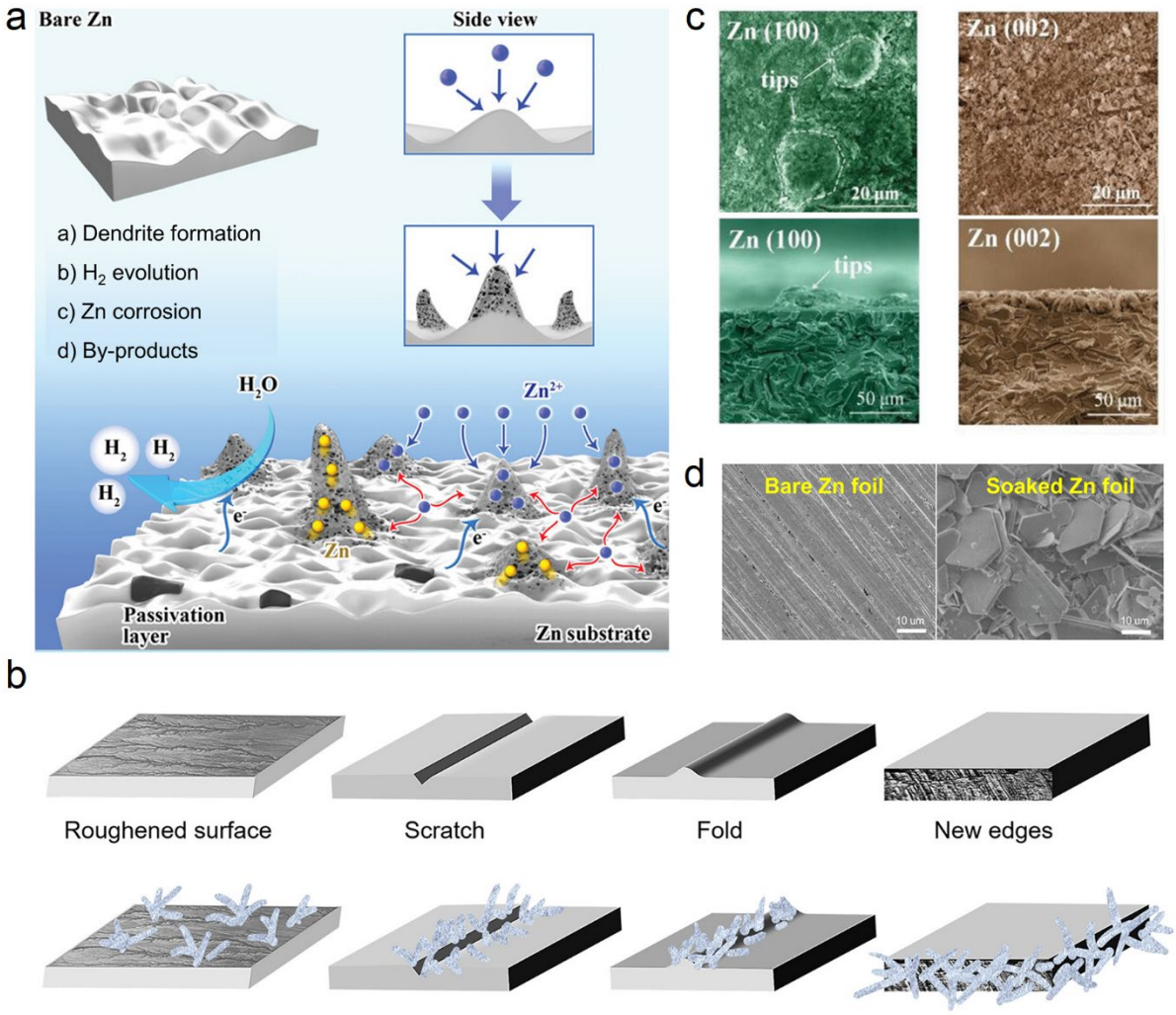


Figure 2.13. a) Schematic diagram of the zinc deposition process on the surface of bare Zn anode[206]. b) Defects on Zn anodes such as roughened surface, surface scratches or folds, and newly exposed unpolished edges, all of which can predispose to the creation of dendritic grains during electrochemical cycling[208]. c) Deposition products morphology of the Zn (100) and Zn (002) planes[209]. d) The morphology of the bare Zn foil and the Zn foil after soaking in 1 M $ZnSO_4$ electrolyte for 7 days[218].

2.3.2. Interface modification of Zn anodes

According to the above discussion, the challenges posed by dendrite formation, hydrogen evolution, and corrosion significantly impede the commercial viability of RAZBs. This section critically evaluates recent advancements in enhancing Zn anode stability and functionality, focusing on interface modification, anode structural design, alloying anode, and liquid electrolyte optimization. Given that the primary occurrences of dendrite growth and the HER mainly occur at the anode/electrolyte interface, the implementation of a surface

modification layer stands out as a direct and potent solution. Such layers fulfill several functions, notably the redistribution of the concentration and electric fields. These actions strategically regulate the ion and molecule migration on the electrolyte side, and electron distribution on the anode side. Consequently, these interventions are designed to promote uniform growth of zinc deposits while effectively suppressing side effects.

2.3.2.1. Redistribution of concentration field

The redistribution of the concentration field effectively modifies the spatial arrangement and movement of Zn^{2+} ions, H_2O molecules, hydrated Zn^{2+} ions, and anions at the anode interface, thus enhancing zinc deposition while inhibiting side reactions. The interface modification layer is an effective strategy to optimize the performance of Zn anodes. The design of these modification layers employs mechanisms such as mechanical confinement within channels and adsorptive interaction with polar groups.

Serving as a buffer layer that isolates active zinc from the bulk electrolyte, particularly through its electronic insulation properties, the concentration field is mechanically regulated by constructing confined channels, such as porous or layered structures[222,223]. For example, as shown in **Figure 2.14**a, confined channel structures like those in hydrogen-substituted graphodiyne (HsGDY) layer selectively allow Zn^{2+} ion migration while blocking larger species, enhancing effective mass transfer[224]. In addition, the porous channel architecture fosters a uniform Zn^{2+} concentration field across the HsGDY–Zn interface, as evidenced by concentration field simulations (**Figure 2.14**b). Moreover, materials such as nanoporous SiO_2, nanoporous $CaCO_3$, kaolin, Zn-based montmorillonite, and Mg–Al-layered double hydroxide further redistribute the concentration field[225–229], though their rigid structure may limit adaptation to anode volume changes, constraining performance improvements in ZIBs.

Beyond the creation of confined channels for mechanical modulation of the concentration field, various organic materials offer a direct and selective approach to control Zn^{2+} ion migration, leveraging specific polar groups to redistribute the concentration field. These groups, capable of donating electron pairs, facilitate the coordination adsorption of Zn^{2+} ions

through robust interactions, altering the solvation structure of $[Zn(H_2O)_6]^{2+}$ ions to decrease desolvation energy[230–234]. In **Figure 2.14**c, the interaction between polar groups and solvated Zn^{2+} ions allow these groups to partially or fully replace H_2O molecules in the solvation shell. In addition, the presence of N, O, and F atoms in certain polar groups can disrupt the solvent sheath by forming H-bonds, thereby dismantling the sheath structure and reducing the coordination number of Zn^{2+} ions[150,235,236]. Similarly, some specific inorganic materials exhibit strong interactions with Zn^{2+} ions, aiding in the adjustment of the concentration field. For instance, electrodeposition in an NH_4F aqueous solution yields a 3D interconnected ZnF_2 matrix (**Figure 2.14**d), which demonstrates enhanced Coulombic attraction towards Zn^{2+} ions compared to bare Zn metal[237]. This interconnected porous structure promotes uniform Zn^{2+} ion flux, improving desolvation effects and transfer kinetics. Furthermore, the adsorptive properties of S, O, and P atoms in ZnS, ZnO, and ZnP layers, respectively, are verified to significantly contribute to the redistribution of the concentration field, optimizing ion migration and enhancing overall battery performance[238–240].

2.3.2.2. Redistribution of electric field

In addition to altering the flux of molecules and ions at the electrolyte/anode interface, directly modulating the electron distribution on the anode side can also influence zinc deposition behavior. This electron redistribution can either homogenize or expand the local electric field, significantly impacting the 2D diffusion of Zn^{2+} ions around nucleation sites[241]. The uneven electric field distribution, often a result of higher local surface charge density due to the “tip effect”, thus the local electric field strength directly correlates with current density[242]. To mitigate dendrite formation while aiming for rapid battery charging, it is essential to decrease the local current density at zinc deposition sites. Introducing a modified conductive layer with a high specific surface area, such as graphene oxide (GO)[243], reduced graphene oxide (rGO)[244,245], graphite[246], carbon nanotubes (CNT)[247], and other carbon-based materials, allows for the partial redistribution of the anode electronic charge. This increases electrochemical activity and provides diversified nucleation sites for zinc deposition, reducing

the local current density and leading to a more uniform electric field[248]. As illustrated in **Figure 2.14**e, 2D-structured MXene materials with metallic conductivity can homogenize the electric field, disrupting the tip effect and promoting uniform Zn nucleation and growth, even under high current densities[249]. In addition, nitrogen-doped graphene oxide (NGO) layers create a stable electric field, reducing electrolyte-anode contact area during cycling and promoting even Zn^{2+} ion distribution[250] (**Figure 2.14**f). However, it's noteworthy that conductive network materials, despite their potential to equalize the electric field and mitigate dendrite growth, possess inherent edges and defects where Zn^{2+} ions tend to deposit preferentially. Consequently, the risk of side reactions at the reaction interface remains a concern.

2.3.3. Controlling Zn texture orientation

As discussed earlier in **Section 2.3.1.1**, the growth dynamics of zinc dendrites are closely related to the preferential growth of specific crystallographic planes. The electrochemical behavior of Zn anodes during Zn^{2+} stripping and plating processes is predominantly determined by the atomic structure of the surface, especially the (100) and (002) planes of Zn metal[209]. By engineering optimal Zn textures and exposing particular planes, one can tune the electrochemical characteristics of Zn anodes. In **Figure 2.15**a, crystals inclined at 0–30° relative to the substrate are observed when the growth favors the (103) and (002) planes. Growth angles between 30–70° emerge for the (101) and (102) planes, while angles of 70–90° are associated with the (100) and (110) planes[251–254]. In addition, the surface of hexagonal close-packed (HCP) Zn in the (100) plane presents an uneven and wavy morphology, leading to non-uniform interfacial charge density and Zn^{2+} ion flux, which predisposes to dendrite formation. Conversely, the (002) plane is comparatively smoother, ensuring a homogeneous charge distribution, thereby facilitating the uniform deposition of Zn microcrystals and promoting horizontal growth via an epitaxial process[209] (**Figure 2.15**b).

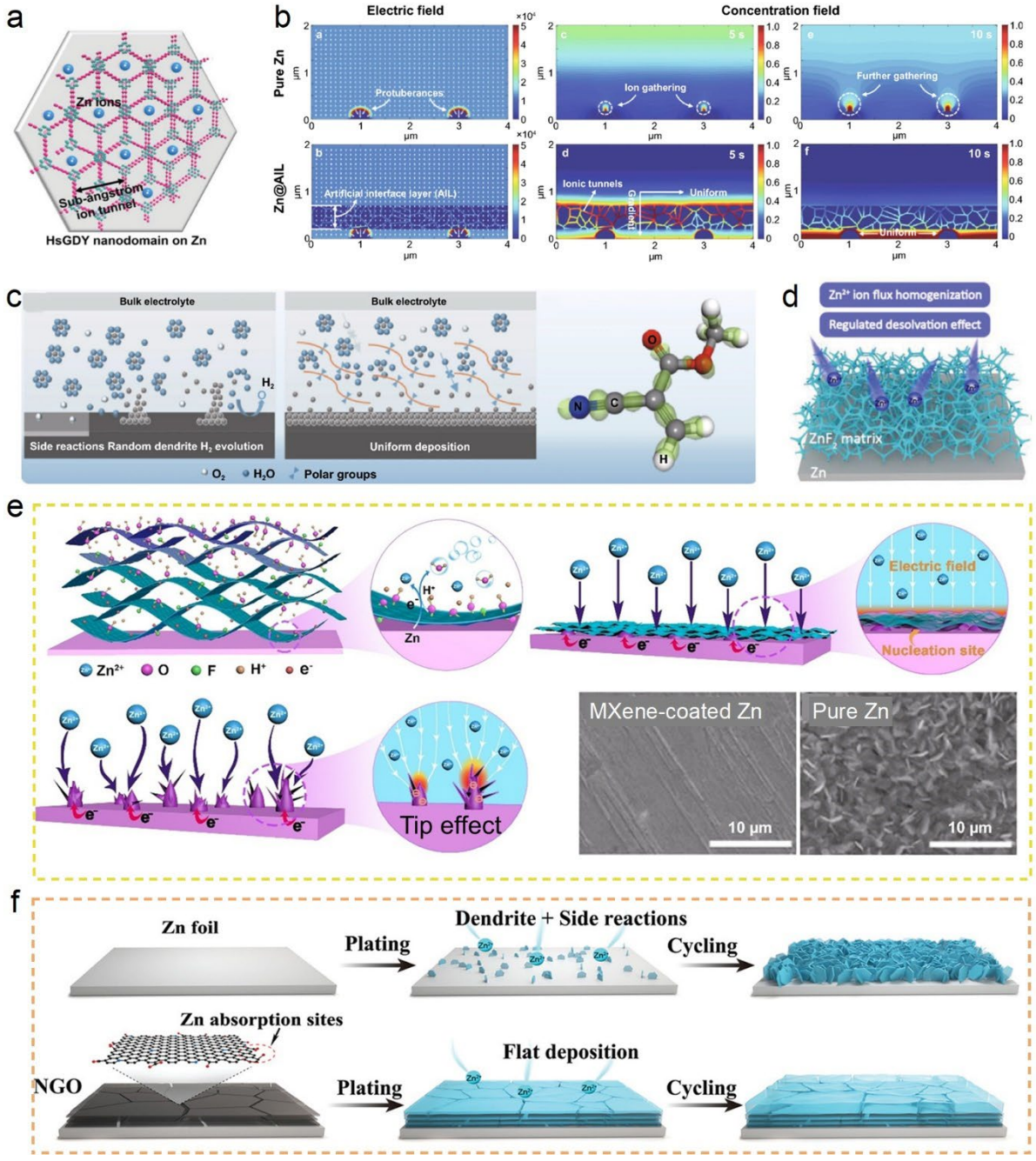


Figure 2.14. a) Schematic illustration of the synthesis of HsGDY. b) Electric and concentration field simulation with protuberances of bare Zn and coated Zn[224]. c) Schematic diagram of the mechanism of cyanoacrylate for suppressing zinc dendrite[233]. d) Schematic diagram of Zn@ZnF_2 electrode regulating Zn^{2+} ion flux[237]. e) Illustration of synchronously reducing and assembling MXene layer on the surface of Zn foil and zinc plating behavior of MXene-coated Zn (top right) and pure Zn (bottom left)[249]. SEM images of cycled MXene-coated Zn and pure Zn. f) Schematic illustration of zinc plating on bare Zn electrode (upper) and NGO@Zn electrode (lower)[250].

Commercial Zn foils often lack a uniform texture orientation, yet it is feasible to direct the crystallization towards the (002) plane during deposition. It has been reported that the 1-butyl-3-methylimidazolium cation ($BMIm^+$ ion) effectively encourages the preferential growth of (002) plane, thus minimizing dendrite development. Specifically, $BMIm^+$ ions adsorb preferentially on the (100) and (101) planes of Zn anodes, compelling Zn^{2+} ions to deposit on the (002) plane and fostering a flat, compact deposition layer[255] (**Figure 2.15**c). Furthermore, sulfonate anion-induced electrodeposition can achieve in-plane oriented Zn textures with prominently exposed Zn(002) plane[256] (**Figure 2.15**d). Unfortunately, current studies predominantly focus on the tendency towards (002) crystal surface exposure rather than achieving full exposure. Thus, advancing texture control for practical application necessitates further comprehensive research. Moreover, existing investigations are conducted at ambient temperatures, leaving the directional deposition of (002) plane under extreme temperature conditions remaining unexplored.

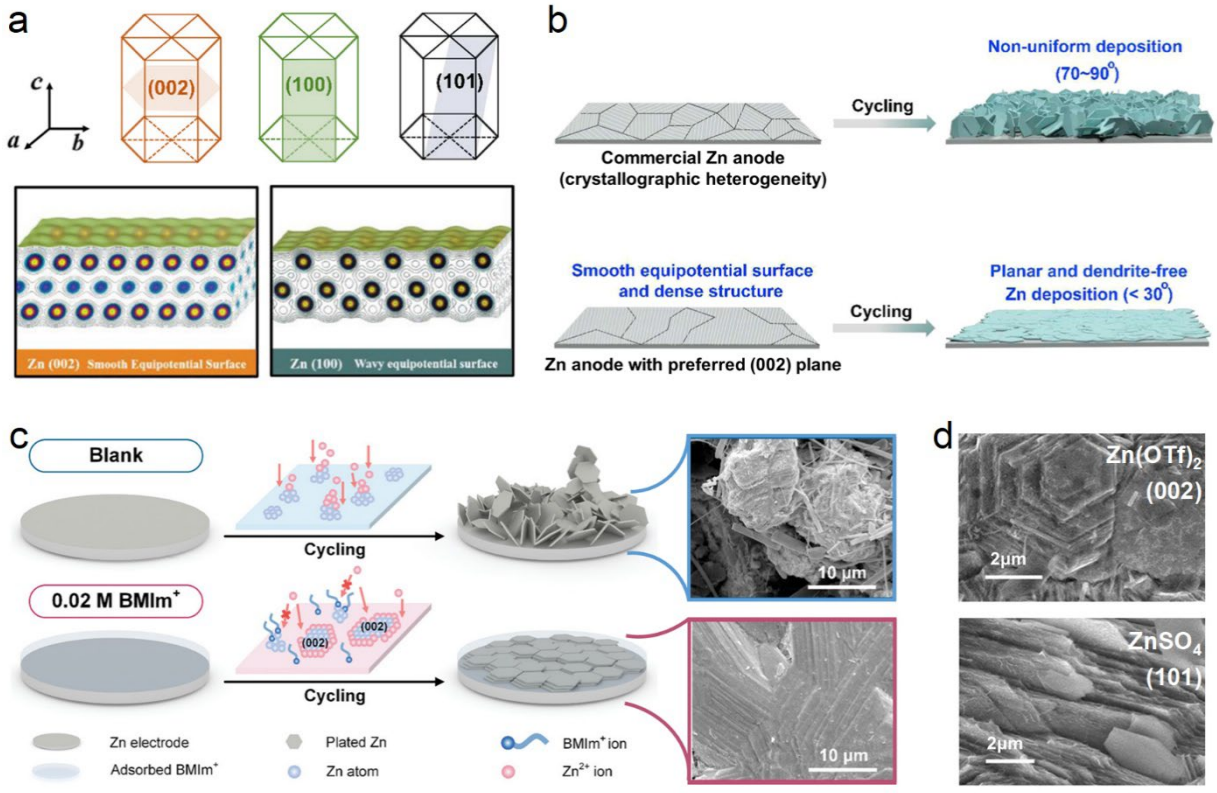


Figure 2.15. a) Crystal structure of the metallic Zn[251]. Surface atomic arrangement and electron equipotential plane of Zn (002) and Zn (100)[209]. b) Schematic illustration of zinc plating on the commercial Zn anode and the Zn anode with preferred (002) plane[251]. c)

Schematic of preferential growth of (002) plane induced by $BMIm^+$ ion during cycling. Morphologies of cycled Zn anodes in Blank and 0.02 M $BMIm^+$ [255]. d) Morphologies of Zn (002) plane after cycling in 2 M $Zn(OTf)_2$ electrolyte and the Zn (101) plane in 2 M $ZnSO_4$ electrolyte[256].

2.3.4. Structural Zn anodes

The structural engineering of Zn anodes has been demonstrated to significantly enhance the performance of ZIBs. Traditional anodes, limited by their planar contact area with the electrolyte, can benefit from a transition to 3D designs that expand the interface for improved electrochemical interaction. While this approach might introduce more opportunities for side reactions, it also increases the number of Zn nucleation sites and lowers the local current density, resulting in reduced polarization and dendrite-free anode[241]. Metal-based structured anodes, particularly those utilizing Cu-based materials such as Cu mesh, Cu foam, and porous Cu, have shown excellent compatibility with zinc due to their Zn-affinity and structural integrity[200,257,258]. By specifically designing these structures, Zn nucleation and growth can be directed, effectively mitigating dendrite formation. For example, Cu mesh modified with CuO nanowires not only increases the surface area but also optimizes ion distribution and the electric field at the anode interface[259] (**Figure 2.16**a). The CuO nanowires, with their low nucleation energy barrier, selectively attract Zn^{2+} ions, facilitating the formation of a uniform 3D copper matrix for dendrite-free zinc deposition. Furthermore, innovations extend to 3D Ni-Zn anodes fabricated using 3D printing technologies, which feature a multi-channel lattice increasing the specific surface area, redistributing the electric field, and encouraging uniform zinc deposition into microchannels[260] (**Figure 2.16**b). This design significantly curtails dendrite growth and boosts electrochemical performance. In addition, zinc has been utilized as the primary material in constructing 3D structures[261–263], exemplified by the development of nanoporous Zn electrodes (npZn) through an alloying–dealloying technique. When designed with sufficiently small pores (<40 nm), these structures significantly influence electrolyte ion concentration within the pores, enriching Zn^{2+} ions, and thus facilitating interface-localized concentrated electrolytes for uniform zinc plating and minimized side reactions[262] (**Figure 2.16**c and d).

However, it is unclear whether the Zn metal structure participates in the deposition/exfoliation processes or whether it just exists as a structure. For 3D structured anodes, selecting a substrate that is zincophilic, non-reactive with the electrolyte, and has an optimal pore size is crucial. Despite their innovative designs, the performance of these structured anodes currently falls short of traditional Zn sheet/Zn foil electrodes, potentially due to the high proportion of inactive zinc in the plating layer and challenges in controlling zinc deposition on the substrate.

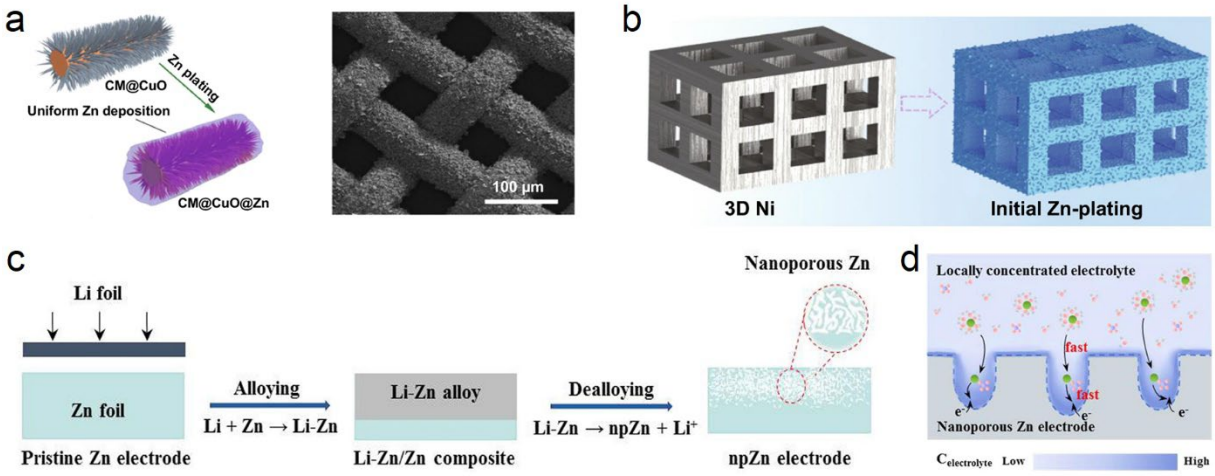


Figure 2.16. a) Schematic illustrations of CM@CuO@Zn. SEM images of Zn anode using reduced CM@CuO as the host[259]. b) Schematic illustration of zinc deposition on the 3D nickel (Ni) substrate[260]. c) Schematic illustration of the preparation of npZn electrode. d) Nanoporous Zn electrode with interface-localized concentrated electrolyte[262].

2.3.5. Electrolyte optimization and design

In addition, electrolyte engineering emerges as a promising approach to enhance Zn anode stability while mitigating cathode dissolution, through the strategic incorporation of additives to promote uniform zinc deposition. Specifically, liquid electrolyte additives, including organic additives and metal ions, significantly influence zinc deposition by diminishing free water activity, inhibiting 2D diffusion, weakening the solvation effect, and forming electrostatic shielding layers[214,241]. This discussion extends from **Section 2.2.2.3**, focusing on the roles of organic and metal ion additives on Zn anode protection.

Metal ion additives are categorized based on their reduction potentials relative to Zn^{2+} (-0.763 V). Ions with more positive reduction potentials, such as Bi^{3+} and Pd^{2+} ions, undergo reduction before Zn^{2+} ions, serving as substrates for zinc deposition and enhancing electrode conductivity for even Zn distribution[264,265]. However, their reduction can complicate battery electrochemistry, potentially impairing performance. Direct contact between Zn anodes and metal ion-enriched electrolytes may also trigger displacement reactions, leading to a metal coating that impedes zinc dissolution and ion transfer at the interface[266,267]. Conversely, ions with lower reduction potentials than Zn^{2+} ion do not participate in redox reactions but rather exert their effect through adsorption on the anode surface, generating electrostatic repulsion. Again with the example of the study by Chen et al., they used Na_2SO_4 additives to facilitate the formation of a smooth Zn anode surface post-cycling[26] (**Figure 2.17**b). The mechanism behind this is that Na^+ ion having a lower reduction potential (-2.71 V) than the Zn^{2+} ion, which will be preferentially attracted to the negatively charged Zn protuberances, thereby creating a positive shield around the Zn protuberance[26,268,269] (**Figure 2.17**a). This electrostatic shielding repels the coming Zn^{2+} ions and promotes their uniform distribution on the substrate, avoiding the continued formation of sharp dendritic products during charging[26]. Moreover, a previous study by our group demonstrated that Pb^{2+} ions serve as a corrosion inhibitor and dendrite suppressor for the Zn anode when $PbSO_4$ is added to the electrolyte[270].

Organic additives, encompassing monomers, surfactants, polymers, and other small molecules, have demonstrated their protective merit for Zn anodes as well[271–280]. These additives utilize their polar groups to adhere to the Zn anode, while their non-polar segments tend to avoid the anode surface, thus modifying the interface and effectively reducing zinc corrosion and influencing zinc dissolution and deposition[271,281,282]. Moreover, the adsorption of polymers increases surface polarization, thereby reducing local current density and decelerating Zn^{2+} ion reduction, which mitigates concentration polarization and hinders ion aggregation (**Figure 2.17**c). Previous studies by our group investigated the effect of polyethylene glycol (PEG) concentration and molecular weight on anode performance[271]. With an increment in PEG200 concentration, there is an initial rise in corrosion potential,

which subsequently begins to decline, whereas the corrosion current density exhibits a contrary pattern. This phenomenon indicates that the quantity of polymer incorporated into the electrolyte necessitates precise optimization to reside within an optimal range. However, the establishment of a comprehensive protective layer on the Zn anode necessitates a significant quantity of organic additives. This requirement can inadvertently elevate both the cost and internal resistance of the battery, potentially impairing overall performance. Thus, research in organic additive applications calls for a deeper investigation to balance protection with cost and performance considerations.

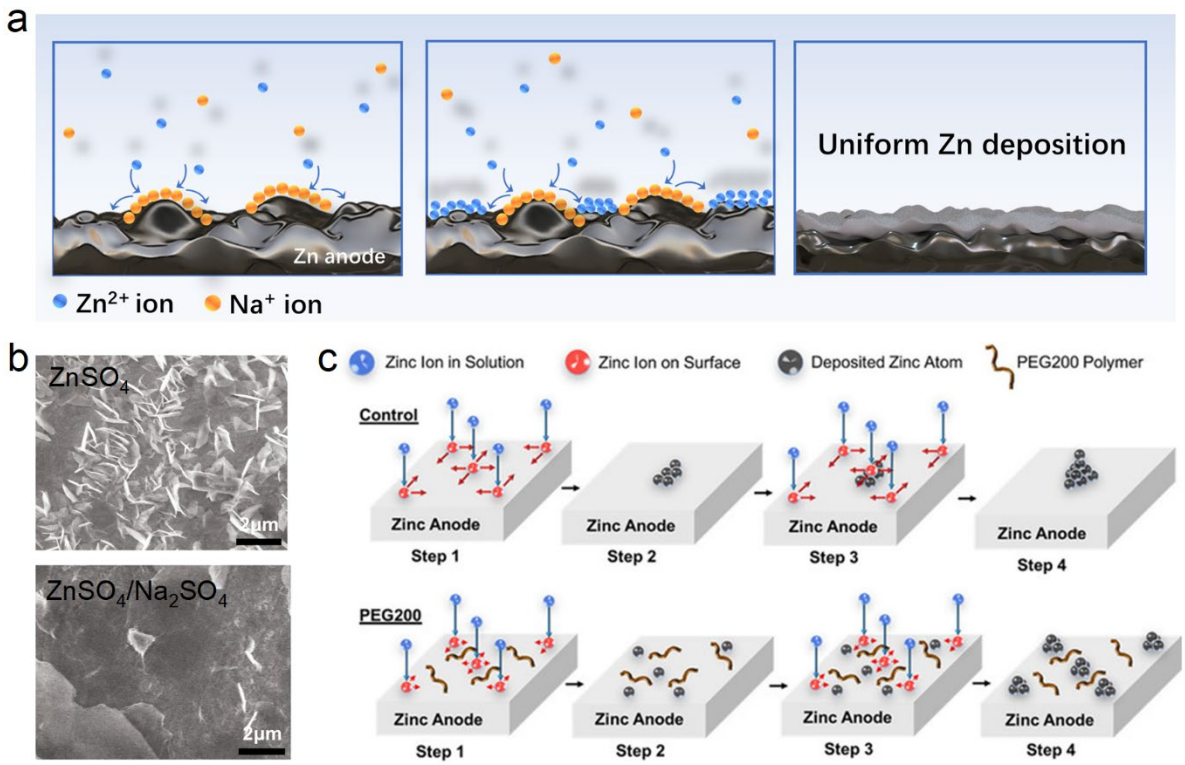


Figure 2.17. a) Schematic of electrostatic shield mechanism applied in Zn^{2+}/Na^{+} electrolyte. b) Morphology of Zn anode surfaces cycled in $ZnSO_4$ and $ZnSO_4/Na_2SO_4$ electrolytes, respectively[26]. c) Schematics of the step-by-step zinc reduction and deposition process in control and PEG200 electrolytes under negative potential bias on the Zn anode[271].

2.4. Energy Storage Mechanisms of RAZBs

The underlying electrochemical reactions governing RAZBs remain less understood than those in established alkali metal ion counterparts, with ongoing discussions and analyses seeking to elucidate their precise mechanisms. Recent scholarly contributions have identified a spectrum of potential reaction mechanisms operative within RAZBs, including Zn^{2+} insertion/extraction, H^+/Zn^{2+} co-insertion/extraction, H_2O/Zn^{2+} co-insertion/extraction, chemical conversion reaction, deposition/dissolution reaction and pseudocapacitive behavior[71,73,120,283–285]. It is noteworthy, however, that the mechanisms of chemical conversion reactions and deposition/dissolution are predominantly associated with manganese-based materials, whereas vanadium-based materials have yet to be implicated in these particular mechanisms. A general classification and illustrative schematic of these proposed energy storage mechanisms for RAZBs is presented in **Figure 2.18**.

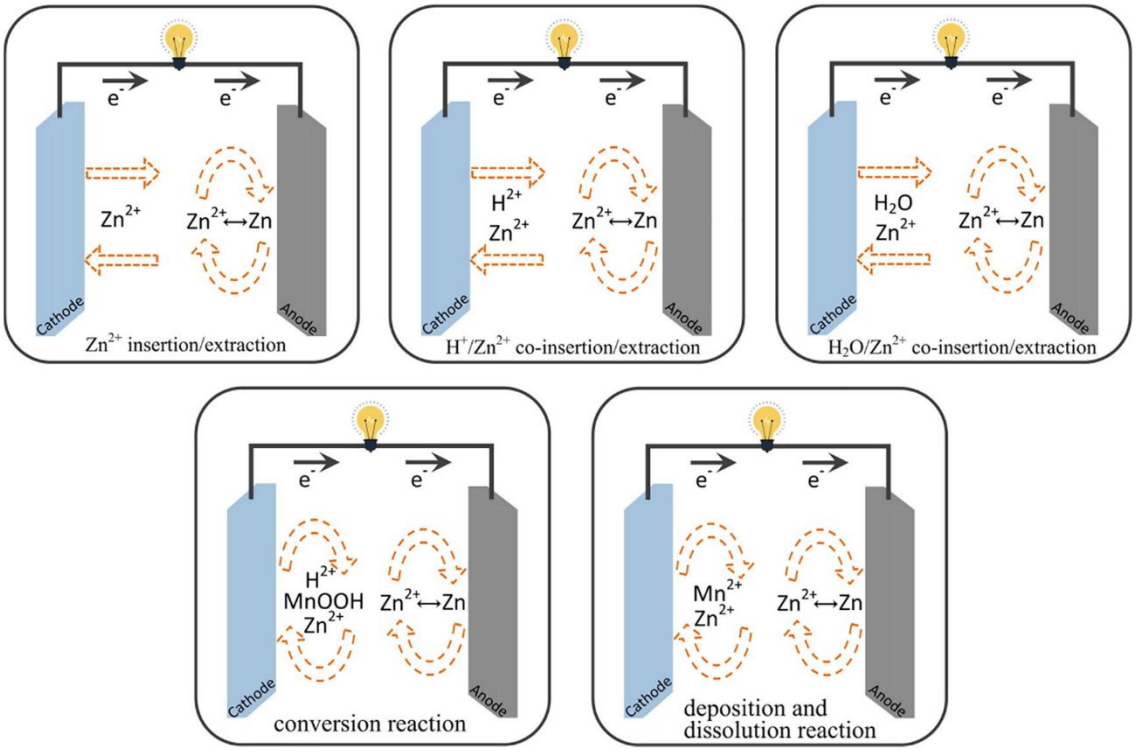


Figure 2.18. General classification and schematic diagram of energy storage mechanisms of RAZBs[71].

2.4.1. Zn^{2+} insertion/extraction mechanism

The reversible insertion and extraction of Zn^{2+} ions in host materials constitute the primary energy storage mechanism in Zn-MnO_2 batteries, similar to the process in traditional LIBs. Kang and colleagues were pioneers in reporting the presence of this mechanism in RAZBs, they suggested a reversible mechanism where Zn^{2+} ions are inserted into/extracted from the α-MnO_2 cathode during the discharge/charge cycles, respectively, while the Zn anode concurrently undergoes dissolution/deposition[33]. However, the exact nature of the energy storage mechanism involving the α-MnO_2 cathode in RAZBs remains a subject of debate. Subsequently, He and his colleagues have supplemented the energy storage mechanisms for other MnO_2 polymorphs. It has been established that the Zn^{2+} insertion/extraction process is applicable to other MnO_2 polymorphs such as β-, γ-, λ-, and δ-MnO_2[126,132,286]. Drawing from Kang et al.'s exploration of the traditional Zn^{2+} insertion/extraction mechanism, generalized equations for different cathode materials can be formulated, where 'A' denotes different cathode materials[119,284]:

$$\text{Cathode:} \quad A + xZn^{2+} + 2xe^{-} \leftrightarrow Zn_xA \tag{10}$$

$$\text{Anode:} \quad Zn \leftrightarrow Zn^{2+} + 2e^{-} \tag{11}$$

$$\text{Overall:} \quad xZn + A \leftrightarrow Zn_xA \tag{12}$$

In the context of vanadium-based oxides, these materials typically exhibit layered, tunneled, or 3D frameworks with large pore space, facilitating the insertion of Zn^{2+} ions. Kim and co-workers were the first to report the use of VO_2 with an open structure as the cathode in a RAZB. Their first-principle calculations suggested that approximately 0.5 mol of Zn^{2+} ions could be inserted into the VO_2 cathode during the discharge process[287]. Specifically, about 0.125 mol of Zn^{2+} ions were intercalated into VO_2 to form $Zn_{0.125}V_2O_5$ at around 0.78 V; further discharge to approximately 0.55 V led to the insertion of an additional 0.375 mol of Zn^{2+} ions, ultimately yielding $Zn_{0.5}V_2O_5$ (as illustrated in **Figure 2.19**a). This process was deemed highly reversible upon recharging. Similar energy storage mechanisms have been proposed for other vanadium-based cathodes, such as $Na_2V_6O_{16}•3H_2O$, $Zn_3V_2O_7(OH)_2•2H_2O$,

$Li_xV_2O_5•nH_2O$, $Ca_{0.24}V_2O_5•0.83H_2O$[63,288–290]. In these compounds, the evolution of the V oxidation state from V^{5+} to V^{4+} or even V^{3+} accommodates the intercalation of Zn^{2+} ions while maintaining a stable crystal framework.

2.4.2. H^+/Zn^{2+} co-insertion/extraction mechanism

Beyond the conventional Zn^{2+} insertion/extraction mechanism in RAZBs, researchers have discovered the participation of hydrogen ions (H^+) as an auxiliary carrier, leading to a dual carrier mechanism involving both H^+ and Zn^{2+} ions. This dual mechanism plays a significant role in enhancing the energy storage capacity and electrochemical properties of the batteries[85,110,119]. Wang et al. were the first to introduce the concept of simultaneous intercalation of H^+ and Zn^{2+} ions in Zn-MnO_2 batteries, a prime example of this mechanism. Through galvanostatic intermittent titration technique (GITT) and CV analyses (**Figure 2.19**b), they demonstrated that the insertion of H^+ ions precede that of Zn^{2+} ions. This process is accompanied by the formation of MnOOH, which subsequently transforms into $ZnMn_2O_4$[291] (**Figure 2.19**c). Similarly, Ji et al. confirmed a reversible H^+/Zn^{2+} co-insertion mechanism in α-MnO_2 cathodes. Initially, H^+ ions are inserted into α-MnO_2, enriching OH^- ions and leading to the formation of $Zn_4SO_4(OH)_6•5H_2O$. Subsequently, Zn^{2+} ions are intercalated into the cathode host, resulting in the creation of hetaerolite $ZnMn_2O_4$[292]. It was observed that the reversibility of Zn^{2+} insertion is less efficient compared to that of H^+ ions. The co-insertion mechanism is also found in the vanadium-based cathode. There is one simultaneous H^+/Zn^{2+} co-intercalation reaction when employing 1 M $ZnSO_4$/1 M Na_2SO_4 mixed electrolyte for $NaV_3O_8•1.5H_2O$ cathode. The corresponding reaction mechanism is formulated by the following equations[26]:

$$3.9H_2O \leftrightarrow 3.9H^+ + 3.9OH^- \quad (13)$$

$$NaZn_{0.1}V_3O_8 \cdot 1.5H_2O + 3.9H^+ + 0.4Zn^{2+} + 4.7e^- \leftrightarrow H_{3.9}NaZn_{0.5}V_3O_8 \cdot 1.5H_2O \quad (14)$$

$$1.95Zn^{2+} + 0.65ZnSO_4 + 3.9OH^- + 2.6H_2O \leftrightarrow 0.65Zn_4SO_4(OH)_6 \cdot 4H_2O \quad (15)$$

The inclusion of smaller and lighter H^+ ions assist in the transfer of Zn^{2+} ions, thus improving the insertion thermodynamics and kinetics[293]. Nonetheless, the specific sites of H^+ insertion within the cathode remain unclear, and the potential impact of H^+ ions on Zn anode stripping/plating and ion diffusion requires further investigation. In addition, the hydrolysis reaction (Equation 13) leads to the formation of by-products like ZSH ($Zn_4SO_4(OH)_6 \bullet xH_2O$) on the cathode surface, and the influence of these by-products on the battery's performance is yet to be fully elucidated.

2.4.3. H_2O/Zn^{2+} co-insertion/extraction mechanism

As described in **Section 2.1.1.2**, structural H_2O or interlayer cations typically expand the layered structure of materials, facilitating the intercalation of hydrated Zn^{2+} ions. This phenomenon is particularly prevalent in electrodes such as V_2O_5, V_6O_{13} and $H_2V_3O_8$[56,60,294,295], where solvated H_2O molecules act as a charge barrier, neutralizing the high charge density of Zn^{2+} ion, thereby reducing electrostatic interactions with the host framework and enhancing Zn^{2+} ion transfer. Mai et al. demonstrated the crucial role of structured H_2O in the Zn^{2+} insertion process. The effective charge of H_2O-solvated Zn^{2+} ion is significantly reduced, decreasing electrostatic interactions with the V_2O_5 framework and thereby promoting Zn^{2+} ion diffusion[60]. In this scenario, H_2O molecules, Zn^{2+} ions, and $CF_3SO_3^-$ ions are simultaneously intercalated to maintain charge balance. As demonstrated in **Figure 2.19**d, the interlayer distance of V_2O_5 reduces from 12.6 Å to 10.4 Å upon charging to 1.3 V, attributed to hydrogen bonding between Zn^{2+}, $CF_3SO_3^-$, H_2O, and lattice oxygen, which draws the V_2O_5 bilayers closer. Upon discharging to 0.2 V, the bilayer distance expands from 10.4 Å to 13.5 Å. Cheng and Huang's teams also discovered that in their respective Zn-vanadate batteries that the structured H_2O intercalation layer not only widens the channel spacing for Zn^{2+} ion storage but also accelerates reaction kinetics[75,296].

In addition, Montree et al. found that pre-insertion of Ca^{2+} ions and H_2O significantly enhances the reversible stability of Zn^{2+} insertion/extraction in manganese-based layered materials. In δ-MnO_2, Ca^{2+} ions and H_2O act as pillars, stabilizing the layered structure[297]. Yu

et al. reported on a $Na_{0.55}Mn_2O_4$•$0.57H_2O$ cathode with co-intercalated Na^+ ions and crystal H_2O. In this system, Na^+ ions and crystal H_2O expand the interlayer distance, thus facilitating the transport of Zn^{2+} ions[298].

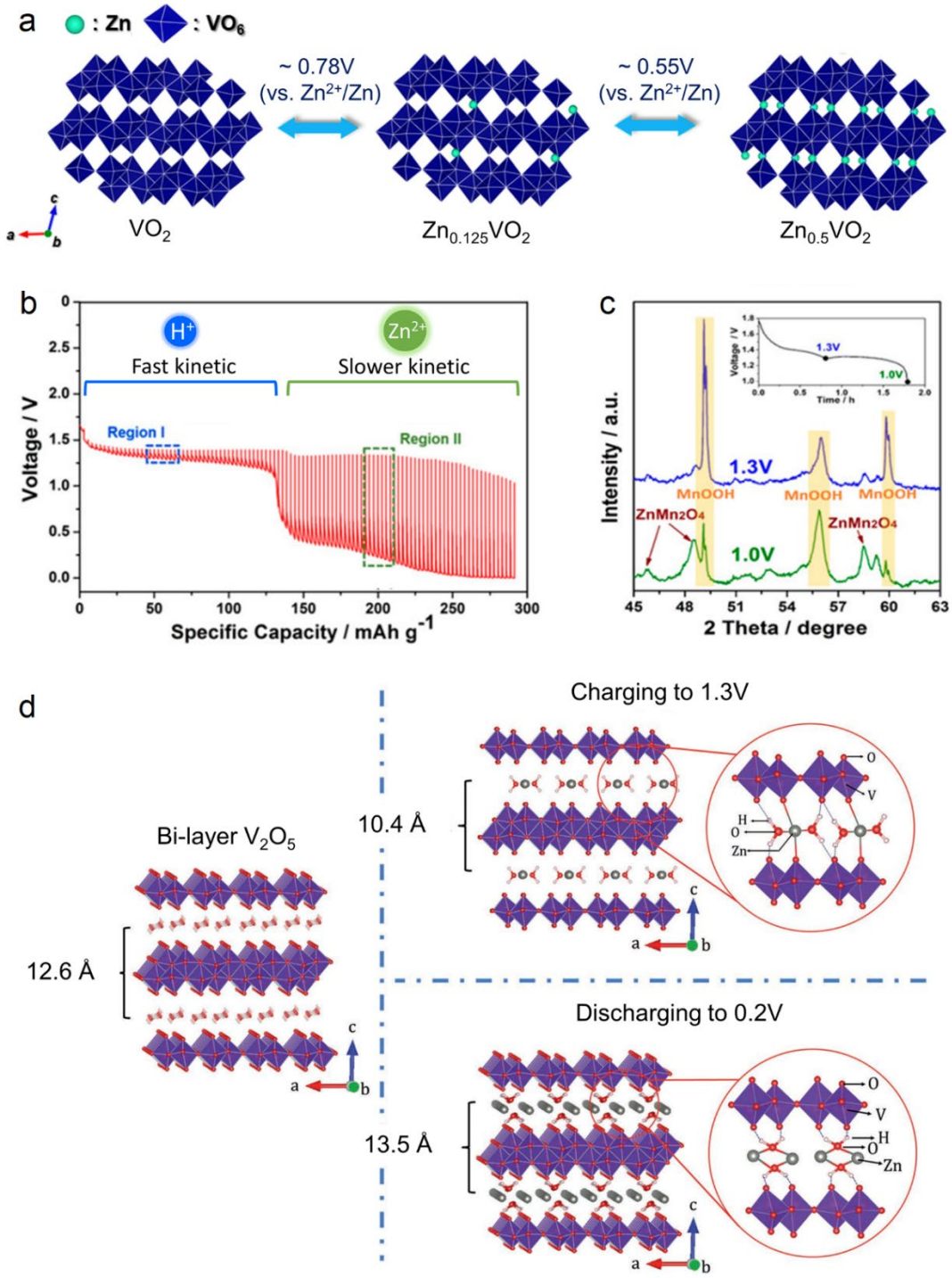


Figure 2.19. a) Schematic illustration of expected mechanism of Zn^{2+} intercalation in VO_2[287]. Investigation of reaction mechanism of the MnO_2@CFP cathode during discharge: b) Discharge GITT profiles of the Zn-MnO_2@CFP cell, and c) *ex situ* XRD patterns of the

MnO_2@CFP cathode at depth of discharge at 1.3 V and 1.0 V, respectively[291]. d) Schematic illustration of crystal structures of pristine V_2O_5, V_2O_5 after charging to 1.3 V and discharging to 0.2 V[60].

2.4.4. Conversion reaction mechanism (manganese-based cathode)

Distinct from the H^+/Zn^{2+} co-insertion mechanism, the conversion reaction mechanism in RAZBs involves a direct charge transfer, potentially offering higher capacities. Liu et al. synthesized α-MnO_2 nanorods and, through morphological and structural analyses of the electrode in its discharged state, suggested the occurrence of a transformation reaction[42]. While previous reports indicated the intercalation of Zn^{2+} ions into α-MnO_2 forming spinel $ZnMn_2O_4$, tunnel, or layered Zn_xMnO_2 phases[33,299,300], high-resolution transmission electron microscopy (HRTEM) results revealed the discharge product to be MnOOH (**Figure 2.20**a). Contrary to being intercalated by Zn^{2+} ions, MnO_2 appeared to react with H^+ ions to form MnOOH, with Zn^{2+} ions and subsequent OH^- ions converting to ZSH, precipitating on the MnO_2 surface. This conversion reaction, involving reversible conversion reaction of MnO_2 accompanied by ZSH precipitation/dissolution, is formulated as follows[42]:

Cathode:
$$H_2O \leftrightarrow H^+ + OH^- \quad (16)$$

$$MnO_2 + H^+ + e^- \leftrightarrow MnOOH \quad (17)$$

$$\frac{1}{2}Zn^{2+} + OH^- + \frac{1}{6}ZnSO_4 + \frac{x}{6}H_2O \leftrightarrow \frac{1}{6}ZnSO_4[Zn(OH)_2]_3 \cdot xH_2O \quad (18)$$

However, this conversion reaction mechanism closely resembles the H^+ ion insertion chemistry discussed in **Section 2.4.2**. To clearly delineate this conversion mechanism, further analytical methodologies are necessary. Qiao et al. developed a high-voltage Zn-MnO_2 cell for a more comprehensive elucidation of the conversion reaction mechanism[174]. The discharge curve of this cell exhibited three distinct regions: D1 (2.0-1.7 V), D2 (1.7-1.4 V), and D3 (1.4-0.8 V) (**Figure 2.20**b). In the D1 high-voltage region, the mechanism is dominated by a conversion reaction where Mn^{4+} in MnO_2 is reduced to Mn^{2+} and then dissolves in the electrolyte; in the D2 region, a conversion reaction between MnO_2 cathode and H^+ ions forms

MnOOH; and in the D3 low-voltage region, it transitions to the Zn^{2+} intercalation mechanism. This reaction (during discharge process) can be represented as:

$$\text{Cathode (initial charge):} \quad Mn^{2+} + 2H_2O \leftrightarrow MnO_2 + 4H^+ + 2e^- \tag{19}$$

$$\text{D1:} \quad MnO_2 + 4H^+ + 2e^- \leftrightarrow Mn^{2+} + 2H_2O \tag{20}$$

$$\text{D2:} \quad MnO_2 + H^+ + e^- \leftrightarrow MnOOH \tag{21}$$

$$\text{D3:} \quad MnO_2 + 0.5Zn^{2+} + e^- \leftrightarrow Zn_{0.5}MnO_2 \tag{22}$$

Furthermore, similar energy storage mechanisms have been identified in β-MnO_2 and δ-MnO_2 electrodes[301,302]. Kang et al. proposed a proton conversion mechanism in the β-MnO_2 cathode, where, in the first discharge cycle, β-MnO_2 transforms into MnOOH and dissolves into Mn^{2+}. In subsequent cycles, the redeposited MnO_2 reacts with protons to form MnOOH and Mn^{2+}, with Mn^{2+} being deposited as MnO_2 during the charging process[302].

2.4.5. Deposition and dissolution reaction mechanism (manganese-based cathode)

As early as 2020，Guo et al. significantly advanced the understanding of the Zn^{2+} ion storage mechanism in Zn-MnO_2 batteries by proposing a dissolution/deposition reaction mechanism[303]. This mechanism entails concurrent H^+ and Zn^{2+} insertion/extraction processes. Initially, the α-MnO_2 reacts with H_2O during discharge, generating Mn^{2+} and OH^- ions. Subsequently, OH^- ions interact with surrounding $ZnSO_4$, forming flaky ZSH on cathode. During the first charging cycle, ZSH and Mn^{2+} ions transform into birnessite Zn_yMnO_2. This reaction cycle repeats, but with the host material evolving from original MnO_2 to birnessite Zn_yMnO_2. In this entire energy storage process, the dissolution/deposition reaction mechanism is predominant, contributing most to the specific capacity, while the accompanying intercalation/de-intercalation reactions play a less significant role. Complementing this, Li's team proposed a MnO_2/Mn^{2+} redox chemical reaction with interfacial regulation[304]. As illustrated in **Figure 2.20**c, during the first discharge, MnO_2 dissolves due to H^+ intercalation, resulting in an increase in the pH value and Mn^{2+} concentration in electrolyte (①). At the end of discharge, ZSH formation occurs, with

complex dissolution/deposition reactions dominating thereafter. The charging cycle commences with co-deposition of Zn^{2+} and Mn^{2+} ions, forming birnessite $Zn_xMn_3O_7$ while ZSH dissolves (②). The reason for the different birnessite products here that I'm considering is caused by the different MnO_2 polymorphs they use. As the cycle progresses, $Zn_xMn_3O_7$ transitions to Mn_7O_{13} through Zn^{2+} extraction and Mn^{2+} deposition (③). This phase transition reverses with the co-insertion of Zn^{2+} and H^+ ions, and further H^+ insertion results in the dissolution of $Zn_xMn_3O_7$ and reformation of ZSH (④-⑤).

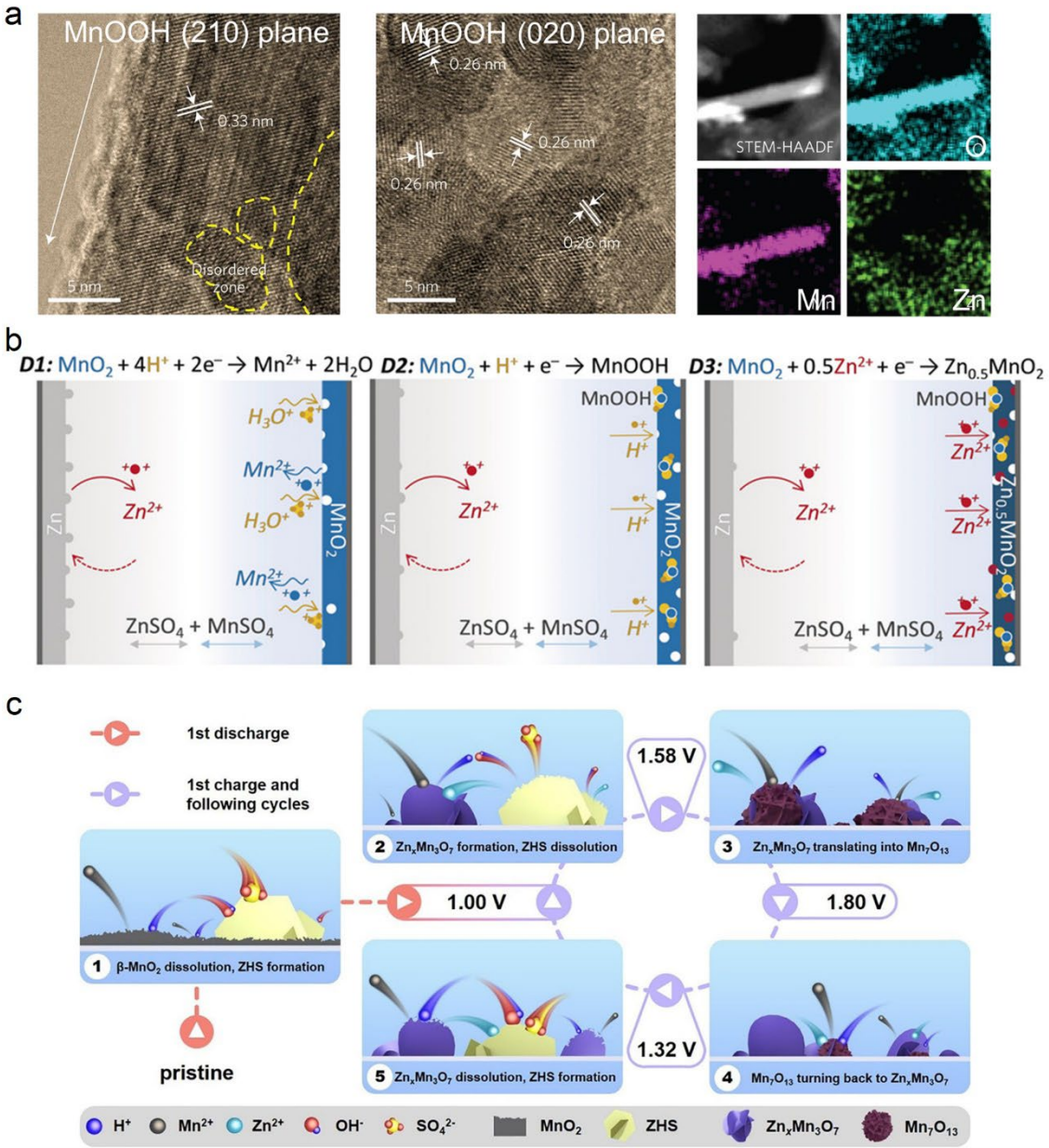


Figure 2.20. a) HRTEM images of MnO_2 discharged to 1 V during the first cycle, and energy dispersive X-ray spectroscopy in scanning transmission electron microscopy (STEM-EDS)

mappings of the elemental distributions of Mn, O, and Zn in the MnO_2 electrode. The lattice fringes of 0.33 and 0.26 nm from the discharged products are consistent with the d spaces from the (210) and (020) planes in monoclinic MnOOH[42]. b) The schematic for different reaction mechanisms in D1, D2 and D3 stages[174]. c) The schematic diagram of the proposed charge storage mechanism of β-MnO_2 cathode[304].

2.4.6. Pseudocapacitive Faradaic process

In addition to diffusion-controlled Faraday processes, the presence of pseudocapacitance (surface-controlled) Faraday processes have been noted in RAZBs. The concept of pseudocapacitance, initially introduced by B.E. Conway, is defined as a Faraday process occurring on an electrode material surface, delineating it from non-Faraday capacitance processes[305]. This concept, however, has been a source of ambiguity in electrochemistry, particularly in studies focusing on electrochemical energy storage and involving metal oxide materials. The contemporary academic discourse presents varied interpretations of pseudocapacitance. Notably, Simon and Dunn have categorized pseudocapacitance into intrinsic and extrinsic types. Intrinsic pseudocapacitance is exhibited by materials demonstrating pseudocapacitive behavior regardless of morphology or particle size[306]. Conversely, extrinsic pseudocapacitance is observed in materials that behave like batteries in bulk form but exhibit pseudocapacitive properties when nanostructured. In Chapter 4, V_2O_5 is classified as extrinsic pseudocapacitance, as its pseudocapacitive traits emerge only after structural modification. To discern and accurately quantify pseudocapacitive contributions in electrode materials, kinetic calculations are recommended. Using CV tests, the relationship between scan rate (v, mV s^{-1}) and current response (i, A) can be analyzed, with the value of b derived from the Equation (23) serving as a determinant for diffusion-controlled or surface-controlled electrochemical processes[307,308]. A reaction is deemed battery-type/diffusion-controlled if the current i varies with the square root of v (b=0.5), while a linear variation of i with v (b$\rightarrow$1) suggests a surface-controlled, capacitive process (as illustrated in **Figure 2.21**a). Higher values of b indicate a significant pseudocapacitive contribution, leading to rapid transfer kinetics and enhanced rate capabilities[308,309]. For instance, the Zn-NVO battery

demonstrates a 67.8% pseudocapacitive contribution at a high scan rate of 0.5 mV s^{-1}, indicative of favorable charge transfer kinetics[26] (**Figure 2.21**b).

$$i = av^b \tag{23}$$

However, Brousse et al. have contested the notion of "extrinsic pseudocapacitance," arguing that such materials exhibit battery-type behavior, as evidenced by electrochemical plateaus rather than straight lines in their discharge curves[310] (**Figure 2.21**c). Despite this, I find Simon and Dunn's perspective more compelling for two reasons: (1) their kinetic calculation approach clearly and accurately differentiates between capacitive and battery-type behaviors in materials; (2) their concept of extrinsic pseudocapacitance accommodates complex electrochemical processes more effectively, such as better interpretation of ion pre-intercalated V_2O_5 behavior.

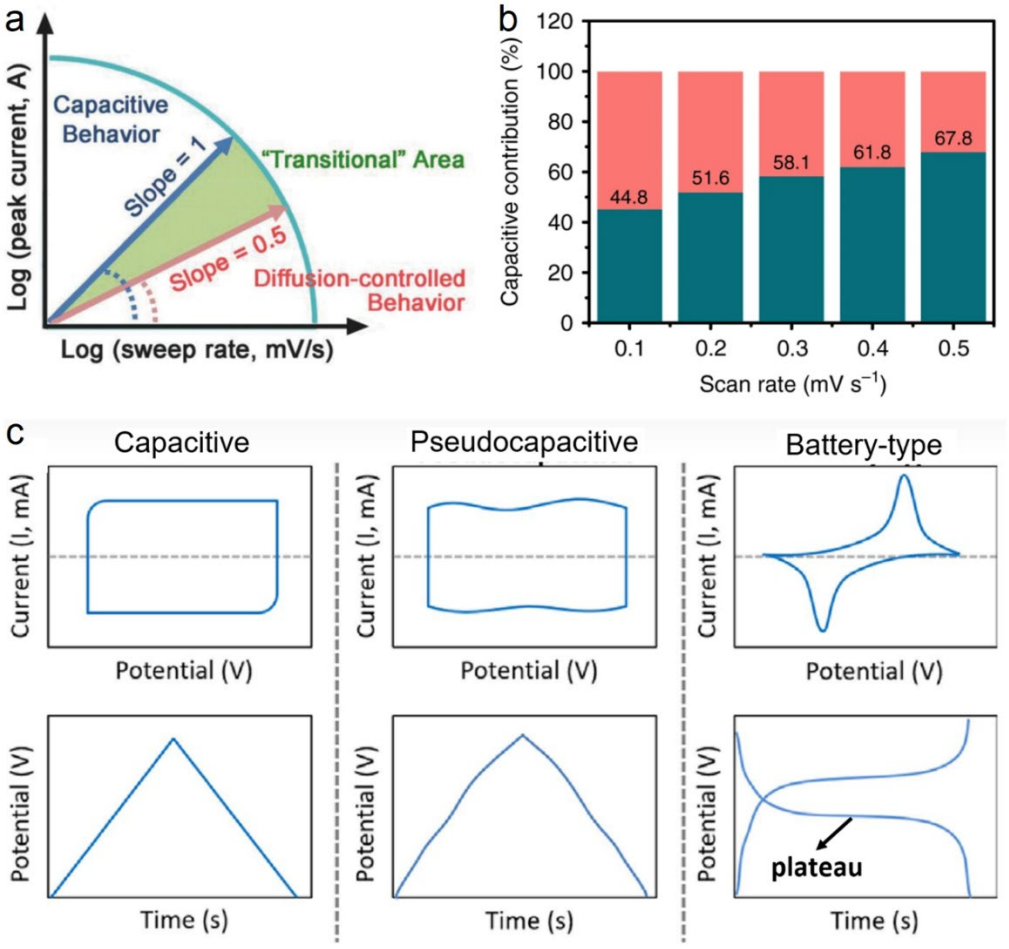


Figure 2.21. a) Power law dependence of the peak current on sweep rate for capacitive materials (b=1) and typical battery-type materials (b=0.5). The "transition" area between capacitive and battery-type materials area is located in the range of b=0.5-1[309]. b) The capacitive contributions at different scan rates in Zn-NVO battery[26]. c) Schematic CVs and corresponding electrochemical charge/discharge curves for various energy storage materials[310].

In a little summary, despite significant strides in recent research, particularly in advancing cathode materials, refining electrolytes, and enhancing Zn anode protection, numerous technical and scientific hurdles persist in the path towards the large-scale application of RAZBs. Moreover, the energy storage mechanisms proposed for RAZBs are multifaceted and yet to be fully matured. The Zn^{2+} insertion/extraction, H^{+}/Zn^{2+} co-insertion/extraction, and H_2O/Zn^{2+} co-insertion/extraction mechanisms are frequently observed in vanadium-based materials. In manganese-based materials, the prevalent mechanisms include Zn^{2+} insertion/extraction, H^{+}/Zn^{2+} co-insertion/extraction, along with chemical conversion reactions, and deposition/dissolution processes. A comprehensive understanding and further exploration of these mechanisms are imperative. Such advancements will catalyze the development of more efficient RAZB systems, addressing the burgeoning demands of contemporary energy storage technologies.

2.5. Project Objectives

The overall goal of this thesis is to develop vanadium-based as well as manganese-based electrodes for next-generation aqueous batteries through advanced fabrication methods. This work will be significant in contributing to both fundamental scientific knowledge and the field of materials engineering. It entails investigating the underlying mechanisms of electrode behavior, specifically examining the influence of electrolyte additives on both cathode and anode functionalities. Furthermore, it aims at the construction of battery systems with high capacity, energy density, and prolonged operational life. The detailed objectives are outlined as follows:

1. Develop a new vanadium-based cathode material featuring dual-cation (Na^+ and Zn^{2+}) pre-intercalation. This involves optimizing the proportion of intercalated cations while preserving the nanowire structure and increasing the specific capacity of the cathode.
2. Develop a specialized electrolyte, pairing it with the aforementioned vanadium-based cathode to establish a dual-cation intercalation system. Employ various electrochemical methodologies to delineate the precise reaction mechanisms of this cathode in the aqueous Zn-vanadium battery.
3. Conduct a comprehensive analysis of the energy storage processes in the MnO_2 cathode, focusing on the effects of electrolyte additive (i.e., Mn^{2+}) on the performance of the Zn anode.
4. Investigate an effective solution to mitigate the effects of side reactions at both cathode and anode in aqueous Zn-MnO_2 batteries.
5. Explore a modification approach for MnO_2 cathode material to upgrade its mass loading and electrochemical performance, with the ultimate goal of improving the commercial viability of high-energy-density aqueous Zn-MnO_2 batteries.

2.6. Thesis Outline

This thesis is systematically divided into eight chapters. Chapter 1 sets the stage by introducing the scope and underlying motivation of this research. This chapter, Chapter 2, offers a comprehensive review of the literature, encompassing topics such as rechargeable aqueous batteries, strategies for cathode material design, zinc anode protection methodologies, and advancements in electrolyte formulations. Chapter 3 briefly lists some of the instruments and experimental setups that will be used in the experiments to avoid redundancy in subsequent chapters. Chapter 4 delves into the innovation of vanadium-based cathode materials, employing a dual-ion pre-intercalation approach to notably enhance the specific capacity by fine-tuning the experimental parameters and optimizing the ion intercalation ratio. This represents a brand-new attempt, as prior studies have predominantly focused on single-ion pre-intercalation, occasionally involving rare metal ions. Furthermore, Chapter 4 explores the dual-ion de-/intercalation mechanism and its impact on electrode performance. Chapter 5 broadens the scope to include MnO_2 cathode materials, uncovering a previously overlooked phenomenon in aqueous Zn-MnO_2 batteries, termed ionic crosstalk. Building on the findings of Chapter 5, Chapter 6 is devoted to the development of porous membranes designed to mitigate the ionic crosstalk phenomenon and enhance the battery performance. Chapter 7 shifts attention to the application of Bi_2O_3-coated MnO_2 materials, mainly discussing their electrochemical results and revealing that the application of Bi_2O_3 coating technology is applicable for larger Zn-MnO_2 batteries (in mAh) and enables them to exhibit superior cycling stability. The thesis reaches its conclusion in Chapter 8, where it synthesizes the principal findings and puts forward recommendations for future studies.

Chapter 3. Experimental Methods

3.1. Cathode Fabrication

The cathode sheet fabrication process is shown in **Figure 3.1**. 70 wt.% active material (e.g., MnO_2), 20 wt.% acetylene black (AB) and 10 wt.% polyvinylidene fluoride (PVDF) were added to a solution of N-methyl-2-pyrrolidone (NMP) and stirred for 5 minutes using a homogenizer (at a speed of 2000 rmp). The slurry was then uniformly coated onto a polyethylene (PE) film (All-Spec 854-36150) with a typical thickness setting of 200 μm. The cathode sheet was then dried in a vacuum oven at 60°C for 8 hours to obtain the cathode sheet.

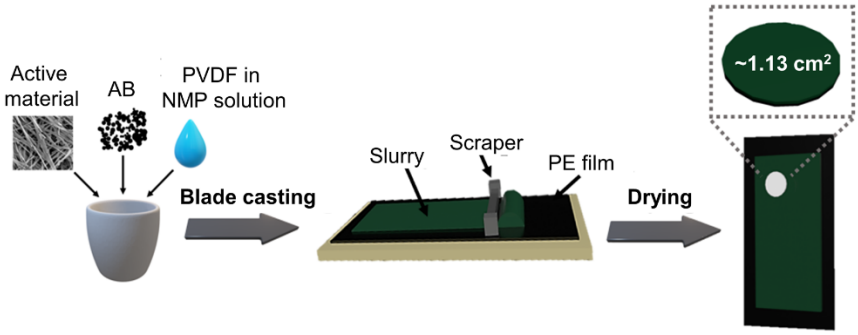


Figure 3.1. Schematic illustration of cathode fabrication process.

3.2. Battery Assembly

3.2.1. Coin cell assembly

CR2025 coin-type cells (**Figure 3.2**a) were utilized for electrochemical tests. The cathode, separator and anode were punched into small discs with different diameters. The coin-type cell was assembled with a cathode sheet (total weight of 19.5±0.2 mg), a single layered absorbed glass mat (AGM, NSG Corporation, diameter: 16 mm, thickness: 0.5 mm, mass: 23.5±0.1 mg) as a separator, and Zn foil (Rotometals, diameter: 12 mm, thickness: 0.1 mm, mass: 12.5±0.1 mg) as an anode. The electrolyte amount for each cell is approximately 140 μL. The calendaring pressure of the coin-type battery was about 2500 psi, held for 5 seconds.

3.2.2. Swagelok-type battery assembly

The battery components of Swagelok-type battery (T-type) (**Figure 3.2**b) are virtually identical to those of coin-type batteries. T-type batteries were assembled with a cathode disc (diameter: 12 mm), double-layered AGM separator (diameter: 12 mm) as separator between cathode and Zn foil (diameter: 12 mm) as an anode. The electrolyte amount is around 1 mL.

3.2.3. Iron plate battery assembly

Large batteries or iron plate batteries (**Figure 3.2**c) were assembled with a cathode square sheet (side length: 3-4 cm), double-layered AGM (side length > 4 cm) as separator between cathode and anode, and Zn foil (thickness: 0.1 mm, side length: 4 cm) as anode. The electrolyte amount for large battery is approximately 1.5 mL.

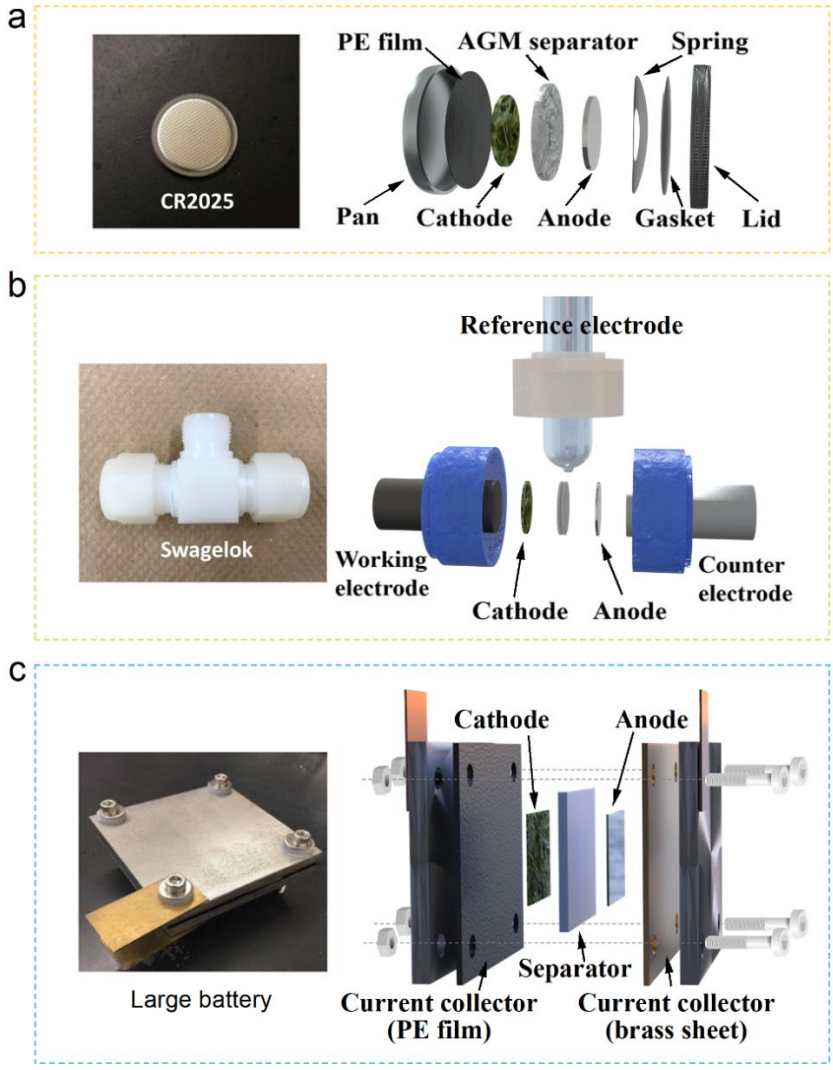


Figure 3.2. External view and internal composition of the a) CR2025 coin-type cell, b) T-type cell (Swagelok), and c) large battery.

3.3. Material Characterization Techniques

3.3.1. X-ray diffraction technique

The structural information of synthesized materials and cycled electrodes was detected by X-ray diffraction (XRD) measurement and analyzed by indexing these patterns against the standard structure of the literature. The Brüker D8 Discover X-ray diffractometer with a copper target and a wavelength of 0.154 nm (Cu-Kα) was applied to carry all XRD experiments in this thesis. For typical sample patterns, data was collected from ~5° to 70° at a scan rate of 1° min^{-1}.

3.3.2. Scanning electron microscopy and energy-dispersive X-ray

The morphology and electrode surface were characterized by scanning electron microscopy (SEM), and in combination with energy-dispersive X-ray (EDS) spectroscopy for identifying the elemental composition of samples. All samples in this thesis were performed on a Zeiss UltraPlus FESEM with an accelerating voltage of 20 kV under vacuum.

3.3.3. X-ray photoelectron spectroscopy

X-ray photoelectron spectroscopy (XPS) was carried out to determine elemental content using a Thermo-VG Scientific ESCALab 250 microprobe. The spectra was obtained via using a 200 μm beam size at 1486.6 eV and 49.3 W. Reported binding energies were normalized against the C1s peak at 284.8 eV. During the measurement, the chamber pressure was maintained at 2.0 nPa, and wide survey (0-1200 eV) was conducted for each sample to determine the surface elemental composition of the samples.

3.3.4. Brunauer-Emmett-Teller

To identify the surface area, volume and average pore diameter of the materials, Brunauer-Emmett-Teller (BET) analysis was performed by Micromeritics ASAP 2020.

3.3.5. Fourier transform infrared spectroscopy

The functional group of the films were characterized using Fourier transform infrared spectroscopy (FT-IR, Brüker Optics Vertex 70 Spectrometer). 400 cm^{-1} 4000 cm^{-1} was selected as the wavenumber range for FT-IR measurement.

3.3.6. Inductively coupled plasma optical emission spectrometry

Teledyne Leeman Labs Prodigy ICP-OES with Echelle grating optical system and Large Format Programmable Array Detector (L-PAD) were conducted to detect the accurate amounts of elemental composition (V, Na, Zn and Mn) of the cathode material. The sample to be tested was dissolved in dilute nitric acid (about 20 mL) and the concentration of each element should exceed its detection limit, which is listed in **Table 3.1**.

Table 3.1. Element detection limit for ICP-OES.

Elements	Detection limit (mg L^{-1})
Na	0.108
Zn	0.016
V	0.004
Mn	0.002

3.4. Electrochemical Characterization Techniques

All electrochemical tests were performed at room temperature, and the capacity measurements were based on the mass of the active material on the cathode.

3.4.1. Cyclic voltammetry

Cyclic voltammetry (CV) was utilized to measure the oxidation and reduction potentials of metal ions in both coin-type and T-type batteries. A Bio-Logic VMP3 electrochemical workstation was performed to obtain the CV curves with different scan rates (unit: mV s^{-1}), the voltage range for aqueous Zn-V_2O_5 battery is 0.2-1.6 V, and for aqueous Zn-MnO_2 battery

is 0.8-1.9 V. AgCl/Ag and graphite rod were respectively employed as a reference and a counter electrode in T-type battery.

3.4.2. Electrochemical impedance spectroscopy

Electrochemical impedance spectroscopy (EIS) is an electrolytic method to measure the impedance and study the electrode kinetics of a system depends on the low amplitude alternating current (AC) potentials over a range of frequencies. By setting up an equivalent circuit (insets in **Figure 3.3**), we can fit the Nyquist plot and thus obtain impedance information for the cell system. In particular, the vicinity of the origin corresponds to the high frequency region, and the intercept of this Nyquist plot in this region is the actual impedance value, which represents the sum of the electrode and electrolyte resistance in this cell, known as the equivalent serial resistance (R_s). While the intercept in the intermediate frequency region (which can be obtained by extending the semicircle) is the sum of R_s and charge transfer resistance (R_{ct}), where we can take the diameter of the semicircle as the value of R_{ct}. R_{ct} represents the resistance of electrons to move between the cathode material and the electrolyte. In addition, the tail in the low frequency region is the Warburg straight line, and the ion diffusion rate in the battery system can be determined by this. EIS test was performed on Bio-Logic VMP3 electrochemical workstation with AC voltage in the frequency range of 100 mHz to 1 MHz.

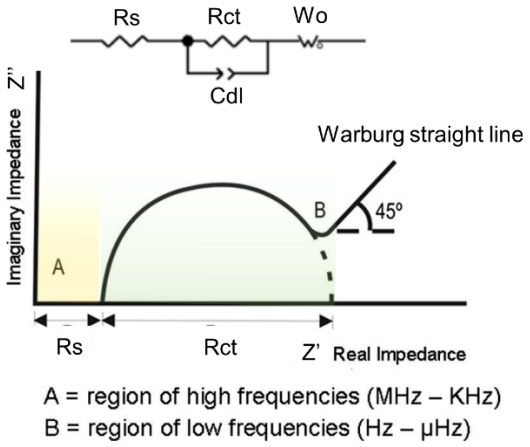


Figure 3.3. An example of Nyquist plot and its equivalent circuit[311].

3.4.3. Linear polarization

Linear polarization (LP) is a broadly used electrochemical method of monitoring corrosion. LP involves the monitoring of the existing relationship between the current from charged electrons and the electrochemical potential, allowing the measurement of corrosion rates and corrosion potentials. A negative shift in the curve indicates a decrease in corrosion potential, which suggests intensified corrosion. Conversely, an increase in corrosion potential indicates that corrosion is inhibited. LP tests were performed on Bio-Logic VMP3 electrochemical workstation with a scan rate of 0.5 mV s^{-1} across a potential range from -0.2–0.2 V in a three-electrode system (**Figure 3.4**). Zn foils were used as working and counter electrode, and AgCl/Ag was used as the reference electrode.

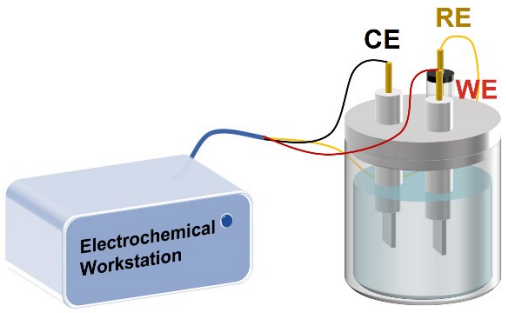


Figure 3.4. Schematic of three-electrode beaker type cell. WE: working electrode, CE: counter electrode, RE: reference electrode.

3.4.4. Linear sweep voltammetry

The electrochemical stability of electrolytes is mainly measured by the ESW (**Section 2.2.1.3**), and the most commonly used method is linear sweep voltammetry (LSV). By analyzing the relationship between changes in voltage and current, we can identify the maximum voltage threshold that the electrolyte material is capable of withstanding. This approach is crucial for determining the compatibility of the electrolyte with high-voltage cathodes. LSV tests was conducted on Bio-Logic VMP3 electrochemical workstation to determine the electrochemical stability window at a scan rate of 10 mV s^{-1} by using a three-electrode system, in which AgCl/Ag was utilized as reference electrode and stainless steel sheet (200-mesh sieve) was used as both working and counter electrodes. The stainless steel

sheets were thoroughly cleaned ultrasonically in high purity alcohol, and then washed three times with high purity water and dried before measurement.

3.4.5. Battery testing

3.4.5.1. Full cell testing

Galvanostatic charge-discharge (GCD) cycling of batteries were performed with constant current protocol by using a Neware battery-testing system at various current densities. When describing a battery, the discharge current is often expressed as a C-rate in order to normalize against battery capacity, which is often very different between battery systems. A C-rate is a measure of the rate at which a battery is discharged relative to its maximum capacity. For example, a 1 C rate describes the current at which the battery will discharge in 1 hour, while a battery with a 5 C rate, being 5 times faster, will discharge in 12 minutes (1/5 hour). The higher the C-rate, the more of a punch the battery can deliver. Some high-performance batteries can be charged and discharged above 1 C with moderate stress. Zn-V_2O_5 batteries were tested under a voltage range of 0.2–1.6 V, and charge/discharge current densities of 1 C=0.2 A g^{-1}. Zn-MnO_2 batteries were tested under 0.8–1.9 V, and charge/discharge current densities of 1 C=0.25 A g^{-1}.

Rate performance was conducted at gradual current rates, and then returned from high to low rates within the voltage range used for cycling tests against the corresponding battery system.

3.4.5.2. Zn symmetric cell testing

Symmetric cells (cells with two identical working electrodes) offer superior advantages in evaluating some key electrode properties, such as reversibility and ion/electron transport kinetics. Although symmetric cell technology has been summarized primarily from lithium battery research, the general considerations and conclusions are broadly applicable to other battery systems, such as Na-, K-, and Zn-ion batteries. Furthermore, the choice of a symmetric cell structure excludes the effects of the differences between the electrodes.

Zn symmetric cells were assembled using Zn foils for both the cathode and anode, and aqueous electrolyte with an AGM separator. All cells were assembled in ambient environment using CR2025 coin cells. The galvanostatic plating/stripping profiles were measured at different areal capacities and different current densities on a Neware battery-testing system.

3.4.6. Self-discharge

Self-discharge in batteries refers to the natural loss of stored charge when a battery is not in use and remains disconnected from any circuit. This phenomenon essentially means that a battery's capacity diminishes even without active consumption. At a fundamental level, the charged state of a battery's electrodes is inherently unstable from a thermodynamic perspective, leading to inevitable internal reactions that diminish the battery's stored energy. Self-discharge is typically divided into two main categories: physical and chemical. Physical self-discharge, characterized by energy loss that can potentially be reversed, often results from microscopic internal short circuits. These shorts can arise from various factors, such as imperfections on the current collector surface, dust particles on the separator, or residual impurities on the electrode plates. Chemical self-discharge, conversely, involves irreversible spontaneous chemical reactions within the battery that lead to a decline in voltage and overall capacity. Unlike physical self-discharge, chemical self-discharge does not produce an electrical current through external circuits but rather through internal chemical interactions among the electrodes and electrolyte. These reactions consume the cathode material, thereby reducing the battery's available energy.

There are various methods to measure battery self-discharge, with the simplest and most straightforward approach being the assessment based on the change in battery capacity before and after a period of rest. Self-discharge behaviors of the assembled Zn-ZNVO batteries (**Chapter 4**) were studied by recording their open-circuit voltage over hold time, after the batteries were repeatedly charged/discharged for 20 cycles at 5 C (1 A g^{-1}) and then kept at an expected voltage for 24 hours through a constant voltage technique.

3.5. Battery Performance Evaluation Metrics

Evaluating battery performance necessitates the meticulous measurement and quantification of various key metrics, including specific capacity, voltage window, mass loading, cyclability, Coulombic efficiency, electrolyte consumption, energy density, and scalability. In a battery system, each parameter can characterize a different aspect of the system's performance, and the following is a list of the various parameters that will be mentioned extensively throughout this thesis:

Specific capacity (in mAh g^{-1})

Specific capacity signifies the charge amount stored per unit mass of active material, serving as a pivotal criterion for comparing different battery systems. The determination of specific capacity is typically executed through constant current charge/discharge cycles within a given voltage window and temperature. Therefore, both preparation and testing conditions affect the specific capacity of the cell.

Voltage window

The voltage window describes the operational potential range, extending from the maximum charging to the minimum discharging limit. Given that a positive electrode with a high voltage plateau and a negative electrode with a low voltage plateau is the preferred combination, meanwhile, the voltage window of the electrolyte must be electrochemically stable.

Mass loading

The mass loading is expressed as the electrode slurry's weight per unit area on the current collector (PE film), which plays a crucial role in battery design. All mass loadings mentioned in this thesis refer only to the mass loadings of the active materials, excluding conductive carbon and binders, if not otherwise specified. Laboratory-scale batteries typically feature low active material mass loading (less than 2 mg cm^{-2}) to minimize electrical resistance and enhance electrolyte permeation, ensuring negligible polarization for maximum

performance studies. Electrodes become thicker as the mass loading increases, thus thick electrodes tend to crack and delaminate after coating and drying, making high mass loading electrodes more difficult to produce. In order to achieve high-capacity batteries, the solution can only be found by combining high specific capacity materials and high mass loading. Therefore, increasing the mass loading of cathode material should be the key focus of high-energy-density batteries.

Coulombic efficiency

Coulombic efficiency is defined as the ratio of specific discharge capacity (mAh g^{-1}) to specific charge capacity (mAh g^{-1}). An ideal efficiency of 100% suggests all Zn^{2+} ions that extract from the cathode at the fully charged state can insert into the cathode at the fully discharged state. Nonetheless, efficiency diminishes below 100% due to the inevitable consumption and entrapment of some Zn^{2+} ions within the cathode from side reactions each cycle, thereby influencing the battery's longevity and capacity retention. The higher the Coulombic efficiency, the less capacity the battery loses per charge/discharge cycle and the longer its potential life.

$$\text{Coulombic efficiency} = \frac{\text{specific discharge capacity of } \boldsymbol{xth} \text{ cycle}}{\text{specific charge capacity of } \boldsymbol{xth} \text{ cycle}} \times 100\% \tag{24}$$

Capacity retention

The capacity retention after *x* cycles was calculated based on the following equation:

$$\text{Capacity retention} = \frac{\text{specific discharge capacity of } \boldsymbol{xth} \text{ cycle}}{\text{specific discharge capacity of } \boldsymbol{1st} \text{ cycle}} \times 100\% \tag{25}$$

where 1st cycle is selected considering that its corresponding Coulombic efficiency is very close to 100%.

Rate capability

The rate capability, or rate performance, of a battery refers to its ability to discharge at varying current densities. It is observed that the capacity deliverable at elevated discharge rates invariably diminishes. Thus, the extent of capacity that can be effectively discharged at such increased rates is a pivotal metric of battery performance. Superior rate performance is indicated by higher capacities maintained under these conditions, highlighting a battery's adaptability to rapid energy demands.

Energy Density (Wh kg^{-1})

The energy density is the amount of electrical energy released per unit mass of the battery. Academic research tends to use large excesses of electrodes and electrolytes in batteries, which may not accurately reflect practical performance metrics. Instead, the industrial evaluation of batteries necessitates a holistic consideration of all variables, including the N/P ratio (the mass ratio of active materials on the anode to those on the cathode) and the volume of electrolyte utilized, to provide a realistic assessment of energy density and overall battery performance.

$$\text{Energy demsity} = \text{sepecific discharge capacity} \times \text{discharge plateau voltage} \quad (26)$$

Chapter 4. High Performance RAZB Enabled by Reversible Zn^{2+}/Na^{+} Co-Intercalation Chemistry

4.1. Introduction

As discussed in **Section 2.1.1**, V_2O_5 stands out due to its unique layered structure and high theoretical capacity, nevertheless, the poor structural stability of V_2O_5 during cycling substantially restrict its practical applications[312–314]. In response, many measures have been taken to improve the electrochemical performance of V_2O_5 cathode in RAZBs. Typically, metallic cations (e.g., Na^+, Mg^{2+} and Ca^{2+}, etc) have been doped into the V_2O_5 layers to improve structure stability, which is called pillar effect[104,269,315–317]. For example, Ling et al. fabricated $Na_{0.56}V_2O_5$ cathode material with a nanobelt structure, which exhibited a high initial discharge capacity of 317 mAh g^{-1} at 0.1 A g^{-1} [85]. Xiong's team demonstrated excellent cyclability and high capacity retention of $Ba_{1.2}V_6O_{16}•3H_2O$ cathode material supported by pre-inserted Ba^{2+} ions[95]. Although these doped cations can assist in enhance the cycling performance of RAZBs, such doping strategy still faces complicated challenges in preventing dissolution of dopant into electrolyte. It greatly alleviates the pillar effect of doped cations and eventually results in the poor cycle life of RAZBs. Meanwhile, the work of electrolytes in Zn-vanadium batteries also makes prominent achievements, among which electrolyte cationic additives (e.g., Li^+, Mg^{2+} and Ca^{2+}, etc.) are widely employed for their straightforward and economical manipulation[156,318–321]. Typically, Wang et al. showed the improvement of battery electrochemical performance by adding 1 M $NaClO_4$ to the electrolyte[320]. Chen et al. also reported that adding Na salts to the $ZnSO_4$ electrolyte can prevent the collapse of $NaV_3O_8•1.5H_2O$ cathode[26]. However, the current research on the cationic additives in Zn-vanadium batteries does not reveal the real role of additive ions (e.g., Na^+) in the stabilization of cathode structure, and the interaction between these additive cations and vanadium oxide during charge/discharge is still unclear. Since the amounts of Na^+ additives used in these works are not in low levels, in-depth studies of the electrochemical reactions of these additive ions with cathode materials, as well as their contribution to the battery capacity are imperative.

In this work, we propose and design an ultra-stable RAZB with highly reversible Zn^{2+}/Na^{+} co-intercalation chemistry in vanadium cathode (**Figure 4.1**), which fundamentally resolves the irreversible dissolution of doped cations in aqueous electrolyte. The discussion is structured into two parts: the fabrication of ZNVO cathode materials and the exploration of their operational mechanisms. Initially, we adopt an ion pre-intercalation strategy to synthesize ZNVO cathode materials, enhancing the specific capacity and longevity of the batteries. Given that the introduction of "pillar" cations tends to decrease the theoretical capacity of these materials, we meticulously optimized the amount of intercalated ions to mitigate this effect. $Zn_{0.3}Na_{0.43}V_2O_5$ cathode material reveals a significantly enhanced performance, which achieves a high specific discharge capacity of 350 mAh g^{-1} at 1 C, greatly outperforms materials such as $V_5O_{12}•1.7H_2O$, Na_xVO_2, $Ag_{1.2}V_3O_8$ and $MgV_2O_6•1.7H_2O$[91,322–324]. Furthermore, we utilized a dual-ion electrolyte in conjunction with the cathode to establish a dual-ion intercalation system in RAZBs. Our investigation into the reaction mechanisms of this dual-ion system employs a variety of electrochemical techniques. We observe that upon discharging the cell to 0.8 V, Na^{+} ions are initially inserted into the cathode, followed by the intercalation of Zn^{2+} ions at 0.55 V. During the charging process, which from 0.7 V to 1.1 V, the Zn^{2+} ions previously incorporated are progressively extracted from the cathode structure. As the charging voltage approaches 1.1 V, the extraction of Na^{+} ions commence. Since the radius of Na^{+} ion is larger than that of Zn^{2+} ion, the firstly inserted Na^{+} ion plays a crucial role in stabilizing the cathode structure, thus preventing collapse or structural degradation throughout the cycling process. This co-intercalation mechanism significantly boosts the cycling stability of the ZNVO cathode material, especially at high current densities. Remarkably, it retains over 90% of its capacity after 4000 cycles and exhibits a superior specific discharge capacity of 209 mAh g^{-1} at 5 C. More importantly, such co-intercalation chemistry can be also applied to other vanadium-based cathode materials such as $H_2V_3O_8$ (HVO) and $Na_{0.33}V_2O_5$ (NVO), all of which demonstrate exceptional cycling stability and long-term cycle life.

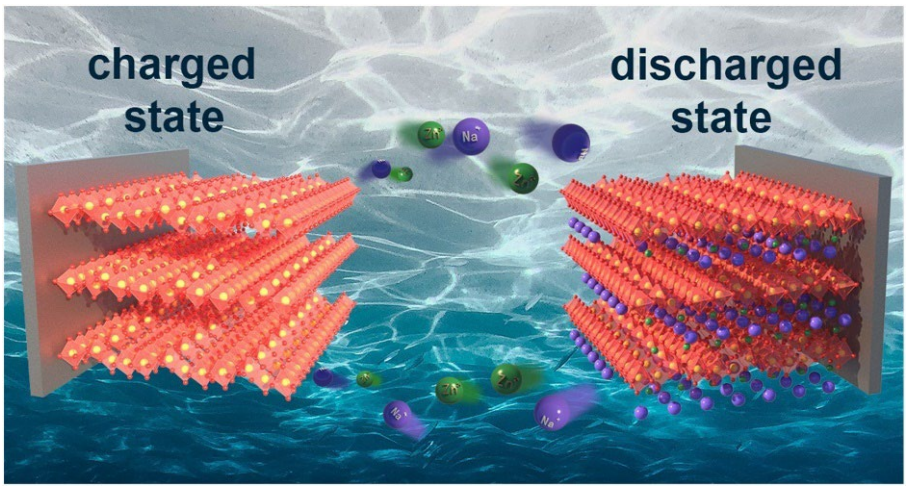


Figure 4.1. Schematic of reversible Zn^{2+}/Na^{+} co-intercalation in vanadium cathode.

4.2. Experimental Methods

4.2.1. Cathode material synthesis

The V_2O_5 nanowires (HVO), Na^{+} pre-inserted V_2O_5 nanowires (NVO) and dual-cation (Zn^{2+} and Na^{+}) pre-inserted V_2O_5 nanowires (ZNVO) materials were prepared by one-step hydrothermal method.

For HVO nanowires preparation, 0.366 g of commercial V_2O_5 (Sigma-Aldrich, purity≥98%) and 0.1 g of polyethylene glycol (Mw~4000) (PEG-4000, Scientific Polymer Products Inc.) were stirred vigorously in 60 mL deionized (DI) water for 30 minutes, and the mixture was then sonicated for at least 20 minutes. Afterwards, the mixture was transferred to a 100 mL Teflon container and sealed it in an autoclave and placed in a high-temperature oven and reacted at 180°C for 72 hours. The preparation process for NVO nanowires closely followed the method used for the HVO sample, with the key difference being the incorporation of a specific amount of Na^{+} solution into the mixture prior to the reaction for NVO material synthesis. As for ZNVO preparation, various molar ratios of Zn:Na were added separately to the mixture. Here we used 1 M sodium hydroxide (NaOH, Sigma-Aldrich, purity≥97%) solution as the Na source and 1 M zinc chloride ($ZnCl_2$, Sigma-Aldrich, purity≥97%) solution as the Zn source. In addition, the reactions were carried out at 190°C for 24 hours, yielding greenish-colored products (**Figure 4.2**). These products were subsequently

washed multiple times with DI water and ethanol, followed by drying in a vacuum oven at 60°C for 2 days.

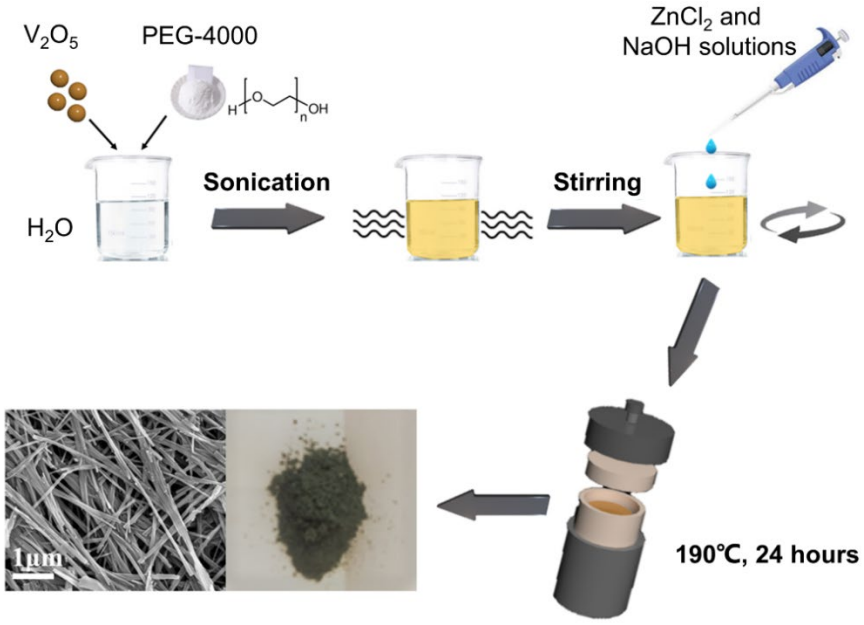


Figure 4.2. Schematic illustrating the experimental procedure of synthesizing ZNVO material.

4.2.2. Other experimental methods

The processes for cathode sheet fabrication, battery assembly, material characterization techniques, and electrochemical testing follow the descriptions provided in **Chapter 3**; therefore, detailed explanations are omitted here. It should be mentioned that the mass loading of the active material in each cell was approximately 3.7±0.2 mg cm^{-2}, and the voltage range of the full cell test is 0.2-1.6 V. Most of the cycling tests were performed at a current density of 5 C, where 1 C=0.2 A g^{-1}. Three types of electrolytes were applied in this work, 2 M zinc sulfate ($ZnSO_4 \cdot 7H_2O$, Sigma-Aldrich, 99%), 1 M sodium sulfate (Na_2SO_4, Sigma-Aldrich, purity≥99%) and 1 M $ZnSO_4$/1 M Na_2SO_4 electrolyte. The pH level and the ion conductivity of three electrolytes are listed in **Table 4.1**.

Table 4.1. pH level and ion conductivity of three electrolytes (at room temperature).

Electrolyte	pH	Ion conductivity (mS cm^{-1})
2 M $ZnSO_4$	4.00±0.03	44.43±0.09
1 M $ZnSO_4$/1 M Na_2SO_4	4.00±0.02	63.34±0.10
1 M Na_2SO_4	3.99±0.02	75.61±0.22

4.3. Results and Discussion

4.3.1. Cathode material fabrication

The morphology and nanostructure of ZNVO is displayed **Figure 4.3**a. It is observed that these nanowires, which are approximately a dozen micrometers in length and 100-300 nm in width, with a tendency to aggregate together. As previously mentioned, the 1D nanowire structure is more favorable to shorten the ion/electron diffusion distance compared with the commercial V_2O_5, and more active sites can be provided for ions to alleviate the volume expansion caused by ion insertion/extraction during cycling. Besides, the pre-inserted ions of the layered oxides establish strong ionic bonds with the O atoms of the framework, resulting in a more stable structure. Elemental mapping further confirms the homogeneous distribution of pre-inserted cations within the ZNVO material, evidencing the successful insertion process. In addition, XPS serves as a precise method for validating the elemental composition. In **Figure 4.3**b, the distinct presence of pre-inserted Zn/Na elements is confirmed through the spectra, aligning with its elemental mapping results.

The XRD pattern of ZNVO illustrated in **Figure 4.3**d reveals the material's high crystallinity. Given ZNVO's novelty, direct matches in existing databases are absent. However, thorough comparative analysis, it was indexed to be related to the substances $Na_{3.25}(OH)_{0.25}(H_2O)_{12}(VO_4)$, $Zn_{0.25}V_2O_5(H_2O)$ and $Zn_3(VO_4)_2(H_2O)_{2.93}$. The XRD data also sheds light on the interlayer spacing within ZNVO, which at 10.76 Å, is significantly wider than the 4.37 Å observed in commercial V_2O_5 (**Figure 4.3**c), thereby providing sufficient space for ion insertion. To pinpoint the optimal pre-intercalation quantity, we synthesized an array of ZNVO materials by varying the Zn:Na ratio. The precise elemental composition of

material was ascertained using ICP-OES, with the molar ratios of Zn:Na for each ZNVO sample detailed in the **Table 4.2**.

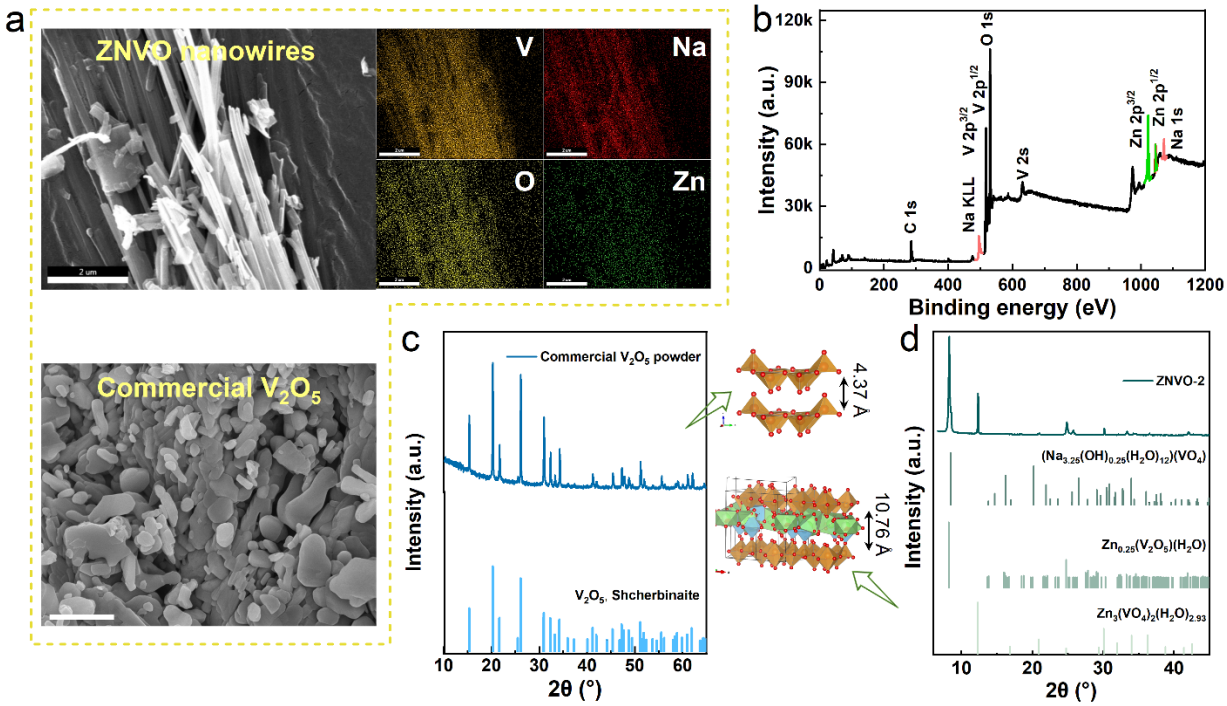


Figure 4.3. a) Morphology of commercial V_2O_5 powder and synthesized ZNVO nanowires. Element mapping of ZNVO material. Scale bar: 2 µm. b) XPS survey spectra of ZNVO sample. XRD patterns of c) commercial V_2O_5 and d) ZNVO-2 sample and schematic diagrams of their corresponding crystal structures. Shcherbinaite (V_2O_5, PDF#97-008-2151), $Na_{3.25}(OH)_{0.25}(H_2O)_{12}(VO_4)$ (PDF#01-070-2496), $Zn_{0.25}V_2O_5(H_2O)$ (PDF#01-086-1238), $Zn_3(VO_4)_2(H_2O)_{2.93}$ (PDF#01-074-2959).

Table 4.2. Molar ratio of Zn:Na for each ZNVO material.

Samples	Zn:Na
ZNVO-1	0.50:1
ZNVO-2	0.71:1
ZNVO-3	1:1
ZNVO-4	1.5:1
ZNVO-5	2.2:1

4.3.2. Electrochemical performance of ZNVO cathode

To explore the influence of pre-intercalated metal ions within the cathode material on battery performance (especially in terms of specific capacity), we conducted galvanostatic cycling tests comparing HVO and ZNVO electrodes within RAZBs. The characterization details for HVO material are delineated in **Figure A1**. As illustrated in **Figure 4.4**a, the ZNVO electrode (red dot) demonstrates a significantly enhanced initial discharge capacity (exceeding 350 mAh g^{-1} at 1 C) compared to the HVO electrode (blue dot) in a 2 M $ZnSO_4$ electrolyte. This superior capacity suggests that the presence of pre-intercalated cations in the cathode material plays a pivotal role in augmenting capacity delivery. Given that the theoretical capacity might decrease due to cation introduction, we prepared five variations of ZNVO materials to identify the optimal ratio of Zn:Na intercalation, labeled from 1 to 5 in ascending order of Zn:Na molar ratio. The cycling performance depicted in **Figure 4.4**b reveals that ZNVO-2 outperforms the other samples in terms of specific capacity and stability, setting the optimal Zn:Na insertion ratio at approximately 0.71 (i.e. $Zn_{0.31}Na_{0.43}V_2O_5$). Moreover, this optimal ZNVO-2 cathode, henceforth referred to as ZNVO, showcases a high specific discharge capacity of 350 mAh g^{-1} at 1 C based on the mass of the active material, surpassing the performance of other cathode materials reported previously (**Figure 4.4**c). Nevertheless, the ZNVO electrode experiences significant capacity decay in subsequent cycles, which can be attributed to the dissolution of cathode materials.

CV is a potentiodynamic electrochemical technique to measure the reduction and oxidation potentials of the chemical species. A cyclic voltammogram trace is obtained by recording the current (I), which flows between the positive and negative electrodes, as a function of the applied voltage (V). **Figure 4.4**d presents the CV profile for the initial cycles of the ZNVO electrode with a 2 M $ZnSO_4$ electrolyte, conducted at a scan rate of 0.1 mV s^{-1}. Notably, there is a high degree of overlap between the 2nd and 3rd cycles of ZNVO electrode, yet the apparent asymmetry and significant disparity between the reduction and oxidation peaks underscore the ZNVO electrode's limited reversibility in 2 M $ZnSO_4$ electrolyte. This

behavior signifies that ions, once de-intercalated from the cathode during the charging phase (as delineated by the three distinct oxidation peaks, each representing a step in the de-intercalation process), face challenges in re-intercalating back into the cathode during discharge. This could be one of the factors leading to capacity degradation. Furthermore, the CV profile of the 1st cycle exhibits slight deviations from the subsequent cycles, aligning with the notable capacity reduction observed between the 1st and 2nd cycles in its cycling performance (red dots in **Figure 4.4**a). In addition, the change or degradation of battery capacity is mirrored in the integral area under the CV curve. As illustrated in **Figure 4.4**e, the response currents of these redox peaks markedly decrease from the 50th to the 200th cycle, and the area of the curve contracts, indicating a rapid capacity decay of the cell during cycling. In **Figure 4.4**f, the impedance of ZNVO electrode reveals an increase in R_{ct} from 4.6 to 47.8 Ω as cycling proceeds in 2 M $ZnSO_4$ electrolyte. Moreover, as seen in the inset, there is a notable increase in the R_s, suggesting potential causes such as cathode material dissolution or the formation of by-products on the cathode surface. In this regard, SEM images of cycled ZNVO cathodes unveil the answer for us. After just 50 cycles, the ZNVO materials exhibit signs of disintegration and dissolution, with the original nanowire structures largely unable to be preserved and the emergence of bulk substances instead (**Figure 4.5**c). Therefore, while the ZNVO material significantly enhances battery capacity, it concurrently faces challenges such as material dissolution and irreversible Zn^{2+} intercalation during cycling. Building on the strategies outlined in previous chapter, our focus shifts towards modifying the electrolyte to address these issues.

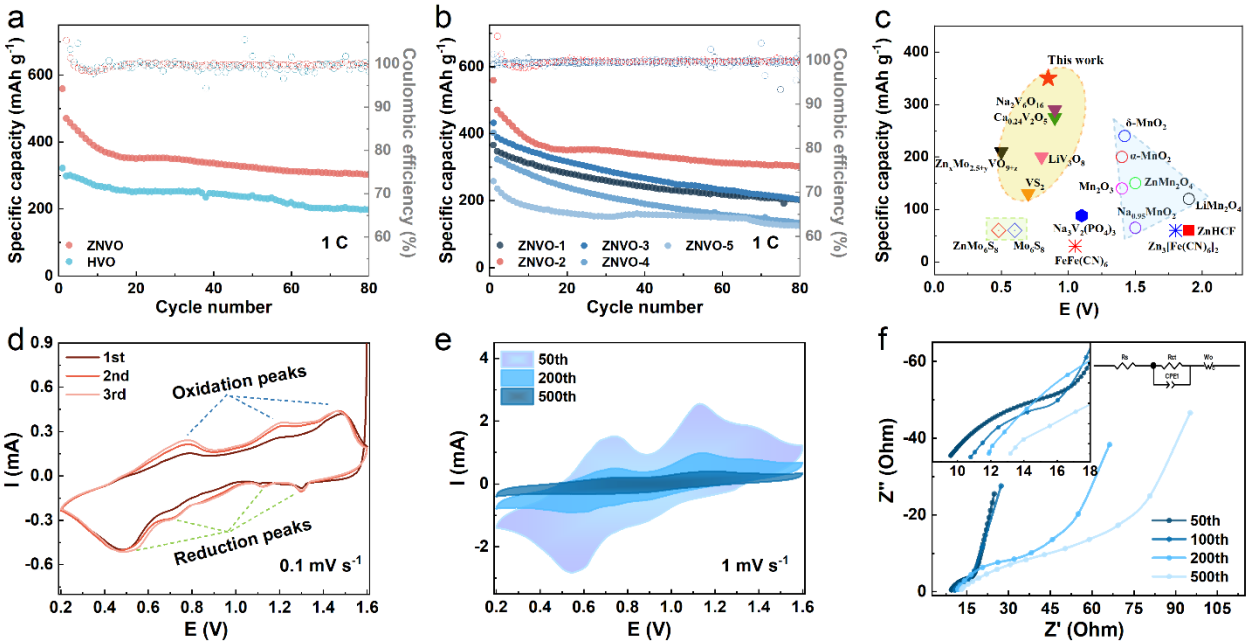


Figure 4.4. a) Cycling performance of HVO and ZNVO electrodes in 2 M $ZnSO_4$ electrolyte at 1 C. b) Cycling performance of ZNVO electrodes with various cations insertion amounts in 2 M $ZnSO_4$ electrolyte. c) Comparison of specific capacity and voltage platform of ZNVO-2 with other reported cathode materials[33,43,44,57,59,63,65,83,269,279,325–330]. CV profiles of ZNVO cathode in 2 M $ZnSO_4$ electrolyte at a scan rate of d) 0.1 mV s^{-1} and e) 1 mV s^{-1} at selected cycle numbers. f) Nyquist plots of ZNVO cathode in 2 M $ZnSO_4$ electrolyte over the frequency range of 100 mHz-1 MHz at selected cycles. Inset is the equivalent circuit diagram.

4.3.3. Electrolyte modification

In an effort to mitigate the issue of cathode material dissolution, our approach involves drawing from prior successful interventions and adjusting the electrolyte composition. Introducing sodium salt into the electrolyte emerged as a straightforward yet potent strategy, necessitating the determination of an optimal sodium salt concentration for effective implementation. Consequently, we conducted a series of battery tests with varying concentrations of Na_2SO_4, ranging from 0.5 to 2 M, added to the $ZnSO_4$ solution (all at ambient temperature). To isolate the influence of salt concentration fluctuations, adjustments were also made to the $ZnSO_4$ concentration concurrently. Analysis of the electrochemical performance data, as illustrated in **Figure 4.5**a, identified that Na^+ concentrations exceeding 1 M yielded superior results. Taking into account both efficiency and cost considerations, we ultimately settled on a 1 M concentration for the Na_2SO_4 additive. Furthermore, it is necessary

for us to perform some evaluations of this new electrolyte. Referring to the electrolyte properties mentioned in **Section 2.2.1**, we examined the ionic conductivity and ESW of this electrolyte. From the data in **Table 4.1**, it can be seen that the ionic conductivity of the $ZnSO_4/Na_2SO_4$ electrolyte is significantly increased. 1 M Na_2SO_4 electrolyte exhibits a higher electrical conductivity than the $ZnSO_4/Na_2SO_4$ electrolyte, which is mainly influenced by the ionic species. The electrochemical stability window of an electrolyte is studied by the LSV technique. In **Figure 4.5**b, the hydrogen evolution reaction (HER) range can be determined by observing the current increase in the lower potential region. The HER onset is evident between 0 V and -0.7 V vs. Zn^{2+}/Zn, where a significant rise in current is observed (green region), indicating the commencement of hydrogen gas evolution. This potential range, from -0.7 V and 0 V vs. Zn^{2+}/Zn, marks the HER region where water is reduced at the electrode surface to produce hydrogen gas. Moreover, all three electrolytes have very a close cathodic stability limit at high potential, while the 1 M Na_2SO_4 electrolyte (yellow line) reaches an anodic stability limit of about -0.35 V. Moreover, the anodic stability limit at low potential of the electrolyte with Na^+ addition (dark red line) broadens by about 0.1 V compared to the one without addition (green line). The Na-rich electrolyte changes the dissolution balance of the Na^+ pre-intercalated in the cathode, thereby protecting the cathode material from continuous dissolution. In **Figure 4.5**c, the morphology of the cathode material in $ZnSO_4/Na_2SO_4$ electrolyte was perfectly preserved after 50th cycle and the nanowires could be clearly observed even after the completion of 200 cycles (**Figure A2**).

Moreover, as described in **Section 2.2.3**, adding Na^+ ions to electrolyte assists in inhibiting zinc dendrite growth on anode surface during the charging process. The reversibility of the Zn anode has a great influence on the cycling stability of the battery. Since the reduction potential of Na^+ (-2.71 V) is much lower than that of Zn^{2+} (-0.76 V), the coming Zn^{2+} ions can be repelled to distribute on adjacent Zn substrate according to the electrostatic shield mechanism. **Figure 4.5**d compares the cycling stability of Zn-Zn symmetric cells in different electrolytes at 0.1 mA cm^{-2} current density with 1 mAh cm^{-2} areal capacity limit. The Zn-Zn cell with 2 M $ZnSO_4$ electrolyte displays random voltage oscillations and a sudden

voltage increase after 120 hours, which may result from a soft short circuit caused by the dynamic dendrites[331]. On the contrary, the battery with $ZnSO_4/Na_2SO_4$ electrolyte exhibits a stable polarization voltage around 29 mV and an ultra-long cycle life of nearly 1500 hours. Similarly, increasing the current density to 5 mA cm^{-2}, the cell containing Na^+ ions in the electrolyte performs substantially better than the one without Na^+ ions on cycling, yielding an extended lifespan of five times (**Figure A3**). As a result, the reversibility of the Zn anode is considerably enhanced and benefits the cycling stability of the full cell. From **Figure 4.5**e, large amounts of harsh and vertical zinc dendrites grow on the anode surface with increasing cycle numbers in 2 M $ZnSO_4$ electrolyte. Conversely, in the $ZnSO_4/Na_2SO_4$ electrolyte, the surface of Zn anode is uniform and smooth. Even after 500 cycles (**Figure 4.5**f), a minimal amount of zinc dendrites is formed in the lateral level which gives a flat morphology to the anode surface, demonstrating the important role of Na^+ ions in suppressing dendrite formation on Zn anodes.

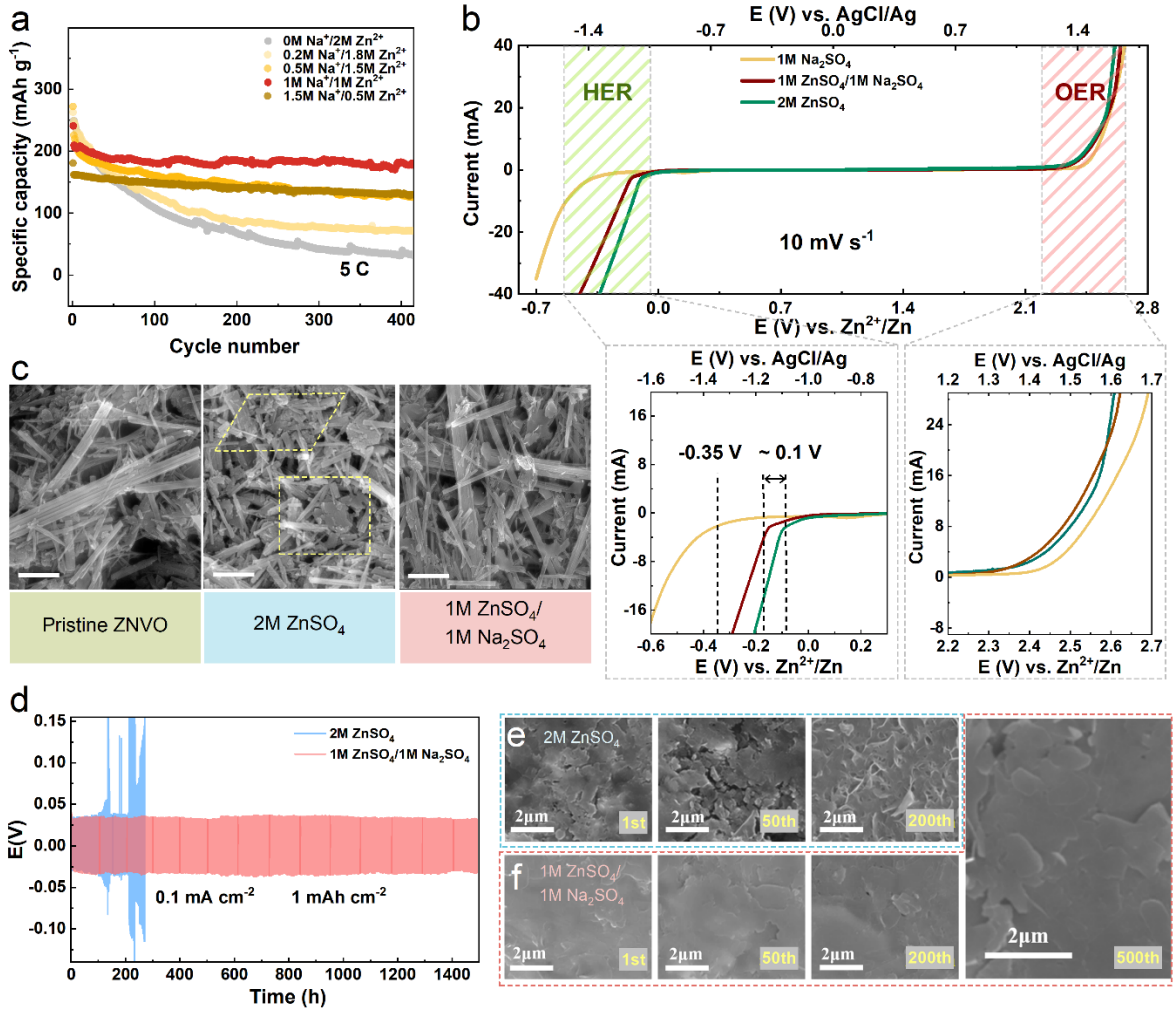


Figure 4.5. a) Cycling performance of a) ZNVO electrodes with various cations insertion amounts in 2 M $ZnSO_4$ electrolyte. b) ESW of different electrolytes in three electrode configuration. Scan rate 10 mV s^{-1}. Magnified view of the regions outlined near anodic (hydrogen evolution reaction, HER) and cathodic (oxygen evolution reaction, OER) extremes. c) Morphology of ZNVO cathode in different electrolytes at 50th cycles. Scale bar: 1 μm. d) Long-term galvanostatic cycling of Zn-Zn symmetric cells at a current density of 0.1 mA cm^{-2} with an areal capacity of 1.0 mAh cm^{-2}. Morphogy of cycled Zn anode in e) 2 M $ZnSO_4$ electrolyte and f) 1 M $ZnSO_4$/1 M Na_2SO_4 electrolyte at the selected cycles. Scale bar: 2 μm.

Surprisingly, this electrolyte is readily compatible with a wide range of vanadium-based cathode materials, the galvanostatic cycling tests of HVO, NVO and ZNVO cathodes in RAZBs are carried out. More details of NVO cathode material characterization are shown in **Figure A4** and **Figure A5**. Given the existence of previous studies on NVO materials, we have chosen to focus the main text on the electrochemical performance of HVO and ZNVO

cathodes. For comprehensive analysis, detailed electrochemical data for NVO cathode are provided in Appendix.

As illustrated in **Figure 4.6**a and **Figure 4.6**b, both HVO and ZNVO cathodes show noticeable capacity drops in the 2 M $ZnSO_4$ electrolyte, and the Coulombic efficiency are away from 100% (**Figure A6**a and **Figure A6**b). After applying Na^+ additive to the $ZnSO_4$ electrolyte, it surprisingly turns out that both cathodes exhibit enhanced electrochemical performance. In particular, the battery with ZNVO cathode, as shown in **Figure 4.6**d, delivers a discharge capacity of 209 mAh g^{-1} at 5 C with approximately 90.9% capacity retention after 4000 cycles. Moreover, the ZNVO cathode achieves close to 100% Coulombic efficiency in a remarkably short duration, as depicted in **Figure 4.6**c. This efficiency suggests that the cathode requires minimal time for activation. Unlike the lengthy activation procedures often necessary for vanadium- or manganese-based cathodes, which may involve applying a small current during the pre-cycle stage for tens of hours or days, our batteries complete the activation process within approximately 1 hour. Excellent capacity retention is also revealed by its GCD plots in **Figure 4.6**e, where it is evident that the incorporation of $ZnSO_4/Na_2SO_4$ electrolyte greatly intensifies the cycling performance of Zn-vanadium cells. Even at a very high current density of 10 C, the capacity retention of ZNVO reaches 85% within 3000 cycles, and the HVO electrode shows almost no capacity degradation over 2500 cycles (**Figure 4.6**f). This superb capacity retention of ZNVO electrode is well outperformed by these published cathode materials listed in **Table A1**. The NVO cathode also significantly enhances the cycle life as shown in **Figure A7**. Moreover, self-discharge is also one of the important parameters for evaluating battery performance. Comparing the self-discharge of Zn-ZNVO cells in different electrolytes in **Figure A8**, it is observed that the voltage drop is reduced by adding Na^+ ions to the cell system and its capacity decay is almost negligible. In other words, the discharge capacity can be almost recovered to the original level, suggesting that the self-discharge becomes minimal with the $ZnSO_4/Na_2SO_4$ electrolyte.

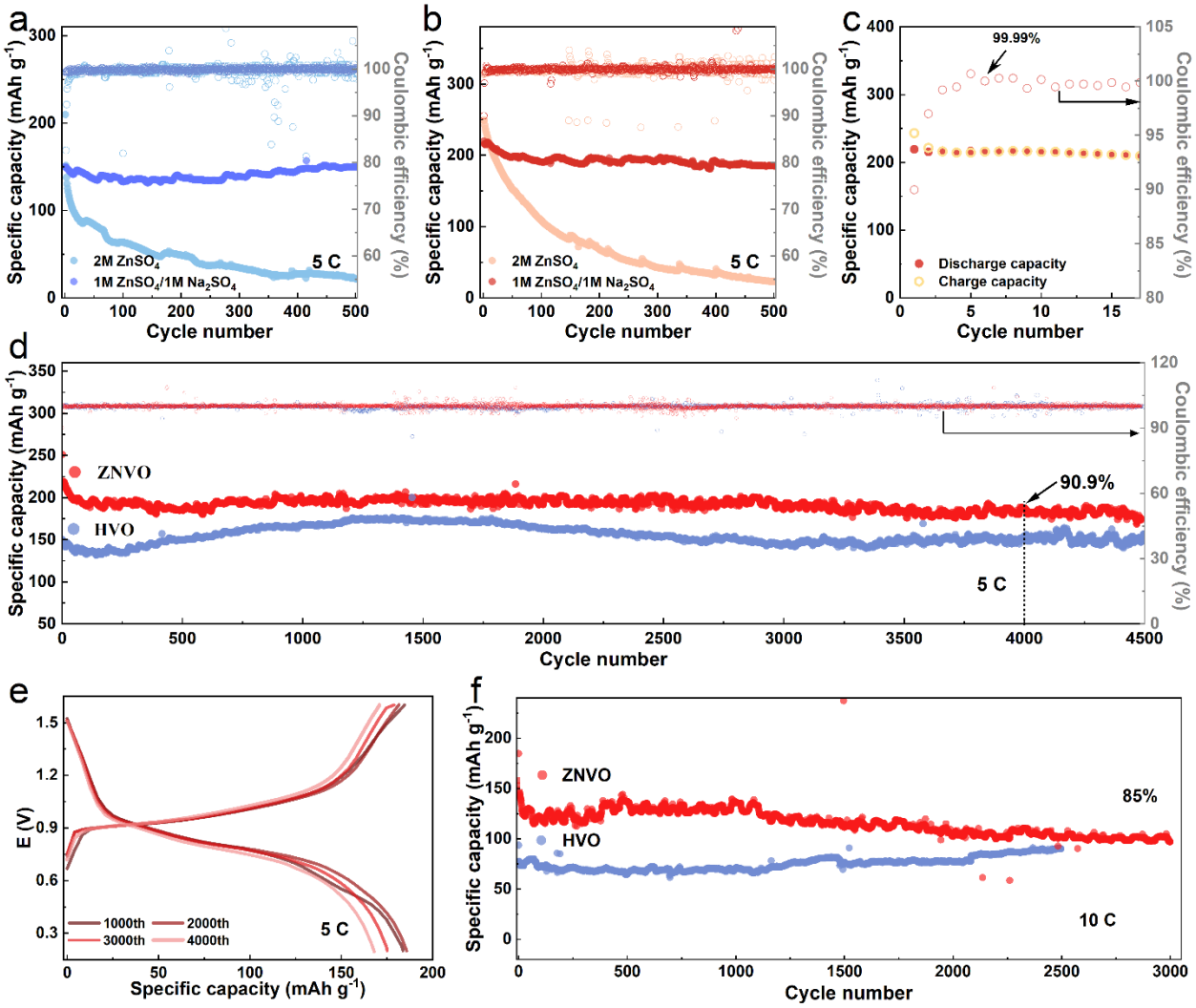


Figure 4.6. Cycling performance of a) HVO and b) ZNVO cathodes in 2 M $ZnSO_4$ and 1 M $ZnSO_4$/1 M Na_2SO_4 electrolytes at 5 C. c) Initial cycles of ZNVO cathode in 1 M $ZnSO_4$/1 M Na_2SO_4 electrolyte at 5 C. d) Long-term cycling performance of HVO and ZNVO cathodes in 1 M $ZnSO_4$/1 M Na_2SO_4 electrolytes at 5 C. The Coulombic efficiency for a narrow y-axis scale is shown in **Figure A6**c. e) GCD profiles of ZNVO cathode in 1 M $ZnSO_4$/1 M Na_2SO_4 electrolyte at 5 C. The average charge voltage is around 1.0 V, and average discharge voltage is around 0.8 V. f) Long-term cycling performance of HVO and ZNVO cathodes in 1 M $ZnSO_4$/1 M Na_2SO_4 electrolytes at 10 C.

Rate capability always plays a key role for the practical deployment of RAZB in grid energy storage solutions. Beyond their excellent capacity retention and longevity, vanadium-based electrodes exhibit superior rate performance when paired with a $ZnSO_4$/Na_2SO_4 electrolyte, as detailed in **Figure 4.7**a and **Figure 4.7**b. Notably, the HVO electrode in a 1 M $ZnSO_4$/1 M Na_2SO_4 electrolyte demonstrates average discharge capacities at various current

densities of 1 C, 2.5 C, 5 C, 10 C, 15 C and 20 C are 326.1, 211.9, 162.1, 131.3, 107.8 and 83.0 mAh g^{-1}, respectively. However, at lower currents, the discharge capacities of HVO and ZNVO electrodes slightly drop compared to those in a 2 M $ZnSO_4$ electrolyte, possibly due to the enhanced dissolution of the cathode material, leading to marginally higher capacities. In particular, applying a lower current to the cell causes the cathode material to dissolve continuously, however, the dissolved material is difficult to be deposited back to its original form, thus the capacity of the battery would decay rapidly in subsequent cycles. The dissolution of cathode materials at low currents suggests that the capacity at these densities is not solely due to ion insertion/extraction but also to the dissolution of vanadium-based materials. This hypothesis was supported by cycling tests on several cell batches at low currents (from 1 C to 3 C). After 10 cycles, the cells were disassembled and it was observed that the separators using a 2 M $ZnSO_4$ electrolyte were observed adhering to some green matters (**Figure 4.7**d and **Figure 4.7**f), i.e., dissolved HVO or ZNVO cathode materials. In addition, the nanowire morphology of the cathode material without Na^+ additive can be significantly damaged. As shown in **Figure 4.7**c and **Figure 4.7**e, both HVO and ZNVO cathode materials are broken into short nanowires in $ZnSO_4$ electrolyte after only 10 cycles, and the nanowire structure of most materials on cathode can hardly be maintained, followed by the formation of some bulk substances instead. Consequently, while HVO and ZNVO electrodes in $ZnSO_4$ electrolyte initially show higher capacities at low currents, this advantage comes at the expense of rapid performance degradation. This leads to a rapid deterioration in battery performance and fail to achieve excellent cycling performance. Even though the ZNVO electrode provides unsatisfactory capacity at low current rates, it performs more favorably when the current rate exceeds 5 C. After reaching 15 C, the average discharge capacity of ZNVO recovers to 308.6 mAh g^{-1} when returning to a low current rate of 1 C, thus achieving more than 100% capacity retention, which is much higher than that in 2 M $ZnSO_4$ electrolyte. This excellent result highlights the significant impact of electrolyte modification on enhancing the electrochemical performance of aqueous Zn-vanadium batteries.

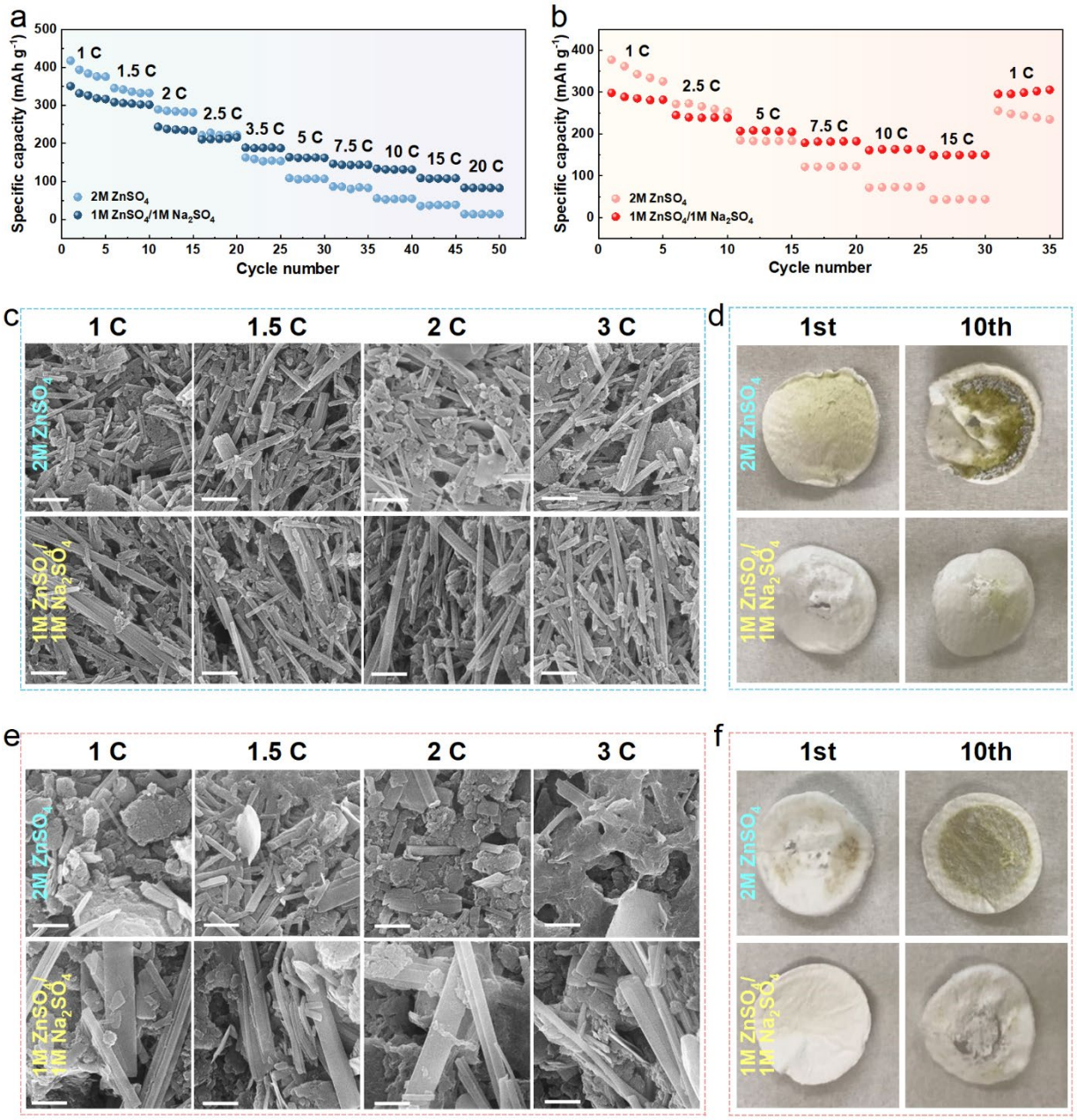


Figure 4.7. Rate performance of a) HVO and b) ZNVO cathodes in different electrolytes. Morphology of c) HVO cathodes and e) ZNVO cathodes after cycling in different electrolytes at various small current densities. Scale bar: 1 µm. Images of the obtained separators from the d) Zn-HVO cells and f) Zn-ZNVO cells after 10th cycle in different electrolytes at 1 C.

In **Figure 4.8**a, the specific capacity over cycles for three individual cells (cell 1, cell 2, cell 3) shows significant stability over an extended number of cycles (up to 3000 cycles). The specific capacity does not show significant decay, and the slight variations between the cells are minimal, which underscores the high reproducibility and reliability of this Zn-ZNVO battery. High reproducibility is critical in battery technology as it ensures that performance

standards can be met consistently in mass production. The data points for specific capacities of the Zn-NVO and Zn-HVO cells in **Figure A9** appear consistent across the different cells tested. Moreover, the Coulombic efficiency remains above 99.8% for most of the cycling process, indicating efficient charge/discharge processes with minimal irreversible losses (**Table A2**). **Figure 4.8**b compares the cycling performance of three different cathodes. ZNVO maintains a higher specific capacity over the long term compared to HVO and NVO. This indicates that our designed ZNVO material has superior structural stability and electrochemical properties compared to other vanadium-based materials, which is conducive to extended cycle life at high current densities, and is important for applications that require rapid charging and discharging. **Figure 4.8**c details the Coulombic efficiency of the three different cathode materials over numerous cycles. While there is some fluctuation, all materials stay within an average range of approximately 99.7% to 100.3% efficiency. The data here suggests good reversibility of the electrochemical reactions during cycling.

For the purpose of demonstrating that our battery system has prospects for practical applications, a large battery with a capacity of 9 mAh was fabricated and employed for cycling test. The cathode was cut to a size of 3.5 cm×3.5 cm and the active material loading was about 45.0±0.3 mg per piece. The significance of testing a larger 9 mAh battery relates to the scalability of the technology from laboratory to practical applications. By fabricating and testing a large battery, it is possible to preliminarily evaluate how the materials and cell design translate to real-world applications. This is especially important for energy storage devices where capacity, not just specific capacity, determines the usability and applicability of the technology. The successful demonstration of cycling tests with a 9 mAh battery, as shown in **Figure 4.8**d and **Figure A10**, indicates that the battery system is not only effective in small, controlled test scenarios but also has the potential to be scaled up. This is a critical step toward commercialization, as it suggests that the battery can maintain its performance characteristics at a size suitable for real-world energy storage demands.

As a short summary, the consistent performance across multiple cells, the stability over thousands of cycles, and the successful demonstration of a 9 mAh battery all contribute to the evidence that this battery technology is a promising candidate for practical energy storage devices. The ability to maintain high Coulombic efficiency and specific capacity over many cycles at a higher current rate (5 C) without significant degradation is particularly encouraging for applications where both high power and energy density are required.

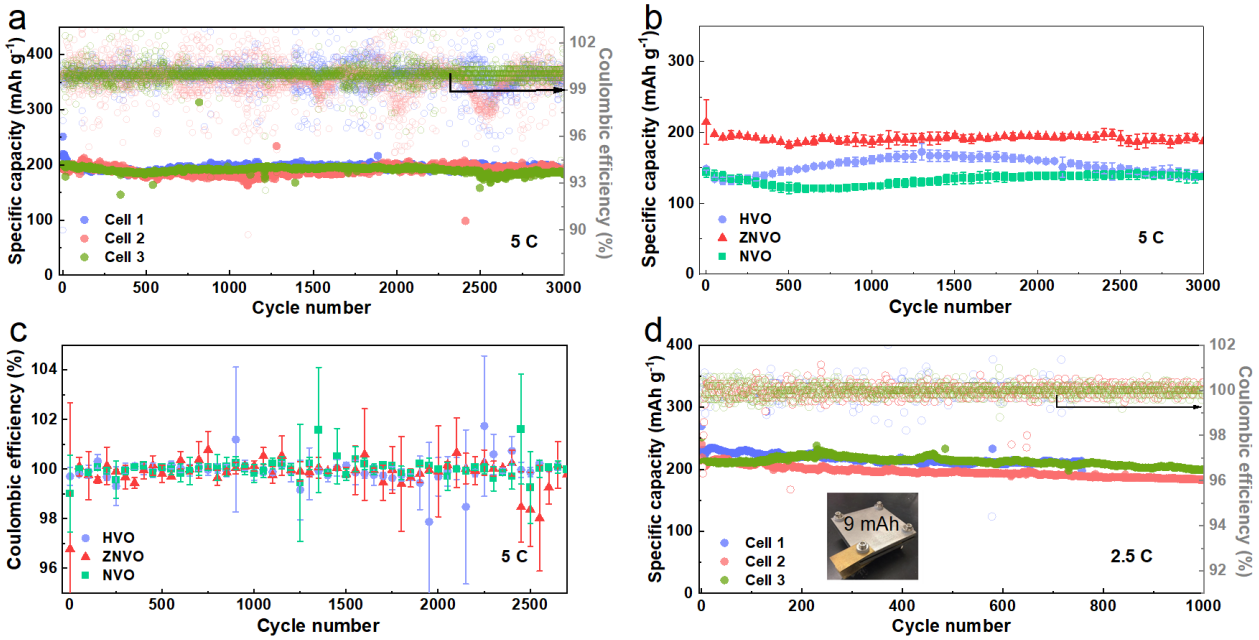


Figure 4.8. a) Cycling performance of ZNVO in 1 M $ZnSO_4$/1 M Na_2SO_4 electrolyte at 5 C. b) Cycling performance and c) Coulombic efficiency plots with standard deviations calculated from three cells for HVO, ZNVO and NVO cathodes at 5 C. d) Cycling performance of ZNVO cathode in 1 M $ZnSO_4$/1 M Na_2SO_4 electrolyte in 9 mAh batteries at 2.5 C.

4.3.4. Energy storage mechanism

Current research on the inclusion of cationic additives in Zn-vanadium battery systems has not yet fully elucidated the true function of these ions (e.g., Na^+) in stabilizing the cathode. To understand and identify the behaviors of Na^+ and Zn^{2+} ions in the cathode material during the charge/discharge process more precisely, we have conducted systematic experiments. Utilizing the HVO cathode as an example, we explored the behaviors of these ions in different

electrolytes. We pursued this investigation by employing a suite of analytical techniques, including CV, XRD, XPS and ICP-OES.

CV measurements were performed at a scan rate of 0.1 mV s^{-1} on HVO cathode in a $ZnSO_4/Na_2SO_4$ electrolyte. The two pairs of redox peaks displayed in **Figure 4.9**a are generally considered as multi-step of Zn^{2+} insertion/extraction or H^+/Zn^{2+} co-insertion /extraction. Our investigation, however, reveals a different reaction mechanism from the previous ones, where a reversible de-/intercalation behavior of Na^+ ion in the Zn-vanadium battery system also existed. To substantiate this discovery, we prepared a 1 M Na_2SO_4 electrolyte with identical pH. This electrolyte was used in isolation from the $ZnSO_4$ and $ZnSO_4/Na_2SO_4$ electrolytes in T-type batteries with HVO cathodes for subsequent CV measurements. It is important to note that in the T-type cells, the Zn anode was substituted with a graphite rod which is served as a counter electrode. This operation effectively removes Zn^{2+} ions from the Graphite/Na_2SO_4 electrolyte/HVO battery, thereby eliminating any influence of Zn^{2+} ion on the peak position of the CV curve.

In the CV profile of the Na_2SO_4 electrolyte (**Figure 4.9**b), one reduction peak located around 0.8 V (peak 3) is obtained, the position of which is similar to the reduction peak 3 of HVO cathode in the $ZnSO_4/Na_2SO_4$ electrolyte (**Figure 4.9**a), and their locations of the oxidation peak 2 also overlap virtually. Since there is no presence of Zn^{2+} ions in the battery system of **Figure 4.9**b, it can be determined that the peak pair 0.8/1.1 V (peak 3/peak 2) represents the insertion/extraction of Na^+ ion. The HVO cathode with Na_2SO_4 electrolyte also displays an additional peak pair at 1.25/1.35 V with weak current intensity, which is one more step of Na^+ insertion/extraction in the HVO cathode[332,333]. Therefore, a multi-step reaction mechanism exists for Na^+ ions in the HVO cathode at a small scan rate. Furthermore, it is noteworthy that the reduction peak 4 located at 0.55 V in **Figure 4.9**a disappears in the Na_2SO_4 electrolyte profile, but it can be observed in the CV curve of $ZnSO_4$ electrolyte (**Figure 4.9**c), indicating that the reduction peak 4 is the insertion of Zn^{2+} ion into the cathode material. Since the positions of the oxidation peak 1 in **Figure 4.9**a and **Figure 4.9**c are

identical, the pair of redox peaks (peak 4/peak 1, 0.55/0.7 V) can be identified as the behavior of Zn^{2+} ion in the cathode. Even though the oxidation peak 2 can be confirmed to represent the Na^+ ion behavior, its response current in Na_2SO_4 electrolyte is reduced compared to the one in $ZnSO_4/Na_2SO_4$ electrolyte. In addition, this oxidation peak 2 can also be observed in $ZnSO_4$ electrolyte. Thus, it is suggested that the de-intercalation process occurs at peak 2 contains both Zn^{2+} ion and Na^+ ion.

Furthermore, to identify this reversible Zn^{2+}/Na^+ co-intercalation also exists in other vanadium cathodes, CV measurements were performed for NVO ($Na_{0.33}V_2O_5$) and ZNVO ($Zn_{0.3}Na_{0.43}V_2O_5$) cathodes, respectively. As exhibited in **Figure 4.9**e, only one peak pair can be observed in the CV profile of NVO cathode in Na_2SO_4 electrolyte. Due to the complete absence of Zn^{2+} ions in this battery (i.e., Graphite/Na_2SO_4 electrolyte/NVO), the presented pair of redox peaks (peak 3/peak 2) is considered as the intercalation/de-intercalation of Na^+ ion in the cathode. For using a $ZnSO_4$ electrolyte, its curve (**Figure 4.9**f) shows similar results to that of HVO. In addition, CV curves of ZNVO cathode are also obtained, whose reduction peaks 3 and 4 can be observed in Na_2SO_4 electrolyte (**Figure 4.9**h) and $ZnSO_4$ electrolyte (**Figure 4.9**i), respectively. It is proved that the intercalation behavior of Na^+ ion occurs when the discharge voltage reaches 0.8 V, and Zn^{2+} ion is inserted into the cathode as the battery continues to discharge to 0.55 V. In addition, we noticed the presence of a third oxidation peak located at a higher potential (~1.4 V). However, as the reaction proceeds, this peak gradually diminishes until it disappears, which we attribute to a small portion of the pre-inserted Na^+ "leakage" from the material lattice. To mitigate this continuous "leakage", we supplemented the electrolyte with an adequate amount of Na^+ ions to support and stabilize the cathode material structure as pillars. In light of these findings, one can conclude that the introduction of Na^+ ions as additives in aqueous Zn-vanadium batteries not only supports the cathode material structure but also facilitates a reversible Zn^{2+}/Na^+ co-intercalation chemistry. This stands in contrast to the traditionally held view that the battery chemistry involves either H^+/Zn^{2+} co-insertion or a multi-step Zn^{2+} de-/intercalation.

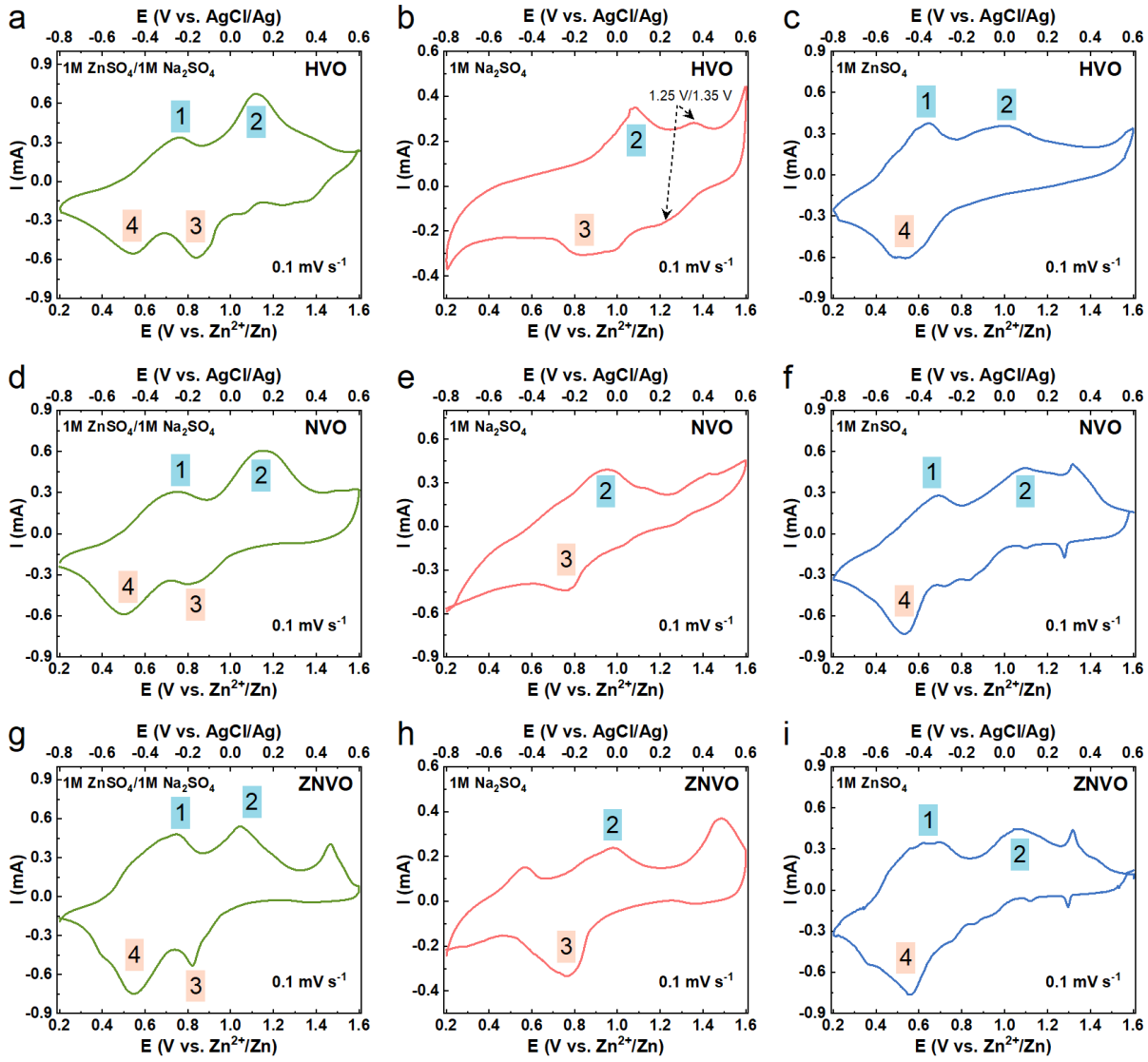


Figure 4.9. CV profiles of a-c) HVO cathode, d-f) NVO cathode and g-i) ZNVO cathode in different electrolytes. The scan rate is 0.1 mV s^{-1}. HVO/NVO/ZNVO electrode was used as the working electrode, AgCl/Ag as the reference electrode and graphite rod as the counter electrode in T-type batteries.

As an effort to further investigate the ion intercalation behaviors, XRD technique is required to supplement the verification. **Figure 4.10**a shows the 2nd GCD profile of HVO cathode in $ZnSO_4/Na_2SO_4$ electrolyte at 1 C, selected voltages were marked in its GCD curves while *ex situ* XRD measurements were performed. From **Figure 4.10**b,when the HVO cathode discharges to 0.55 V (point d), a peak at 8.2° can be observed, which is indexed to the (001) reflection of ZVO ($Zn_{0.25}V_2O_5{\bullet}H_2O$)[334]. It indicates that Zn^{2+} ions are inserted into the HVO structure at this discharging voltage, resulting in the formation of ZVO; the reflection

(001) then fully disappears as charging over 1.1 V (point h) since Zn^{2+} ions are extracted from the HVO lattice. Moreover, as can be seen from the enlarged **Figure 4.10**c and **Figure 4.10**d, a shoulder located at 10.7° to the right of the HVO peak and another one at 32.8° appear at a charging voltage of 0.55 V, corresponding to the (110) and (402) reflections of ZVO (ZnV_3O_8)[335], respectively. These two peaks gradually intensify as charging process continues; while during discharge, they both diminish until almost disappearing at 1.1 V. Incorporating the CV results (**Figure 4.9**a), we note that a very pronounced reduction peak is present at a discharge voltage of 0.8 V, and this peak becomes significantly reduced as charging exceeds 1.1 V. Following the peak index, which is found to be the (001) reflection of NVO (NaV_2O_5)[336], one can directly evidence that Na^+ ions are intercalated into the HVO cathode material structure at around 0.8 V and deintercalated from the HVO at a charging voltage of 1.1 V. Further supporting the fact that Na^+ ions as an electrolyte additive do insert/extract from the vanadium-based cathode during cycling, this finding is in perfect agreement with the previous CV profile. The appearance of the aforementioned representative ZVO and NVO reflections can be illustrated in **Figure 4.10**e. From the counter map (**Figure 4.10**f), the reflection peaks of HVO display a regular shift during the charge and discharge process, which suggests that the ions migrate freely from the HVO lattice. Therefore, the reversible de-/intercalation processes of Na^+ and Zn^{2+} ions between the HVO cathode and electrolyte are validated by this *ex situ* XRD patterns, which offer solid evidence for the reversibility of the Zn^{2+}/Na^+ co-intercalation mechanism.

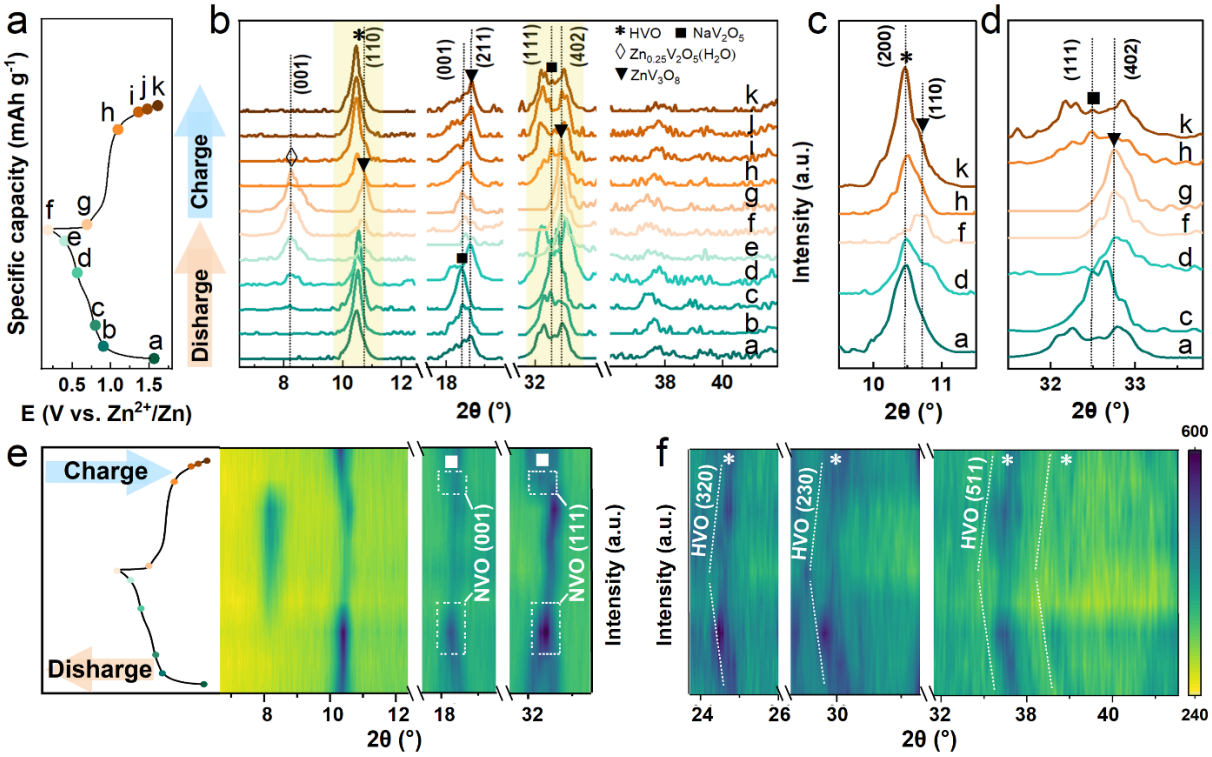


Figure 4.10. a) GCD curve of cycled HVO cathode in 1 M $ZnSO_4$/1 M Na_2SO_4 electrolyte at 2nd cycle. Current rate is 1 C. b) *Ex situ* XRD pattern of cycled HVO electrode in 1 M $ZnSO_4$/1 M Na_2SO_4 electrolyte at determined voltages. $Zn_{0.25}V_2O_5•H_2O$, PDF# 01-086-1238, ZnV_3O_8, PDF# 04-011-2142, NaV_2O_5, PDF# 04-010-2339. c) and d) are *Ex situ* XRD patterns of the yellow areas after magnification. e) Contour map of the corresponding areas in the upper *ex situ* XRD pattern. f) Contour map of HVO reflection peaks migration with varying voltages. The inset scale represents the peak intensity, with 600 for high-intensity and 240 for low-intensity.

To further determine the ion migrations during charging/discharging, the composition of the product on the cathode can be obtained directly by ICP-OES technique. The positive electrode products used for the ICP-OES test had been rinsed sufficiently with DI water, thus the interference of the electrolyte components on the results could be excluded. The concentrations of Na and Zn on cathodes vary with the charging/discharging process as shown in **Figure 4.11**a and **Figure 4.11**b, respectively. It is observed that the amount of Na in the HVO electrode reduces during discharging and increases during charging, which is in perfect agreement with the previously verified insertion/extraction behavior of Na^+ ions in the cathode material. Furthermore, we notice that a significant gap is exhibited in Na concentration between the discharge voltages of 0.9 V and 0.8 V, i.e., a large amount of Na^+

ions migrate from electrolyte into the cathode. Similarly, the Zn concentration shows the same trend as Na, with the noticeable amount of change occurring as the voltage decreases from 0.8 V to 0.55 V. Moreover, results of the effects on Zn concentration variations at HVO cathode for electrolytes with and without Na^+ additives are collected in **Figure 4.11**c. The comparison finds that at the fully discharged state (0.2 V), adding Na^+ ions enable more Zn^{2+} ions to be stored in HVO cathode. In contrast, in the battery system without Na^+ addition, the amount of Zn^{2+} ions on the HVO cathode is obviously less and much more Zn^{2+} ions remain on the cathode when charging ends compared to its initial onset (at the beginning of discharge). This finding suggests that Na^+ ions can assist more Zn^{2+} ions to insert into the cathode, as well as reflects the fact that Zn^{2+} ions will not be confined and provides more insertion vacancies for the coming Zn^{2+} ions in the subsequent process.

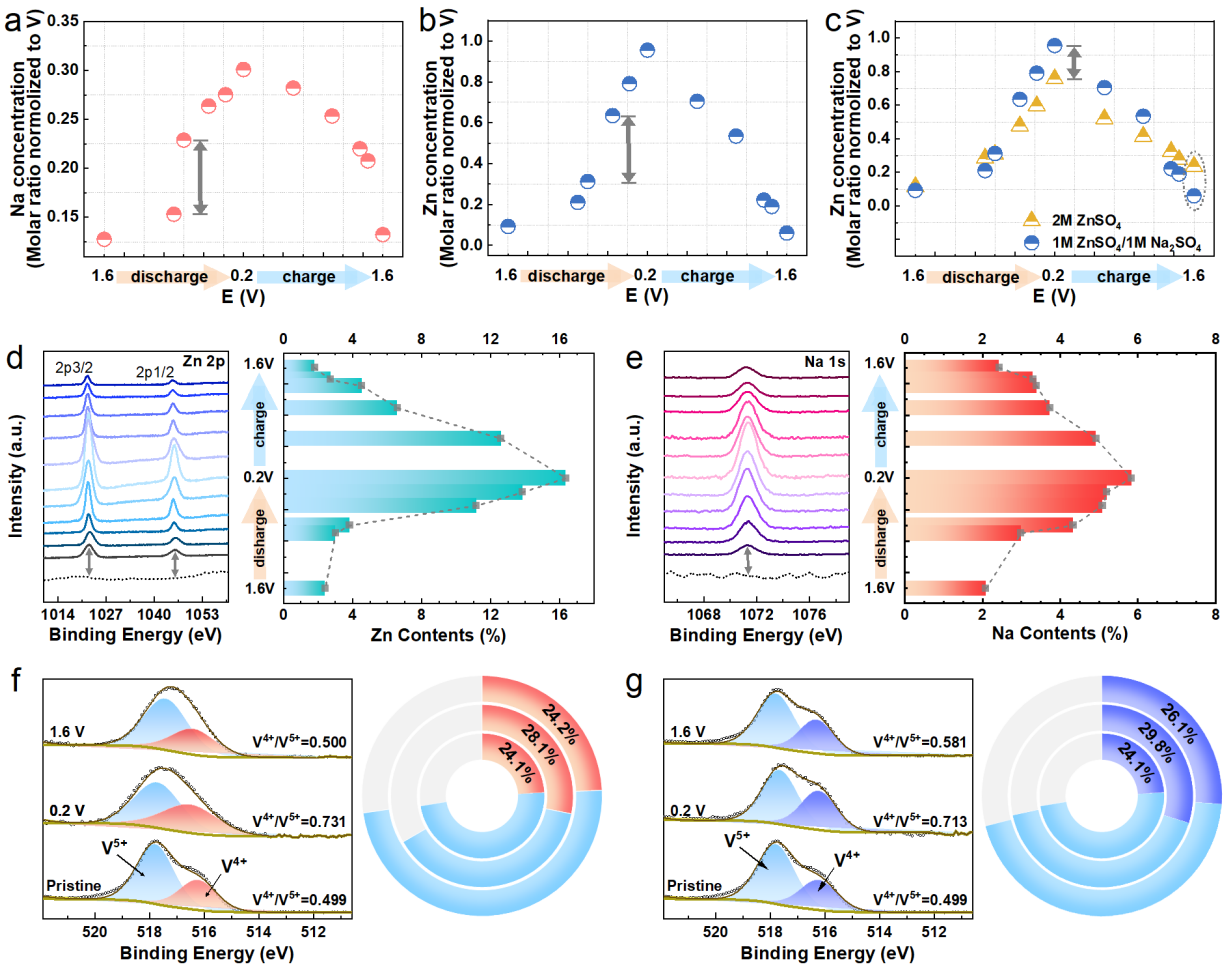


Figure 4.11. The molar ratio of a) Na and b) Zn normalized to V in 1 M $ZnSO_4$/1 M Na_2SO_4 electrolyte at various charge/discharge states. c) The molar ratio of Zn in different electrolytes

at various charge/discharge states. XPS spectra of d) Zn 2p and e) Na 1s with their content percentages on the cycled HVO cathode under varying voltages. XPS spectra of V $2p_{3/2}$ at fully discharged (0.2 V) and fully charged (1.6 V) states in f) 1 M $ZnSO_4$/1 M Na_2SO_4 and g) 2 M $ZnSO_4$ electrolytes. Inset pie charts are the respective percentages of V^{4+} and V^{5+}.

Moreover, XPS results reveal the chemical state changes of Zn 2p and Na 1s in HVO cathodes under varied cycling states. As shown in **Figure 4.11**d, no trace of Zn 2p signals is detected on the pristine HVO cathode, conversely, the characteristic peaks of Zn $2p_{3/2}$ and Zn $2p_{1/2}$ at 1022.3 eV and 1045.5 eV are found to increase gradually as it discharges, and a maximum is reached at 0.2 V with a relative Zn content of 16.4%. This indicates that Zn^{2+} ions are continuously intercalated into the HVO cathode during this process, in turn, the majority of Zn^{2+} ions flows out from the cathode upon reverse charging, which is reflected in the weakening of its characteristic peak. Once the charging is finished, however, the characteristic peaks of Zn can still be observed, these residual Zn could be attributed to a portion of electrolyte remaining on the cathode surface or the formation of ZnV_3O_8[101,337,338]. The variation of Na on cathodes in **Figure 4.11**e shows a similar profile to that of Zn, even though its relative content in the HVO lattice is comparatively less, and the surface-adsorbed or lattice-trapped Na^+ species may contribute to the corresponding weak Na 1s signal at its fully charged state. The chemical states of V 2p in the pristine and cycled cathodes can also be analyzed by XPS technique. Of them, multi-valent states of V^{5+} and V^{4+} appears on the pristine HVO cathode with the corresponding binding energies of 517.8 eV and 516.2 eV for V $2p_{3/2}$, respectively. In $ZnSO_4$/Na_2SO_4 electrolyte as shown in **Figure 4.11**f, the content ratio of V^{4+}/V^{5+} in the pristine HVO is calculated to 0.499, then it increases to 0.731 when the cell is discharged to 0.2 V and an enhancement of V^{4+} characteristic peak is observed, which implies a reduction of V^{5+} in the electrode material to V^{4+} as ion intercalation occurs[339,340]. Since metal ions will coordinate with the oxygen in the lattice after entering the HVO layers, resulting in a lowered V valence. In contrast, the content ratio recovers to an extremely close value (0.500) to the initial state after the battery is charged to 1.6 V, indicating that this Zn^{2+}/Na^+ co-intercalation is highly reversible[87,103]. However, in the absence of Na^+ ion additive (**Figure 4.11**g), this content ratio is as high as 0.581 at the same state of charge,

illustrating that a large amount of Zn^{2+} ions are confined in the material lattice, which is consistent with the ICP-OES results. Therefore, the presence of a Zn^{2+}/Na^{+} co-insertion mechanism is evident from the ICP-OES and XPS results. Incorporating the CV profile of HVO cathode with $ZnSO_4/Na_2SO_4$ electrolyte in **Figure 4.9**a, Zn^{2+} and Na^{+} de-/intercalation mechanism in HVO cathode can be illustrated in **Figure 4.12**. During the discharge, Na^{+} ions in the electrolyte are first inserted into the cathode at a voltage of 0.8 V, with a minor expansion of the layer spacing. Then the Zn^{2+} ions in the electrolyte insert into the cathode when it discharges to 0.55 V, at which point the layer spacing expands to 8.475 Å. In the charging range from 0.7 V to 1.1 V, the previously inserted Zn^{2+} ions are gradually extracted from the cathode. As the charging voltage approaches 1.1 V, Na^{+} ions in the HVO cathode comes out accompanied by Zn^{2+} ions, the layer spacing is reduced to 8.351 Å at the fully charged state. Since the radius of Na^{+} ion is larger than that of Zn^{2+} ion, the Na^{+} ions inserted into the material first can serve as pillars to support the cathode laminar structure, thus allowing Zn^{2+} ions to be easily and freely inserted into or extracted from the positive electrode without noticeable deformation. Therefore, such reversible intercalation chemistry allows vanadium-based cathodes to store more Zn^{2+} ions and realize a high-performance rechargeable aqueous Zn-vanadium battery.

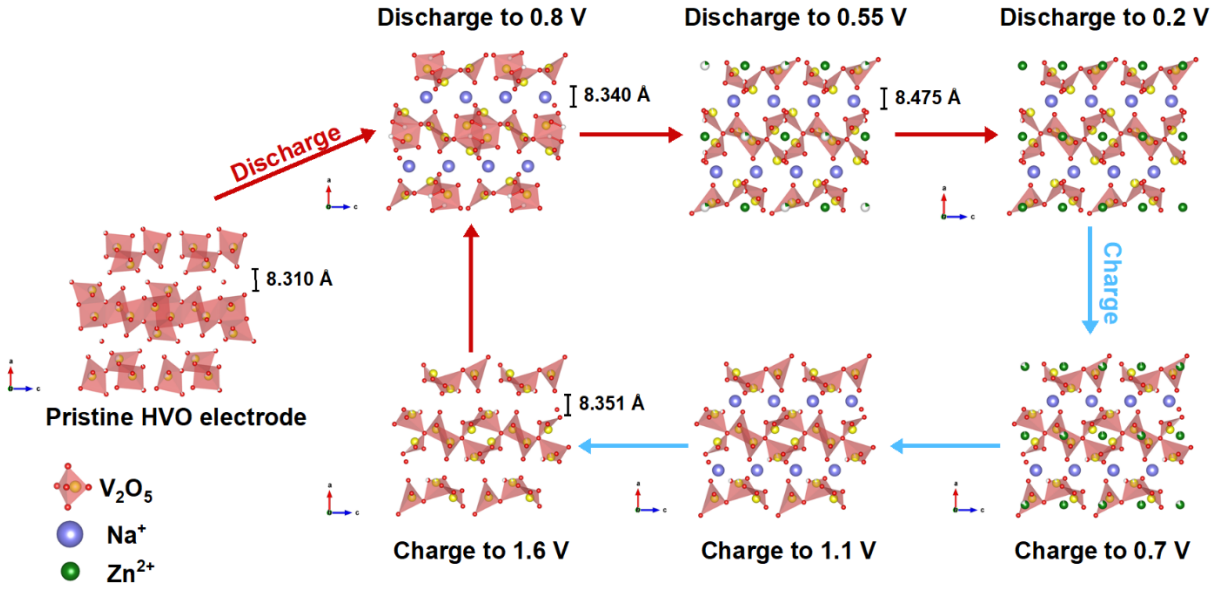


Figure 4.12. Schematic illustration of Zn^{2+} and Na^+ de-/intercalation mechanism in HVO cathode.

Furthermore, we conducted XRD measurements on the cathodes after cycling to determine the evolution of their structure. From the results, it can be seen that the cathode with $ZnSO_4/Na_2SO_4$ electrolyte exhibits higher crystallinity and the diffraction peaks are barely shifted or diminished (**Figure 4.13**b and **Figure 4.13**d). In contrast, without the presence of the Zn^{2+}/Na^+ co-intercalation mechanism, the XRD profiles of the cathode materials in **Figure 4.13**a and **Figure 4.13**c yield changes with the increased cycle number. For example, the more significant changes in the HVO structure are the two diffraction peaks framed out in **Figure 4.13**a. In particular, the peak located at 19.2° (labeled as (1)) disappears gradually as the cycling progressed, while the intensity of the other diffraction peak (2) located at 33.1°also reduces noticeably. Conversely, the corresponding reflection peaks in **Figure 4.13**b remain virtually the same. Therefore, it can be determined that this Zn^{2+}/Na^+ co-intercalation mechanism can stabilize the material structure and facilitate the realization of high performance Zn-vanadium batteries. The EIS result indicates that the ZNVO material can be well-preserved in $ZnSO_4/Na_2SO_4$ electrolytes after 200 cycles, which is mostly attributed to the mechanism of Na^+ action on the cathode material (**Figure 4.13**e).

As previously noted, the decline in cell capacity for the ZNVO cathode, when employing a $ZnSO_4$ electrolyte, manifests as a reduction in the integrated area of the CV curve (**Figure 4.4**e). This suggests that without the contribution of the Zn^{2+}/Na^+ co-intercalation mechanism, the Zn-ZNVO cell is susceptible to capacity degradation during cycling. On the contrary, since Na^+ ions reversibly intercalate/de-intercalate within the cathode material, two pairs of redox peaks and the integrated curve areas in **Figure 4.13**f remain essentially constant with increasing cycle number. The positive effects of the Zn^{2+}/Na^+ co-intercalation chemistry on the HVO and NVO cathodes are also manifested in their test results (**Figure 4.13**g and **Figure A11**). Moreover, the cycled HVO cathode morphology, as observed in **Figure A12**, exhibits exceptional retention of the original nanowire post-cycling in a $ZnSO_4/Na_2SO_4$ electrolyte. This contrasts significantly with the HVO cathode cycled in $ZnSO_4$ electrolyte, where structural degradation is apparent.

In addition, we observed that in **Figure 4.13**g, the redox peaks shift as a function of the cycle number, indicative of several underlying electrochemical and material processes occurring during the battery cycling. This shift can primarily be attributed to structural changes in the HVO electrode material, induced by repeated ion insertion and extraction, including phase transitions and lattice distortions, which alter the thermodynamics and kinetics of the redox reactions. Over multiple cycles, ion diffusion within the HVO electrode material can become increasingly hindered due to structural degradation or clogging of ion pathways, further contributing to the peak shifts.

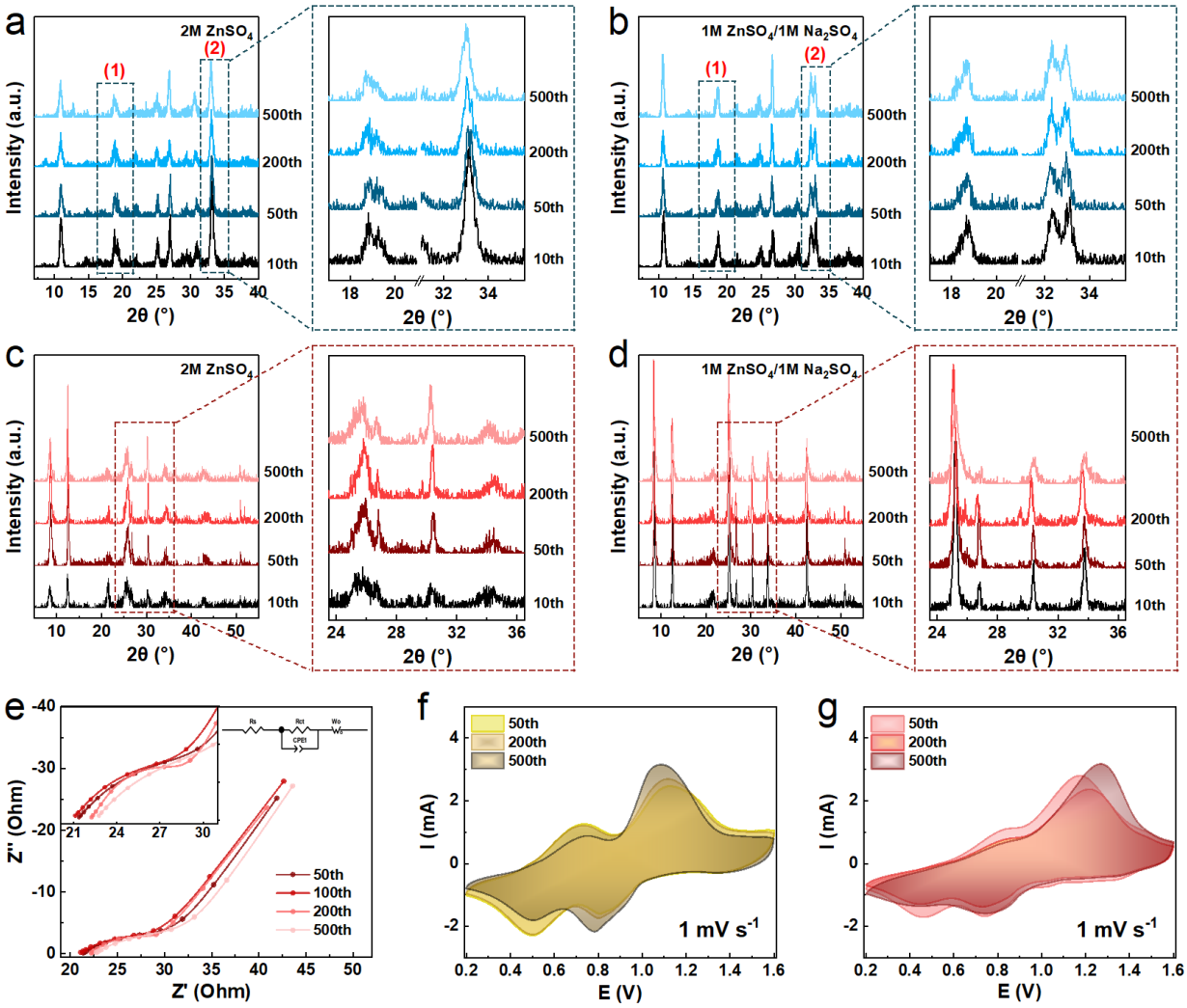


Figure 4.13. *Ex situ* XRD patterns of a) and b) HVO cathodes, c) and d) ZNVO cathodes in different electrolyte at selected cycle numbers. e) Nyquist plots of ZNVO cathode in 1 M $ZnSO_4$/1 M Na_2SO_4 electrolyte over the frequency range of 100 mHz-1 MHz. Inset is the equivalent circuit diagrams. CV profiles of f) ZNVO cathode and g) HVO cathode in 1 M $ZnSO_4$/1 M Na_2SO_4 electrolyte at selected cycle numbers.

Furthermore, it is noticed that the peak pair at 0.8/1.1 V is enhanced with an increasing cycle number, which is possibly due to the compensation of the capacity loss of Zn^{2+} ions from long cycles by Na^+ ions at a later stage. In this regard, the ZNVO cathodes after cycling are then subjected to CV tests in $ZnSO_4$ and Na_2SO_4 electrolytes, respectively, to estimate the respective capacity occupancies of Na^+ (rouge) and Zn^{2+} (mint) by integrating their curve areas, and the results are shown in **Figure 4.14**a-c. The calculated capacity contribution of Na^+ de-/intercalation in the ZNVO cathode rises from 38.4% at 50th cycle to 50.7% at 500th

cycle, with a corresponding decline in the capacity contribution of Zn^{2+} ions (**Figure 4.14**d). This result validates our previous speculation and reveals that Na^{+} ion contribute to the battery capacity.

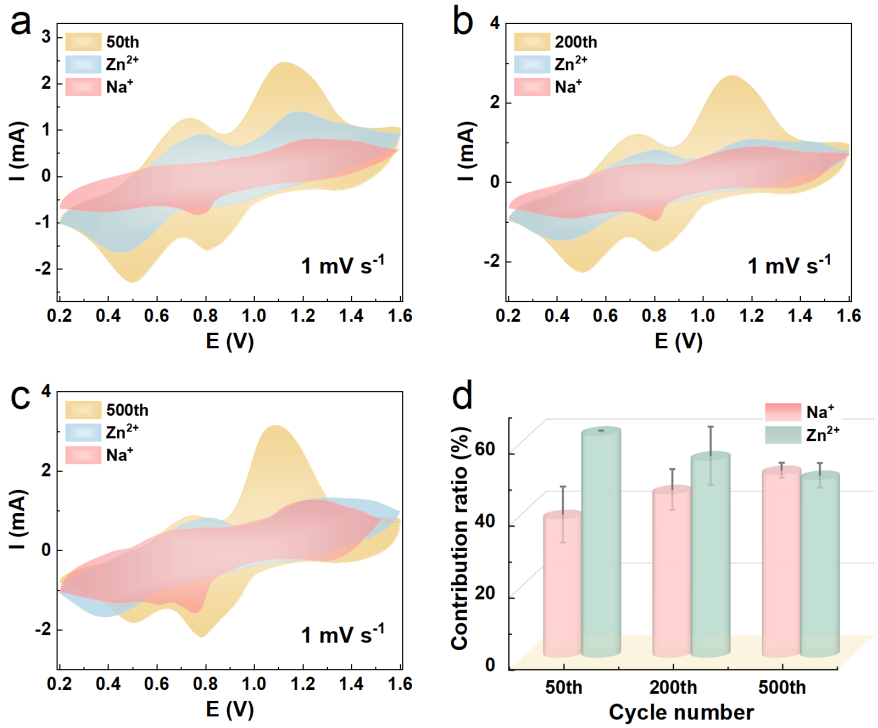


Figure 4.14. CV profiles of ZNVO cathode in 1 M $ZnSO_4$/1 M Na_2SO_4 electrolyte at its a) 50th cycle, b) 200th cycle and c) 500th cycle. Yellow: total capacity; mint: capacity contribution of Zn^{2+} de-/intercalation; rouge: capacity contribution of Na^{+} de-/intercalation. d) Capacity contribution of Na^{+} ion (rouge) and Zn^{2+} ion (mint) from ZNVO cathode in 1 M $ZnSO_4$/1 M Na_2SO_4 electrolyte at different cycles (averaged over three samples), with respective standard deviations of ±7.06% (Na^{+} at 50^{th} cycle), ±0.08% (Zn^{2+} at 50^{th} cycle), ±5.65% (Na^{+} at 200^{th} cycle), ±7.70% (Zn^{2+} at 200^{th} cycle), ±2.09% (Na^{+} at 500^{th} cycle) and ±3.40% (Zn^{2+} at 500^{th} cycle).

Since the vanadium-based materials belong to the extrinsic pseudocapacitance[341], the study of their pseudocapacitve behavior in Zn-ion batteries is particularly necessary. To comparatively understand the mechanism of Zn^{2+}/Na^{+} co-intercalation and single Zn^{2+} insertion in the cathode, a vanadium electrode with different electrolytes is taken for CV tests at different scan rates. The HVO cathode was used here to exclude the effect of pre-inserted cations. As shown in **Figure 4.15**a and **Figure 4.15**b, the CV curves maintain a similar shape at different sweep rates, and accordingly, both the 1st and 2nd anodic peaks shift slightly with

increasing rates of scanning, indicating the fast electrochemical kinetics of the HVO cathode[337]. As reported in previous studies, the reaction kinetics of surface-controlled and diffusion-controlled are different which can be studied according to the following equation (Equation (23) was already mentioned in **Section 2.4.6**) through the relationship between the scan rates (v) and peak currents (i)[342,343]:

$$i = av^b \tag{23}$$

which can be reformulated as:

$$\log(i) = b\log(v) + \log(a) \tag{27}$$

where b denotes the slope of the log(i) vs. log(v) plot, which typically ranges from 0.5 to 1. When the b value approaches 0.5, the electrochemical process is dominated by ion diffusion control; while if the b value approaches 1, the charge/discharge process will be dominated by surface control (or pseudocapacitive behavior)[308,309]. In $ZnSO_4$ electrolyte, the b values of peaks 1, 2 and 4 in **Figure 4.15**a are calculated by fitting the log(i) vs. log(v) curve (**Figure 4.15**d), and they all yielded results close to 0.5, suggesting that the electrochemical reactions of Zn^{2+} in Zn-HVO cells are mainly controlled by ion diffusion. As for the calculation results of the HVO cathode in $ZnSO_4/Na_2SO_4$ electrolyte, except for peak 4 which is nearly equal to 0.5, peaks 2 and 3 are in the range of 0.5-1 (**Figure 4.15**e). The peak 1 in this battery is not targeted in the calculation because its peak intensity remains constant or even decreases as the sweep speed rises (**Figure 4.15**b). We believe that it is possible due to the cathode material which makes it difficult for Zn^{2+} ions to extract from the cathode at this point, and instead Zn^{2+} ions are released from the cathode at 1.1 V (Peak 2) along with Na^+ ions. Correspondingly, the intensity of peak 2 shows a greater increase than other peaks. As previously stated, the insertion of Zn^{2+} ions occurs at peak 4, which has a corresponding b value close to 0.5, hence the process of Zn^{2+} entering the cathode at this point is dominated by ion diffusion control. The relevant b values for the other peaks are 0.701 and 0.839, thus the ion behaviors at these voltage states are synchronously controlled by ion diffusion and surface

capacitance. Also, calculations performed for the test results of ZNVO cathode yielded similar outcomes, as illustrated in **Figure 4.15**c and **Figure 4.15**f. Its higher b values of peaks 1 and 4 might be attributed to the influence of ion pre-insertion, but overall, the reversible behavior of Na^+ ion at the electrode powers the enhancement of surface-controlled capacitance, which contributes to the excellent rate performance of Zn-vanadium batteries at high current densities. In addition, we note that the oxidation peak at high voltage gradually disappears as the scan rate increases, which we attribute to kinetic limitations of the electrochemical reactions. At higher scan rates, the time available for electrochemical processes is significantly reduced, leading to a diminished current response for slower electrochemical reactions, such as the oxidation peak at high voltage. This phenomenon is primarily attributed to several factors: the diffusion layer near the electrode surface becomes thinner, limiting the diffusion of reactants to the electrode surface; the rate of charge transfer is slower than the potential sweep rate, preventing the reaction from reaching completion; and surface processes such as adsorption and desorption of species on the electrode become less effective. These combined effects result in the observed attenuation or disappearance of the oxidation peak at higher scan rates.

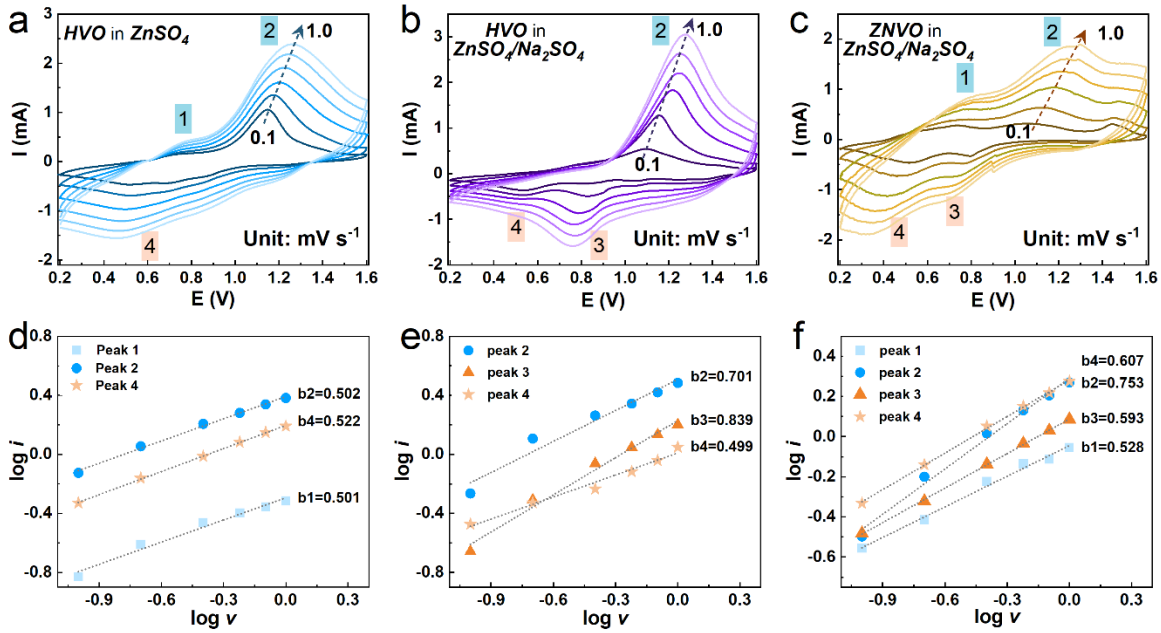


Figure 4.15. CV curves of a) HVO cathode in 2 M $ZnSO_4$ electrolyte, b) 1 M $ZnSO_4$/1 M Na_2SO_4 electrolyte, and c) ZNVO cathode in 1 M $ZnSO_4$/1 M Na_2SO_4 electrolyte. The range of scan rate is 0.1-1 mV s^{-1}. d) The corresponding plots of log(i) vs. log(v) for HVO and ZNVO cathodes in different electrolytes.

Furthermore, in terms of the power-law relationship, the surface-contributed capacity can be quantified through the following equation[344,345]:

$$i = k_1 v + k_2 v^{\frac{1}{2}} \tag{28}$$

or

$$\frac{i}{v^{\frac{1}{2}}} = k_1 v^{\frac{1}{2}} + k_2 \tag{29}$$

where i, $k_1 v$, and $k_2 v^{\frac{1}{2}}$ represent the current response, capacitance, and ionic diffusion contributions, respectively[325]. Accordingly, the respective capacitance contribution at various scan rates can be obtained. As shown in **Figure 4.16**b and **Figure 4.16**c, both HVO and ZNVO cathodes exhibit a steady growth in capacitance contribution as the scan rate is increased, and the percentage of their capacitance contribution surges to more than 80% after elevating the scan rate to 1 mV s^{-1}. In comparison, the capacitive contribution of the HVO

cathode in the $ZnSO_4$ electrolyte is significantly less than that in $ZnSO_4/Na_2SO_4$ electrolyte, with a capacity contribution of only 39% at a scan rate of 1 mV s^{-1} (**Figure 4.16**a), which demonstrates that the incorporation of Na^+ ions enables the Zn-vanadium batteries to have favorable charge transfer kinetics[26].

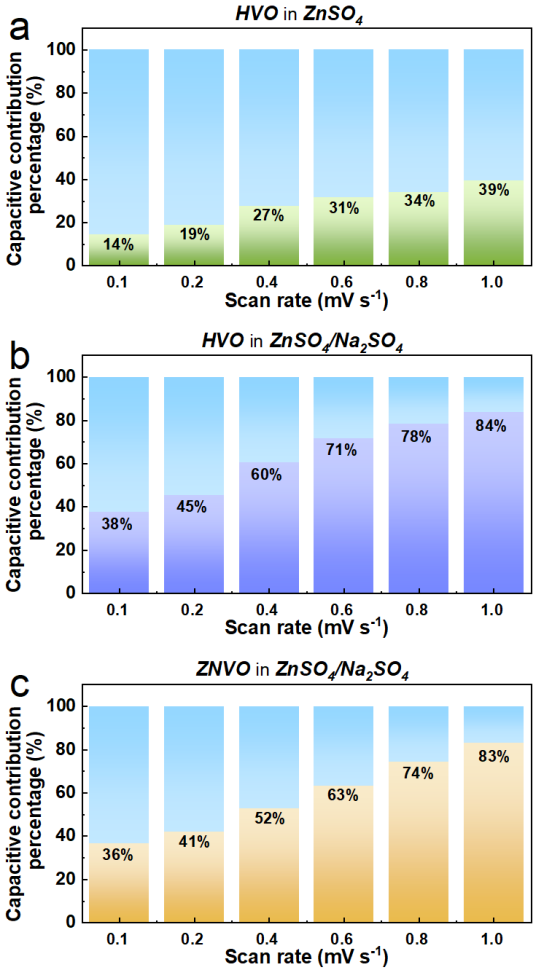


Figure 4.16. The capacitive contribution percentage at different scan rates of a) HVO cathode in 2 M $ZnSO_4$ electrolyte, b) 1 M $ZnSO_4$/1 M Na_2SO_4 electrolyte, and c) ZNVO cathode in 1 M $ZnSO_4$/1 M Na_2SO_4 electrolyte.

4.4. Conclusion

In summary, we have developed an ultra-stable RAZB characterized by a novel and highly reversible Zn^{2+}/Na^+ co-intercalation mechanism within vanadium-based cathodes. The core of our research revolves overcoming the persistent challenge of V_2O_5 cathode material dissolution during cycling, thereby unlocking the door to significantly improved battery

stability. Our research is organized into two main parts: the synthesis of $Zn_{0.3}Na_{0.43}V_2O_5$ (ZNVO) cathode materials using a pre-intercalation method, an in-depth analysis of the mechanism involved. By finely tuning the concentration of intercalated ions, the optimized ZNVO cathode showcases an extraordinary discharge capacity of 350 mAh g^{-1} at 1 C, outperforming many other vanadium-based cathode materials. Furthermore, the employment of a 1 M $ZnSO_4$/1 M Na_2SO_4 electrolyte alongside the ZNVO cathode forms a dual-ion intercalation system, pivotal for the electrochemical performance of RAZBs. Our extensive electrochemical evaluations reveal a sequential insertion process: Na^+ ions first intercalate at a discharge voltage of 0.8 V, followed by Zn^{2+} ions at 0.55 V. During the reverse charging process, Zn^{2+} ions are extracted first during the charging stage from 0.7 V to 1.1 V, followed by Na^+ ions as the voltage rises to 1.1 V. The larger ionic radius of Na^+ plays a decisive role in maintaining the structural integrity of the cathode, thereby averting structural collapse over repetitive cycling. This co-intercalation chemistry has significantly enhanced the cycling performance of the ZNVO cathode, particularly evident at high current densities, with a capacity retention of over 90% after 4000 cycles, and a discharge capacity of 209 mAh g^{-1} at 5 C. More importantly, this Zn^{2+}/Na^+ co-intercalation mechanism is not exclusive to ZNVO, it has also been successfully applied to other vanadium-based materials such as HVO and NVO, all of which display superior cycling stability and extended lifespan. Expanding upon this, the scalability of this technology is initially tested by fabricating larger 9 mAh batteries. These high-capacity cells mirrored the exceptional performance of their smaller counterparts (coin-type cells), demonstrating that this advanced aqueous Zn-ZNVO battery is scalable and has great potential to be translated into practical energy storage solutions.

However, there are some shortcomings in this study:

(1) Additional characterizations and electrochemical tests are necessary to clarify the advantages of the pre-inserted ratio of 0.7:1 (ZNVO-2) material over other ratios. For example, to explore the effect of different pre-insertion ratios on nanowire morphology and their corresponding CV curves. Merely demonstrating cycling performance is insufficient.

(2) It also remains to be determined whether structural H_2O is incorporated in the ZNVO material (which is expected); if present, the role of this structural H_2O requires further elucidation (this will be challenging).

Chapter 5. Unveiling the Ionic Crosstalk in Aqueous Zn-MnO_2 Batteries

5.1. Introduction

In the research on RAZBs, my study transitions from vanadium-based cathode materials to manganese-based cathode materials due to several compelling reasons. Firstly, in terms of performance, manganese-based cathode materials such as MnO_2 exhibit higher specific capacity and better cycling stability compared to V_2O_5 materials. Specifically, MnO_2 can contribute a theoretical capacity of 616 mAh g^{-1}, which is higher than the 589 mAh g^{-1} theoretical capacity of V_2O_5[346,347]. With appropriate material design and modification, manganese-based materials demonstrate significant improvements in structural stability and cycling life. Furthermore, these materials exhibit superior capacity retention during cycling, being less prone to structural degradation and capacity decay. Secondly, regarding safety and environmental impact, vanadium compounds are known to possess a certain level of toxicity, which can adversely affect both the environment and human health. In contrast, manganese-based materials are relatively non-toxic and environmentally benign, making them more suitable for large-scale production and application. Thirdly, from the perspective of resource availability and cost, vanadium resources are relatively scarce and expensive (30-60 USD kg^{-1}), limiting their economic feasibility for widespread application. Conversely, manganese resources are abundant, inexpensive, and easily accessible, providing significant cost advantages (2-10 USD kg^{-1}). Moreover, manganese resources are widely distributed globally, ensuring stable and sustainable supply chains. Additionally, MnO_2 operates at a higher working voltage compared to many vanadium-based cathodes, contributing to an overall increase in the energy density of the battery[348–351]. This higher working voltage, combined with the greater specific capacity, allows manganese-based RAZBs to achieve significantly improved energy density, making them more efficient for energy storage applications.

However, despite these advantages, aqueous Zn-MnO_2 batteries face several issues. Within this, both the MnO_2 cathode and the Zn anode face distinct yet interrelated challenges that impede the performance and longevity of the Zn-MnO_2 battery. Persistent challenges with the MnO_2 cathode include low electrical conductivity, volumetric instability due to structural changes, irreversible phase transitions, and severe dissolution, leading to capacity degradation[352–355]. Moreover, the Zn anode is plagued with issues such as dendrite growth, non-uniform zinc deposition and corrosion, which compromise electrode stability[356–358]. Recent advancements in addressing these challenges for the MnO_2 cathode have included nanostructuring of the active material to enhance conductivity[359–361], doping additives to mitigate phase transitions[362–364], and surface modification to reduce material dissolution[365,366]. For the Zn anode, developments have focused on incorporating electrolyte additives to suppress dendrite formation[367,368], structural anode designs for uniform zinc deposition[369,370], and employing alloyed materials to improve anode stability or reversibility[371]. Despite these improvements, a critical gap remains in understanding the effects of active species, particularly Zn^{2+} and Mn^{2+} ions, on their respective counter electrodes within the Zn-MnO_2 battery system. Investigating the interactions and influences of these ions on the electrodes could provide comprehensive insights into further optimizing battery performance.

Crosstalk, in a broad sense, denotes the interaction or interference between distinct components within a system, resulting in unintended effects. Electrode crosstalk, a prevalent phenomenon in lithium-ion batteries, describes the process in which by-products (e.g., transition metal ions, gaseous, etc.) generated at one electrode migrate through the separator to the other electrode, initiating detrimental side reactions at the counter electrode[372–375]. In a significant discovery, we observe the presence of ionic crosstalk in the aqueous Zn-MnO_2 battery. Distinct from electrode crosstalk in lithium-ion batteries, the ionic crosstalk phenomenon observed in this study involves the transfer of active species (i.e, Mn^{2+} and Zn^{2+} ions) between the MnO_2 cathode and the Zn anode, which significantly triggers electrode destabilization and degrades battery performance. The existing literature reveals a dearth of comprehensive investigation into the ionic crosstalk in the aqueous Zn-MnO_2 battery system,

with most studies focusing solely on the unidirectional effects of active species on the counter electrodes[353,376]. In contrast, our work elucidates the bidirectional ionic crosstalk phenomenon, including both cathode-to-anode and anode-to-cathode. Our observations illuminate the migration of dissolved Mn^{2+} ions from the MnO_2 cathode towards the Zn anode, instigating notable fluctuations in Mn^{2+} concentration near the anode surface, consequently accelerating anode corrosion and dendrite growth. A constrained Mn^{2+} concentration gradient in the electrolyte can significantly affect the crystallographic orientation of zinc deposits, suppressing the growth of (100) and (110) crystal planes while promoting the (002) plane[351,377–379]. Conversely, significant Mn^{2+} concentration gradients within the electrolyte detrimentally affect the Zn anode, leading to irregular deposition and uneven surface morphology, along with severe corrosion[380]. On the other hand, the surplus of Zn^{2+} ions emanating from the anode impacts the dissolution/deposition process of MnO_2 on the cathode. This results in the persistent formation of $Zn_x(MnO_2)_y$ (referred to as ZMO) on the cathode surface, which may undergo an irreversible transition from amorphous nanosheets (ZMO-S) into lowly crystallized nanoplates (Woodruffite ZMO, or ZMO-P). The accumulation of these ZMO-P hinders physical contact between the conductive carbon, current collector, and active cathode materials, impeding their complete dissolution/deposition and fostering capacity decline over prolonged cycling[353,355,381]. Such crosstalk behavior of Zn^{2+} and Mn^{2+} ions are likely responsible for the occurrence of irreversible damage to the electrodes, culminating in suboptimal electrochemical performance and eventual battery failure.

In this chapter, we delve into the previously overlooked phenomenon of ionic crosstalk in the Zn-MnO_2 battery, offering a comprehensive analysis of its implications. Following this, the next chapter will introduce an effective strategy aimed at mitigating this effect to improve the performance of aqueous Zn-MnO_2 batteries.

5.2. Experimental Methods

5.2.1. Material synthesis

The β-MnO_2 nanorods were prepared by one-step hydrothermal method. Specifically, 0.05 M manganese sulfate ($MnSO_4 \cdot H_2O$, Sigma-Aldrich, 99%) solution and 0.05 M ammonium persulfate ($(NH_4)_2S_2O_8$, Sigma-Aldrich, 98%) solution were stirred vigorously in DI water for 1 hour. Then transferred the solution to a 100 mL Teflon container and sealed it in an autoclave and placed in a high-temperature oven and reacted at 140°C for 12 hours. The obtained black colored product was washed several times with DI water and ethanol, then dried in a vacuum oven at 60°C overnight.

5.2.2. Other experimental methods

The processes for cathode sheet fabrication, battery assembly, material characterization techniques, and electrochemical testing follow the descriptions provided in **Chapter 3**; therefore, detailed descriptions are omitted here. It should be noted that the mass loading of the active material in each cell was approximately 3.0±0.2 mg cm^{-2}, and the voltage range of the full cell test is 0.8-1.9 V. Three types of electrolytes were applied in this work, 2 M $ZnSO_4$, diluted sulfuric acid (H_2SO_4, Sigma-Aldrich, 95-98%) and 2 M $ZnSO_4$+0.2 M $MnSO_4$ solutions with pH=4.0±0.1.

Based on our group's previous studies and ongoing research, it has been concluded that the 2 M $ZnSO_4$+0.2 M $MnSO_4$ electrolyte formulation is optimal for aqueous Zn-MnO_2 cells[325,382]. In addition, other electrolyte compositions have also been evaluated in prior work by this group, but they have either resulted in suboptimal performance or stability issues. For instance, higher concentrations of $MnSO_4$ did not significantly improve performance and sometimes resulted in undesirable side reactions. Conversely, lower concentrations of $ZnSO_4$ reduced ionic conductivity, impairing the battery's rate performance. Therefore, the chosen electrolyte formulation (2 M $ZnSO_4$+0.2 M $MnSO_4$) provides an optimal ion conductivity, supporting efficient and stable operation of aqueous Zn-MnO_2 cells.

5.3. Results and Discussion

5.3.1. The ionic crosstalk effect of Mn^{2+} on Zn anodes

The practice of adding a moderate concentration of Mn^{2+} ions to the $ZnSO_4$ electrolyte is commonly employed to improve the performance of aqueous Zn-MnO_2 batteries. A critical electrochemical process in these systems is the Mn^{3+} disproportionation reaction, which involves the transformation of Mn^{3+} ions into Mn^{2+} and Mn^{4+}. The reaction can be represented as $2Mn^{3+} \rightarrow Mn^{2+} + Mn^{4+}$, where manganese ions primarily exist in the divalent state (Mn^{2+}) within the electrolyte, while Mn^{4+} is typically in the form of MnO_2 [383]. The presence of Mn^{2+} ions in the electrolyte facilitates these redox reactions, improving overall battery efficiency and longevity. By optimizing the concentration of Mn^{2+}, the electrochemical performance of aqueous Zn-MnO_2 batteries can be significantly enhanced, leading to better energy storage and extended cycle life. Although extensive studies have been conducted on the effects of Mn^{2+}-enriched electrolytes on MnO_2 cathodes, their impact on Zn anodes has received less attention. Electrowinning research indicates that introducing Mn^{2+} ions into $ZnSO_4$ solutions can reduce zinc metal corrosion and influence the morphology of zinc deposits by interacting with Mn^{2+} ions[380,384,385]. To more directly observe the positive influence of Mn^{2+} ions on the Zn anode, the *in situ* optical visualization setup was constructed for this purpose (as shown in **Figure 5.1**a). The core of this setup is a video microscope camera connected to a computer monitor, and a bracket adjuster (**Figure 5.1**b). This visualization system employs Zn foil as both working and counter electrodes. These electrodes are positioned parallel to each other with a designated gap to ensure they remain non-contact (**Figure 5.1**c). The electrodes and the electrolyte are placed between two glass slides, sealed by a rubber gasket to prevent leakage of the electrolyte. The zinc deposition process was conducted through an electrochemical workstation connected to this setup. In this work, we used a 2.2 M $ZnSO_4$ electrolyte to isolate the influence of salt concentration, it is observed that a Zn-Zn symmetric cell exhibits more uniform zinc deposition on the Zn electrode in the presence of Mn^{2+} ions during charging. Notably, after 900 s of deposition time under a constant current, considerable flakes growing

vertically along the Zn electrode edge can be observed in the 2.2 M $ZnSO_4$ electrolyte (**Figure 5.1**d), in contrast to the smoother surface observed with Mn^{2+} ions present (**Figure 5.1**e). This implies the role of Mn^{2+} ions in promoting uniform zinc deposition and hindering vertical dendrite growth.

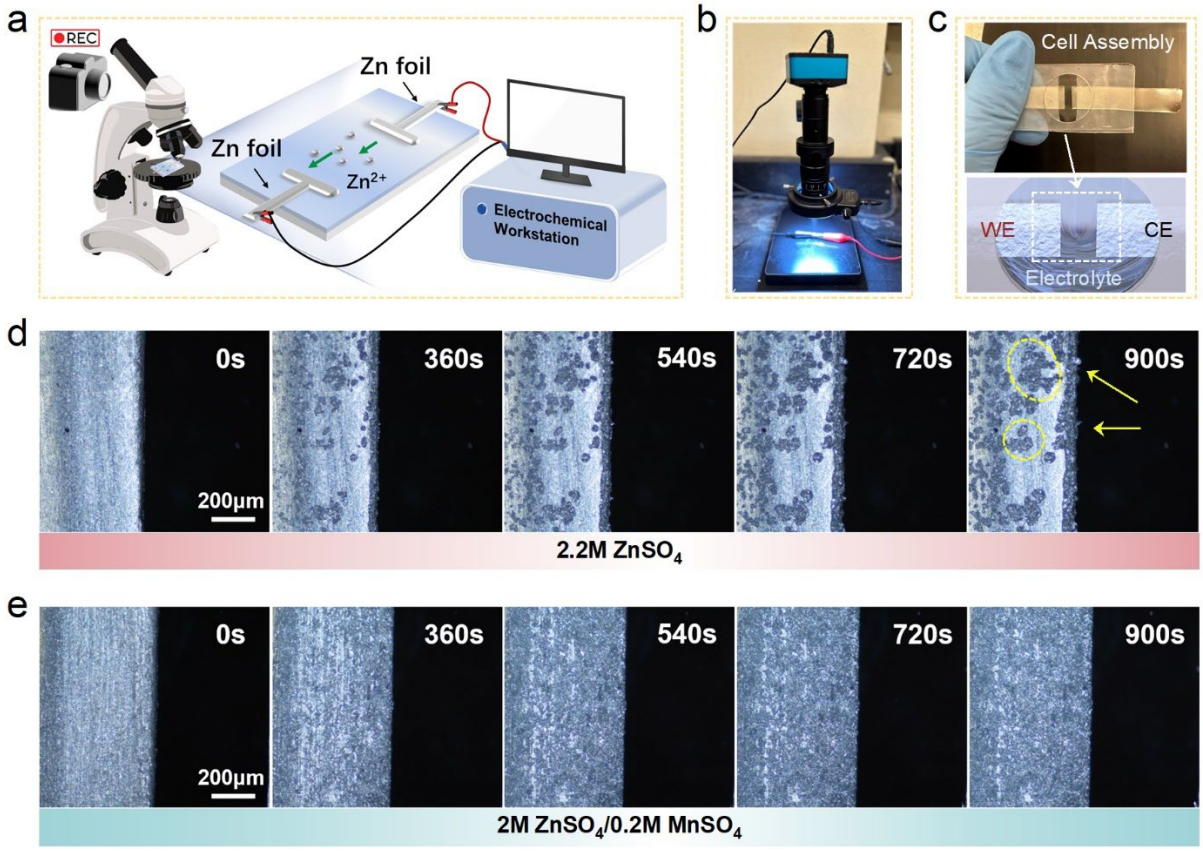


Figure 5.1. a) Schematic diagram of the *in situ* optical visualization observation device. b) Actual image of the *in situ* optical visualization observation setup. c) Schematic of a symmetric transparent electrochemical cell. *In situ* optical visualization observations of zinc deposition in d) 2.2 M $ZnSO_4$ electrolyte and e) 2 M $ZnSO_4$/0.2 M $MnSO_4$ electrolyte at various deposition times. Scale bar: 200 μm.

Although some electrowinning studies have constrained Mn^{2+} concentration to a narrow range for improving zinc product purity[385–387], our research further explores the optimal Mn^{2+} concentration in the $ZnSO_4$ electrolyte through linear polarization (LP) measurements. **Figure 5.2**a and **Figure 5.2**b reveal the effect of adding different Mn^{2+} amounts to $ZnSO_4$ electrolyte on the corrosion potential of zinc metal. The results indicate that adding 0.2-0.3 M Mn^{2+} to the electrolyte significantly reduces the corrosion potential. However, given the lower cost of 0.2

M, the electrolyte we mainly used in the electrochemical experiments in later chapters was the one containing 0.2 M Mn^{2+}. In **Figure 5.2**c, the Zn-Zn symmetric cell with 0.2 M Mn^{2+} addition exhibits superior stability, in contrast to the cell with 0.5 M Mn^{2+} addition, which shows noticeable unstable cycling profiles and high voltage hysteresis. Although 0.1 M Mn^{2+} addition maintains relatively stable cycling performance, the curve manifests distinct fluctuations after approximately 87 hours. Upon closer examination of the enlarged profiles, it becomes evident that 0.2 M addition results in a lower voltage hysteresis of 78 mV compared to 147 mV of 0.1 M at 11 hour. Surprisingly, the cell containing 0.2 M Mn^{2+} continues to undergo reversible plating/stripping at a consistently low voltage hysteresis (84 mV at 87 hour).

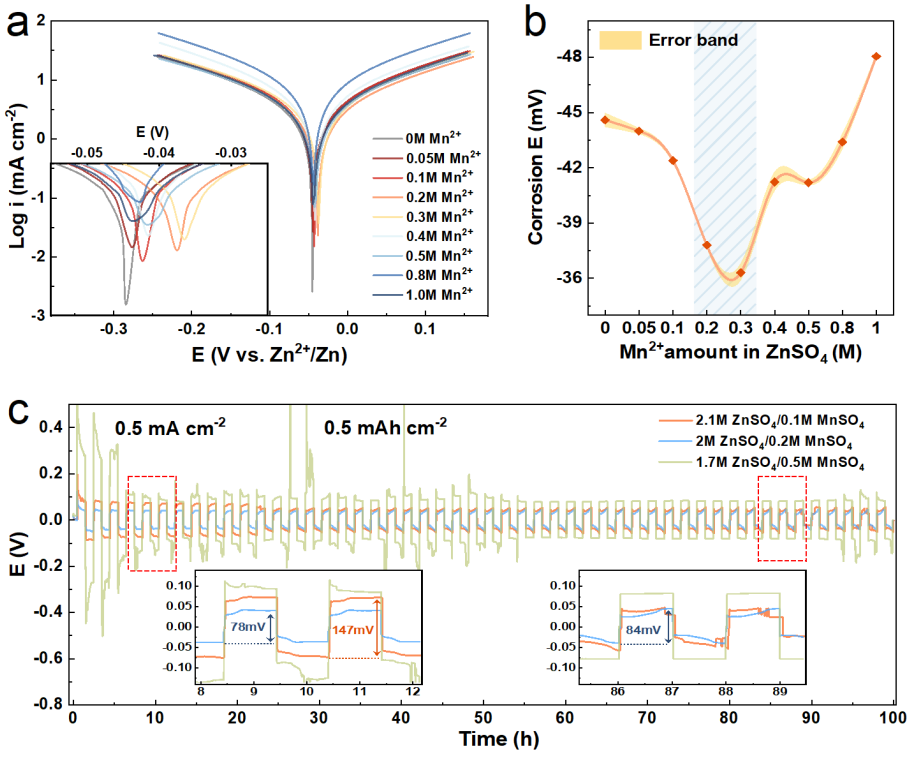


Figure 5.2. a) LP curves of Zn-Zn symmetrical cells using $ZnSO_4$ electrolytes with different Mn^{2+} additions, with a scan rate of 0.1 mV s^{-1}. b) The corresponding Zn corrosion potential in $ZnSO_4$ electrolyte with different Mn^{2+} additions. c) Galvanostatic cycling performance of Zn-Zn symmetric cells in different electrolytes at a current density of 0.5 mA cm^{-2} and an areal capacity of 0.5 mAh cm^{-2}. Insets: detailed voltage profiles at specific cycling times.

Furthermore, we note that varying Mn^{2+} concentration distinctly influences the crystallographic orientation of zinc deposits. Typically, Zn (110) and (100) planes which align

vertically to the Zn electrode surface are conducive to dendritic growth, whereas (002) plane with parallel growth to the substrate is preferable to promote close-packed deposition and result in a smooth electrode surface[388–390]. The XRD spectra presented in **Figure 5.3**a reveal notable variations in the crystalline structure of Zn after 100 hours of plating/stripping with different Mn^{2+} concentrations in the electrolyte. With the addition of 0.2 M Mn^{2+}, there is a marked increase in the intensity of the (002) plane, accompanied by a decrease in the (100) and (110) planes. However, increasing the Mn^{2+} concentration to 0.5 M leads to a strengthening of the (100) and (110) planes, which suggests that higher Mn^{2+} concentrations can induce Zn^{2+} ions to deposit along the vertical planes. The relative texture coefficient (RTC) results of Zn electrodes cycled in various electrolytes are in agreement with the above findings (**Figure 5.3**b). The RTC was calculated as the following formula[389,391]:

$$RTC_{(hkl)} = \frac{I_{(hkl)}/I_{0(hkl)}}{\sum(I_{(hkl)}/I_{0(hkl)})} \times 100\% \quad (30)$$

where $I_{(hkl)}$ is the intensity obtained from textured sample, and $I_{0(hkl)}$ is the intensity of the standard oriented sample (i.e., from pristine Zn foil data). The larger the RTC value, the more obvious the texture. With the inclusion of 0.2 M Mn^{2+}, the RTC for the (002) plane escalates from 21.59 to 44.86, whereas the RTCs for the (100) and (110) planes diminish from 25.57 to 13.99 and from 17.18 to 11.09, respectively. The morphologies and crystal structures of zinc deposits, following cycling in various electrolytes, are depicted in **Figure 5.3**c. Zinc deposits obtained from the Mn-free electrolyte are primarily composed of moderately sized, dendrite-like zinc slices. Contrasting this, the use of 0.2 M Mn^{2+} decreases the crystal size and yields compact deposits with a sheet-like structure, which aligns parallel to the Zn substrate. Upon further increasing the Mn^{2+} concentration to 0.5 M, there is a notable augmentation in the size of the zinc slices, resulting in deposits that bear a striking resemblance to those formed in the Mn-free electrolyte. **Figure B1** illustrates the cycling performance of symmetric cells with an areal capacity of 0.5 mAh cm^{-2} at 0.5 mA cm^{-2} in the presence and absence of 0.2 M Mn^{2+}. The cell with 0.2 M Mn^{2+} addition demonstrates significantly improved cycling performance,

with a lower voltage hysteresis of about 78.6 mV after 15 hours of cycling, compared to 350 mV in the cell without Mn^{2+} ions. In $ZnSO_4$ electrolyte, voltage hysteresis rises to 548 mV after 50 hours, which is ascribed to the rampant side reaction and extensive dendrite growth on the Zn electrode surface, thus severely compromising the reversible zinc plating/stripping. The symmetric cell with 0.2 M Mn^{2+} remains stable for over 300 hours at 1 mA cm^{-2}/0.5 mAh cm^{-2} (**Figure 5.3**d), significantly outperforming the cell in $ZnSO_4$ electrolyte, which experiences a sudden and irreversible voltage increase after about 80 hours of cycling. Compared to the symmetric cell without Mn^{2+} ions, it exhibits a significantly lower voltage hysteresis with a stable voltage distribution over its entire lifetime. Rate performance tests of symmetric cells with a constant areal capacity of 0.5 mAh cm^{-2} at various current densities, from 0.2 to 2 mA cm^{-2}, further confirm the benefits of 0.2 M Mn^{2+} addition (**Figure B2**). It is evident that the cell supplemented with 0.2 M Mn^{2+} consistently exhibits lower voltage hysteresis at all current densities and maintains excellent stability and high reversibility at elevated current densities, outperforming cells with $ZnSO_4$ electrolyte, which experiences noticeable instability as the current density rises to 0.5 mA cm^{-2} (~80 hours).

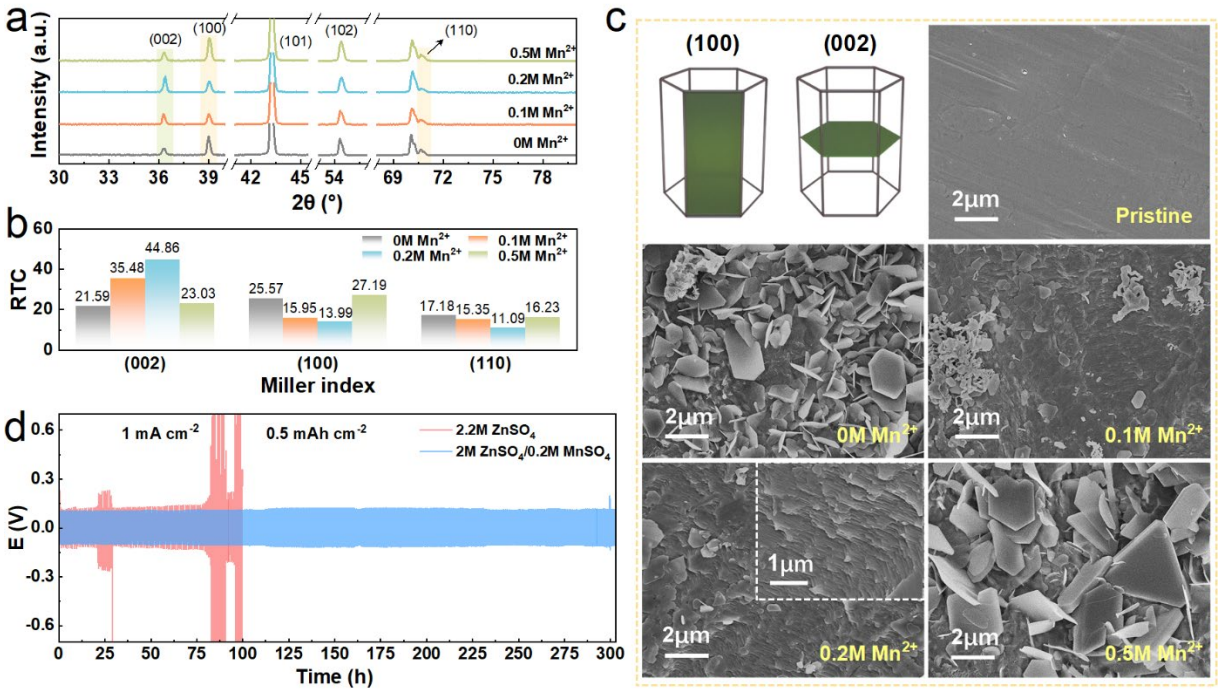


Figure 5.3. a) *Ex situ* XRD patterns of Zn electrodes after plating/stripping in $ZnSO_4$ electrolyte with different Mn^{2+} additions for 100 hours at 0.5 mA cm^{-2} and 0.5 mAh cm^{-2}. b)

The RTC of Zn electrodes cycled in different electrolytes. c) Morphology of pristine Zn electrode surface, and Zn electrode surface in $ZnSO_4$/0 M Mn^{2+}, $ZnSO_4$/0.1 M Mn^{2+}, $ZnSO_4$/0.2 M Mn^{2+}, $ZnSO_4$/0.5 M Mn^{2+} electrolytes after cycling for 100 hours at 0.5 mA cm^{-2} and 0.5 mAh cm^{-2}. Scale bar: 2 μm. Inset in c) is the enlarged view, scale bar: 1 μm. d) Long-term galvanostatic cycling performance of Zn-Zn symmetric cells in different electrolytes at a current density of 1 mA cm^{-2} and an areal capacity of 0.5 mAh cm^{-2}.

Despite the above benefits, Mn^{2+} concentration in the electrolyte can fluctuate significantly in practical scenarios due to the continual dissolution of the MnO_2 cathode, leading to an escalation in Mn^{2+} levels. To scrutinize this dissolution dynamic, extended cycling experiments using a three-electrode system were conducted to explore how the corrosion potential of Zn is influenced by varying rates of Mn^{2+} concentration (ranging from 0 to 100 mM h^{-1}). The results, depicted in **Figure 5.4**a and **Figure 5.4**b, clearly show that the Mn^{2+} concentration changes in the electrolyte lead to a notable corrosive impact on zinc metal. A discernible negative shift in corrosion potential is evident with increasing variation rate of Mn^{2+} concentration, and notably, the detrimental effects on zinc metal become markedly pronounced when Mn^{2+} concentration varies beyond 61 mM h^{-1}. Hence, it is crucial to note that substantial variations in Mn^{2+} concentration in the electrolyte do not necessarily give good results. These observations underscore the nuanced and multifaceted interactions between Mn^{2+} ion and the Zn anode in aqueous Zn-MnO_2 batteries. On one side, Mn^{2+} ions at a proper concentration can significantly improve the performance of the Zn anode by promoting uniform zinc deposition, facilitated by their interaction with the electrode surface. However, a change in Mn^{2+} concentration exceeding a certain threshold triggers accelerated corrosion and dendrite growth, which counteracts the positive effects observed at appropriate and stable Mn^{2+} concentrations. The pronounced disparities in Mn^{2+} concentrations can be primarily attributed to the vigorous dissolution of the MnO_2 cathode, leading to the migration of Mn^{2+} ions towards the vicinity of the Zn anode and establishing a high concentration gradient on its surface. We define this phenomenon as ionic crosstalk, where the Mn^{2+} ions originating from the cathode migrate to anode, triggering detrimental side reactions. The implication of this finding is significant, as it underscores the dynamic interplay between the cathode and anode, and its impact on the stability and performance of Zn anodes. Therefore,

the variation of Mn^{2+} concentration in the electrolyte or near the anode has to be meticulously controlled to mitigate its crosstalk effect, which may be a vital factor in optimizing the performance of aqueous Zn-MnO_2 battery.

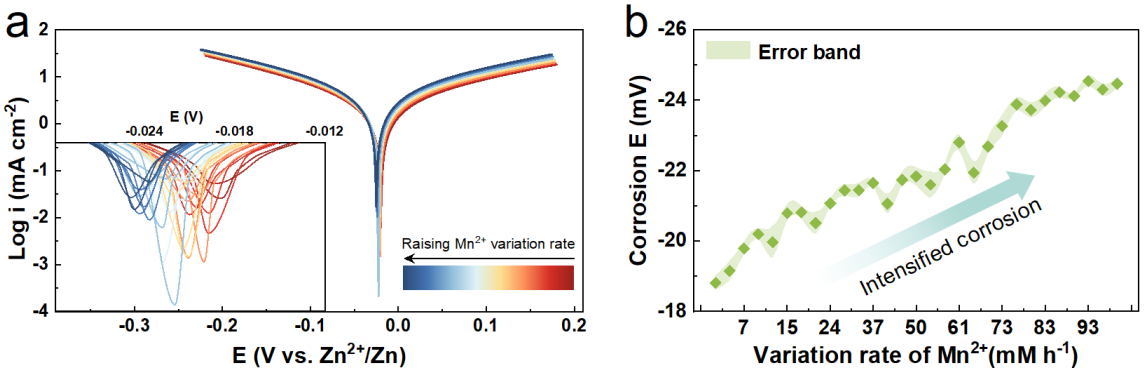


Figure 5.4. a) The obtained LP curves as the Mn^{2+} variation rate in the $ZnSO_4$ electrolyte increases. The scan rate is 0.5 mV s^{-1}. b) The corresponding change in Zn corrosion potential with the Mn^{2+} variation rate. The error band is obtained from three trials.

5.3.2. The ionic crosstalk of Zn^{2+} on MnO_2 cathodes

It has been previously proposed that MnO_2 undergoes a reaction with zinc sulfate hydroxide hydrate, resulting in the formation of Zn-vernadite or Zn-birnessite, which progressively accumulates on the cathode surface during extended cycling[353,376]. This accumulation compromises the physical contact between active materials and conductive carbon, precipitating a decline in capacity for MnO_2 cathodes. The central factor in this phenomenon involves the crosstalk behavior of Zn^{2+} ions and directly influences deposition/dissolution of MnO_2 and the cathode composition. In the initial cycles, Zn^{2+} ions released from the Zn anode accumulate on the cathode and form flaky $Zn_4SO_4(OH)_6{\bullet}nH_2O$ (ZSH), which then reacts with dissolved Mn^{2+} to generate $Zn_x(MnO_2)_y$ nanosheets (ZMO-S) as cycling continues. After 100 cycles in the $ZnSO_4$ electrolyte, significant changes in the surface morphology of the MnO_2 cathode are observed (**Figure 5.5**a), with the original nanorod structures giving way to sheet-like ZMO-S formations due to dissolution, primarily driven by H^+ intercalation[354,376]. This effect is further exacerbated by Zn^{2+} ionic crosstalk, giving the way to the transition from nanorods into ZMO-S. With further cycling, these ZMO-

S aggregates evolve into dense nanoplates (ZMO-P) layer, extensively enveloping the cathode surface and creating discernible cracks after 300 cycles. This phenomenon is even more pronounced in the $ZnSO_4/MnSO_4$ electrolyte, as observed in **Figure B3**. As a complement to the cathode surface analysis, EDS analysis confirms the composition of the dense material covering the electrodes after long-term cycling in both electrolytes is ZMO, as evidenced in **Figure 5.5**b and **Figure B4**. Therefore, the ionic crosstalk in the aqueous Zn-MnO_2 battery encompasses not only the migration of Mn^{2+} ions from the cathode to anode but also the movement of Zn^{2+} ions from the anode to cathode.

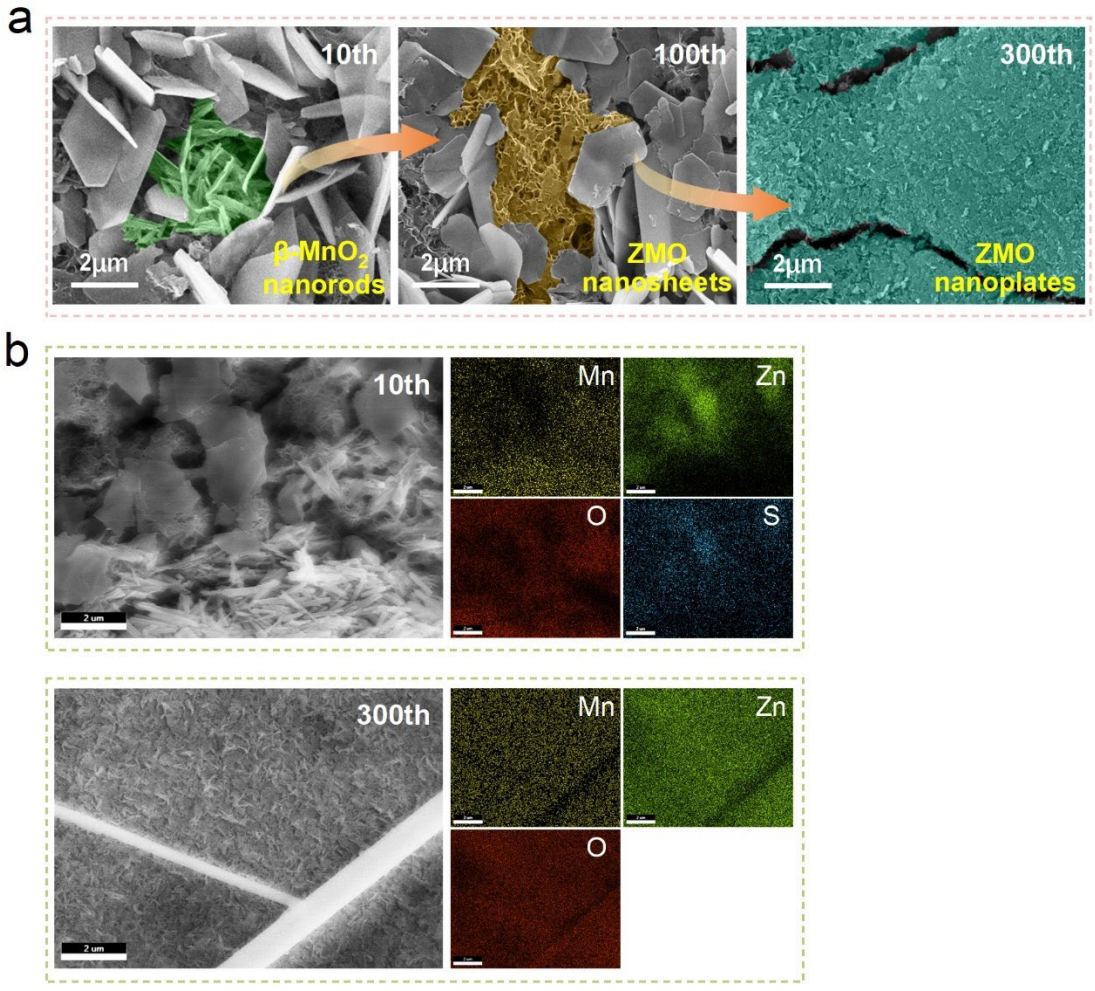


Figure 5.5. a) Morphology evolution of the MnO_2 cathode in the discharged state at selected cycle numbers in 2 M $ZnSO_4$ electrolyte. b) Elemental mapping images of MnO_2 cathode in 2 M $ZnSO_4$ electrolyte at 10th discharge and 300th discharge. Scale bar: 2 μm.

To ascertain that the crosstalk observed on the MnO_2 cathode is attributed to Zn^{2+} ions stripping from the Zn anode, we conducted experiments with the Zn^{2+} ions completely

omitted from the electrolyte, replaced by an H_2SO_4 solution of identical pH (4.0±0.1). The MnO_2 cathodes at the fully discharged state after 5 cycles were examined by using XRD technique. As shown in **Figure 5.6**a, the cycled cathode shows a distinct diffraction peak at 8.52°, which is indexed to (002) diffraction plane of ZSH ($Zn_4SO_4(OH)_6•4H_2O$). This observation indicates that the Zn^{2+} ion influencing the MnO_2 cathode indeed stems from the Zn anode, as evidenced by the early formation of ZSH. Besides, the structural evolution of MnO_2 and the generation of ZMO during prolonged cycling were monitored. The XRD profiles in **Figure 5.6**b display diffraction peaks indicative of ZSH (blue), MnOOH (yellow), and MnO_2 (orange). As the cathode undergoes cycling in a $ZnSO_4$ electrolyte, the intensities of these diffraction peaks gradually decrease. After 300 cycles, both ZSH and MnOOH are nearly disappearing, while only a minimal amount of MnO_2 remains on the cathode. Conversely, the peaks of ZMO (green), specifically the crystal planes located at 19.0° and 36.2°, become more pronounced as the number of cycling extends, suggesting the continual generation of ZMO on the cathode. Given that the MnO_2 cathodes were examined at a fully discharged state, the resulting ZMOs are likely crystalline nanoplates (i.e., ZMO-P) that do not fully dissolve, as opposed to amorphous nanosheets (i.e., ZMO-S). The reduction in MnOOH and ZSH peak intensities implies decreased MnO_2 dissolution, possibly due to a significant portion of MnO_2 has been irreversibly transformed into ZMO-P. This phase transition, alongside the formation of a dense ZMO-P barrier layer on the cathode, obstructs H^+ intercalation. XRD results (**Figure 5.6**c) of MnO_2 cathodes in a $ZnSO_4/MnSO_4$ electrolyte further supports these findings, showing a rapid disappearance of active material peaks within 100 cycles, indicative of swift ZMO-P formation. These outcomes are attributable to the Zn^{2+} ionic crosstalk, which results in the generation of numerous ZMO-P, subsequently degrading the capacity and performance of the cathode. XPS technique was utilized to accurately identify the elemental composition and the respective chemical states, thereby elucidating the constituents of the cathode. As depicted in **Figure 5.6**d, the discharged MnO_2 cathode exhibits multivalent Mn states post-cycling, with the binding energies of 642.40 eV for Mn^{3+} and 644.77 eV for Mn^{4+}. These Mn-based substances correspond to Mn^{3+} and Mn^{4+} are

MnOOH and ZMO-P, respectively. Notably, in the $ZnSO_4$ electrolyte, a progressive increase in Mn^{4+} content and the emergence of a distinct Mn^{4+} peak signify an irreversible phase transition of MnO_2 into ZMO-P due to Zn^{2+} ionic crosstalk during battery operation.

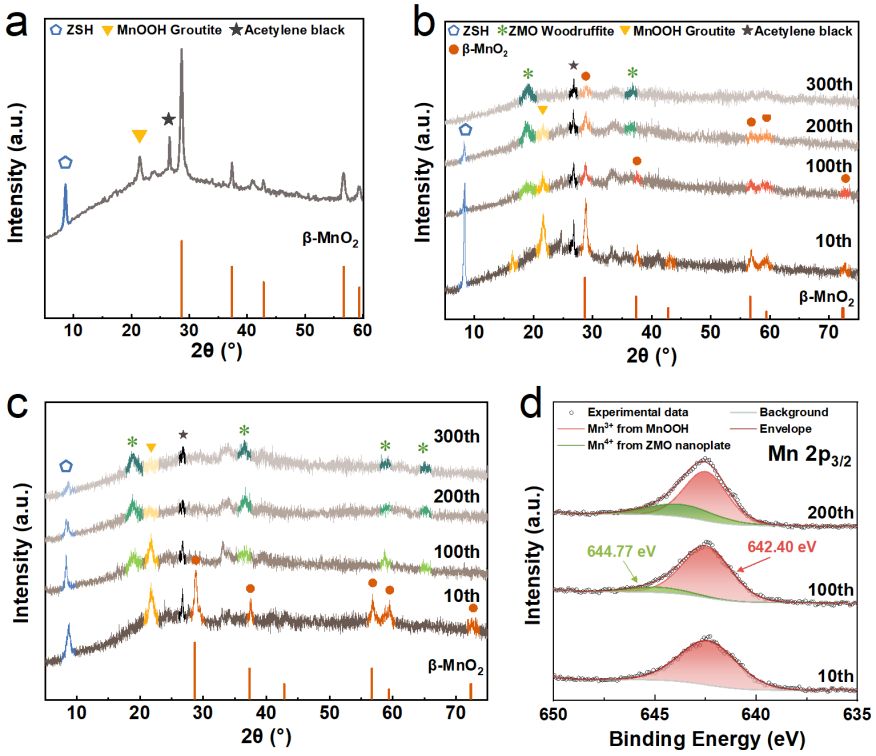


Figure 5.6. a) *Ex situ* XRD patterns of MnO_2 cathodes in H_2SO_4 electrolyte at 5th discharge. *Ex situ* XRD patterns of MnO_2 cathodes in the discharged state in b) 2 M $ZnSO_4$ electrolyte and c) 2 M $ZnSO_4$/0.2 M $MnSO_4$ electrolyte at selected cycle numbers. ZSH ($Zn_4SO_4(OH)_6 \bullet 4H_2O$, PDF# 00-044-0673), MnOOH Groutite (PDF# 99-000-1423), ZMO Woodruffite ($(Zn,Mn)_2Mn_5O_{12} \bullet 4H_2O$, PDF# 99-000-4329), β-$MnO_2$ (PDF# 04-005-4881). d) XPS spectra of Mn 2p from the discharged MnO_2 cathodes.

The *in situ* XRD technique was further adopted to elucidate the irreversible phase transitions experienced by the MnO_2 material on cathode within a single cycle. Prior to observation, the cell underwent preliminary cycling for 24 hours (about 30 cycles) to ensure its activation. The end of the first discharge, as recorded in the GCD following activation (**Figure 5.7**a), reveals a pronounced reduction in the peak intensities of the (110), (101), (211), and (220) planes corresponding to MnO_2, indicating a rapid depletion of the active material (i.e., MnO_2). Subsequently, the emergence of the (102), (003), and (213) planes attributable to the by-product ZMO-P is noted during the reverse charging. Particularly notable is the

observation at the end of the second discharge, where the diffraction peaks corresponding to neither MnOOH nor MnO_2 recover to their original positions, but instead are slightly shifted to higher angles. For instance, the MnO_2 (101) plane is distinctly shifts to a higher angle (lower d-spacing) following re-discharge, positioning the diffraction peak of the discharged product intermediate to those of MnO_2 (101) and ZMO (213). This suggests a considerable portion of the active material is irreversibly transitioned into lowly crystallized ZMO-P, which impedes the complete dissolution of the charging product ZMO-S. According to the corresponding 2D synchrotron grazing-incidence X-ray diffraction (GIXRD) patterns (**Figure 5.7**b and c), vividly display the shifts in the crystallographic planes of MnOOH (101), MnO_2 (110) and (101) subsequent to two consecutive discharges.

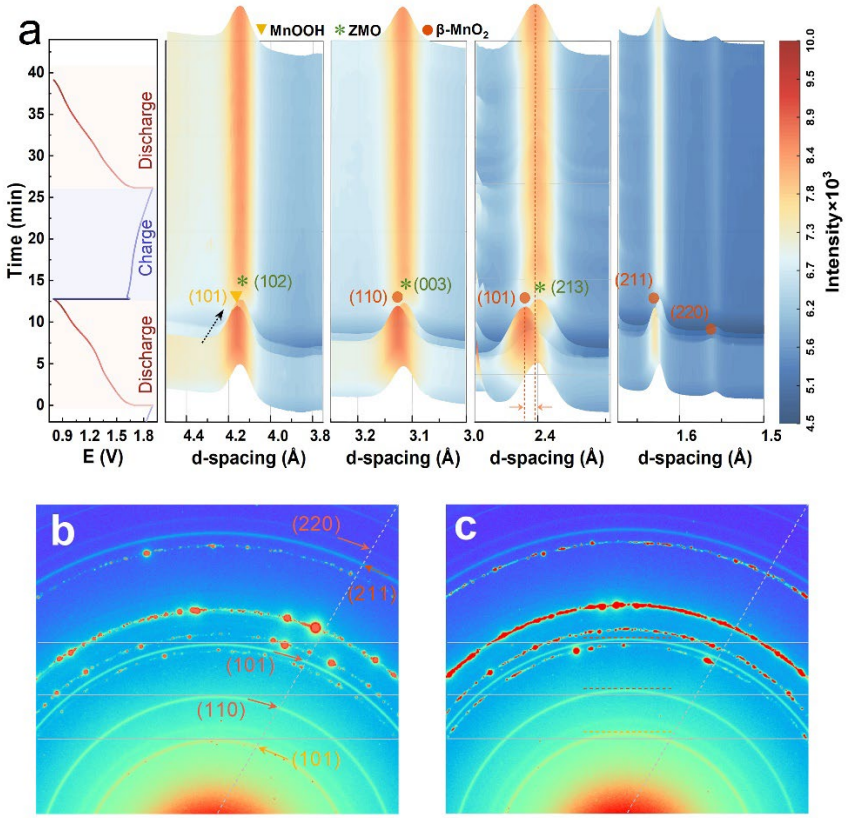


Figure 5.7. a) GCD curve and *in situ* XRD counter map of MnO_2 cathode in 2 M $ZnSO_4$ electrolyte at determined voltages. The applied current density is 2 C. GIXRD patterns of the MnO_2 cathode corresponding to b) the first discharge and c) the second discharge of the GCD curves in a).

In light of the above findings, one can conclude that the dissolution of MnO_2 and Zn^{2+} ionic crosstalk behavior collectively instigates the premature and rapid thickening of ZMO-P. The pristine MnO_2 cathode undergoes severe dissolution during discharge and releases numerous Mn^{2+} ions, which co-deposit with Zn^{2+} ions near the cathode during charging to form ZMO-S and ZSH on the cathode surface. This repetitive dissolution and redeposition cycle promotes the irreversible transition from amorphous ZMO-S to lowly crystalized ZMO-P. Although ZMO-S exhibits favorable electrochemical activity and may provide partial capacity, the transformed ZMO-P is less electrochemically active and hinders H^+ intercalation while fails to dissolve, thereby degrading the cathode's electrochemical performance. Consequently, addressing this issue necessitates hindering the formation of ZMO-P and maintaining the production of active ZMO-S throughout the battery cycling process. To illustrate these findings, we present a schematic diagram (**Figure 5.8**) that elucidates the consequences of ionic crosstalk on electrode in the aqueous Zn-MnO_2 battery. This diagram specifically highlights how Zn^{2+} ionic crosstalk induces an irreversible phase transition from MnO_2 to ZMO-P, which impedes the dissolution of the active material and reduces the electrochemical activity and efficiency of the cathode. Furthermore, the impact of Mn^{2+} ionic crosstalk on the Zn anode is especially pronounced under significant Mn^{2+} concentration gradients, leading to irregular deposition patterns and dendrite formation. Observations also indicate that in electrolytes with low or absent Mn^{2+} ions, the uniform deposition of zinc products is adversely affected. These insights underscore the importance of comprehending and mitigating ionic crosstalk in aqueous Zn-MnO_2 batteries to enhance electrode performance and ensure the long-term reliability of these energy storage systems.

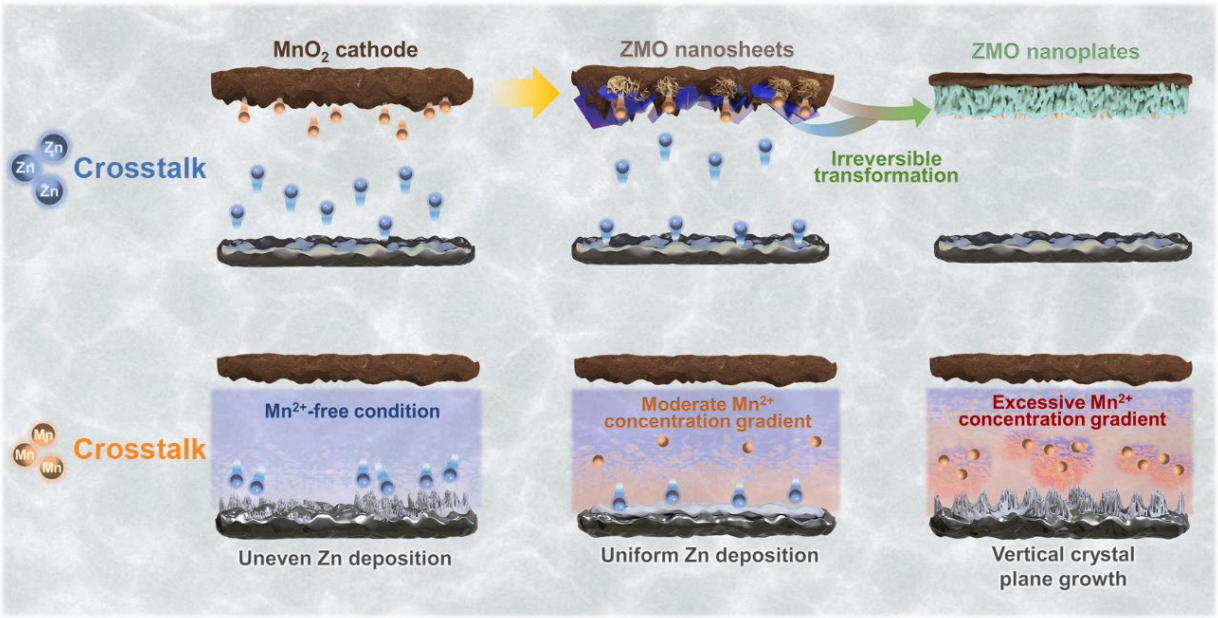


Figure 5.8. Schematic illustration of the Zn^{2+} ionic crosstalk effect (upper) and Mn^{2+} ionic crosstalk effect (lower) in the aqueous Zn-MnO_2 battery.

5.4. Conclusion

This work pioneers the discovery of bidirectional ionic crosstalk phenomenon, an aspect previously overlooked in the field of aqueous Zn-MnO_2 batteries. Through *in situ* optical visualization observations, we observe that a stable Mn^{2+} concentration fosters uniform zinc deposition, while notable fluctuations in Mn^{2+} concentration induce rapid dendrite growth. In addition, XRD and LP results reveal the intensification of vertical planes (100) and (110) in the zinc deposits and severe anodic corrosion caused by Mn^{2+} ionic crosstalk, which undoubtedly increases the risk of internal short-circuiting of the cell. Moreover, we uncover that Zn^{2+} ions are catalysts for the phase transition of the cathode material. Zn^{2+} ions stripped from the anode co-deposit with Mn^{2+} ions during charging and form ZMO-S on the cathode surface. The repeated dissolution and redeposition of this material as the battery cycling progresses not only promotes the transformation of amorphous ZMO-S to low-crystalline ZMO-P, but also degrades the cathode's charging and discharging efficiencies. Although some prior studies have detailed the phase transition of ZMO at the cathode, they have not comprehensively addressed the crosstalk behavior of Zn^{2+} and Mn^{2+} ions. Our findings provide a crucial complement to these studies and underscore the detrimental effects of ionic crosstalk on electrodes.

Furthermore, there are some concerns related to this work that require further attention:

(1) Although we elaborate that violent Mn^{2+} concentration changes affect the deposition morphology of the Zn anode, the increase in Mn^{2+} concentration from 0.2 M to 0.5 M (for example, in a 140 μL electrolyte) requires the dissolution of over 3.65 mg of MnO_2 cathode material, which is apparently unrealistic in our coin-type cell. The average mass of active material on the cathode in a coin cell is about 3.40 mg. Therefore, we need to fill in the blanks between 0.2 M and 0.5 M and add a couple of additional experiments with other Mn^{2+} concentrations.

(2) It is also unfortunate that since the transition from ZMO-S to ZMO-P is a continuously cumulative process (which may require hundreds of cycles), it is challenging to find a suitable technique to characterize this long process.

Chapter 6. An Effective Method for Mitigating Zn^{2+}/Mn^{2+} Ionic Crosstalk

6.1. Introduction

In **Chapter 5**, we report a previously neglected phenomenon in aqueous Zn-MnO_2 batteries, which we have defined as "ionic crosstalk". This discovery sheds light on how ionic crosstalk can degrade cycling lifespan and heighten the potential for internal short circuits, which can critically affect the overall battery performance. To fundamentally mitigate the crosstalk effect of Zn^{2+} and Mn^{2+} ions at the electrodes, in this chapter, we introduce a cathode electrolyte interface in the form of a poly(vinylidene fluoride-co-hexafluoropropylene) (PVDF-HFP)-based membrane, denoted as PM, which is applied over the MnO_2 cathode surface. PVDF-HFP was chosen as the polymer substrate for the membranes because of its superior mechanical stability and lower crystallinity relative to other polymers[392–395]. The nanocomposite membrane with specific pore designs was created through the efficient and convenient dry phase inversion method[396–398]. As a result, this PM possesses enriched polarizable fluorinated functional groups and a hierarchical porous structure, facilitates strong interactions with cations and effectively controls ion release. This PM implementation ensures an even ion distribution and simultaneous regulation of both Zn^{2+} and Mn^{2+} ion fluxes. Such a strategy can markedly mitigates adverse ionic crosstalk effects at the electrodes, promotes targeted in situ generation of reactive ZMO-S at the cathode, and ensures uniform zinc deposition at the anode (**Figure 6.1**), thereby prolonging the operational durability of both electrodes. Upon evaluating the electrochemical performance of aqueous Zn-MnO_2 batteries with PM, a specific capacity of 187.7 mAh g^{-1} is attained over 1000 cycles at 2 C, giving a capacity retention exceeding 97%. Furthermore, it offers 1.5 times longer lifespan in cycling tests and higher coin-type cell capacity (0.56 mAh) in comparison to other state-of-the-art aqueous Zn-MnO_2 battery systems. Most importantly, the cycling performance of these batteries demonstrate high reproducibility, with average Coulombic efficiencies of over 99.8% and minimal capacity deviation of ±5.01 mAh g^{-1} (2.66%). Such high consistency in battery

performance demonstrates the reliability of the PM approach. We are confident that this straightforward and effective method has great potential and promises to advance the development of aqueous Zn-MnO_2 batteries for real-world energy storage applications.

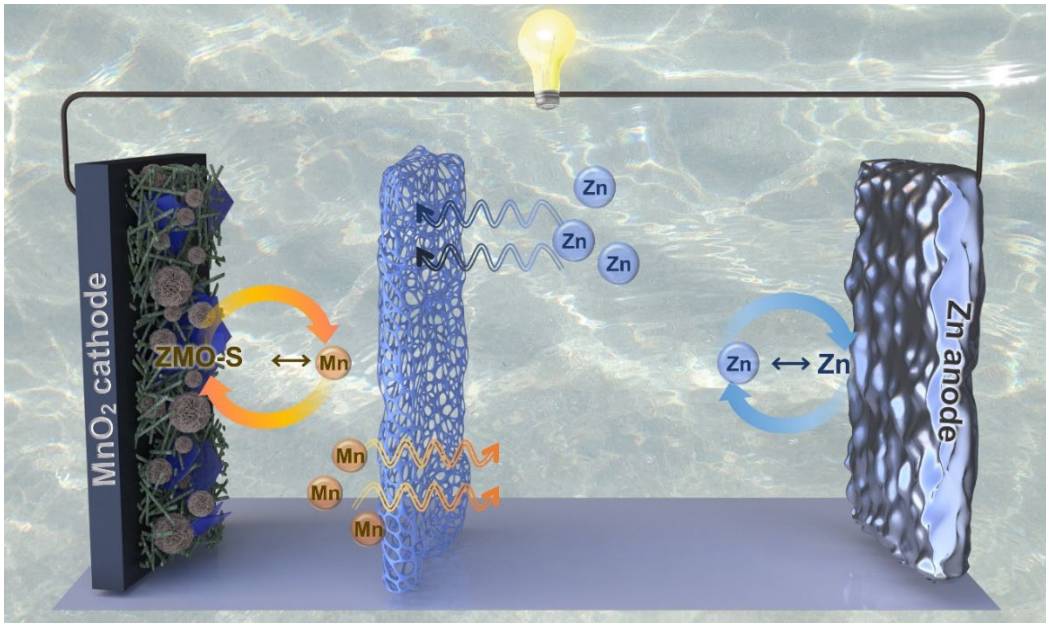


Figure 6.1. Schematic of the PM function in the aqueous Zn-MnO_2 battery.

6.2. Experimental Methods

6.2.1. PM fabrication

The casting solution used for PM fabrication was formulated with poly(vinylidene fluoride-co-hexafluoropropylene) (PVDF-HFP, Sigma-Aldrich, Mw~400,000), acetone (Sigma-Aldrich, 99.5%) and DI water. First, a 5 wt.% PVDF-HFP solution was prepared by dissolving PVDF-HFP pellets in acetone at room temperature. Second, DI water was dropped into the 5 wt.% PVDF-HFP solution at various mass ratios (DI-H_2O:PVDF-HFP=0.2:1, 0.5:1, 0.7:1, 1:1 , 1:1.5 and 2:1) and stirred continuously for 30 minutes at room temperature.

Subsequently, a spin coater (SETCAS LLC, KW-4A) was employed to prepare PM-coated MnO_2 cathodes (PM-MnO_2). The operating principle of this spin coater relies on dispensing a liquid onto the surface of a rotating sample. Centrifugal force then ensures the liquid spreads out evenly across the sample surface, ultimately forming a uniform coating

layer. In practice, a bare MnO_2 cathode sheet is secured onto the rotating stage with a vacuum pump to prevent displacement during the high-speed rotation. Both the rotation speed and time can be adjusted to produce a consistent coating on the electrode surface. Typically, the higher the rotation speed, the thinner the thickness of the film. During the coating process, the time and speed were set at 10 s and 2000 rpm, respectively. Then, for the drying process, the time and speed were aet as 15 s and 4000 rpm, respectively. To control the thickness of PM, the applied casting solution is 60 μL.

6.2.2. Other experimental methods

The processes for cathode sheet fabrication, battery assembly, material characterization techniques, and electrochemical testing follow the descriptions provided in **Chapter 3**; therefore, detailed descriptions are omitted here. It should be noted that the mass loading of the active material in each cell was approximately 3.0±0.2 mg cm^{-2}, and the voltage range of the full cell test is 0.8-1.9 V. The cycling tests were performed at a current density of 1 C and 2 C, where 1 C=0.25 A g^{-1}. Three types of electrolytes were applied in this work, 2 M $ZnSO_4$, diluted H_2SO_4 and 2 M $ZnSO_4$/0.2 M $MnSO_4$ solutions with pH=4.0±0.1.

6.3. Results and Discussion

6.3.1. PM fabrication and characterization

With the objective of maintaining consistent Mn^{2+} concentrations and prevent excess Zn^{2+} ions from reaching the cathode surface, we implemented a strategy of applying a cathode electrolyte interface (i.e., PM) on the MnO_2 cathode. In addition, for rapid and even film application on the MnO_2 cathode, the spin-coating technique was utilized to enhance the overall procedural efficacy. As depicted in **Figure 6.2**a, the casting solution, when applied to the cathode, disperses quickly due to rotational motion, forming an opaque film after the transparent solution evaporates. The subsequent phase separation between water and PVDF-HFP during acetone evaporation results in a dry PM, characterized by a nanoporous structure as revealed in **Figure 6.2**b. The membrane features a unique honeycomb-like structure with

an interconnected network of nano-sized and discernible pores, forming a highly porous structure that prevents excess ion permeation. Notably, high water content in the casting solution adversely affects pore formation, with a water to PVDF-HFP mass ratio exceeding 1 leading to pore collapse. Ratios above 0.7 result in unstable films characterized by blurred and ruptured skeleton edges, and overly small pores (ratio of 0.2) can impede ion transport, thereby affecting electrode capacity utilization. The EIS data in **Figure C1** demonstrates that membranes fabricated with a ratio of 0.5 have lower R_{ct}, which ensures favorable battery performance. Moreover, the cycling performance of the cathodes with different PMs is depicted in **Figure C2**. The data reveal that the battery with the bare MnO_2 cathode exhibits a rapid initial capacity increase, which peaks and then drastically declines, suggesting rapid depletion of the cathode material and results in battery failure. In contrast, PMs fabricated with ratios of 0.2:1, 0.5:1, and 1:1 demonstrate improved capacity retention. Notably, the 0.5:1 ratio maintains the specific capacity over 150 cycles, indicating an optimized cathode stabilization and electrochemical reactivity. Thus, the PM with 0.5:1 ratio was chosen for cathode coating to form optimal pore sizes and maintain better battery performance.

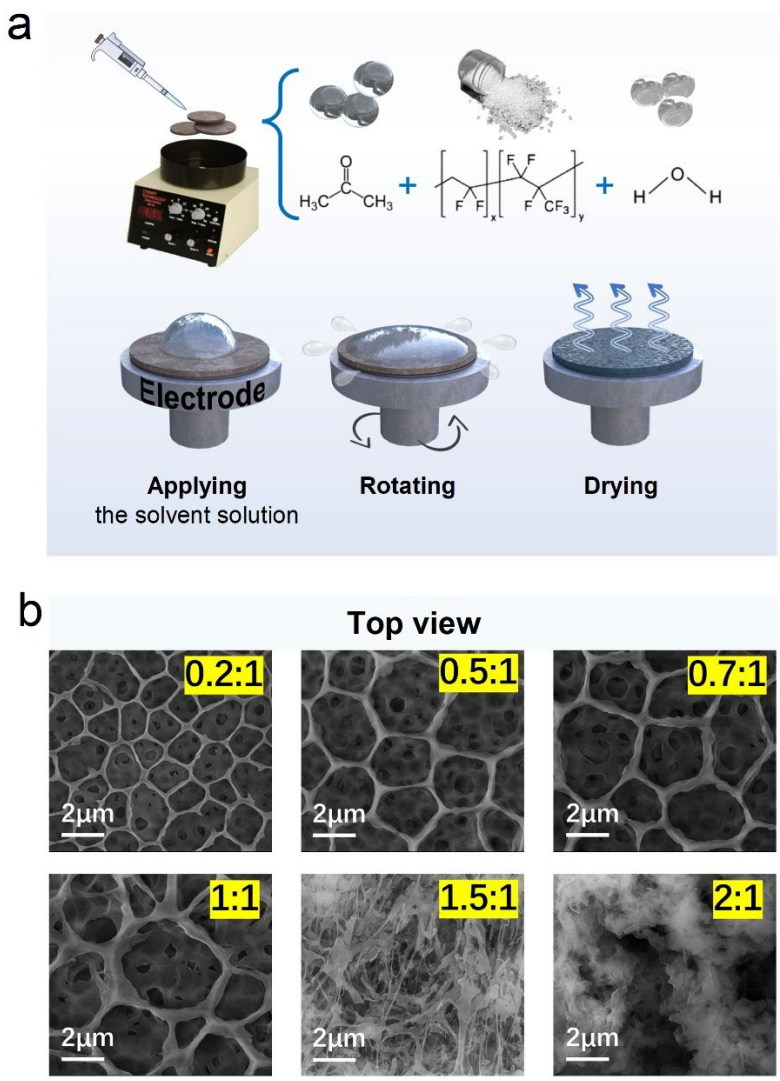


Figure 6.2. a) Schematic diagram of the PM fabrication process. b) PM surface morphology based on various mass ratios (H_2O:PVDF-HFP=0.2:1, 0.5:1, 0.7:1, 1:1 , 1:1.5 and 2:1). Scale bar: 2 μm.

The cross-sectional view in **Figure 6.3**a elucidates the hierarchical structure of the PM, averaging around 2.33 μm in thickness. **Figure 6.3**b illustrates a schematic of this structure, wherein the dissolved ions from the electrode necessitate their sequential passage through the porous layers to reach the electrolyte. Furthermore, the FT-IR analysis in **Figure 6.3**c is instrumental in identifying the specific chemical functional groups present in the PM. The β-phase of PVDF-HFP, characterized by heightened polarity, exhibits strong interactions with cations, thereby facilitating a more uniform redistribution of ion flux[393,394,399]. The FT-IR spectroscopy further corroborates the presence of the β-phase in the PM, discerned at 875 cm^{-1} and 1069 cm^{-1} [400,401]. Notably, the absorption peak observed at 1176 cm^{-1} signifies the

symmetric stretching vibrations of $–CF_2$, while a minor shoulder around 1208 cm^{-1} corresponds to the asymmetric vibration of this band. In addition, the peak at 1400 cm^{-1} is ascribed to the $–CH_2$ wagging vibration[402,403]. In this case, the high density of fluorinated groups, which possess polarizable characteristics, interact strongly with cations, such as Zn^{2+} and Mn^{2+} ions. These interactions facilitate a more even and controlled distribution of ions within the membrane, thus governing the uniform ion deposition onto the electrode surface. The porous nature of the PM, as indicated by BET technique in **Figure 6.3**d. The N_2 adsorption/desorption isotherms of PM material exhibit a typical reversible type IV adsorption isotherm with small H3 hysteresis loops[403–405]. The BET analysis reveals the surface area of PM to be 7.3599 $m^2\ g^{-1}$. Using the Barrett–Joyner–Halenda (BJH) method, the average pore size is calculated at approximately 35.8588 nm with a pore size distributed within the range of 2–170 nm, indicating a hierarchical porous structure. The hierarchical porous structure of the PM establishes it as an effective selective barrier, regulating Mn^{2+} ion flux from the cathode to the electrolyte and limits excessive Zn^{2+} ions to deposit on the MnO_2 cathode. In other words, this structural property of PM controls the release/passage of ions. Through controlling ion migration, PM not only prevents undesirable side reactions but also maintains the reactivity of the materials on the cathode.

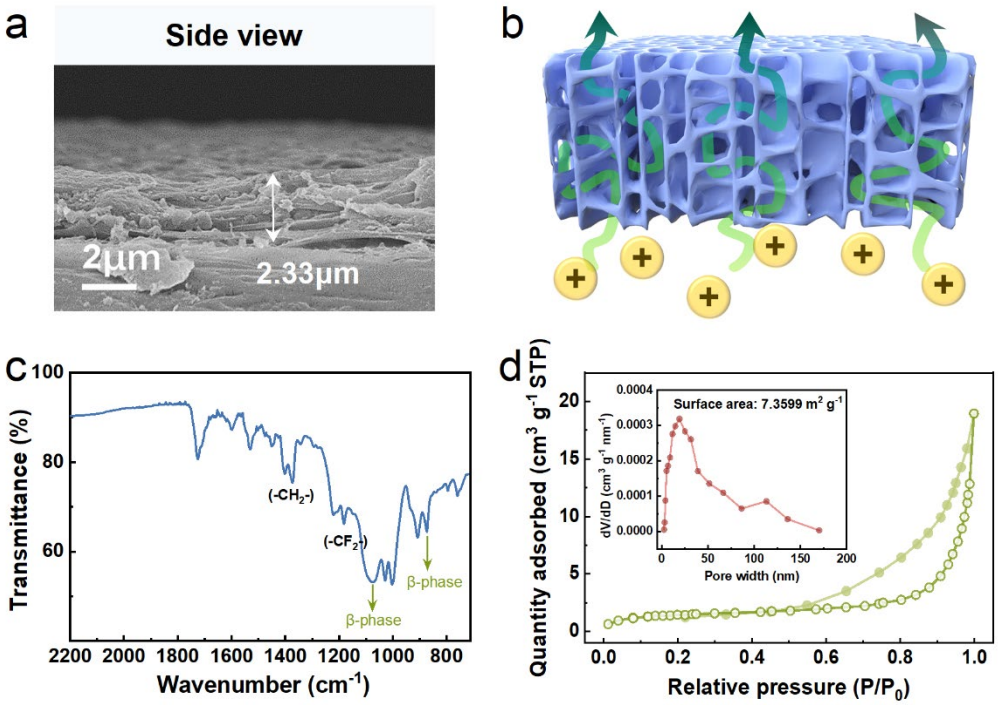


Figure 6.3. a) Cross-sectional SEM images of the PM (H_2O:PVDF-HFP=0.5:1). Scale bar: 2 μm. b) Side view schematic of a PM with a hierarchical porous structure. Green arrows represent long migration paths of ions in the PM. c) FT-IR spectra of the PM. d) Nitrogen adsorption/desorption curve of PM. The inset shows the BJH pore size distribution of PM.

6.3.2. The inhibitory effect of the PM on Mn^{2+} ionic crosstalk

The positive effect of PM on Zn anodes was explored through *in situ* optical visualization technique, observing the charging dynamics within a full cell configuration. In this setup, the Zn foil connected to the positive electrode in the schematic (**Figure 5.1**a) was replaced with either a bare MnO_2 cathode or a PM-MnO_2 cathode, and electrochemical charging tests were conducted using an electrochemical workstation. In a $ZnSO_4$ electrolyte, observations from **Figure 6.4**a and **Figure 6.4**b reveal that the battery equipped with PM-MnO_2 cathode exhibits significantly improved charging behavior, characterized by uniform zinc deposition and the absence of gas evolution, which contrasts starkly with the outcomes observed in batteries without the PM. This trend persists in $ZnSO_4$/$MnSO_4$ electrolyte (**Figure C3**), where dendrite formation became visible just 180 s (from 540 to 720 s) after charging without PM. By 900 s, deposits on the Zn electrode extended to the MnO_2 electrode side, ultimately causing an electrical short-circuit in the cell. Further, the protective role of PM was

evident in the suppression of dendritic growth and the prevention of anode corrosion, as confirmed by surface characterization after various cycling intervals. Within a $ZnSO_4$ electrolyte (**Figure 6.4**c and **Figure 6.4**d), Zn anodes paired with PM-MnO_2 cathodes maintained a smoother surface texture and showed enhanced resistance to corrosion, highlighting the PM's ability to stabilize the electrochemical environment and promote uniform ion deposition. Supplementary findings, particularly with Zn anodes subjected to cycling in a $ZnSO_4$/$MnSO_4$ electrolyte (**Figure C4**), further affirm the protective influence of PM against dendritic growth and anode corrosion over time.

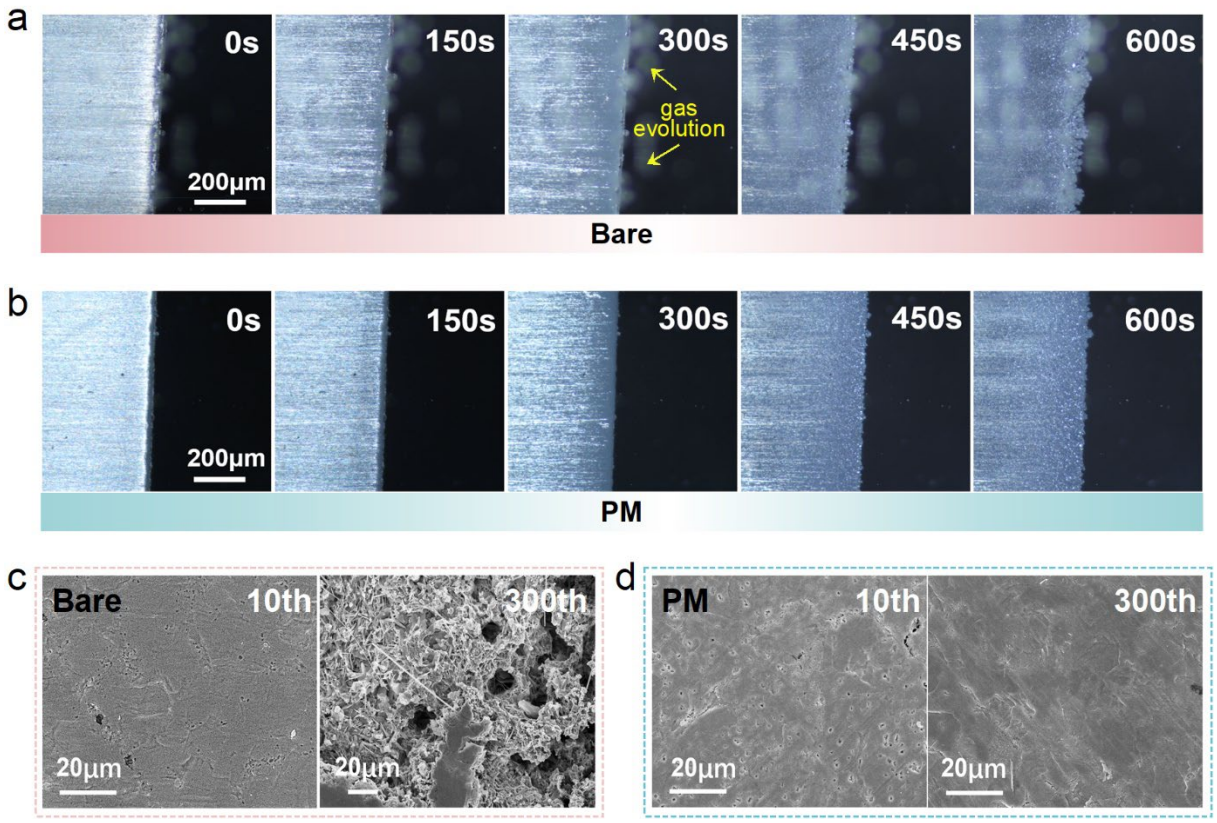


Figure 6.4. *In situ* optical visualization observations of Zn anodes paired with a) bare MnO_2 and b) PM-MnO_2 cathodes in 2 M $ZnSO_4$ electrolyte within transparent electrochemical cells at various deposition times. Scale bar: 200 μm. Morphology of cycled Zn anode surface paired with c) bare MnO_2 and d) PM-MnO_2 cathodes in 2 M $ZnSO_4$ electrolyte. Scale bar: 20 μm.

To investigate the stabilizing impact of PM on Mn^{2+} concentration in the electrolyte during structural reconstruction of the deposition layer, XRD patterns of the Zn anode after

extended cycling were examined. **Figure 6.5**a demonstrates that when paired with a bare cathode, the Zn anode shows a marked increase in the intensity of the (100) and (110) planes compared to pristine Zn metal. For Zn anode coupled with a PM-coated cathode, the intensity of the (002) plane increases and significantly exceeds that of the (100) plane after 300 cycles. The results indicate a preferential orientation shift in crystal growth towards the Zn (002) plane in cells with PM, unlike in cells without PM, where the growth favors the (100) and (110) planes. Analysis of XRD spectra from Zn anodes after prolonged cycling in a $ZnSO_4/MnSO_4$ electrolyte (**Figure C5**) corroborates this effect, underscoring PM's role in directing crystal growth and enhancing the performance of Zn anodes during battery cycling.

The main causative factor underlying the observation of ionic crosstalk phenomenon in aqueous Zn-bare MnO_2 cells is likely the violent dissolution of MnO_2, which surges the Mn^{2+} concentration in the electrolyte. This sharp increase disrupts the equilibrium of Mn^{2+}, thereby harmful to the plating process of zinc metal. ICP-OES analysis provides a direct measurement of the Mn^{2+} concentration variations in the electrolyte. As indicated in **Figure 6.5**b and **Figure 6.5**c, in Mn^{2+}-free electrolyte, any rise in Mn concentration mainly arises from the ongoing dissolution of Mn-based material on the cathode during cycling. Particularly, in the battery without PM, there is a noticeable increase in Mn concentration as the cycle count advances, which is twofold higher than in the battery with PM. Using 140 μL of electrolyte in a coin cell, reaching this concentration means that nearly 30% of the active material is dissolved. In stark contrast, the cell incorporating PM exhibits considerably lower increases in Mn concentration. This discrepancy can be attributed to the confinement of Mn^{2+} ions by the enriched polarizable fluorinated functional groups present in the PM, as illustrated in **Figure 6.5**d. In addition, the hierarchical porous structure effectively regulates Mn^{2+} ion flux, thus controlling the release of Mn^{2+} ions during MnO_2 dissolution. According to the ICP-OES findings, the incorporation of PM consistently moderates the ion concentration by regulating the migration of Mn^{2+} ions from the cathode to the electrolyte, effectively shielding the Mn^{2+} ionic crosstalk. Consequently, PM creates a well-stable environment during cycling,

significantly diminishing the corrosion rate of the Zn anode and promoting a smoother zinc deposition surface.

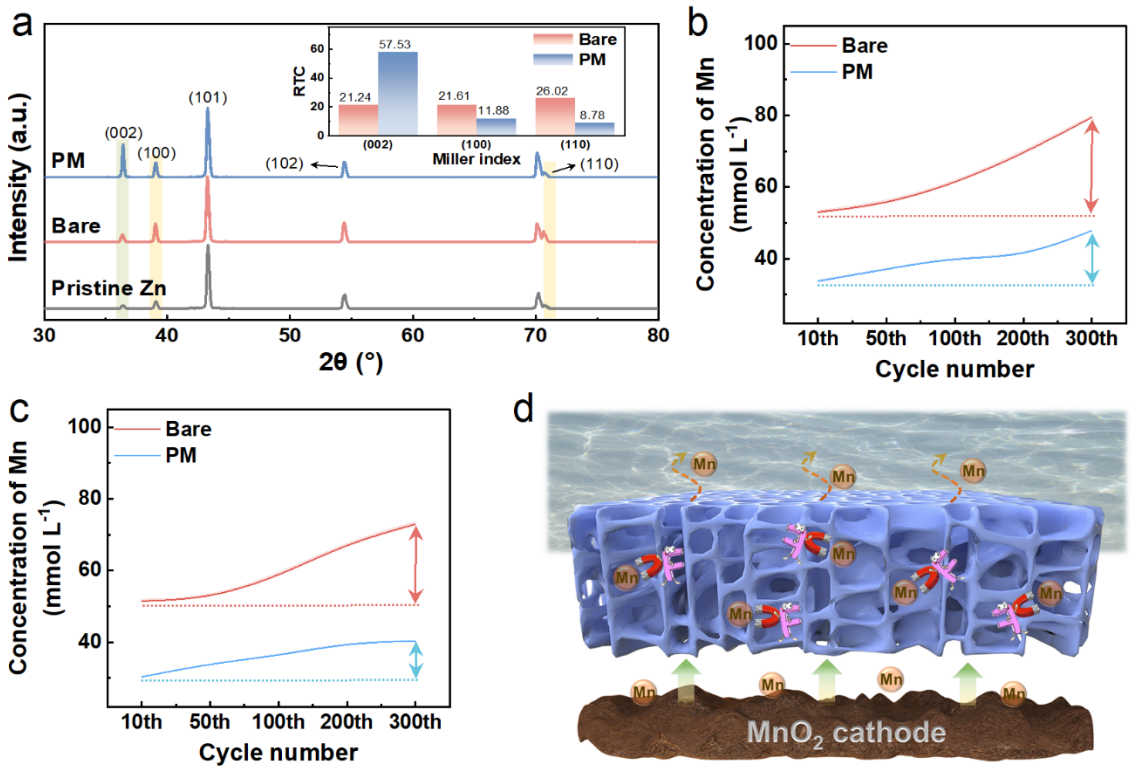


Figure 6.5. a) *Ex situ* XRD patterns of Zn anodes paired with bare and PM-MnO_2 cathodes after 300 cycles in 2 M $ZnSO_4$ electrolyte. Inset: the RTC of Zn anodes paired with bare and PM-MnO_2 cathodes (300 cycles). The Mn concentration in 2 M $ZnSO_4$ electrolyte at a b) fully discharged state and c) fully charged state for different cycle numbers. d) Schematic diagram of Mn^{2+} ions passing through the PM.

6.3.3. The inhibitory effect of the PM on Zn^{2+} ionic crosstalk

Concurrently, the adoption of PM provides considerable results in mitigating the crosstalk of Zn^{2+} ion at the MnO_2 cathode. Firstly, in the H_2SO_4 electrolyte (**Figure 6.6**a), after the 5th cycle of discharge, ZSH formation is detected on the cathode surface, but to a significantly lesser extent compared to the cathode without PM coating (**Figure 5.6**a). This suggests that the PM acts as a selective barrier, preventing excess Zn^{2+} ions from reaching the cathode surface and thus reducing the production of ZSH. Furthermore, covering a PM protective layer on the cathode yields consistent peak diffractions of ZSH, MnOOH, and MnO_2 even after 300 cycles, as evidenced in **Figure 6.6**b. This underscores the sustained

reactivity of the cathode over a prolonged operation. Notably, the formation of ZMO-P is minimal within the initial 200 cycles, with only a marginal detection after 300 cycles. This is due to the fact that PM effectively inhibits the formation of ZMO-P through its hierarchical porous structure and functional properties. The PM's hierarchical porous structure acts as a selective barrier that regulates the flux of Mn^{2+} ions from the cathode to the electrolyte and limits excessive Zn^{2+} ion deposition. This controlled ion migration prevents localized concentrations of ions that could lead to uncontrolled growth of ZMO nanostructures. Additionally, the high density of fluorinated groups within the PM interacts strongly with cations such as Zn^2 and Mn^{2+}, ensuring a uniform redistribution of ion flux. These interactions facilitate even and controlled ion distribution, thereby preventing the formation of undesirable side reactions and aggregation of ions, which are key factors in the formation of ZMO-S and ZMO-P. These findings underscore PM's efficacy in suppressing the accumulation of non-dissolvable ZMO-P, thus contributing to enhanced electrode durability. Further corroborated by XRD analysis of cathodes cycled in a $ZnSO_4/MnSO_4$ electrolyte, there is no noticeable ZMO-P formation on PM-MnO_2 cathodes after prolonged cycles (**Figure C6**). The XPS analysis in **Figure 6.6**c demonstrates a minimal detection of Mn^{4+} on the cathode surface with PM, suggesting an absence of ZMO-P and aligning with the XRD outcomes. Moreover, **Figure C7** discloses a minor Mn^{4+} presence, approximately 4.16%, on the PM-MnO_2 cathode after 300 cycles, compared to a significant 28.4% on electrodes without PM within just 200 cycles (**Figure 6.6**d).

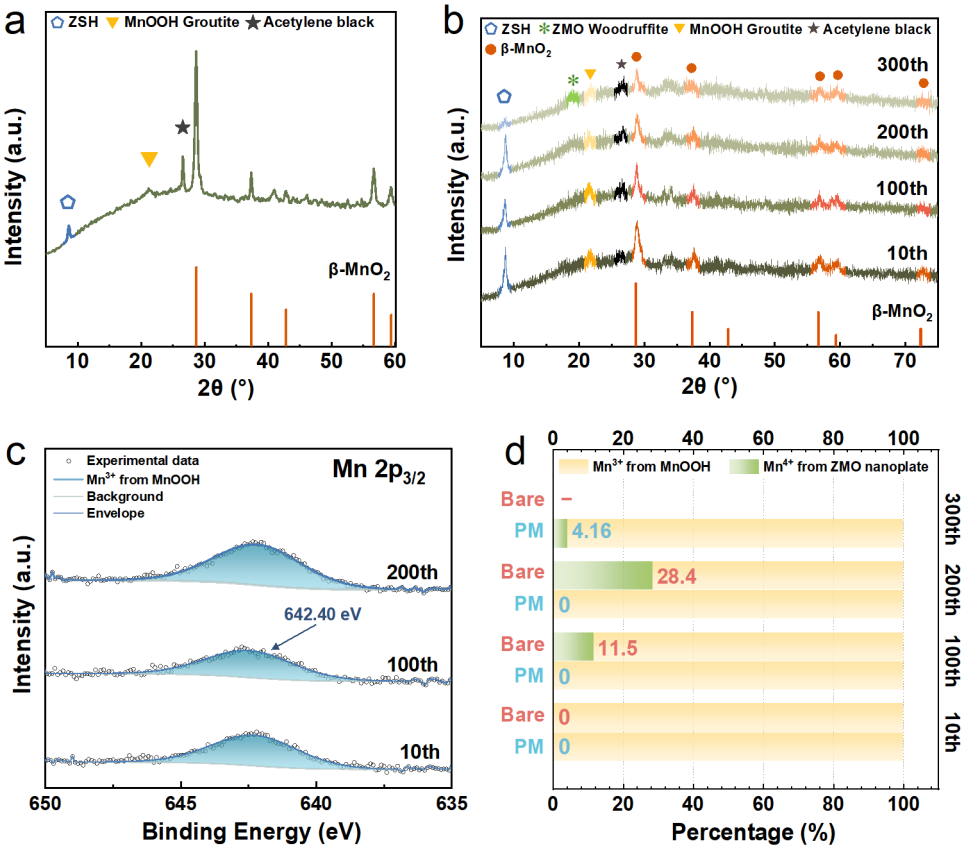


Figure 6.6. a) *Ex situ* XRD patterns of MnO_2 cathodes in H_2SO_4 electrolyte at 5th discharge. b) *Ex situ* XRD patterns of MnO_2 cathodes in the discharged state in 2 M $ZnSO_4$ electrolyte at selected cycle numbers. ZSH ($Zn_4SO_4(OH)_6 \bullet 4H_2O$, PDF# 00-044-0673), MnOOH Groutite (PDF# 99-000-1423), ZMO Woodruffite ($(Zn,Mn)_2Mn_5O_{12} \bullet 4H_2O$, PDF# 99-000-4329), β-$MnO_2$ (PDF# 04-005-4881). c) XPS spectra of Mn 2p from the discharged PM-MnO_2 cathodes. d) Percentage contents of Mn^{3+} and Mn^{4+} on bare and PM-MnO_2 cathodes based on XPS results.

From the *in situ* XRD patterns shown in **Figure 6.7**a, it is evident that the positions and d-spacing of the MnOOH and MnO_2 crystal planes remain relatively unchanged after two discharges, suggesting stability of the PM-MnO_2 cathode during the electrochemical process. In addition to this, the reversible formation and dissolution of the (410) plane, which is representative of the ZSH, underscore the excellent reversible electrochemical reaction of this PM-MnO_2 cathode. However, there is a slight attenuation in the intensity of the MnO_2 (110) and (211) planes throughout the cycling, which could be indicative of a minor consumption of MnO_2 or its partial transformation into amorphous ZMO-S. The GIXRD patterns presented in **Figure 6.7**b and **Figure 6.7**c further corroborate these findings. The presence of defined and

invariant diffraction rings, particularly the MnOOH(101), MnO_2(110) and (211) planes, indicate reversible electrochemical reactions at the cathode during charging and discharging as well as a significant inhibitory role of PM on the generation of ZMO-P.

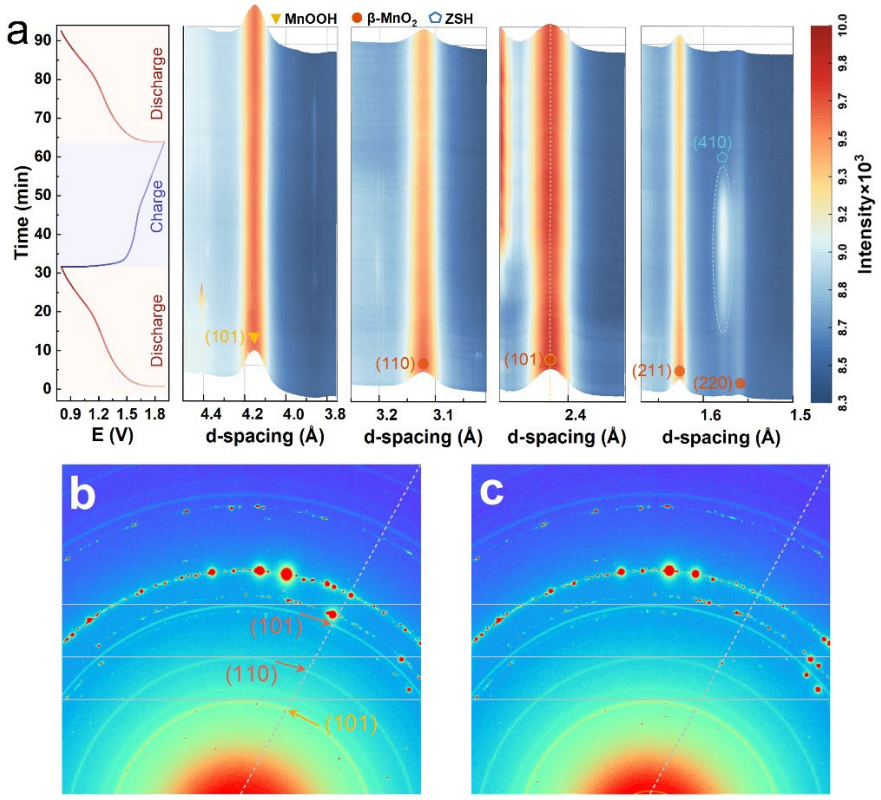


Figure 6.7. a) GCD curve and *in situ* XRD counter map of PM-MnO_2 cathode in 2 M $ZnSO_4$ electrolyte at determined voltages after 24 hours activation. The applied current density is 2 C. GIXRD patterns of the PM-MnO_2 cathode corresponding to b) the first discharge and c) the second discharge of the GCD curves.

The morphology of the PM-MnO_2 cathode (**Figure 6.8**a) exhibits negligible change after extended cycling, particularly in an electrolyte containing Mn^{2+} additives (**Figure C8**a). Over time, the ZMO-S accumulates into a larger volume, yet the MnO_2 nanorods remain discernible beneath the PM coverage. This finding is in stark contrast to the morphology of electrodes without PM, which are extensively covered by dense ZMO-P (**Figure 5.5**a), illustrating that PM prevents the deposition of bulk ZMO-P on the cathode by controlling the transport of Zn^{2+} ions toward the cathode surface. Elemental mapping image (**Figure 6.8**b, **Figure 6.8**c and **Figure C8**b) reveal distinct and recognizable distribution contours for individual elements, indicating negligible ZMO-P formation or deposition on the cathode

surface. Therefore, PM restricts the undesired formation of ZMO-P and favors the in situ deposition of reactive ZMO-S by regulating the Zn^{2+} ion flux.

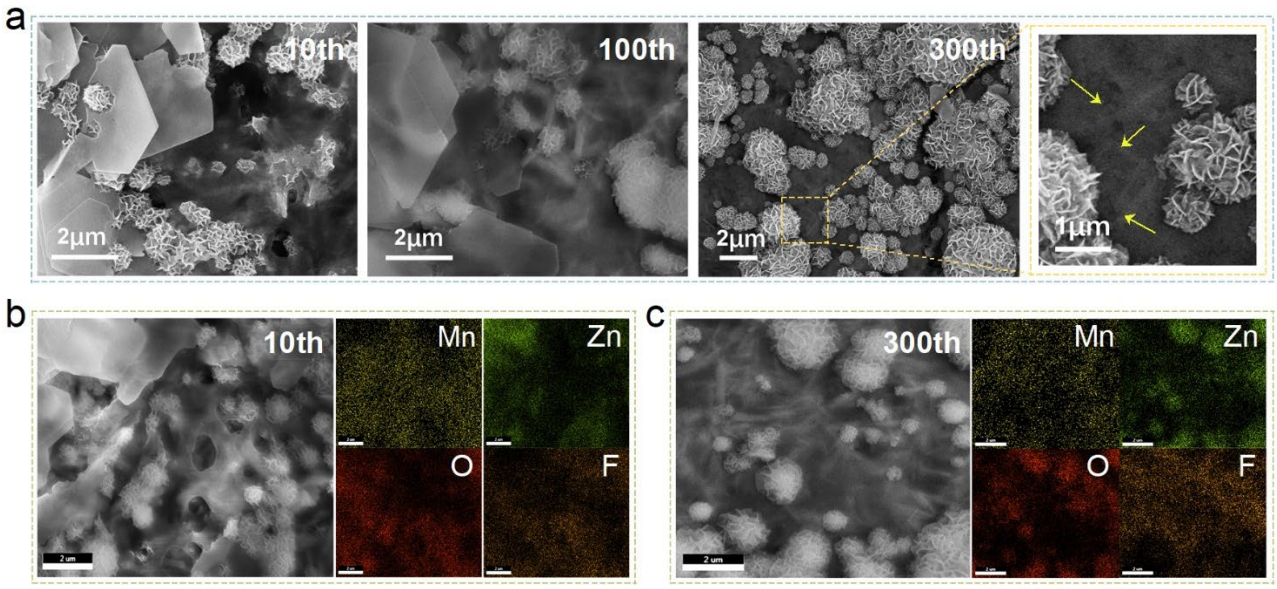


Figure 6.8. a) Morphology evolution of the PM-MnO_2 cathode in the discharged state at selected cycle numbers in 2 M $ZnSO_4$ electrolyte. Scale bars: 2 μm and 1 μm. Elemental mapping images of PM-MnO_2 cathode in 2 M $ZnSO_4$ electrolyte after b) 10th discharge and c) 300th discharge. Scale bar: 2 μm.

To assess the capability of PM in limiting Zn^{2+} ion migration, Zn^{2+} ion transference numbers (t_{Zn2+}) were determined via potentiostatic polarization in Zn-Zn symmetric cells (**Figure 6.9**a-c). The calculated t_{Zn2+} for PM-Zn stands at 0.56, lower than bare Zn (0.81) but considerably higher than PP-Zn (0.11) (as listed in **Table C2**). The PP membrane (polypropylene, Celgard 2340) restricts Zn^{2+} ion passage owing to its extremely small pore size and hydrophobic nature. However, the PM with larger pore size allows Zn^{2+} ion movement to a certain degree, minimizing detrimental interactions between ZMO-S and Zn^{2+} ions by shielding high Zn^{2+} ion flux close to the cathode. This controlled release effect inhibits the accumulation of ZMO-S and its transition into ZMO-P, evident from the lack of slate (i.e., ZMO-P) coverage on the cathode after extended operational time. In addition, the ability of PM to control Mn^{2+} ion release is verified by a lower transference number (t_{Mn2+} = 0.17) compared to the uncovered electrode (t_{Mn2+} = 0.26) (**Figure 6.9**d, **Figure 6.9**e and **Table C3**). We also note that PM exerts a greater restriction on the movement of Mn^{2+} ions

than Zn^{2+} ions in the identical concentration of $MnSO_4$ and $ZnSO_4$ electrolytes. These findings suggest that regulating the Zn^{2+} ion release via PM can decelerate the irreversible phase transition of ZMO, consequently preserving the high reactivity of the cathode material and ensuring that the cathode continues to deliver capacity over prolonged cycling.

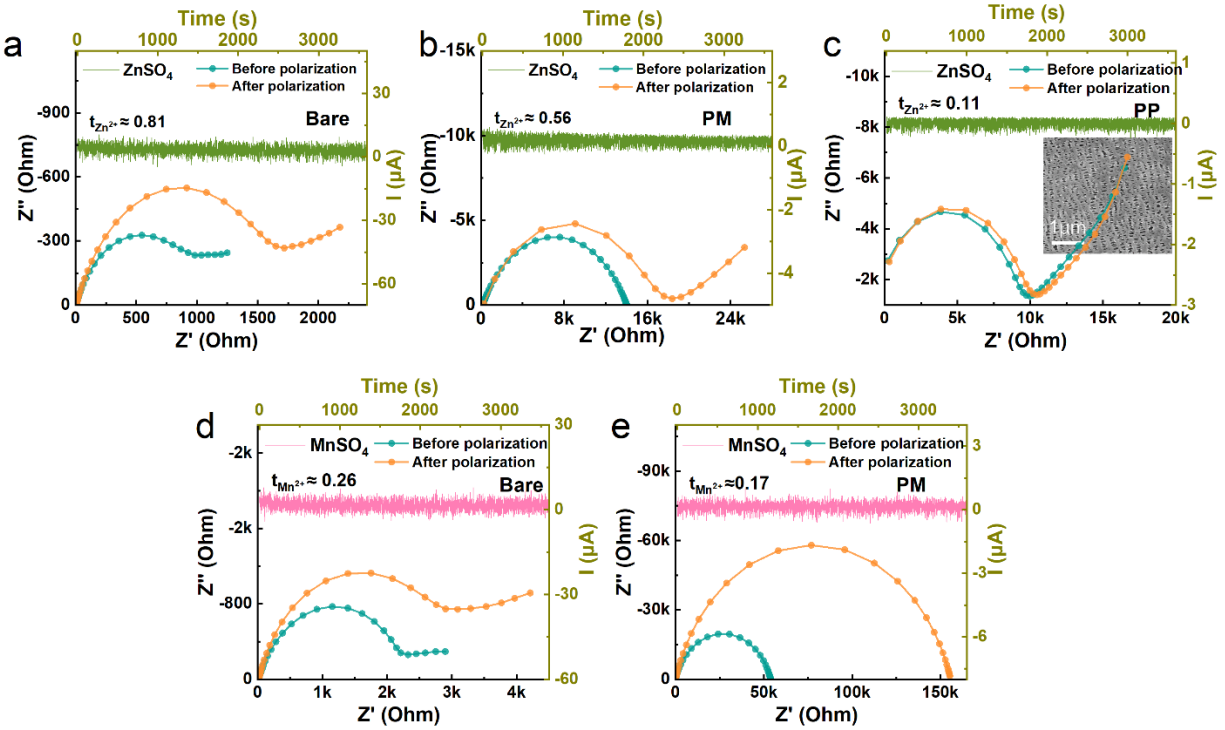


Figure 6.9. Current-time curves at the bias potential of 10 mV and Nyquist plots before and after polarization of a) bare Zn-Zn, b) PM Zn-Zn c) PP Zn-Zn symmetric cells in 2 M $ZnSO_4$ electrolyte. Inset: the morphology of PP film (Celgard 2340). Scale bar: 1 μm. Current-time curve at the bias potential of 10 mV and Nyquist plots before and after polarization of b) bare Zn-Zn and c) PM Zn-Zn symmetric cells in 2 M $MnSO_4$ electrolyte.

6.3.4. Electrochemical performance evaluation

The influence of the PM on the performance of aqueous Zn-MnO_2 batteries was comprehensively assessed through a series of electrochemical tests. **Figure 6.10**a illustrates the cycling performance of the battery with and without PM at a current density of 1 C. Initially, both batteries exhibit comparable specific discharge capacity, yet a noticeable divergence occurs in their cycling behavior over time. In the absence of a PM, the battery undergoes a swift decline in capacity after 180 cycles. In contrast, the PM-equipped battery

demonstrates excellent endurance, maintaining its capacity beyond 400 cycles with no noticeable degradation and delivering a specific capacity of 226.8 mAh g^{-1}. Moreover, the Coulombic efficiency depicted in **Figure 6.10**b remains consistently around 99.5% for the PM-battery, indicating improved cell stability, unlike the fluctuating Coulombic efficiency of the bare cathode. The initial decline in Coulombic efficiency within the first 50 cycles may relate to the extended material transformation of MnO_2 to ZMO-S, particularly at lower current densities. At an elevated current density of 2 C, the PM-equipped battery exhibits satisfactory capacity and electrochemical stability, maintaining a specific discharge capacity of 187.7 mAh g^{-1} with 97% capacity retention over 1000 cycles (**Figure 6.10**c). Nevertheless, the battery without PM shows an initial capacity increase, followed by a consistently decline with a Coulombic efficiency deviating from 100% (**Figure 6.10**d). The GCD profiles depicted in **Figure 6.10**e and **Figure 6.10**f further underscore the excellent capacity retention of PM-battery, showcasing a significant leap in cycling performance for aqueous Zn-MnO_2 batteries enhanced with the PM approach.

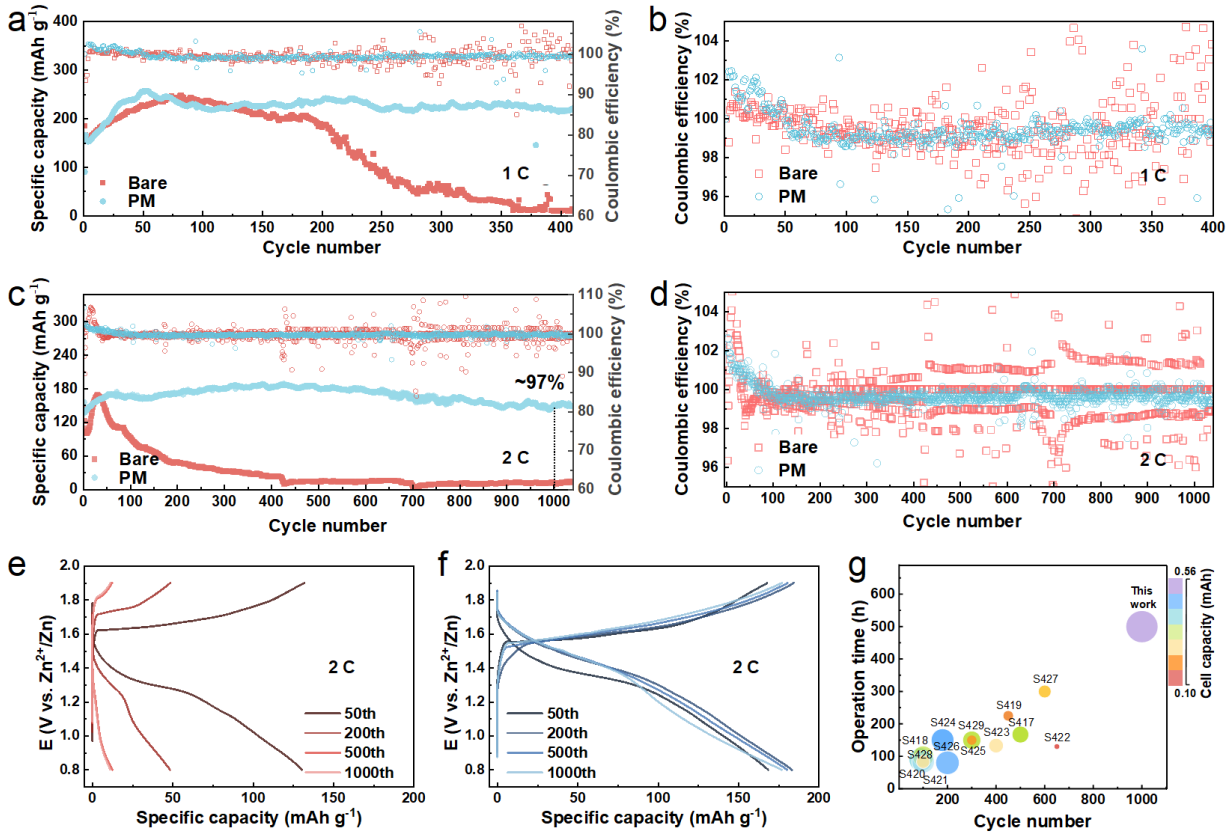


Figure 6.10. a) Cycling performance of bare MnO_2 and PM-MnO_2 electrodes in 2 M $ZnSO_4$/0.2 M $MnSO_4$ electrolytes at 1 C and b) Coulombic efficiency with a narrow y-axis scale. c) Long-term cycling stability of bare MnO_2 and PM-MnO_2 cathodes in 2 M $ZnSO_4$/0.2 M $MnSO_4$ electrolyte at 2 C and d) Coulombic efficiency with a narrow y-axis scale. GCD profiles of e) bare cathode and f) PM-cathode in 2 M $ZnSO_4$/0.2 M $MnSO_4$ electrolyte at 2 C. The average charge voltage of PM-equipped battery is around 1.61 V, and average discharge voltage is around 1.30 V. g) The comparison of cycle number, operation time and cell capacity with previously reported aqueous Zn-MnO_2 batteries. More details are listed in **Table C1**.

In the comparative analysis of operation time and lifespan, our PM-equipped battery stands out significantly against other reported aqueous Zn-MnO_2 battery systems, as illustrated in **Figure 6.10**g. While comparable studies at similar current densities typically demonstrate operational times ranging from 100 to 325 hours, our innovative battery system notably prolongs this to exceed 500 hours. Furthermore, at a current density of 2 C, where competing batteries retain at approximately 600 cycles, our advanced system surpasses 1000 cycles with ease. Moreover, our coin-type cell achieves a capacity of up to 0.564 mAh. An additional encouraging aspect of our research results lies in the extraordinary reproducibility

and reliability of our battery system. The electrochemical data from multiple sets of the PM-equipped batteries were highly consistent (**Figure 6.11**). Three parallel batteries which constructed simultaneously, exhibit an average Coulombic efficiency exceeding 99.8% over the span of 1000 cycles. Furthermore, these batteries exhibit a low deviation in specific capacity, averaging at a mere ±5.01 mAh g^{-1} with a deviation of just 2.66%. Such compelling evidence of our battery system's prolonged durability and stability not only accentuates its readiness for real-world energy storage applications but also marks a significant advancement in the quest for reliable and sustainable power solutions.

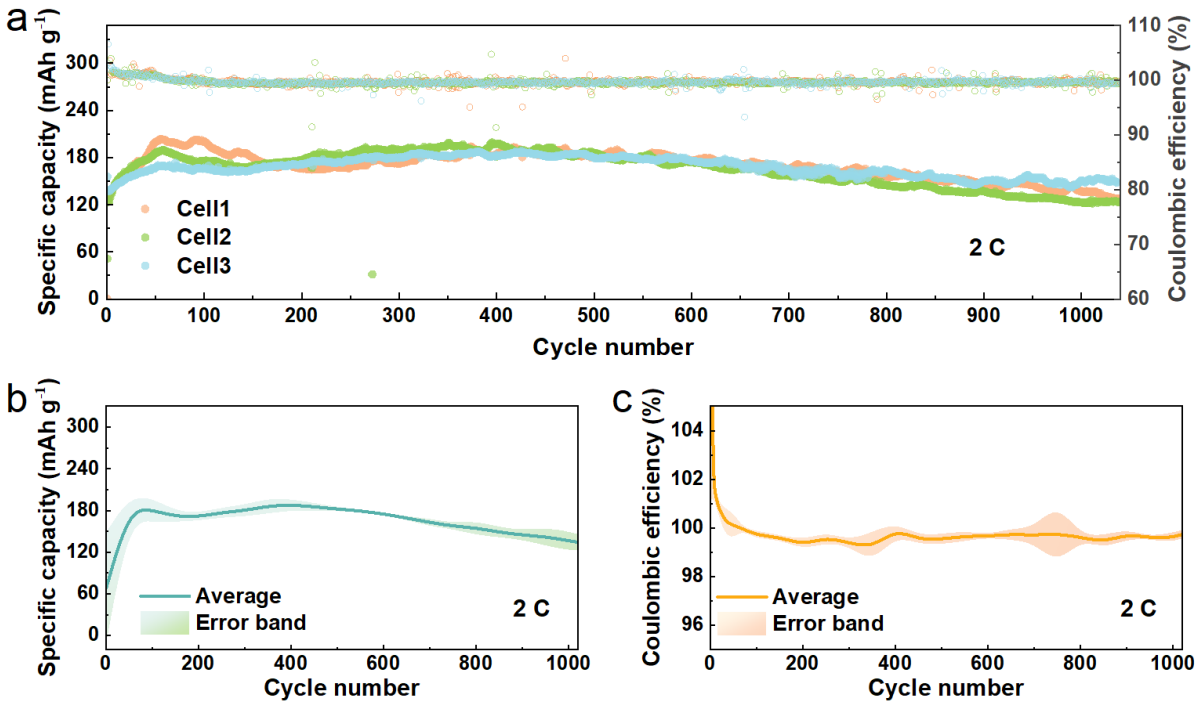


Figure 6.11. a) Cycling performance of PM-coated battery in 2 M $ZnSO_4$/0.2 M $MnSO_4$ electrolyte at 2 C. b) The cycling performance and c) Coulombic efficiency plots with standard deviations calculated from three cells.

The CV technique was employed to investigate the effect of PM coating on the redox reactions of the electrode. Both the PM-coated and bare MnO_2 cathodes in **Figure 6.12**a exhibit similar redox peak pairs, indicating that the PM coverage does not affect the MnO_2 redox reaction. Analysis of the integrated area of CV curves offers insights into the capacity decay of the battery. **Figure 6.12**b shows a sharp decline in response currents of redox peaks from the 100th to the 300th cycle, with the disappearance of the redox peak at 1.2/1.6 V after

100 cycles, probably due to a phase transition at the electrode. This decline in the integrated area reflects the capacity degradation of the Zn-MnO_2 cell over time. On the contrary, the integrated curve area in **Figure 6.12**c is roughly maintained with increasing cycle number, while the redox peak (1.2/1.6 V) slightly decreases, presumably due to the Zn^{2+} intercalation reaction on the cathode is gradually dominated by the H^+ intercalation or MnO_2 dissolution[347,406]. Nyquist plots and the respective equivalent circuit diagrams in **Figure 6.12**d and **Figure 6.12**e elucidate differences between bare MnO_2 and PM-MnO_2 cathodes at various cycling stages. The PM-MnO_2 cathode displays consistently lower R_{ct} from the 50th cycle onwards, maintaining this value throughout subsequent cycles. In contrast, the bare MnO_2 cathode exhibits a notable increase in R_{ct}, rising from 21.6 Ω to 283.5 Ω over cycling, as detailed in **Table C4**. Besides, the R_s of the bare MnO_2 cathode fluctuates markedly during cycling, as shown in the inset of **Figure 6.12**d. This increase in impedance could potentially be related to the dissolution of cathode material or the formation of by-products (e.g., ZMO-P) on the cathode. This assertion is supported by the morphological changes observed in PM-MnO_2 cathode (**Figure C8**a) and bare cathodes (**Figure B3**) after cycling in the $ZnSO_4$/$MnSO_4$ electrolyte.

Rate capability is a key evaluation factor for batteries to enable practical manufacture in grid energy storage application. In addition to high-capacity retention and long cycle life, PM-equipped battery with $ZnSO_4$/$MnSO_4$ electrolyte exhibits exceptional rate performance (**Figure 6.12**f). The PM-equipped battery delivers average specific discharge capacities of 277.2, 263.8, 242.1, 192.0, 149.1, 118.5 and 96.14 mAh g^{-1} at current densities of 0.2 C, 0.5 C, 1 C, 2 C, 3 C, 4 C and 6 C, respectively. After reaching the high current density of 6 C, the average discharge specific capacity recovers to 234.8 mAh g^{-1} when returning to a low current density of 1 C. The PM-battery demonstrates approximately 97% capacity retention, significantly surpassing the bare one. Moreover, the GCD profile of the PM-equipped battery at elevated current densities is displayed in **Figure C9**.

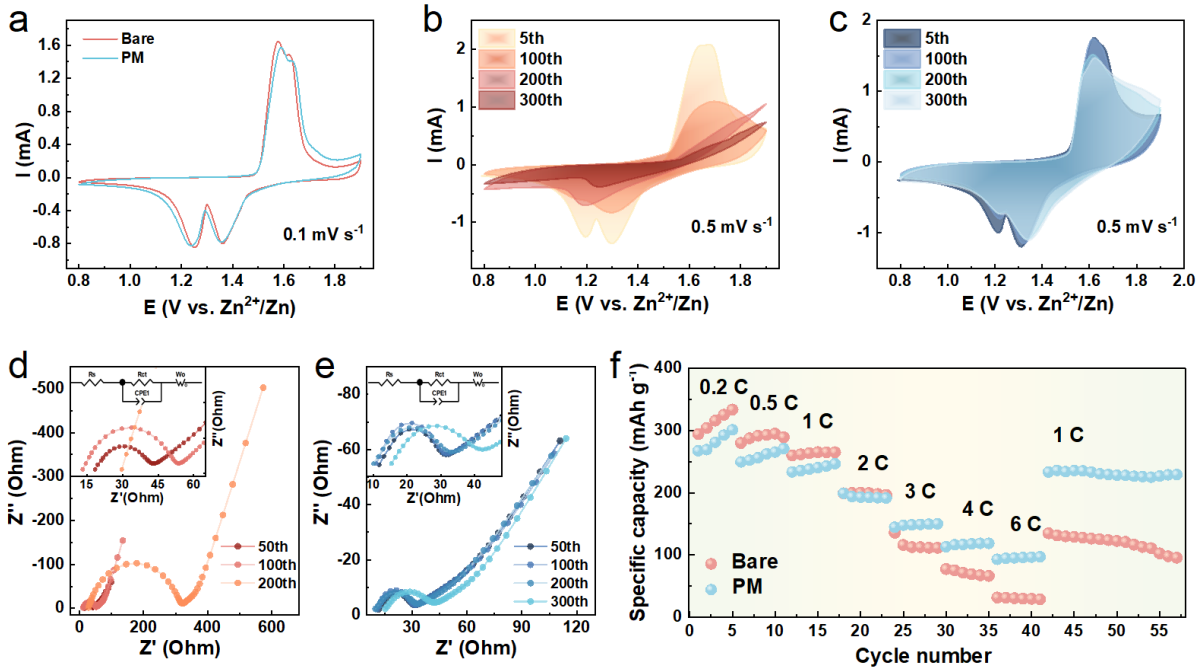


Figure 6.12. a) CV profiles of bare MnO_2 and PM-MnO_2 cathodes in 2 M $ZnSO_4$/0.2 M $MnSO_4$ electrolyte at 3rd cycle. CV profiles of b) bare MnO_2 and c) PM-MnO_2 cathode in 2 M $ZnSO_4$/0.2 M $MnSO_4$ electrolyte at selected cycle numbers. Nyquist plots of d) bare MnO_2 cathode and e) PM-MnO_2 cathode in 2 M $ZnSO_4$/0.2 M $MnSO_4$ electrolyte over the frequency range of 10 mHz-1 MHz. Insets are the enlarged profiles and equivalent circuit diagrams. f) Rate performance of bare MnO_2 and PM-MnO_2 cathodes in 2 M $ZnSO_4$/0.2 M $MnSO_4$ electrolyte.

This study delves into the detrimental effects of ionic crosstalk on electrode performance and unveils the transformative role of PM incorporation on the ionic behavior, as illustrated in **Figure 6.13**. Without the PM interface, unregulated Zn^{2+} ions migration from anode to cathode triggers irreversible phase transitions and the formation of densely ZMO-P. Concurrently, the transit of Mn^{2+} ions towards the anode exacerbates corrosion and causes uneven zinc deposition, compounding challenges. The integration of PM within the Zn-MnO_2 battery system introduces a noticeable shift, effectively mitigating the adverse consequences of Zn^{2+}/Mn^{2+} ionic crosstalk. The PM's enriched polarizable fluorinated functional groups, in synergy with its hierarchical porous architecture, masterfully regulate Zn^{2+} and Mn^{2+} ion fluxes. This strategic regulation fosters the in situ deposition of ZMO-S on the cathode and

restrains irregular dendrite growth on the anode, bolstering electrode durability and elevating the battery's electrochemical performance.

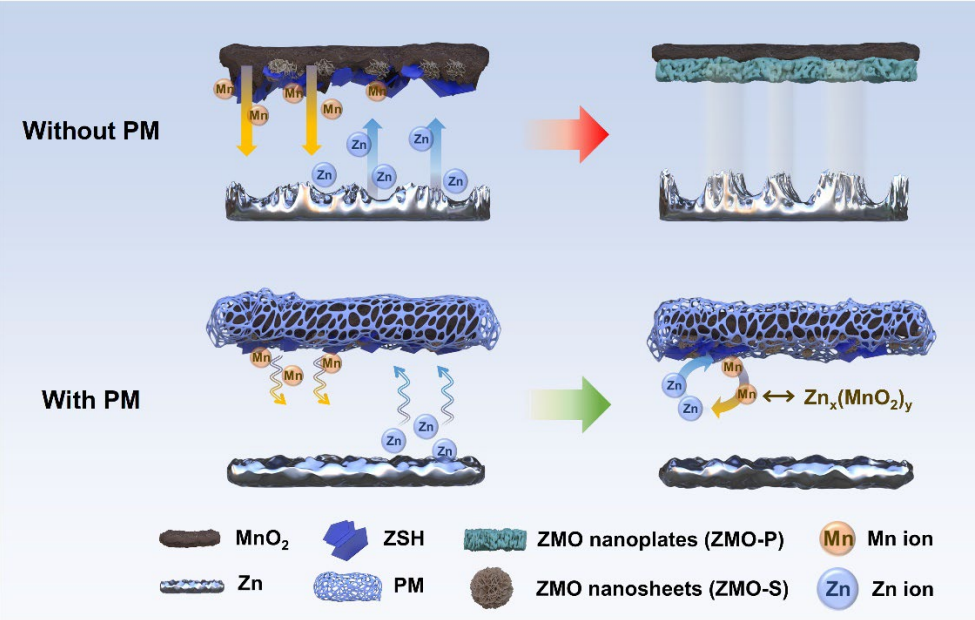


Figure 6.13. Schematic illustration of the PM function in the aqueous Zn-MnO_2 battery.

6.4. Conclusion

This study underscores the importance of ion-controlled transport mechanisms in augmenting electrode efficacy and overall battery performance. To address the ionic crosstalk issues in the aqueous Zn-MnO_2 battery, we utilized a PVDF-HFP-based porous membrane (PM) distinguished by its unique "ion-controlled release" capacity. The PM's design, featuring enriched polarizable fluorinated functional groups within a hierarchical porous framework, is instrumental in finely regulating ion flux, ensuring uniform ion distribution and control over the movement of Zn^{2+} and Mn^{2+} ions. The PM's hierarchical porous architecture acts as a refined sieve to enhance ion selectivity, while the fluorinated functional groups engage in strong interactions with the cations, stabilizing their movement and promoting a more uniform deposition pattern. This dual-action approach mitigates adverse crosstalk effects at the electrode interfaces, facilitating the targeted in situ generation of reactive ZMO-S on the cathode and ensuring even zinc deposition on the anode. As a result of these strategic interventions, the aqueous Zn-MnO_2 battery equipped with the PM exhibits a specific capacity of 187.7 mAh g^{-1} over 1000 cycles at a current density of 2 C, achieving a commendable capacity retention of 97%. Most importantly, the cycling performance of these batteries was highly reproducible, with average Coulombic efficiencies beyond 99.8% for three parallel cells and a minimal capacity deviation (±5.01 mAh g^{-1}). This advancement heralds a significant leap in the stability and longevity of such battery systems, charting a course towards more durable and reliable energy storage solutions. Further exploration into the fundamental mechanisms of ionic crosstalk phenomena will deepen our comprehension and aid in devising targeted strategies to counter the adverse effects, thereby propelling the advancement of Zn-MnO_2 batteries across various application fields.

Future in-depth investigations will be essential to refine this work:

(1) Investigating the pH variations in the cell in response to charging and discharging voltages could corroborate the assertion that the H^+ intercalation or MnO_2 dissolution reactions are inhibited. Moreover, besides exploring the ion concentration changes during

prolonged battery cycling, the Zn^{2+} and Mn^{2+} ion concentration changes within a single cycle warrants further study.

(2) While the origin of the active species (Zn^{2+} and Mn^{2+} ions) causing ionic crosstalk remains questionable, it is challenging to distinguish them from the electrolyte components (2 M $ZnSO_4$/0.2 M $MnSO_4$) necessary for the battery's operation. It is good to note that our experimental observations indicate a change in Mn^{2+} ion concentration, and the primary factor contributing to this change is the dissolution of MnO_2 material. To support our claim that the active species responsible for ionic crosstalk originate from the electrodes, it is crucial to also detect the concentration of Zn^{2+} ions.

(3) In addition, the amount of ZSH substance generated on the cathode during discharge should not be underestimated, thus it is essential to explore the role of the ZSH in the reversible reaction (ZMO-S dissolution/deposition) on the cathode and to determine its contribution to the overall capacity.

Chapter 7. Unlocking High-capacity Aqueous Zn-MnO_2 Batteries with Bismuth Oxide Surface Modification

7.1. Introduction

In the development of high-performance cathodes, one of the major challenges is achieving high material mass loading without compromising the electrode's electrochemical performance and stability. Increasing the mass loading of active materials in the cathode is desirable as it allows for higher energy density and capacity of the battery. However, this increase can lead to several performance issues. At higher mass loadings, the electrode may suffer from decreased electrical conductivity, poor ion diffusion, and reduced accessibility to the active material, which can impair the overall electrochemical performance[407–409]. Specifically, higher mass loading can result in longer ion diffusion paths, reduced effective surface area for electrochemical reactions, and increased resistance, which collectively diminish the charge and discharge rates and can lower the overall capacity and efficiency of the battery[407]. To address this challenge, recent studies have proposed several strategies for achieving high mass loadings in cathodes. These strategies include optimizing material synthesis through the use of nanostructured materials to enhance surface area and capacity, as well as improving conductivity by doping or coating with conductive agents, such as carbon black or graphene[410–413]. Advancements in electrode fabrication techniques, such as precise coating methods and the use of highly conductive binders, also contribute to achieving high mass loadings[414]. However, there are limitations to these approaches, as the synthesis of nanostructured materials can be complex with low yields, and conductive doping or coatings may not fully address stability issues and are costly. Additionally, improved fabrication techniques may fall short in preventing material dissolution or structural breakdown at high mass loadings.

In light of these limitations, surface modification of active materials has emerged as an effective method. Among various materials employed for surface modification, metal oxides

stand out for their chemical stability, conductivity, and facilitation of ion transport. Notably, coatings with titanium dioxide (TiO_2), cobalt oxide (Co_3O_4), and aluminum oxide (Al_2O_3) have been shown to substantially improve the cycle life and capacity of Zn-MnO_2 batteries[415–417]. However, these metal oxides offer potential advantages, they often require complex, costly synthesis methods that can impact scalability and uniformity. This complexity underscores the need for alternative materials that can be applied more efficiently. The utilization of Bi_2O_3 in modifying MnO_2 is particularly notable for its simplicity, eliminating the need for complicated structural or morphological control, and a tedious heat treatment process[266,418,419]. This approach enhances electrode performance and longevity while effectively supporting high mass loading, simplifying the battery scaling process, and demonstrating great potential for commercial applications.

The effectiveness of Bi_2O_3 in increasing mass loading while preserving cathode performance is grounded in several key mechanisms. The Bi_2O_3 coating enhances the electrical conductivity of the MnO_2 cathode[418], which is crucial for maintaining efficient electron transport even at increased mass loadings. Furthermore, Bi_2O_3 forms stable interfaces between MnO_2 and the electrolyte, preventing the excessive approach of Zn^{2+} ions and the subsequent formation of inactive by-products (e.g.,$Zn_x(MnO_2)_y$ substances), thus preserving the electrochemical activity of the electrode. Additionally, the Bi_2O_3 layer allows for the selective passage of H^+ ions, supporting the intercalation/de-intercalation reactions necessary for high mass loading while mitigating the dissolved Mn^{2+} ions into the electrolyte. Consequently, the Bi_2O_3-modified MnO_2 cathode can achieve high mass loading while maintaining stability, performance, and longevity, making it a highly effective material for high-capacity energy storage applications.

In this study, we significantly enhance the performance of MnO_2 cathode via a novel approach that integrates liquid-phase in situ encapsulation with a straightforward heat treatment, introducing a minimal amount yet effective Bi_2O_3 coating. This approach allows us to escalate the mass loading of the cathode material beyond 16 mg cm^{-2} and to apply a large

cell for its electrochemical evaluation. Notably, the Bi_2O_3-coated MnO_2 (BMO) cathodes demonstrate superior electrochemical performance, with a capacity retention of 72.7% after 330 cycles at 0.2 C, with an operational calendar life exceeding 60 days. Moreover, the high degree of consistency in performance demonstrated in multiple battery tests underscores the reliability of this cathode material. These testing results for high-capacity batteries serve as a pivotal step towards transitioning from laboratory-scale experiments to industrial application.

7.2. Experimental Methods

7.2.1. Cathode material synthesis

The Bi_2O_3-coated MnO_2 cathode material was prepared by liquid-phase in situ encapsulation with a straightforward heat treatment. Specifically, 3 wt.% of bismuth nitrate pentahydrate ($Bi(NO_3)_3 \cdot 5H_2O$, ≥98%) and 97 wt.% of β-MnO_2 were first ground for 10 minutes, then added to the ethanol solution and stirred continuously at 600 rpm for 12 hours at room temperature. The material was then washed several times with ethanol and DI water and dried overnight at 60°C. The dried material was ground into fine powder and subjected to calcination. It was heated in a muffle furnace to 500°C at a rate of 5°C min^{-1} and held for 2 hours to obtain the final modified product.

The modification of Al_2O_3 coating was carried out by sol-gel process. 3 wt.% aluminum nitrate nonahydrate ($Al(NO_3)_3 \cdot 9H_2O$, ≥98%) and stoichiometric ammonium hydroxide solution (NH_4OH, 30% NH_3 basis) were dissolved in ethanol solution with constant stirring. Subsequent to achieving a homogeneous solution, 97 wt.% of β-MnO_2 powder was slowly added into the mixture under vigorous stirring, which was maintained for 2 hours at 80°C. Throughout the process, the pH was consistently adjusted to approximately 8 by the addition of diluted NH_4OH solution. Following this, the mixture was dried at 60°C and subsequently subjected to calcination in air at 550°C for 4 hours, resulting in the formation of the Al_2O_3-coated material.

The TiO_2 coating was fabricated utilizing a thermotic-control approach. Initially, 97 wt.% of β-MnO_2 (0.97 g) along with 4 mL of NH_4OH solution were dispersed in 300 mL of ethanol under sonication for 30 minutes to ensure uniform dispersion. This was followed by the addition of 3 wt.% titanium butoxide (TNBT, 97%) (30 μL) to the above mixture, and the mixed solution was then reacted under magnetic stirring at 70°C for 1 hour. The precursor was washed with ethanol and dried at 60°C overnight. The dried precursor was then calcinated in air at a temperature of 500°C for 2 hours to obtain the TiO_2-coated sample.

The ε-MnO_2 was synthesized by co-precipitation followed by calcination. Specifically, 200 mL 1.05 M sodium carbonate (Na_2CO_3, ≥99.5%) solution and 200 mL 1.00 M $MnSO_4$ solution were gradually added to 30 mL of ethanol under continuous stirring, followed by stirring at 600 rpm for 2 hours, and then standing for 2 hours. Afterwards, the precursor ($MnCO_3$) was washed several times with DI water and ethanol, respectively. The washed sample was dried under vacuum at 60℃ overnight. The dried precursor was calcined in a muffle furnace at 410℃ for 8 hours to obtain ε-MnO_2.

7.2.2. Cathode fabrication and battery assembly

High mass-loading cathode fabrication

A slurry containing 80 wt.% active material (e.g., β-MnO_2), 5 wt.% AB, 5 wt.% sphere-like graphite powders (KS-6) and 10 wt.% PVDF was prepared in NMP solution. This slurry was uniformly coated onto the conductive PE film by a doctor blade technique. The cathode sheets were then vacuum dried overnight at 60°C and used for coin-type cells with a thickness of 400 μm and for large cells with a thickness of 650 μm. It should be noted that the mass loading of the active material in each coin-type cell was approximately 9.0±0.1 mg cm^{-2} (mass of cathode material in each cell is >10 mg), and in each large cell was over 16 mg cm^{-2}.

Large (iron-plate) battery assembly

Large batteries or iron plate batteries were assembled with a cathode sheet (2.5 cm×3 cm), double-layered AGM (4 cm×4 cm) as separator between cathode and anode, and Zn foil (3

cm×3 cm, thickness: 0.1 mm) as anode, and tightened with screws. The electrolyte amount for large battery is approximately 1.5 mL.

Other experimental methods

The processes for coin-type battery assembly, material characterization techniques, and electrochemical testing follow the descriptions provided in **Chapter 3**; therefore, detailed descriptions are omitted here. It should be noted that the voltage range of the full cell test is 0.8-1.9 V. The cycling tests were performed at a current density of 1 C and 2 C, where 1 C=0.25 A g^{-1}. The 2 M $ZnSO_4$/0.2 M $MnSO_4$ electrolyte with pH=4.0±0.1 was applied in this work.

7.3. Results and Discussion

7.3.1. Cathode material characterization

The nanowire structure of the cathode material is shown in **Figure 7.1**a, the elemental mapping shows that bismuth (Bi) elements are uniformly distributed on the MnO_2 nanowires. Moreover, the XRD spectra of the modified MnO_2 material (**Figure 7.1**b) reveal the presence of (200) diffraction peak representing Bi_2O_3, confirming the successful incorporation of the Bi_2O_3 coating without altering the crystal structure of the pristine MnO_2. The XPS spectrum in **Figure 7.1**c provides valuable information regarding the elemental composition and the chemical states of the elements present. Peaks corresponding to Bi, Mn, O, and other elements are visible, confirming the presence of bismuth in the material, which further substantiates the successful implementation of the surface modification from the EDS and XRD analyses. In the detailed analysis of the high-resolution scans for the Bi 4f and O 1s peaks, a fitting approach employing the Gaussian-Lorentzian distribution was applied. **Figure 7.1**d illustrates the spectrum for the Bi 4f core level, revealing two distinct spin-orbit doublet peaks (J = 5/2 and 7/2) positioned at 164.4 (Bi $4f_{5/2}$) and 159.1 eV (Bi $4f_{7/2}$), respectively. The observed separation of 5.3 eV between these peaks aligns with previously reported findings, thereby substantiating the presence of Bi in its +3 oxidation state Bi(III)[420–422]. Moreover, peaks at

164.7 eV and 159.4 eV are associated with the Bi(V) states. The analysis of the O 1s spectrum, as depicted in **Figure 7.1**e, was conducted by fitting it into three distinct peaks. The peak at 529.5 eV corresponds to lattice oxygen (O_{Latt}), whereas the peak at 531.3 eV is attributed to chemisorbed oxygen (O_{Surf})[423–425]. This differentiation supports the formation of a Bi_2O_4 interphase, incorporating both Bi(III) and Bi(V) and characterized by the presence of oxygen vacancies. Literature suggests that such oxygen deficiencies are conducive to enhancing the charge transfer process[426]. Lastly, the peak at 533.6 eV is identified with hydroxyl groups[421,423,424]. Thus, binding energies are consistent with the expected values for the oxidation states of the elements in Bi_2O_3 and MnO_2, suggesting that the Bi_2O_3 coating layer is chemically bonded to the MnO_2 surface. This is critical, as it implies not only a physical coating but also potential changes in the electrochemical properties due to the interaction between Bi and MnO_2. Furthermore, to validate the superiority of the coating material Bi_2O_3 over other metal oxides, we also synthesized Al_2O_3- (AMO) and TiO_2-modified (TMO) cathode materials concurrently. The morphology, elemental analysis and composition, and crystallinity of these materials are presented in **Figure D1**, **Figure D2** and **Figure D3**.

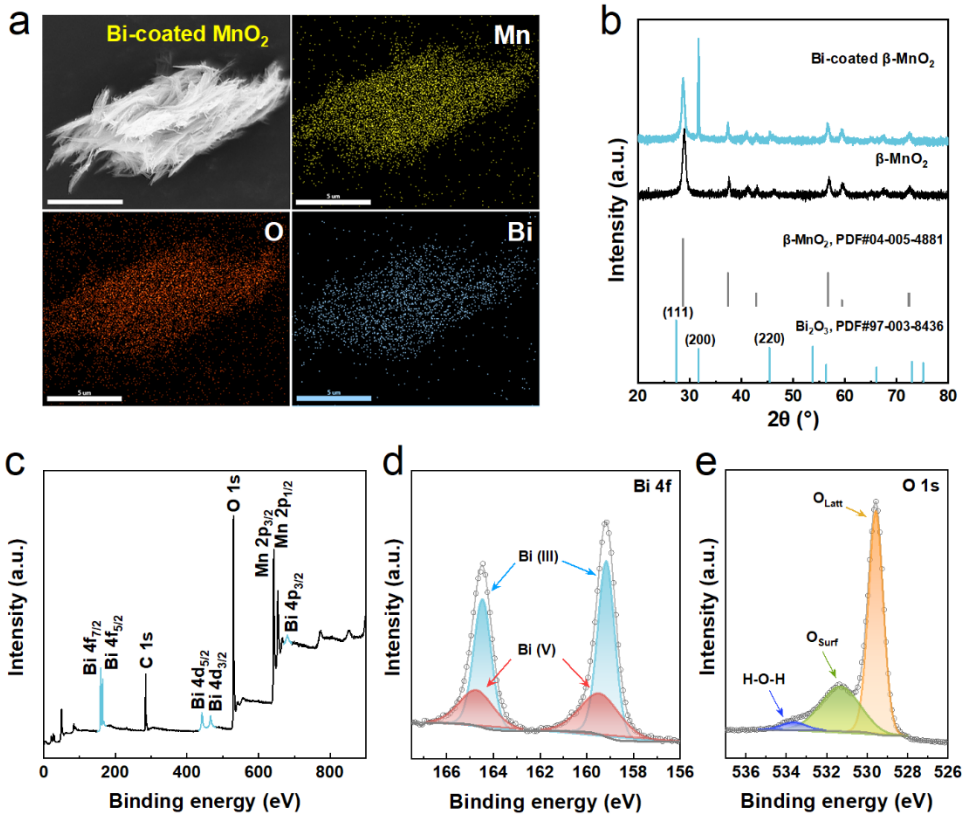


Figure 7.1. a) Morphology and EDS elemental mapping of Bi-coated MnO_2 nanowires. Scale bar: 5 µm. b) XRD patterns of Bi-coated MnO_2 nanowires. Bismuth trioxide (Bi_2O_3, PDF#97-003-8436), β-MnO_2 (PDF# 04-005-4881). XPS spectra of the BMO sample: c) a survey spectrum, d) Bi 4f and e) O 1s.

7.3.2. Coin-type cell electrochemical performance

Figure 7.2a presents a comparative analysis of the electrochemical cycling behavior of β-MnO_2 and Bi-coated (BMO) cathodes at 0.2 C. Notably, the mass loading of the active material on these cathodes employed for coin-type battery testing exceeded 9 mg cm^{-2}, which is considerably higher than the typical 1-3 mg cm^{-2}. The β-MnO_2 cathode, denoted by orange markers, manifests a discernible decay in capacity after a mere 10 cycles. Conversely, the BMO cathode, indicated by blue markers, consistently sustains a specific capacity exceeding 200 mAh g^{-1} within 50 cycles, underlining the bolstered stability and electrochemical efficiency attributable to the Bi_2O_3 coating layer. Post-initial fluctuations, the Coulombic efficiency of the BMO cathode converges towards stability, a phenomenon frequently observed as electrochemical systems undergo conditioning in the initial cycles at a lower

current density. Distinctive electrochemical behaviors between the β-MnO_2 and BMO cathodes are further delineated in **Figure 7.2**c and **Figure 7.2**d. Specifically, the β-MnO_2 cathode showcases voltage plateaus that undergo a pronounced decline within 50 cycles, suggestive of the electrode's structural deterioration. In stark contrast, the BMO cathode exhibits significantly sustained discharge plateaus, thereby demonstrating excellent capacity retention over repeated cycles. Under the stress of an elevated current rate of 1 C (**Figure 7.2**b), the BMO cathode maintains superlative cycling performance, retaining a specific capacity markedly superior to that of the β-MnO_2 cathode, and demonstrating minimal capacity degradation over 150 cycles. Furthermore, the BMO cathode consistently exhibits a Coulombic efficiency nearing 99.5%, indicative of the high reversibility of its electrochemical reactions through consecutive charging and discharging processes. In addition, the CV profile of the β-MnO_2 cathode in **Figure D4**a elucidates broadened redox peaks alongside diminished response currents, indicating sluggish electrochemical kinetics and compromised reversibility inherent to the redox processes. This observation aligns with the reduced specific capacity and the downward trend in Coulombic efficiency presented in **Figure 7.2**a. Conversely, the BMO cathode displays well-defined and symmetrical peaks, signifying enhanced reversibility in the electrochemical reactions, which is congruent with its consistent Coulombic efficiency.

To substantiate the electrochemical preeminence of the Bi_2O_3 coating relative to alternative metal oxides, cathode materials modified with Al_2O_3 (AMO) and TiO_2 (TMO) coatings were also synthesized and evaluated. As illustrated in **Figure D4**b, the AMO cathode exhibits less defined and asymmetric peaks, suggesting that this cathode material undergoes a poor electrochemical performance. The TMO cathode, on the other hand, exhibits more conspicuous and symmetric redox peaks, reflecting a higher degree of electrochemical reactivity and reversibility in the preliminary cycles. However, the subsequent cycling tests in **Figure D4**c indicate that the TMO cathode, despite an initially high capacity, then suffers a rapid capacity decline, culminating in complete failure after 20 cycles. This phenomenon was replicated across multiple cells composed with the TMO cathode, and its deficient cycling performance at 1 C (**Figure D4**d) suggests that the electrochemical stability of TMO cathodes

is inferior to that of BMO cathodes. Therefore, these results demonstrates that the application of Bi_2O_3 as a coating material substantially elevates the electrochemical properties of MnO_2 cathode materials, surpassing other metal oxide coatings by engendering improved charge-discharge reversibility.

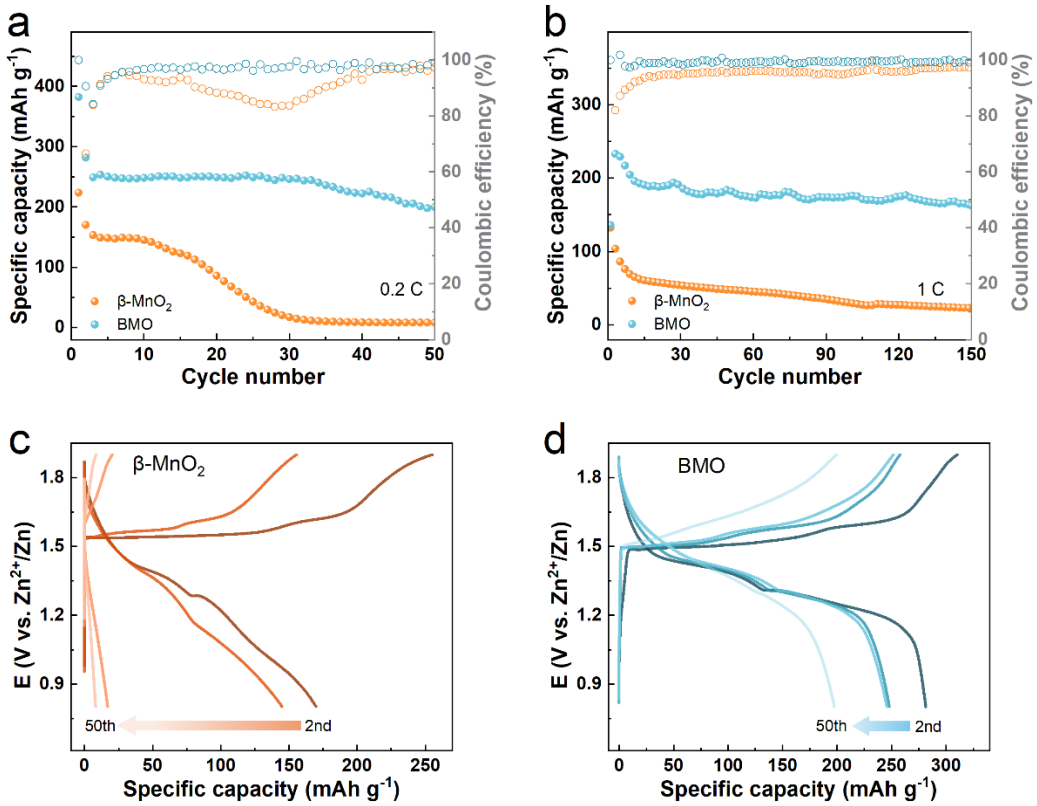


Figure 7.2. Cycling performance of β-MnO_2 and BMO cathodes in 2 M $ZnSO_4$/0.2 M $MnSO_4$ electrolyte at a) 0.2 C and b) 1 C. The active material mass loading is around 9 mg cm^{-2}. The charging/discharging plateaus of c) β-MnO_2 cathode and d) BMO cathode in 2 M $ZnSO_4$/0.2 M $MnSO_4$ electrolyte at 0.2 C.

The cycling stability of cathodes is additionally reflected in the integrated area under their CV curves. In **Figure 7.3**a**,** the β-MnO_2 cathode exhibits a notable peak broadening coupled with a decline in response current as the cycles progress. Such phenomena may be ascribed to the dissolution of the active material and the concomitant formation of by-products (e.g., $Zn_x(MnO_2)_y$ nanoplates) on the cathode surface, which is due to repeated electrochemical reactions, thereby precipitating capacity decay. In comparison, the CV profiles of the BMO cathode (**Figure 7.3**b) maintain a commendable consistency in peak shape and integral area

over multiple cycles, indicating a superior electrochemical stability. The minimal alterations in peak response currents and the relative constancy of peak positions underscore a transition towards a more reversible electrochemical process, with concomitantly lower degradation of the electrode material. These observations postulate that the Bi_2O_3 coating serves as a protective barrier, mitigating the irreversible transition of the active material and facilitating more effective electron transfer pathways during redox process. After 100 cycles, a slight weakening of the response current was observed. This alteration could stem from the formation of new substances on the cathode surface or a phase transition that affects the migration of ions. Nyquist plots provide further information for a comprehensive understanding of the electrochemical behavior of cathode materials in aqueous batteries, imperative for elucidating their electrochemical attributes. For the β-MnO_2 cathode, as seen in **Figure 7.3**c, the R_{ct} incrementally expands throughout cycling, originating at 16.7 Ω in the 10th cycle and surging to 147 Ω by the 200th cycle (**Table D1**). This substantial rise indicates a degradation in electrochemical kinetics, possibly due to the formation of $Zn_x(MnO_2)_y$ nanoplates on the cathode, thus impeding charge transfer processes. In contrast, the BMO cathode (**Figure 7.3**d) maintains notable stability in R_{ct} within cycles from 10th to 200th, implying a consistent charge transfer capabilities throughout cycling. Noteworthy is the BMO cathode's display of an additional semicircle within the Nyquist plot, suggestive of interfacial impedance (R_i). This feature, when integrated with findings from XPS results (**Figure 7.1**), intimates the existence of a distinct coating layer or interface which modulates charge transfer dynamics. The stable nature of the BMO cathode's interphase, alongside its consistent R_i values, implies an intact interfacial structure that facilitates reliable cycling performance. Conversely, the AMO cathode, as shown in **Figure D5**a, reveals the vanishing of the R_i as early as the 50th cycle, presumably implicating the deterioration or compromise of the Al_2O_3 coating. This implies that the Al_2O_3 coating exhibits electrochemical instability within a limited cycling regime, potentially exacerbating the cathode material's direct exposure to the electrolyte, which could hasten material dissolution and irreversible phase transitions, thereby shortening the cycle life and degrading the performance of the electrode. For the TMO

cathode (**Figure D5**b), an initial constancy in R_i is observed within the first 50 cycles. Nevertheless, a considerable increase in R_i is detected at 100th cycle. This change likely signifies an alteration in the TiO_2 coating, possibly due to the attenuation in its structure. Such evolution eventually results in the disappearance of the interface layer and a significant growth in the R_{ct} by the 200th cycle, reflecting a compromise of the TiO_2 coating layer, which is critical in preserving the integrity and conductivity of the electrode. Therefore, the Bi_2O_3 coating layer coating layer exemplifies unparalleled endurance and electrochemical stability, which corroborates sustained operational performance and extended lifespan, underpinned by a consistent charge transfer resistance and robust interface.

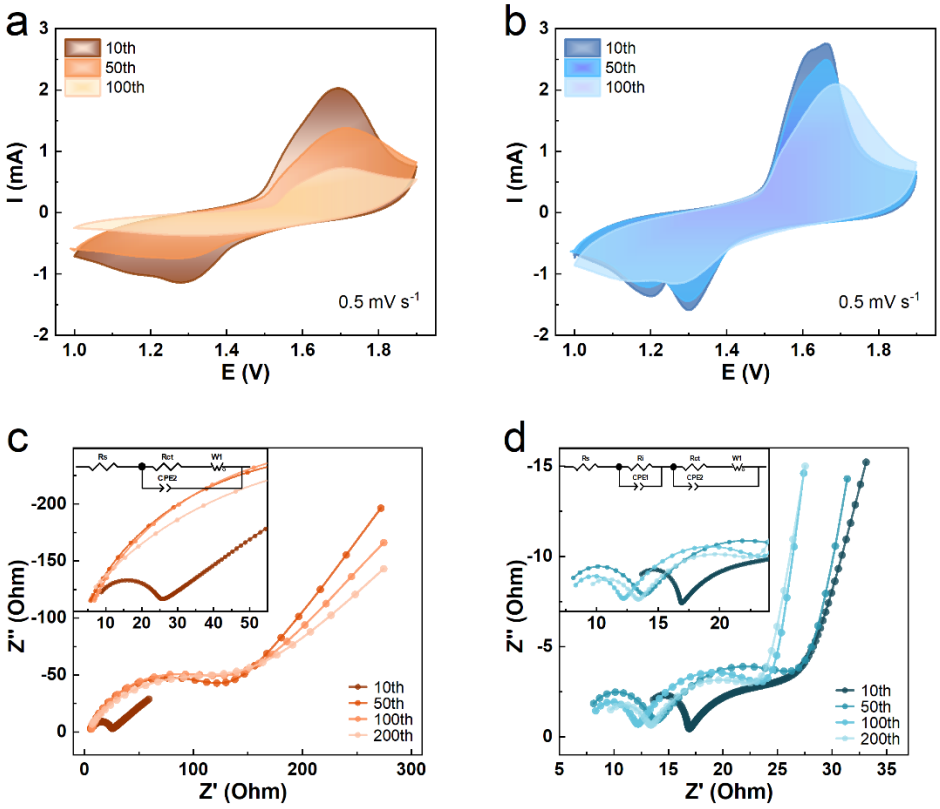


Figure 7.3. CV profiles of a) β-MnO_2 and b) BMO cathodes at determined cycle numbers, with a scan rate of 0.5 mV s^{-1}. Nyquist plots of c) β-MnO_2 and d) BMO cathodes in 2 M $ZnSO_4$/0.2 M $MnSO_4$ electrolyte over the frequency range of 100 mHz-1 MHz at selected cycles. Inset is the corresponding equivalent circuit diagram.

The depiction of cycling performance accompanied by standard deviation, as illustrated in **Figure 7.4**a and **Figure 7.4**b, offers quantifiable insights into the reproducibility and

reliability of cells outfitted with BMO cathodes. These standard deviations were calculated based on three cells under identical test conditions. At a current rate of 1 C, the cells exhibit a slight decrease in specific capacity during the initial cycles, thereafter maintaining the specific capacity of over 130 mAh g^{-1} after 200 cycles, and the average capacity deviation is approximately ±6.50 mAh g^{-1} which underscores an excellent battery reproducibility. Concurrently, the average Coulombic efficiency is maintained around 99.4%, indicating efficient charge-discharge processes and minimal propensity for irreversible capacity loss of the BMO cathode. In addition, a plateau in capacity is observed subsequent to the initial tens of cycles at 2 C, insinuating that the cathode structure attains an equilibrium state promptly, even under the stress of doubled current load. Despite the initial drop in capacity, the material exhibits a capacity retention surpassing 80% after 1000 cycles, which is a positive indicator for long-term use. The Coulombic efficiency at 2 C also merits attention; despite exhibiting some fluctuations during the initial 20 to 30 cycles, it predominantly remains above 99% with an average over 1000 cycles noted at 99.8±0.2%. The data points and average values for specific capacities and Coulombic efficiency of the Zn-BMO cells are detailed in **Figure D6** and **Table D2**. This is a salient consideration for practical applications of RAZBs, as higher mass loadings correlate to higher energy densities, making the material more suitable for real-world energy storage solutions. The exceptional cycling reproducibility and elevated Coulombic efficiency at such significant mass loadings reinforce the potentiality of the BMO cathode for industrial-scale battery applications. When compared with other recently reported Zn-MnO_2 batteries as shown in **Figure 7.4**c, our battery delivers a relatively large capacity (1.94 mAh) at a higher mass loading. Moreover, our cells demonstrate endurance over 1000 cycles under a comparable current density (2 C), equating to 1.43 times the longevity of comparative batteries. This underscores the efficacy of the Bi_2O_3 coating in preserving cathode integrity through repeated cycling, synonymous with reduced capacity loss and bolstered long-term stability, which are desirable attributes for battery materials in practical applications.

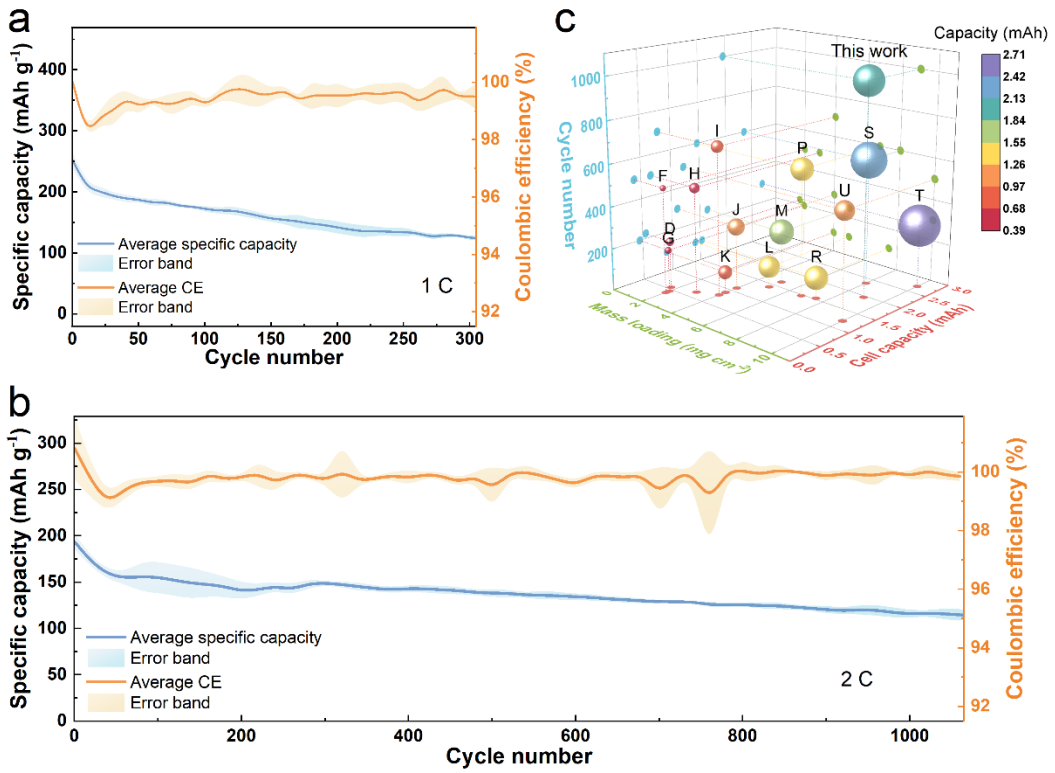


Figure 7.4. Cycling performance of BMO cathode in 2 M $ZnSO_4$/0.2 M $MnSO_4$ electrolyte at a) 1 C and b) 2 C. The standard deviations in these plots are calculated based on three cells. c) The comparison of cell cycle number, active material mass loading with recently reported coin-type Zn-MnO_2 batteries. More details are listed in **Table D3**.

7.3.3. Large cell electrochemical performance

Large batteries (**Figure 7.5**a) are indispensable for practical applications, the necessity of which stems from the demand for batteries that are not only capable of high energy storage but also exhibit stable and durable performance. Hence, evaluating the performance of cathode materials in large batteries or iron-plate batteries is critical for advancing the field of aqueous battery technology. In an effort to validate the viability of BMO cathodes for large-scale energy storage, a series of electrochemical evaluations were performed using BMO and β-MnO_2 cathodes with a 2 M $ZnSO_4$/0.2 M $MnSO_4$ electrolyte. As illustrated in **Figure D7**, the BMO cathode displays excellent stability with a specific capacity of 401.8 mAh g^{-1} at 0.2 C, achieving a capacity retention of 93.0% after 70 cycles. It is paramount to note that these tests were executed with material mass loadings in excess of 9 mg cm^{-2}, with the active material on the cathode surpassing 65 mg—a sextuple increment relative to the mass

employed in previous electrochemical assessments using button-type cells. The relatively stable cycling performance of the BMO cathode, particularly in comparison to the β-MnO_2 cathode, implies that the Bi_2O_3 coating technology has the potential to be scaled up. This is particularly evident when considering the battery calendar life (**Figure 7.5**b), where the Zn-BMO cell demonstrates a superior cell capacity of over 20 mAh after a 50-day operational period, highlighting the protective efficacy of the Bi_2O_3 coating in the preservation of cathode material. This layer proves instrumental not merely in mitigating material dissolution but also in the effective suppression of detrimental side reactions, thus augmenting the overall performance and longevity of the battery. Charge/discharge profiles (**Figure 7.5**c) further corroborate the BMO cathode's ability to maintain the electrochemical plateaus, indicative of robust reversibility and electrochemical stability, both of which are vital for long-term battery operation. Remarkably, even with a material mass loading amplified to over 16 mg cm^{-2}, the BMO cathode sustains a commendable capacity over prolonged cycling (**Figure 7.5**d). With an active material mass exceeding 120 mg, the cell exhibits a capacity retention of 72.7% over 60 days (equivalent to 330 cycles), thereby showcasing the practicability of employing BMO cathodes with elevated mass loading without considerable degradation in capacity retention. Such findings solidify the prospective integration of BMO cathodes into high-demand energy storage systems.

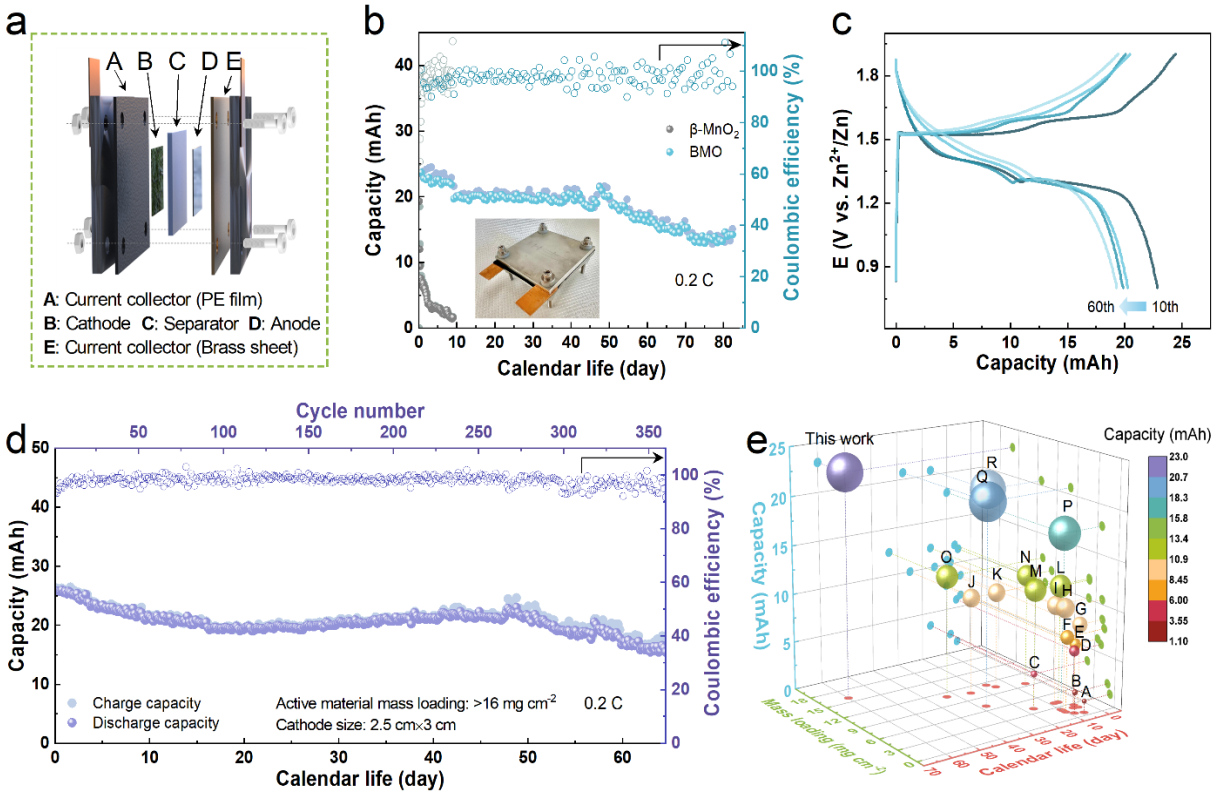


Figure 7.5. a) Internal view of the large battery. b) Cycling performance of β-MnO_2 and BMO cathodes in 2 M $ZnSO_4$/0.2 M $MnSO_4$ electrolyte at 0.2 C. The active material mass loading >9 mg cm^{-2}. c) The corresponding charging/discharging plateaus. d) Cycling performance of the BMO cathode in 2 M $ZnSO_4$/0.2 M $MnSO_4$ electrolyte at 0.2 C. The active material mass loading >16 mg cm^{-2}. e) The comparison of cell calendar life, active material mass loading and cell capacity with recently reported zinc-ion batteries. More details are listed in **Table D4**.

A comparative evaluation with existing zinc-ion battery technologies brings the exceptional attributes of the BMO cathode to the fore, showcasing its superior cell capacity and exceptional calendar life. This performance is markedly evident under conditions of increased mass loadings, as illustrated in **Figure 7.5**e. The minimal standard deviation in cycling performance for multiple cells in **Figure 7.6** demonstrates the reproducibility and reliability of this BMO cathode, factors which are imperative for its commercialization and practical application. Moreover, the Coulombic efficiency of these cells (**Figure D8**b) not only consistently remains at an elevated level but also exhibits a progressive improvement

during operation, highlighting the electrochemical capability of the cells and signifying a pronounced mitigation of side reactions.

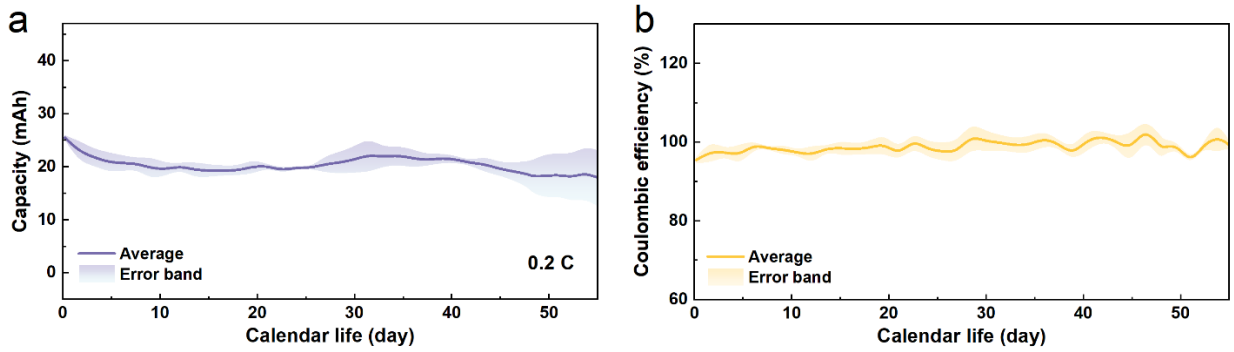


Figure 7.6. The standard deviations of a) cycling performance and b) Coulombic efficiency of BMO cathodes in 2 M $ZnSO_4$/0.2 M $MnSO_4$ electrolyte at 0.2 C. The active material mass loading >16 mg cm^{-2}. These plots are calculated based on three cells.

Building upon these advancements, we have extended this modification technique to other polymorphs of MnO_2 (e.g., ε-MnO_2), which also shown significant improvements in cycling performance. As demonstrated in **Figure 7.7**a, the ε-MnO_2 cathode material modified with Bi_2O_3 coating (denoted as BMO (ε)) maintains a discharge specific capacity of about 160 mAh g^{-1} after 100 cycles in a coin-type cell. Moreover, in **Figure D9**, the cycling results of multiple cells exhibit excellent consistency with a small capacity deviation of ±6.00 mAh g^{-1}. In a large battery, it reaches a cell capacity of 26.6 mAh when tested at 0.5 C with a considerable mass loading of over 20 mg cm^{-2}, and achieves a capacity retention of over 80% after 400 cycles (**Figure 7.7**b). Notably, further increasing the current rate to 2 C and 5 C resulted in batteries showing 90% capacity retention (1200 cycles, **Figure 7.7**c) and 70% capacity retention (2700 cycles, **Figure 7.7**d), respectively.

The adoption of BMO cathodes engenders the creation of batteries boasting the amplified energy storage capacities requisite for more exigent applications, which could contribute to the broader acceptance of aqueous batteries in sectors that demand resilient energy solutions, including grid storage, electric vehicles, and portable electronic devices. Furthermore, our research has the potential to energize continued research into cathode designs with high mass loading, thereby fostering the transition toward aqueous battery

systems that offer a more sustainable and safer alternative to conventional lithium-ion counterparts.

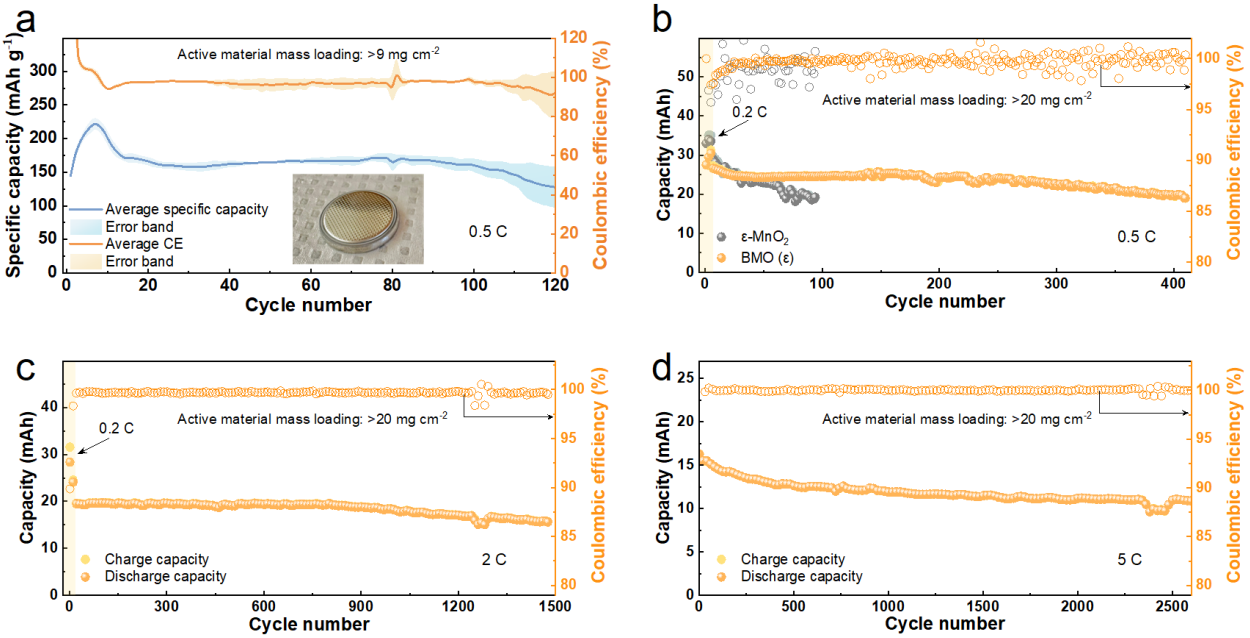


Figure 7.7. a) The standard deviations of cycling performance of BMO (ε) cathodes in coin-type batteries at 0.5 C. The active material mass loading >9 mg cm^{-2}. The standard deviation in this plot is calculated based on three cells. Cycling performance of ε-MnO_2 and BMO (ε) cathodes in large batteries with 2 M $ZnSO_4$/0.2 M $MnSO_4$ electrolyte at the current densities of b) 0.5 C, c) 2 C and d) 5 C. The active material mass loading >20 mg cm^{-2}.

7.4. Conclusion

In this study, we employ a straightforward in situ encapsulation technique to adeptly fabricate Bi_2O_3-coated MnO_2 cathode materials, thereby significantly increasing the mass loading of cathode material from the typical 1-3 mg cm^{-2} to 9 mg cm^{-2}. Electrochemical assessments conducted on coin-type cells reveal that the BMO cathode material demonstrates exceptional electrochemical performance, particularly in terms of cycle stability and Coulombic efficiency—key indicators of viability for high-energy-density battery applications. To further investigate the high mass loading characteristics of the BMO cathode, we assess the cycling performance of BMO cathodes in larger battery configurations, enhancing the mass loading to a surprising 16 mg cm^{-2}. This progression to larger batteries is crucial, offering a more realistic approximation of the operational conditions faced by energy storage systems. The BMO cathode maintains its superior electrochemical properties observed in the smaller coin cells and exhibits an exceptional capacity to endure the heightened demands of increased mass loadings. Specifically, it displays a notable capacity retention of 72.7% over 330 cycles (equivalent to a 60-day operational calendar life), underscoring its potential to operate effectively under the high-energy demands typical of industrial-scale applications.

These findings highlight the promising potential of BMO cathodes in advancing aqueous Zn-MnO_2 battery technology. The cathode's ability to uphold high specific capacities and its electrochemical and structural integrity at increased mass loadings heralds a new era in the development of high-performance aqueous zinc-ion batteries. Such batteries, enhanced with BMO cathodes, are well-positioned to meet the escalating demands for sustainable and dependable energy storage solutions, particularly in areas where energy density and durability are critical. Moreover, the significance and utility of reproducibility experiments in this context cannot be overstated. These experiments are instrumental in validating the consistency, reliability, and scalability of the Bi_2O_3 coating technology. By demonstrating reproducible results in multiple tests, it not only affirms the feasibility of the Bi_2O_3 coating

approach, but also strengthens confidence in the potential for commercialization and widespread application of this technology. This commitment to reproducibility lays a solid foundation for the advancement of aqueous battery systems and signifies a meaningful step towards influencing the future of sustainable energy storage solutions.

To further demonstrate the great potential of this surface modification technique, we plan to extend its application to other MnO_2 polycrystals, including α-MnO_2, γ-MnO_2, and δ-MnO_2. We will conduct a series of electrochemical performance evaluations using coin-type batteries, large batteries, and pouch batteries to showcase the superiority of BMO cathode materials.

Chapter 8. Conclusion and Future Work

8.1. Conclusion

In this thesis, we present a comprehensive exploration of innovative strategies aimed at enhancing the performance and stability of vanadium-based and manganese-based cathode materials. Each project delves into the synthesis, characterization, and optimization of cathode materials for aqueous zinc-ion batteries. Through these studies, we not only achieve significant improvements in battery capacity and cycling stability but also offer new insights into the underlying mechanisms influencing ion transport and electrode interactions.

The research in Chapter 4 pioneers the development of a robust rechargeable Zn-vanadium battery system, featuring a highly reversible Zn^{2+}/Na^{+} co-intercalation mechanism within vanadium-based cathodes, specifically $Zn_{0.3}Na_{0.43}V_2O_5$ (ZNVO). By addressing the longstanding issue of cathode material dissolution, our work significantly enhances battery stability. The synthesis of ZNVO cathodes employs a pre-intercalation technique, yielding an optimized material that demonstrates an exceptional discharge capacity of 350 mAh g^{-1} at 1 C rate, significantly outperforming existing vanadium-based counterparts. Utilizing a 1 M $ZnSO_4$/1 M Na_2SO_4 electrolyte, the system achieves dual-ion intercalation, which is essential for superior electrochemical performance. Electrochemical assessments reveal a sequential intercalation and de-intercalation process of Na^{+} and Zn^{2+} ions, maintaining over 90% capacity after 4000 cycles as well as achieving a discharge capacity of 209 mAh g^{-1} at 5 C. This co-intercalation strategy, applicable to various vanadium oxides, demonstrates scalability and potential for high-capacity energy storage applications, evidenced by the successful fabrication and testing of larger 9 mAh cells.

In Chapter 5, we illuminate the intricate dynamics of ionic crosstalk of Mn^{2+} and Zn^{2+} ions within the aqueous Zn-MnO_2 battery system, elucidating a previously underexplored mechanism critical to battery performance. Through a multifaceted analytical approach, including *in situ* optical visualization and XRD, we reveal how Mn^{2+} migration from the

MnO_2 cathode to the Zn anode influences zinc deposition and promotes dendritic growth. This Mn^{2+} ionic crosstalk exacerbates anode corrosion, deteriorates anode surface morphology, and increases the risk of internal short-circuiting of the battery. In addition, we discover a rapid formation of zinc sulfate hydroxide (ZSH) on the cathode driven by Zn^{2+} ions stripped from the anode, which continues to crosstalk the cathode and results in an irreversible phase transition in the cathode material. This research highlights the profound effect of Zn^{2+}/Mn^{2+} ionic crosstalk on the counterpart electrodes' electrochemical performance, offering significant insights into overcoming the challenges hindering its advancement towards practical energy storage solutions.

To address the ionic crosstalk phenomenon, in Chapter 6, we adopt a porous membrane (PM) based on PVDF-HFP for ion-controlled release and elucidate its key role in mitigating the ionic crosstalk and improving the performance of aqueous Zn-MnO_2 batteries. The PM, characterized by its hierarchical porous structure and fluorinated functional groups, enables ion flux regulation and ensures uniform distribution of Zn^{2+} and Mn^{2+} ions in the vicinity of the electrode. This not only counters the detrimental effects of ionic crosstalk at electrodes but also promotes uniform zinc deposition on the anode and targeted reactive $Zn_x(MnO_2)_y$ nanosheets (ZMO-S) generation on the cathode. The incorporation of PM results in a battery that delivers an exceptional specific capacity of 187.7 mAh g^{-1} at 2 C, with a capacity retention of 97% and Coulombic efficiency of over 99.8% after 1000 cycles.

In Chapter 7, we introduce a novel in situ encapsulation strategy for fabricating Bi_2O_3-coated MnO_2 (BMO) cathode materials, achieving an unprecedented mass loading of up to 9 mg cm^{-2}, far exceeding the typical 1-3 mg cm^{-2}. Our electrochemical evaluation in coin-type and larger battery configurations showcases the BMO cathode's exceptional electrochemical performance, including excellent cycle stability and Coulombic efficiency. Notably, in large battery testing, the BMO cathode exhibits 72.7% capacity retention after 330 cycles (equivalent to a calendar life of 60 days) with a mass loading of 16 mg cm^{-2}. This significant enhancement in mass loading capacity without compromising electrochemical stability or

performance underscores the BMO cathode's potential for high-energy-density aqueous Zn-MnO_2 battery applications. Furthermore, rigorous reproducibility experiments confirm the consistency and reliability of this surface modification technique, bolstering the feasibility of scaling up this technology for industrial applications. Such advancement represents a critical step towards meeting the growing demand for sustainable, high-performance energy storage solutions.

Throughout my PhD research, I have explored two distinct cathode materials, each with its own unique set of challenges and breakthroughs. However, it is the manganese-based cathode materials that stand out as the most significant contribution of my work. The advancements made in understanding and optimizing manganese-based electrodes have not only demonstrated superior performance characteristics but also provided valuable insights into the underlying crosstalk mechanisms. This work has the potential to significantly impact the development of more efficient and sustainable battery technologies.

8.2. Future Work

In practical applications, identifying cathode materials that exhibit both prolonged cycle life and consistent performance remains a significant challenge. Rechargeable aqueous zinc-ion batteries (RAZBs) face several obstacles in their adoption for large-scale energy storage applications:

(1) The discharge voltage platform for RAZBs typically ranges between 0.6-1.8 V, considerably lower than the 3.2-5.0 V range observed in lithium-ion batteries, and a narrow electrochemical window (~1.23 V) which significantly impacts the energy density (unit: Wh kg^{-1}) that can be achieved.

(2) The energy density of RAZBs, at 70-140 Wh kg^{-1}, is substantially below that of lithium-ion batteries (200-300 Wh kg^{-1} for commercial use), limiting their competitiveness in energy-intensive applications.

(3) Another significant drawback of RAZB is their poor performance at low temperatures. The low-temperature performance of RAZB is primarily compromised by the reduced ionic conductivity of the electrolyte at lower temperatures, leading to slower ion migration and impaired electrochemical reactions. Consequently, the capacity and power output of aqueous batteries are diminished at lower temperatures, leading to reduced efficiency and performance.

(4) Side reactions on electrodes are a critical issue that severely affects the battery performance. The occurrence of hydrogen evolution reaction (HER) and oxygen evolution reaction (OER) in RAZBs leads to the depletion of aqueous electrolytes, further affecting the battery's efficiency and operational lifespan.

Despite these limitations, RAZBs hold significant promise for sustainable energy storage solutions. Their use of water-based electrolytes makes them inherently safer and more environmentally friendly compared to organic solvents used in many conventional batteries. Moreover, the abundant and low-cost materials used in aqueous batteries contribute to their overall sustainability. To advance the development of RAZBs, several next steps are essential. Firstly, improving the operating voltage range and energy density of RAZBs through the development of novel electrolytes and advanced electrode materials. Enhancing the low-temperature performance by exploring new additives or modifications to the electrolyte can also improve their practical usability in diverse environmental conditions. Additionally, addressing issues related to electrolyte stability and anode corrosion through innovative design and protective coatings will further enhance the longevity and reliability of these batteries. Future research should focus on optimizing these aspects to make aqueous batteries a viable alternative to conventional energy storage systems. By overcoming these challenges, aqueous batteries can contribute to more sustainable and efficient energy storage solutions.

8.2.1. Vanadium-based cathode materials

The role of pre-intercalated crystal water

To enhance the structural stability of the cathode material during the repeated insertion and extraction of Zn^{2+} ions, we have incorporated structural pillars within the interlayer to fortify the crystal structure. Beyond the employment of metal ions, the integration of pre-intercalated crystal water has been identified as a pivotal element in reinforcing the structure of vanadium-based cathodes. Some studies have proposed that the crystal water functions not only as a "water lubricant" to facilitate the swift movement of Zn^{2+} ions during the battery's charge-discharge cycles, but also serves as a charge-shielding medium to diminish the electrostatic forces between the intercalated Zn^{2+} ions and the active material. This dual role is hypothesized to enhance the kinetics of Zn^{2+} ion transport, facilitating a more efficient exchange between the electrolyte and the electrode. Given these premises, our future efforts need to further refine the reaction mechanism of vanadium-based materials, dissect and understand the operational dynamics of these interlayer pillars and the role of pre-intercalated water. We also need to reveal the specific interactions and effects these elements on the overall battery performance, aiming to optimize the structural and electrochemical properties of the cathode materials for enhanced battery technologies.

Surface modification and crystal structure engineering

The efficiency of the cathode's cycling process is frequently compromised by a multitude of side reactions and phase changes, leading to the deterioration of the crystal lattice and a subsequent reduction in cycling performance. In response to these challenges, the application of negatively charged functional groups (e.g., carboxylic groups) to modify the cathode surface presents a viable route to mitigate these detrimental effects. Such functional groups can repulse negatively charged hydroxyl radicals, thereby preventing their accumulation on the electrode surface and consequently bolstering the material's structural integrity. Therefore, future work will concentrate on the systematic development and empirical assessment of electrode surface modifications through the incorporation of negatively charged functional groups. This endeavor will include a comprehensive evaluation of the functional groups' impact on the electrochemical stability and durability of the

electrode materials. Concurrently, efforts will be directed towards refining interface design and executing crystallographic alterations to optimize the lattice structure for improved Zn^{2+} ion accommodation and mobility. These investigations will aim to elucidate the mechanistic underpinnings of enhanced zinc ion storage and retrieval within vanadium-based cathodes, ultimately contributing to the development of more efficient and durable battery systems.

A focus on water dynamics in cathode

While the co-intercalation mechanism of Zn^{2+}/Na^{+} has been identified in this thesis, the concurrent H^{+} insertion/extraction process presents a significant ambiguity, particularly regarding its relationship with the crystal structure and electrode performance. Furthermore, given the predominant origin of H^{+} ions from aqueous electrolyte (i.e., water), elucidating water's role during the charge/discharge cycles stands as a critical challenge for the development of vanadium-based cathodes. Water in vanadium-based RAZBs typically manifests in three distinct states: as crystalline water, solvated water, and chemisorbed water molecules on the electrode surface. Addressing this complexity necessitates the application of in situ characterization along with isotopic labeling techniques to track the behavior of H_2O molecules within the electrolyte. Future research endeavors will aim at providing a deeper understanding of water's role and will focus on elucidating the intricate relationships between H^{+} insertion, water states, vacancy defects, and their collective impact on the electrochemical performance of the cathode. Through these advanced analytical approaches, we aim to uncover the fundamental mechanisms in vanadium-based cathodes, thereby paving the way for the design of more efficient and robust RAZB systems.

Optimizing vanadium cathodes for commercial goals

Vanadium-based cathode materials confront several challenges, including limited operating voltages, volumetric energy density, and material loading capabilities. Typically, the operating voltage of vanadium-based compounds is less than 1 V, thus further advancements are required to bolster energy density. Some studies suggested to incorporate anion groups with strong electron-withdrawing ability (e.g., F^{-} and PO_4^{3-}) into V_2O_5, which

could elevate the average operating voltage to 1.1 V, or even 1.6 V. This approach raises the operating voltage but sacrifices capacity, thus future research efforts should focus on investigating the effects of these introduced groups on the crystal structure and operational voltage of vanadium-based cathodes. Enhancing voltage should be conducted with a definitive structure-performance relationship, not pursued indiscriminately. Moreover, the inherently low volumetric energy density of vanadium-based cathodes underscores the need for innovative design strategies. It is imperative to design and synthesize vanadium-based cathodes that feature specialized nanostructures, particularly layered ones, to significantly increase volumetric energy density through improved ion/electron transfer efficiencies. Furthermore, there exists a crucial requirement to develop innovative processing techniques aimed at elevating the mass loading of vanadium-based cathode material without compromising capacity. Such advancements are essential for ensuring a balance between the capacities of anode and cathode materials, ultimately contributing to the advancement of the overall performance of energy storage devices.

In addition, the practical application of vanadium-based cathodes in ZIBs requires consideration of the complex preparation process of vanadium oxides and their toxicity. These factors also play a crucial role in determining the feasibility and viability of vanadium-based cathodes in practical applications.

8.2.2. Manganese-based cathode materials

Advancements in coating technologies for electrochemical enhancement

The development of innovative coating materials presents a promising pathway to significantly enhance the electrochemical performance of electrodes. Specifically, polymer materials endowed with homogenous active sites, superior conductivity, and hydrophilic characteristics are poised to markedly improve electrode functionalities. Moreover, the exploration of synergistic interactions among multi-component coating materials merits rigorous investigation. For example, a dual-layer coating, integrating both electronic and ionic conducting layers, has been shown to effectively mitigate surface side reactions while simultaneously boosting the conductivity of manganese-based oxide cathode materials. Furthermore, these coating layers play a pivotal role in establishing a uniform electric field, thereby preventing the dendritic growth observed in zinc anodes. Future research should concentrate on the systematic exploration and characterization of novel coating materials, emphasizing the identification and synthesis of polymers with optimized electronic properties and surface interactions. Such investigations should include the development of bilayer coatings that combine electronic and ionic conductive properties, tailored specifically for MnO_2 cathodes and Zn anodes. It is also important to evaluate the impact of these coatings on suppressing undesired side reactions and dendritic growth, alongside their ability to enhance overall battery performance.

Innovative approaches in electrolyte additive research

The exploration of novel electrolyte additives represents a vital avenue for enhancing the performance of energy storage systems. These additives are crucial for modulating Zn^{2+} ion deposition on the zinc anode surface and influencing the cathode interface to improve the cathodic material's cyclic stability. The development of hydrophilic electrolyte additives (e.g., silk protein sericin) emerges as a particularly promising strategy, capable of effectively immobilizing free water molecules, thereby mitigating undesired surface side reactions. Given the inherent limitations of individual electrolyte additives, a synergistic approach that

leverages the combined effects of multiple additives may offer a pathway to achieve superior battery performance. Broadly speaking, future efforts in this domain should focus on the meticulous design and synthesis of multifunctional electrolyte additives, along with an in-depth understanding of the complex interactions between these additives and the electrochemical system. This will involve comprehensive electrochemical testing and analysis to ascertain the optimal combinations of additives that lead to enhanced performance metrics. In addition, the impact of these additives on the overall electrolyte composition, electrode interface stability, and battery longevity needs thorough investigation. By pursuing these focused areas of research, we can unlock new potentials in electrolyte additive formulations.

Elucidating the role of byproducts and intermediates in electrochemical processes

The formation of by-products and intermediate products on the cathode surface during electrochemical reactions is a phenomenon that significantly influences battery performance. These substances can impede the transfer of electrons and ions, restrict the battery's capacity, and potentially alter the fundamental reaction mechanisms. Despite their critical impact, there still remains a lack of consensus regarding the nature, structure, and factors influencing the formation of these intermediates. Future research endeavors must therefore prioritize the comprehensive investigation of by-products and intermediate products arising during electrochemical reactions. This entails:

(1) Identifying and characterizing the types and structures of these intermediates and by-products, utilizing advanced analytical techniques to ascertain their composition and formation mechanisms.

(2) Exploring the impact of these compounds on battery performance, including their role in electron and ion transfer processes, capacity limitations, and alterations to reaction pathways.

(3) Developing methodologies to mitigate the adverse effects of these substances, which may involve the synthesis of novel materials designed to resist by-product formation or the formulation of additives that can neutralize detrimental intermediates.

(4) Establishing a systematic understanding of the factors that promote the formation of these intermediates, ranging from electrolyte composition to operational conditions, in order to devise strategies that can minimize their impact.

By addressing these focal points, future research can bridge the current knowledge gap regarding the influence of by-products and intermediates on electrochemical systems, ultimately leading to the development of more robust and efficient battery technologies.

Advancing multi-strategy modifications for Mn-based cathodes: synergies, applications, and economic viability

While individual modification strategies offer distinct advantages for enhancing the performance of cathode materials, relying on a singular approach often falls short in concurrently optimizing structural stability, energy density, and rate performance. The exploration of synergistic effects stemming from combined modification strategies on the electrochemical behaviors of cathode materials remains an under investigated area. Achieving a comprehensive understanding of these synergistic mechanisms is crucial for harnessing the full potential of cathode enhancements.

For Mn-based cathodes to transition from theoretical models to practical application, a holistic optimization strategy encompassing the entire battery system is imperative. This involves the iterative refinement of various battery components, such as the development of functional electrolytes, the introduction of multifunctional separators, and the innovation of zinc anode, ensuring that each element contributes to the overall performance improvement of the battery. Moreover, the economic aspects, including a thorough cost-benefit analysis, must be incorporated into the development process to evaluate the financial feasibility of these advanced cathode materials. Understanding the economic implications is vital for assessing the potential for commercialization and large-scale adoption. Furthermore, elucidating the specific storage mechanisms of such advanced cathode material is essential. This detailed understanding will facilitate the targeted design of modifications and the prediction of their effects on battery performance. Future research should focus on:

(1) Systematically investigating the synergistic effects of multiple modification strategies on Mn-based oxide cathodes, utilizing advanced analytical techniques to unravel the underlying mechanisms.

(2) Conducting comprehensive optimizations at the whole battery level, which entails not only improving the cathode material but also enhancing related battery components for superior overall performance.

(3) Integrating economic evaluations early in the research process to ensure that proposed solutions are not only technically viable but also economically feasible.

(4) Deepening the understanding of the storage mechanisms inherent to Mn-based materials of various crystalline types (e.g., α-, β-, γ-, ε-, etc.), which is pivotal for guiding future modifications and applications.

Addressing these areas will pave the way for the development of Mn-based oxide cathodes with superior performance, cost-effectiveness, and practical applicability, marking significant progress in the field of advanced energy storage technologies.

Cathode design for enhanced performance in low-temperature environments

Given the drastic climatic shifts observed globally, the imperative for energy storage systems capable of operating in extremely low temperatures has never been more critical. In such environments, mild RAZBs face not only the challenge of aqueous solution freezing but also the significantly reduced diffusion kinetics of Zn^{2+} ions. The defect engineering, doping and hybridization with conductive materials are all possible strategies to improve the low temperature performance of RAZB. However, the implementation of these methods requires a detailed understanding of the structural and electrochemical properties of the materials at low temperatures. Therefore, in-depth studies involving cryogenic temperature testing, advanced microscopy, and *in situ* spectroscopy techniques to analyze the cathode's behavior in low-temperature conditions are essential. Moreover, computational modeling and simulations

could offer valuable insights into the mechanisms at guiding the experimental design and optimization of cathode materials for low-temperature applications.

By addressing these key areas, the research aims to unlock new possibilities for the development of robust RAZBs, ensuring their effective performance in cold climates and expanding their applicability across a wider range of environmental conditions.

References

1. IEA. *Electricity 2024 - Analysis and Forecast to 2026*. https://www.iea.org/reports/electricity-2024 (2024).

2. IEA. *World Energy Outlook 2023*. https://www.iea.org/reports/world-energy-outlook-2023, License: CC BY 4.0 (report); CC BY NC SA 4.0 (Annex A) (2023).

3. IEA. *World Energy Outlook 2021*. https://www.iea.org/reports/world-energy-outlook-2021 (2021).

4. Zhang, Z. & Zhang, S. S. Challenges of Key Materials for Rechargeable Batteries. in *Rechargeable Batteries: Materials, Technologies and New Trends* (eds. Zhang, Z. & Zhang, S. S.) 1–24 (Springer International Publishing, Cham, 2015). doi:10.1007/978-3-319-15458-9_1.

5. Liang, Y. *et al.* A review of rechargeable batteries for portable electronic devices. *InfoMat* **1**, 6–32 (2019).

6. Hossain, E., Faruque, H. M. R., Sunny, M. S. H., Mohammad, N. & Nawar, N. A Comprehensive Review on Energy Storage Systems: Types, Comparison, Current Scenario, Applications, Barriers, and Potential Solutions, Policies, and Future Prospects. *Energies* **13**, 3651 (2020).

7. He, P. *et al.* Building better zinc-ion batteries: A materials perspective. *EnergyChem* **1**, 100022 (2019).

8. Jia, X., Liu, C., Neale, Z. G., Yang, J. & Cao, G. Active Materials for Aqueous Zinc Ion Batteries: Synthesis, Crystal Structure, Morphology, and Electrochemistry. *Chem. Rev.* **120**, 7795–7866 (2020).

9. Zhang, C., Wei, Y.-L., Cao, P.-F. & Lin, M.-C. Energy storage system: Current studies on batteries and power condition system. *Renew. Sustain. Energy Rev.* **82**, 3091–3106 (2018).

10. Hameer, S. & van Niekerk, J. L. A review of large-scale electrical energy storage. *Int. J. Energy Res.* **39**, 1179–1195 (2015).

11. Deng, D. Li-ion batteries: basics, progress, and challenges. *Energy Sci. Eng.* **3**, 385–418 (2015).

12. Dunn, B., Kamath, H. & Tarascon, J.-M. Electrical Energy Storage for the Grid: A Battery of Choices. *Science* **334**, 928–935 (2011).

13. Feng, X. *et al.* Investigating the thermal runaway mechanisms of lithium-ion batteries based on thermal analysis database. *Appl. Energy* **246**, 53–64 (2019).

14. Wang, Q. *et al.* Thermal runaway caused fire and explosion of lithium ion battery. *J. Power Sources* **208**, 210–224 (2012).

15. Feng, X. *et al.* Thermal runaway mechanism of lithium ion battery for electric vehicles: A review. *Energy Storage Mater.* **10**, 246–267 (2018).

16. Li, Y. *et al.* Designing Low Toxic Deep Eutectic Solvents for the Green Recycle of Lithium-Ion Batteries Cathodes. *ChemSusChem* **17**, e202301953 (2024).

17. Wang, J. *et al.* Toward Direct Regeneration of Spent Lithium-Ion Batteries: A Next-Generation Recycling Method. *Chem. Rev.* **124**, 2839–2887 (2024).

18. Huang, B., Pan, Z., Su, X. & An, L. Recycling of lithium-ion batteries: Recent advances and perspectives. *J. Power Sources* **399**, 274–286 (2018).

19. Gutsch, M. & Leker, J. Costs, carbon footprint, and environmental impacts of lithium-ion batteries – From cathode active material synthesis to cell manufacturing and recycling. *Appl. Energy* **353**, 122132 (2024).

20. Zanoletti, A., Carena, E., Ferrara, C. & Bontempi, E. A Review of Lithium-Ion Battery Recycling: Technologies, Sustainability, and Open Issues. *Batteries* **10**, 38 (2024).

21. Song, M., Tan, H., Chao, D. & Fan, H. J. Recent Advances in Zn-Ion Batteries. *Adv. Funct. Mater.* **28**, 1802564 (2018).

22. Kundu, D., Adams, B. D., Duffort, V., Vajargah, S. H. & Nazar, L. F. A high-capacity and long-life aqueous rechargeable zinc battery using a metal oxide intercalation cathode. *Nat. Energy* **1**, 1–8 (2016).

23. Huang, S., Zhu, J., Tian, J. & Niu, Z. Recent Progress in the Electrolytes of Aqueous Zinc-Ion Batteries. *Chem. – Eur. J.* **25**, 14480–14494 (2019).

24. Huang, J. *et al.* Recent Progress of Rechargeable Batteries Using Mild Aqueous Electrolytes. *Small Methods* **3**, 1800272 (2019).

25. Li, H. *et al.* Advanced rechargeable zinc-based batteries: Recent progress and future perspectives. *Nano Energy* **62**, 550–587 (2019).

26. Wan, F. *et al.* Aqueous rechargeable zinc/sodium vanadate batteries with enhanced performance from simultaneous insertion of dual carriers. *Nat. Commun.* **9**, 1656 (2018).

27. Winter, M. & Brodd, R. J. What Are Batteries, Fuel Cells, and Supercapacitors? *Chem. Rev.* **104**, 4245–4270 (2004).

28. Cheng, F. Y., Chen, J., Gou, X. L. & Shen, P. W. High-Power Alkaline Zn–MnO2 Batteries Using γ-MnO2 Nanowires/Nanotubes and Electrolytic Zinc Powder. *Adv. Mater.* **17**, 2753–2756 (2005).

29. Wang, X. *et al.* An Aqueous Rechargeable Zn//Co3 O4 Battery with High Energy Density and Good Cycling Behavior. *Adv. Mater. Deerfield Beach Fla* **28**, 4904–4911 (2016).

30. Senguttuvan, P. *et al.* A High Power Rechargeable Nonaqueous Multivalent Zn/V2O5 Battery. *Adv. Energy Mater.* **6**, 1600826 (2016).

31. Liu, Z. *et al.* Dendrite-Free Nanocrystalline Zinc Electrodeposition from an Ionic Liquid Containing Nickel Triflate for Rechargeable Zn-Based Batteries. *Angew. Chem. Int. Ed.* **55**, 2889–2893 (2016).

32. Shoji, T., Hishinuma, M. & Yamamoto, T. Zinc-manganese dioxide galvanic cell using zinc sulphate as electrolyte. Rechargeability of the cell. *J. Appl. Electrochem.* **18**, 521–526 (1988).

33. Xu, C., Li, B., Du, H. & Kang, F. Energetic Zinc Ion Chemistry: The Rechargeable Zinc Ion Battery. *Angew. Chem.* **124**, 957–959 (2012).

34. Myers, R. *The Basics of Chemistry*. Westport: Greenwood Press (2003).

35. Holze, R. Handbook of battery materials, Daniel C, Besenhard†, J.O., eds, 2nd ed., 2011, XXXIV + 989 p., 285 £; ISBN: 978-3-527-32695-2. *J. Solid State Electrochem.* **16**, 2845–2846 (2012).

36. Fu, J. *et al.* Electrically Rechargeable Zinc–Air Batteries: Progress, Challenges, and Perspectives. *Adv. Mater.* **29**, 1604685 (2017).

37. Wruck, W. J., Reichman, B., Bullock, K. R. & Kao, W.-H. Rechargeable Zn - MnO2 Alkaline Batteries. *J. Electrochem. Soc.* **138**, 3560 (1991).

38. Eustace, D. J. Bromine Complexation in Zinc-Bromine Circulating Batteries. *J. Electrochem. Soc.* **127**, 528 (1980).

39. Gu, H. Mathematical Analysis of a Zn / NiOOH Cell. *J. Electrochem. Soc.* **130**, 1459 (1983).

40. Yan, C. *et al.* Stretchable Silver-Zinc Batteries Based on Embedded Nanowire Elastic Conductors. *Adv. Energy Mater.* **4**, 1301396 (2014).

41. Yao, H.-R., You, Y., Yin, Y.-X., Wan, L.-J. & Guo, Y.-G. Rechargeable dual-metal-ion batteries for advanced energy storage. *Phys. Chem. Chem. Phys.* **18**, 9326–9333 (2016).

42. Pan, H. *et al.* Reversible aqueous zinc/manganese oxide energy storage from conversion reactions. *Nat. Energy* **1**, 1–7 (2016).

43. He, P. *et al.* Layered VS2 Nanosheet-Based Aqueous Zn Ion Battery Cathode. *Adv. Energy Mater.* **7**, 1601920 (2017).

44. Zhang, L., Chen, L., Zhou, X. & Liu, Z. Towards High-Voltage Aqueous Metal-Ion Batteries Beyond 1.5 V: The Zinc/Zinc Hexacyanoferrate System. *Adv. Energy Mater.* **5**, 1400930 (2015).

45. Dong, H. *et al.* Insights on Flexible Zinc-Ion Batteries from Lab Research to Commercialization. *Adv. Mater.* **33**, 2007548 (2021).

46. Gourley, S. W. D., Brown, R., Adams, B. D. & Higgins, D. Zinc-ion batteries for stationary energy storage. *Joule* **7**, 1415–1436 (2023).

47. Tarascon, J.-M. & Armand, M. Issues and challenges facing rechargeable lithium batteries. *Nature* **414**, 359–367 (2001).

48. Bensalah, N. & De Luna, Y. Recent Progress in Layered Manganese and Vanadium Oxide Cathodes for Zn-Ion Batteries. *Energy Technol.* **9**, 2100011 (2021).

49. Booth, S. G. *et al.* Perspectives for next generation lithium-ion battery cathode materials. *APL Mater.* **9**, 109201 (2021).

50. Fang, G., Zhou, J., Pan, A. & Liang, S. Recent Advances in Aqueous Zinc-Ion Batteries. *ACS Energy Lett.* **3**, 2480–2501 (2018).

51. Shin, J. & Choi, J. W. Opportunities and Reality of Aqueous Rechargeable Batteries. *Adv. Energy Mater.* **10**, 2001386 (2020).

52. Jin, J., Geng, X., Chen, Q. & Ren, T.-L. A Better Zn-Ion Storage Device: Recent Progress for Zn-Ion Hybrid Supercapacitors. *Nano-Micro Lett.* **14**, 64 (2022).

53. Wang, X. *et al.* Advances and Perspectives of Cathode Storage Chemistry in Aqueous Zinc-Ion Batteries. *ACS Nano* **15**, 9244–9272 (2021).

54. Goodenough, J. B. & Kim, Y. Challenges for rechargeable batteries. *J. Power Sources* **196**, 6688–6694 (2011).

55. Qian li, Wei, T., Ma, K., Yang, G. & Wang, C. Boosting the Cyclic Stability of Aqueous Zinc-Ion Battery Based on Al-Doped V10O24·12H2O Cathode Materials. *ACS Appl. Mater. Interfaces* **11**, 20888–20894 (2019).

56. Zhang, N. *et al.* Rechargeable Aqueous Zn–V2O5 Battery with High Energy Density and Long Cycle Life. *ACS Energy Lett.* **3**, 1366–1372 (2018).

57. Zhang, N. *et al.* Cation-Deficient Spinel ZnMn2O4 Cathode in Zn(CF3SO3)2 Electrolyte for Rechargeable Aqueous Zn-Ion Battery. *J. Am. Chem. Soc.* **138**, 12894–12901 (2016).

58. Han, S.-D. *et al.* Mechanism of Zn Insertion into Nanostructured δ-MnO2: A Nonaqueous Rechargeable Zn Metal Battery. *Chem. Mater.* **29**, 4874–4884 (2017).

59. Jiang, B. *et al.* Manganese Sesquioxide as Cathode Material for Multivalent Zinc Ion Battery with High Capacity and Long Cycle Life. *Electrochimica Acta* **229**, 422–428 (2017).

60. Yan, M. *et al.* Water-Lubricated Intercalation in V2O5·nH2O for High-Capacity and High-Rate Aqueous Rechargeable Zinc Batteries. *Adv. Mater.* **30**, 1703725 (2018).

61. He, P. *et al.* Sodium Ion Stabilized Vanadium Oxide Nanowire Cathode for High-Performance Zinc-Ion Batteries. *Adv. Energy Mater.* **8**, 1702463 (2018).

62. Ming, F. *et al.* Layered MgxV2O5·nH2O as Cathode Material for High-Performance Aqueous Zinc Ion Batteries. *ACS Energy Lett.* **3**, 2602–2609 (2018).

63. Xia, C., Guo, J., Li, P., Zhang, X. & Alshareef, H. N. Highly Stable Aqueous Zinc-Ion Storage Using a Layered Calcium Vanadium Oxide Bronze Cathode. *Angew. Chem. Int. Ed.* **57**, 3943–3948 (2018).

64. Jia, Z., Wang, B. & Wang, Y. Copper hexacyanoferrate with a well-defined open framework as a positive electrode for aqueous zinc ion batteries. *Mater. Chem. Phys.* **149–150**, 601–606 (2015).

65. Li, G. *et al.* Towards polyvalent ion batteries: A zinc-ion battery based on NASICON structured Na3V2(PO4)3. *Nano Energy* **25**, 211–217 (2016).

66. Li, W., Wang, K., Cheng, S. & Jiang, K. A long-life aqueous Zn-ion battery based on Na3V2(PO4)2F3 cathode. *Energy Storage Mater.* **15**, 14–21 (2018).

67. Ko, J. S. *et al.* NASICON Na3V2(PO4)3 Enables Quasi-Two-Stage Na+ and Zn2+ Intercalation for Multivalent Zinc Batteries. *Chem. Mater.* **32**, 3028–3035 (2020).

68. Zhang, L., Wang, W., Zhang, H., Han, S. & Wang, L. Research Progress and Challenge of Aqueous Zinc Ion Battery. *Acta Chim. Sin.* **79**, 158 (2021).

69. Zhou, T. *et al.* Recent Developments and Challenges of Vanadium Oxides (VxOy) Cathodes for Aqueous Zinc-Ion Batteries. *Chem. Rec.* **22**, e202100275 (2022).

70. Xu, X. *et al.* Vanadium-Based Nanomaterials: A Promising Family for Emerging Metal-Ion Batteries. *Adv. Funct. Mater.* **30**, 1904398 (2020).

71. Liu, N. *et al.* Recent advances and perspectives on vanadium- and manganese-based cathode materials for aqueous zinc ion batteries. *J. Energy Chem.* **59**, 134–159 (2021).

72. Guo, Y., Wei, Y., Li, H. & Zhai, T. Layer Structured Materials for Advanced Energy Storage and Conversion. *Small* **13**, 1701649 (2017).

73. Wan, F. & Niu, Z. Design Strategies for Vanadium-based Aqueous Zinc-Ion Batteries. *Angew. Chem.* **131**, 16508–16517 (2019).

74. Yu, H. *et al.* Cu doped V2O5 flowers as cathode material for high-performance lithium ion batteries. *Nanoscale* **5**, 4937–4943 (2013).

75. Chen, X., Wang, L., Li, H., Cheng, F. & Chen, J. Porous V2O5 nanofibers as cathode materials for rechargeable aqueous zinc-ion batteries. *J. Energy Chem.* **38**, 20–25 (2019).

76. Zhou, W. *et al.* Rod-like anhydrous V2O5 assembled by tiny nanosheets as a high-performance cathode material for aqueous zinc-ion batteries. *RSC Adv.* **9**, 30556–30564 (2019).

77. Wang, X. *et al.* Vanadium pentoxide nanosheets as cathodes for aqueous zinc-ion batteries with high rate capability and long durability. *Appl. Surf. Sci.* **502**, 144207 (2020).

78. Qin, H., Chen, L., Wang, L., Chen, X. & Yang, Z. V2O5 hollow spheres as high rate and long life cathode for aqueous rechargeable zinc ion batteries. *Electrochimica Acta* **306**, 307–316 (2019).

79. Li, R., Zhang, H., Zheng, Q. & Li, X. Porous V2O5 yolk–shell microspheres for zinc ion battery cathodes: activation responsible for enhanced capacity and rate performance. *J. Mater. Chem. A* **8**, 5186–5193 (2020).

80. Zhao, Q. *et al.* Preintercalation Strategy in Manganese Oxides for Electrochemical Energy Storage: Review and Prospects. *Adv. Mater.* **32**, 2002450 (2020).

81. Stark, M. S., Kuntz, K. L., Martens, S. J. & Warren, S. C. Intercalation of Layered Materials from Bulk to 2D. *Adv. Mater.* **31**, 1808213 (2019).

82. Wan, J. *et al.* Tuning two-dimensional nanomaterials by intercalation: materials, properties and applications. *Chem. Soc. Rev.* **45**, 6742–6765 (2016).

83. Alfaruqi, M. H. *et al.* Electrochemical Zinc Intercalation in Lithium Vanadium Oxide: A High-Capacity Zinc-Ion Battery Cathode. *Chem. Mater.* **29**, 1684–1694 (2017).

84. Tang, F., Zhou, W., Chen, M., Chen, J. & Xu, J. Flexible free-standing paper electrodes based on reduced graphene oxide/δ-NaxV2O5·nH2O nanocomposite for high-performance aqueous zinc-ion batteries. *Electrochimica Acta* **328**, 135137 (2019).

85. Gao, P. *et al.* A Durable Na0.56V2O5 Nanobelt Cathode Material Assisted by Hybrid Cationic Electrolyte for High-Performance Aqueous Zinc-Ion Batteries. *ChemElectroChem* **7**, 283–288 (2020).

86. Zhang, G. *et al.* Rich Alkali Ions Preintercalated Vanadium Oxides for Durable and Fast Zinc-Ion Storage. *ACS Energy Lett.* **6**, 2111–2120 (2021).

87. Wan, F., Huang, S., Cao, H. & Niu, Z. Freestanding Potassium Vanadate/Carbon Nanotube Films for Ultralong-Life Aqueous Zinc-Ion Batteries. *ACS Nano* **14**, 6752–6760 (2020).

88. Hao, Y. *et al.* Pillaring Effect of K Ion Anchoring for Stable V2O5-Based Zinc-Ion Battery Cathodes. *ChemNanoMat* **6**, 797–805 (2020).

89. Sambandam, B. *et al.* K2V6O16·2.7H2O nanorod cathode: an advanced intercalation system for high energy aqueous rechargeable Zn-ion batteries. *J. Mater. Chem. A* **6**, 15530–15539 (2018).

90. Lan, B. *et al.* Metallic silver doped vanadium pentoxide cathode for aqueous rechargeable zinc ion batteries. *J. Alloys Compd.* **787**, 9–16 (2019).

91. Guo, S. *et al.* Structural perspective on revealing energy storage behaviors of silver vanadate cathodes in aqueous zinc-ion batteries. *Acta Mater.* **180**, 51–59 (2019).

92. Shan, L. *et al.* Reversible Zn-driven reduction displacement reaction in aqueous zinc-ion battery. *J. Mater. Chem. A* **7**, 7355–7359 (2019).

93. Deng, W. *et al.* High-Capacity Layered Magnesium Vanadate with Concentrated Gel Electrolyte toward High-Performance and Wide-Temperature Zinc-Ion Battery. *ACS Nano* **14**, 15776–15785 (2020).

94. Zhu, K., Wu, T. & Huang, K. A High Capacity Bilayer Cathode for Aqueous Zn-Ion Batteries. *ACS Nano* **13**, 14447–14458 (2019).

95. Wang, X. *et al.* Boosting Zinc-Ion Storage Capability by Effectively Suppressing Vanadium Dissolution Based on Robust Layered Barium Vanadate. *Nano Lett.* **20**, 2899–2906 (2020).

96. Guan, X. *et al.* Tremella-like Hydrated Vanadium Oxide Cathode with an Architectural Design Strategy toward Ultralong Lifespan Aqueous Zinc-Ion Batteries. *ACS Appl. Mater. Interfaces* **13**, 41688–41697 (2021).

97. Pang, Q. *et al.* Aluminium pre-intercalated orthorhombic V2O5 as high-performance cathode material for aqueous zinc-ion batteries. *Appl. Surf. Sci.* **538**, 148043 (2021).

98. Xu, W. *et al.* Sn stabilized pyrovanadate structure rearrangement for zinc ion battery. *Nano Energy* **81**, 105584 (2021).

99. Zhu, K., Wu, T., van den Bergh, W., Stefik, M. & Huang, K. Reversible Molecular and Ionic Storage Mechanisms in High-Performance Zn0.1V2O5·nH2O Xerogel Cathode for Aqueous Zn-Ion Batteries. *ACS Nano* **15**, 10678–10688 (2021).

100. Ma, L. *et al.* Achieving Both High Voltage and High Capacity in Aqueous Zinc-Ion Battery for Record High Energy Density. *Adv. Funct. Mater.* **29**, 1906142 (2019).

101. Yang, Y. *et al.* Transition metal ion-preintercalated V2O5 as high-performance aqueous zinc-ion battery cathode with broad temperature adaptability. *Nano Energy* **61**, 617–625 (2019).

102. Li, J. *et al.* Multi-Scale Investigations of δ-Ni0.25V2O5·nH2O Cathode Materials in Aqueous Zinc-Ion Batteries. *Adv. Energy Mater.* **10**, 2000058 (2020).

103. Wang, L., Huang, K.-W., Chen, J. & Zheng, J. Ultralong cycle stability of aqueous zinc-ion batteries with zinc vanadium oxide cathodes. *Sci. Adv.* **5**, eaax4279 (2019).

104. Liu, Y., Li, Q., Ma, K., Yang, G. & Wang, C. Graphene Oxide Wrapped CuV2O6 Nanobelts as High-Capacity and Long-Life Cathode Materials of Aqueous Zinc-Ion Batteries. *ACS Nano* **13**, 12081–12089 (2019).

105. Zhao, H. *et al.* In Operando Synchrotron Studies of NH4+ Preintercalated V2O5·nH2O Nanobelts as the Cathode Material for Aqueous Rechargeable Zinc Batteries. *ACS Nano* **14**, 11809–11820 (2020).

106. Xu, L. *et al.* Ammonium ion intercalated hydrated vanadium pentoxide for advanced aqueous rechargeable Zn-ion batteries. *Mater. Today Energy* **18**, 100509 (2020).

107. Tamilselvan, M., Sreekanth, T. V. M., Yoo, K. & Kim, J. Wide interlayer spacing ammonium vanadate (NH4)0.37V2O5.0.15(H2O) cathode for rechargeable aqueous zinc-ion batteries. *J. Ind. Eng. Chem.* **93**, 176–185 (2021).

108. Liu, Y. *et al.* Employing "one for two" strategy to design polyaniline-intercalated hydrated vanadium oxide with expanded interlayer spacing for high-performance aqueous zinc-ion batteries. *Chem. Eng. J.* **399**, 125842 (2020).

109. Yan, H. *et al.* Organic pillars pre-intercalated V4+-V2O5·3H2O nanocomposites with enlarged interlayer and mixed valence for aqueous Zn-ion storage. *Appl. Surf. Sci.* **534**, 147608 (2020).

110. Bin, D. *et al.* Organic-Inorganic-Induced Polymer Intercalation into Layered Composites for Aqueous Zinc-Ion Battery. *Chem* **6**, 968–984 (2020).

111. Zhang, W. *et al.* The Current Developments and Perspectives of V2O5 as Cathode for Rechargeable Aqueous Zinc-Ion Batteries. *Energy Technol.* **9**, 2000789 (2021).

112. Chen, H., Rong, Y., Yang, Z., Deng, L. & Wu, J. V2O3@Amorphous Carbon as a Cathode of Zinc Ion Batteries with High Stability and Long Cycling Life. *Ind. Eng. Chem. Res.* **60**, 1517–1525 (2021).

113. Liu, Y., Liu, Y., Wu, X. & Cho, Y.-R. General Carbon Modification Avenue to Construct Highly Stable V2O5 Electrodes for Aqueous Zinc-Ion Batteries. *ACS Sustain. Chem. Eng.* **11**, 13298–13305 (2023).

114. Xu, N. *et al.* Flexible electrode material of V2O5 carbon fiber cloth for enhanced zinc ion storage performance in flexible zinc-ion battery. *J. Power Sources* **533**, 231358 (2022).

115. Wang, X. *et al.* A flexible carbon nanotube@V2O5 film as a high-capacity and durable cathode for zinc ion batteries. *J. Energy Chem.* **59**, 126–133 (2021).

116. Chen, H., Qin, H., Chen, L., Wu, J. & Yang, Z. V2O5@CNTs as cathode of aqueous zinc ion battery with high rate and high stability. *J. Alloys Compd.* **842**, 155912 (2020).

117. Liu, C., Li, R., Liu, W., Shen, G. & Chen, D. Chitosan-Assisted Fabrication of a Network C@V2O5 Cathode for High-Performance Zn-Ion Batteries. *ACS Appl. Mater. Interfaces* **13**, 37194–37200 (2021).

118. Xue, T. & Fan, H. J. From aqueous Zn-ion battery to Zn-MnO2 flow battery: A brief story. *J. Energy Chem.* **54**, 194–201 (2021).

119. Chen, D., Lu, M., Cai, D., Yang, H. & Han, W. Recent advances in energy storage mechanism of aqueous zinc-ion batteries. *J. Energy Chem.* **54**, 712–726 (2021).

120. Zhang, N. *et al.* Materials chemistry for rechargeable zinc-ion batteries. *Chem. Soc. Rev.* **49**, 4203–4219 (2020).

121. Zhao, Y., Zhu, Y. & Zhang, X. Challenges and perspectives for manganese-based oxides for advanced aqueous zinc-ion batteries. *InfoMat* **2**, 237–260 (2020).

122. Mo, F. *et al.* A smart safe rechargeable zinc ion battery based on sol-gel transition electrolytes. *Sci. Bull.* **63**, 1077–1086 (2018).

123. Nithyadharseni, P., Reddy, M. V., Fanny, H., Adams, S. & Chowdari, B. V. R. Facile one pot synthesis and Li-cycling properties of MnO2. *RSC Adv.* **5**, 60552–60561 (2015).

124. Islam, S. *et al.* Facile synthesis and the exploration of the zinc storage mechanism of β-MnO2 nanorods with exposed (101) planes as a novel cathode material for high performance eco-friendly zinc-ion batteries. *J. Mater. Chem. A* **5**, 23299–23309 (2017).

125. Wei, C., Xu, C., Li, B., Du, H. & Kang, F. Preparation and characterization of manganese dioxides with nano-sized tunnel structures for zinc ion storage. *J. Phys. Chem. Solids* **73**, 1487–1491 (2012).

126. Yuan, C. *et al.* Investigation of the intercalation of polyvalent cations (Mg2+, Zn2+) into λ-MnO2 for rechargeable aqueous battery. *Electrochimica Acta* **116**, 404–412 (2014).

127. Lee, J., Ju, J. B., Cho, W. I., Cho, B. W. & Oh, S. H. Todorokite-type MnO2 as a zinc-ion intercalating material. *Electrochimica Acta* **112**, 138–143 (2013).

128. Alfaruqi, M. H. *et al.* A layered δ-MnO2 nanoflake cathode with high zinc-storage capacities for eco-friendly battery applications. *Electrochem. Commun.* **60**, 121–125 (2015).

129. Chen, L., An, Q. & Mai, L. Recent Advances and Prospects of Cathode Materials for Rechargeable Aqueous Zinc-Ion Batteries. *Adv. Mater. Interfaces* **6**, 1900387 (2019).

130. Zhou, A. *et al.* Manganese-based cathode materials for aqueous rechargeable zinc-ion batteries: recent advance and future prospects. *Mater. Today Chem.* **27**, 101294 (2023).

131. Hatakeyama, T., Okamoto, N. L. & Ichitsubo, T. Thermal stability of MnO2 polymorphs. *J. Solid State Chem.* **305**, 122683 (2022).

132. Zhang, N. *et al.* Rechargeable aqueous zinc-manganese dioxide batteries with high energy and power densities. *Nat. Commun.* **8**, 405 (2017).

133. Liu, G. *et al.* K+ pre-intercalated manganese dioxide with enhanced Zn2+ diffusion for high rate and durable aqueous zinc-ion batteries. *J. Mater. Chem. A* **7**, 20806–20812 (2019).

134. Zhang, H. *et al.* Boosting the Zn-ion storage capability of birnessite manganese oxide nanoflorets by La3+ intercalation. *J. Mater. Chem. A* **7**, 22079–22083 (2019).

135. Wang, D. *et al.* A Superior δ-MnO2 Cathode and a Self-Healing Zn-δ-MnO2 Battery. *ACS Nano* **13**, 10643–10652 (2019).

136. Wang, J. *et al.* Superior-Performance Aqueous Zinc Ion Battery Based on Structural Transformation of MnO2 by Rare Earth Doping. *J. Phys. Chem. C* **123**, 22735–22741 (2019).

137. Ji, J. *et al.* Promoting Proton Migration Kinetics by Ni2+ Regulating Enables Improved Aqueous Zn-MnO2 Batteries. *ENERGY Environ. Mater.* **6**, e12340 (2023).

138. Zhang, Y. *et al.* Defect Promoted Capacity and Durability of N-MnO2–x Branch Arrays via Low-Temperature NH3 Treatment for Advanced Aqueous Zinc Ion Batteries. *Small* **15**, 1905452 (2019).

139. Liu, Y. *et al.* Paraffin Based Cathode–Electrolyte Interface for Highly Reversible Aqueous Zinc-Ion Battery. *ACS Appl. Energy Mater.* **5**, 4840–4849 (2022).

140. Shang, H. *et al.* MnO2@V2O5 microspheres as cathode materials for high performance aqueous rechargeable Zn-ion battery. *J. Electroanal. Chem.* **890**, 115253 (2021).

141. Wang, J., Wang, J.-G., Liu, H., Wei, C. & Kang, F. Zinc ion stabilized MnO2 nanospheres for high capacity and long lifespan aqueous zinc-ion batteries. *J. Mater. Chem. A* **7**, 13727–13735 (2019).

142. Zhang, H. *et al.* Extracting oxygen anions from ZnMn2O4: Robust cathode for flexible all-solid-state Zn-ion batteries. *Energy Storage Mater.* **21**, 154–161 (2019).

143. Fenta, F. W. *et al.* Electrochemical transformation reaction of Cu–MnO in aqueous rechargeable zinc-ion batteries for high performance and long cycle life. *J. Mater. Chem. A* **8**, 17595–17607 (2020).

144. Xiong, T. *et al.* Defect Engineering of Oxygen-Deficient Manganese Oxide to Achieve High-Performing Aqueous Zinc Ion Battery. *Adv. Energy Mater.* **9**, 1803815 (2019).

145. Islam, S. *et al.* In Situ Oriented Mn Deficient ZnMn2O4@C Nanoarchitecture for Durable Rechargeable Aqueous Zinc-Ion Batteries. *Adv. Sci.* **8**, 2002636 (2021).

146. Guo, X. *et al.* Defect-engineered Mn3O4/CNTs composites enhancing reaction kinetics for zinc-ions storage performance. *J. Energy Chem.* **68**, 538–547 (2022).

147. Yang, B. *et al.* MnO nanoparticles with cationic defects encapsulated in nitrogen-doped porous carbon for high-performance aqueous zinc-ion batteries. *J. Alloys Compd.* **889**, 161680 (2021).

148. Wang, C. *et al.* γ-MnO2 nanorods/graphene composite as efficient cathode for advanced rechargeable aqueous zinc-ion battery. *J. Energy Chem.* **43**, 182–187 (2020).

149. Liu, Y. *et al.* Mn2+ Ions Confined by Electrode Microskin for Aqueous Battery beyond Intercalation Capacity. *Adv. Energy Mater.* **10**, 2002578 (2020).

150. Zhang, T. *et al.* Fundamentals and perspectives in developing zinc-ion battery electrolytes: a comprehensive review. *Energy Environ. Sci.* **13**, 4625–4665 (2020).

151. Guo, S. *et al.* Fundamentals and perspectives of electrolyte additives for aqueous zinc-ion batteries. *Energy Storage Mater.* **34**, 545–562 (2021).

152. Liu, C., Xie, X., Lu, B., Zhou, J. & Liang, S. Electrolyte Strategies toward Better Zinc-Ion Batteries. *ACS Energy Lett.* **6**, 1015–1033 (2021).

153. Wang, Y. *et al.* Electrolyte Engineering Enables High Performance Zinc-Ion Batteries. *Small* **18**, 2107033 (2022).

154. Ming, J., Guo, J., Xia, C., Wang, W. & Alshareef, H. N. Zinc-ion batteries: Materials, mechanisms, and applications. *Mater. Sci. Eng. R Rep.* **135**, 58–84 (2019).

155. Yan, H. *et al.* Insight into the electrolyte strategies for aqueous zinc ion batteries. *Coord. Chem. Rev.* **452**, 214297 (2022).

156. Zhang, Y. *et al.* Rechargeable Aqueous Zinc-Ion Batteries in MgSO4/ZnSO4 Hybrid Electrolytes. *Nano-Micro Lett.* **12**, 60 (2020).

157. Li, H. *et al.* An extremely safe and wearable solid-state zinc ion battery based on a hierarchical structured polymer electrolyte. *Energy Environ. Sci.* **11**, 941–951 (2018).

158. Qiu, W. *et al.* High-performance flexible quasi-solid-state Zn–MnO2 battery based on MnO2 nanorod arrays coated 3D porous nitrogen-doped carbon cloth. *J. Mater. Chem. A* **5**, 14838–14846 (2017).

159. Wang, G. *et al.* A High-Voltage, Dendrite-Free, and Durable Zn–Graphite Battery. *Adv. Mater.* **32**, 1905681 (2020).

160. Ma, L. *et al.* Hydrogen-Free and Dendrite-Free All-Solid-State Zn-Ion Batteries. *Adv. Mater.* **32**, 1908121 (2020).

161. Zhou, Q., Ma, J., Dong, S., Li, X. & Cui, G. Intermolecular Chemistry in Solid Polymer Electrolytes for High-Energy-Density Lithium Batteries. *Adv. Mater.* **31**, 1902029 (2019).

162. Suo, L., Hu, Y.-S., Li, H., Armand, M. & Chen, L. A new class of Solvent-in-Salt electrolyte for high-energy rechargeable metallic lithium batteries. *Nat. Commun.* **4**, 1481 (2013).

163. Wu, K. *et al.* Recent Advances in Polymer Electrolytes for Zinc Ion Batteries: Mechanisms, Properties, and Perspectives. *Adv. Energy Mater.* **10**, 1903977 (2020).

164. Zhang, C. *et al.* A ZnCl2 water-in-salt electrolyte for a reversible Zn metal anode. *Chem. Commun.* **54**, 14097–14099 (2018).

165. Zhao, S. *et al.* A Heteroanionic Zinc Ion Conductor for Dendrite-Free Zn Metal Anodes. *Adv. Mater.* **35**, 2300195 (2023).

166. Zhi, J., Zhao, S., Zhou, M., Wang, R. & Huang, F. A zinc-conducting chalcogenide electrolyte. *Sci. Adv.* **9**, eade2217 (2023).

167. Naveed, A. *et al.* A Highly Reversible Zn Anode with Intrinsically Safe Organic Electrolyte for Long-Cycle-Life Batteries. *Adv. Mater.* **31**, 1900668 (2019).

168. Naveed, A., Yang, H., Yang, J., Nuli, Y. & Wang, J. Highly Reversible and Rechargeable Safe Zn Batteries Based on a Triethyl Phosphate Electrolyte. *Angew. Chem. Int. Ed.* **58**, 2760–2764 (2019).

169. Liu, Z. *et al.* Voltage issue of aqueous rechargeable metal-ion batteries. *Chem. Soc. Rev.* **49**, 180–232 (2020).

170. Yang, H. *et al.* Constructing a Super-Saturated Electrolyte Front Surface for Stable Rechargeable Aqueous Zinc Batteries. *Angew. Chem. Int. Ed.* **59**, 9377–9381 (2020).

171. Qiu, H. *et al.* Zinc anode-compatible in-situ solid electrolyte interphase via cation solvation modulation. *Nat. Commun.* **10**, 5374 (2019).

172. Faro, T. M. C., Thim, G. P. & Skaf, M. S. A Lennard-Jones plus Coulomb potential for Al3+ ions in aqueous solutions. *J. Chem. Phys.* **132**, 114509 (2010).

173. Dezfoli, A. A., Mehrabian, M. A. & Hashemipour, H. Molecular Dynamics Simulation of Heavy Metal Ions in Aqueous Solution Using Lennard-Jones 12-6 Potential. *Chem. Eng. Commun.* **202**, 1685–1692 (2015).

174. Chao, D. *et al.* An Electrolytic Zn–MnO2 Battery for High-Voltage and Scalable Energy Storage. *Angew. Chem.* **131**, 7905–7910 (2019).

175. Hou, Z. *et al.* Surfactant widens the electrochemical window of an aqueous electrolyte for better rechargeable aqueous sodium/zinc battery. *J. Mater. Chem. A* **5**, 730–738 (2017).

176. Cao, L., Li, D., Deng, T., Li, Q. & Wang, C. Hydrophobic Organic-Electrolyte-Protected Zinc Anodes for Aqueous Zinc Batteries. *Angew. Chem. Int. Ed.* **59**, 19292–19296 (2020).

177. Li, N. *et al.* Bi-Cation Electrolyte for a 1.7 V Aqueous Zn Ion Battery. *ACS Appl. Mater. Interfaces* **12**, 13790–13796 (2020).

178. McLarnon, F. R. & Cairns, E. J. The Secondary Alkaline Zinc Electrode. *J. Electrochem. Soc.* **138**, 645 (1991).

179. Shaigan, N., Qu, W. & Takeda, T. Morphology Control of Electrodeposited Zinc from Alkaline Zincate Solutions for Rechargeable Zinc Air Batteries. *ECS Meet. Abstr.* **MA2010-01**, 758 (2010).

180. Han, C., Li, W., Liu, H. K., Dou, S. & Wang, J. Principals and strategies for constructing a highly reversible zinc metal anode in aqueous batteries. *Nano Energy* **74**, 104880 (2020).

181. Kasiri, G., Trócoli, R., Bani Hashemi, A. & La Mantia, F. An electrochemical investigation of the aging of copper hexacyanoferrate during the operation in zinc-ion batteries. *Electrochimica Acta* **222**, 74–83 (2016).

182. Venkata Narayanan, N. S., Ashokraj, B. V. & Sampath, S. Ambient temperature, zinc ion-conducting, binary molten electrolyte based on acetamide and zinc perchlorate: Application in rechargeable zinc batteries. *J. Colloid Interface Sci.* **342**, 505–512 (2010).

183. Hu, Z., Li, Y., Gu, J. & Kan, J. Effect of Electrolyte Composition on Zn Electrode in Weak Acidic Aqueous Electrolyte. *Int. J. Electrochem. Sci.* **11**, 8571–8580 (2016).

184. Mainar, A. R. *et al.* An overview of progress in electrolytes for secondary zinc-air batteries and other storage systems based on zinc. *J. Energy Storage* **15**, 304–328 (2018).

185. Zhou, J. *et al.* Investigation of V2O5 as a low-cost rechargeable aqueous zinc ion battery cathode. *Chem. Commun.* **54**, 4457–4460 (2018).

186. Peng, Z. *et al.* Novel layered iron vanadate cathode for high-capacity aqueous rechargeable zinc batteries. *Chem. Commun.* **54**, 4041–4044 (2018).

187. Wang, F. *et al.* Highly reversible zinc metal anode for aqueous batteries. *Nat. Mater.* **17**, 543–549 (2018).

188. Xu, M., Ivey, D. G., Xie, Z., Qu, W. & Dy, E. The state of water in 1-butly-1-methyl-pyrrolidinium bis(trifluoromethanesulfonyl)imide and its effect on Zn/Zn(II) redox behavior. *Electrochimica Acta* **97**, 289–295 (2013).

189. Suo, L. *et al.* "Water-in-salt" electrolyte enables high-voltage aqueous lithium-ion chemistries. *Science* **350**, 938–943 (2015).

190. Yamada, Y. *et al.* Unusual Stability of Acetonitrile-Based Superconcentrated Electrolytes for Fast-Charging Lithium-Ion Batteries. *J. Am. Chem. Soc.* **136**, 5039–5046 (2014).

191. Zhao, J. *et al.* “Water-in-deep eutectic solvent” electrolytes enable zinc metal anodes for rechargeable aqueous batteries. *Nano Energy* **57**, 625–634 (2019).

192. Hu, P. *et al.* Zn/V2O5 Aqueous Hybrid-Ion Battery with High Voltage Platform and Long Cycle Life. *ACS Appl. Mater. Interfaces* **9**, 42717–42722 (2017).

193. Blanc, L. E., Kundu, D. & Nazar, L. F. Scientific Challenges for the Implementation of Zn-Ion Batteries. *Joule* **4**, 771–799 (2020).

194. Ye, Z. *et al.* Advances in Zn-ion batteries via regulating liquid electrolyte. *Energy Storage Mater.* **32**, 290–305 (2020).

195. Qiu, N., Chen, H., Yang, Z., Sun, S. & Wang, Y. Synthesis of manganese-based complex as cathode material for aqueous rechargeable batteries. *RSC Adv.* **8**, 15703–15708 (2018).

196. Zhao, S. *et al.* Unravelling the reaction chemistry and degradation mechanism in aqueous Zn/MnO2 rechargeable batteries. *J. Mater. Chem. A* **6**, 5733–5739 (2018).

197. Chamoun, M., Brant, W. R., Tai, C.-W., Karlsson, G. & Noréus, D. Rechargeability of aqueous sulfate Zn/MnO2 batteries enhanced by accessible Mn2+ ions. *Energy Storage Mater.* **15**, 351–360 (2018).

198. Ma, L. *et al.* Initiating a mild aqueous electrolyte Co3O4/Zn battery with 2.2 V-high voltage and 5000-cycle lifespan by a Co(III) rich-electrode. *Energy Environ. Sci.* **11**, 2521–2530 (2018).

199. Liu, B. *et al.* Novel 3D Nanoporous Zn–Cu Alloy as Long-Life Anode toward High-Voltage Double Electrolyte Aqueous Zinc-Ion Batteries. *Small* **16**, 2001323 (2020).

200. Li, C. *et al.* Spatially homogeneous copper foam as surface dendrite-free host for zinc metal anode. *Chem. Eng. J.* **379**, 122248 (2020).

201. Cui, Y. *et al.* Challenges, Strategies, and Perspectives of Anode Protection in Aqueous Zinc-Ion Batteries. *ACS Mater. Lett.* 611–626 (2024) doi:10.1021/acsmaterialslett.3c01385.

202. Li, H., Guo, S. & Zhou, H. Recent advances in manipulating strategy of aqueous electrolytes for Zn anode stabilization. *Energy Storage Mater.* **56**, 227–257 (2023).

203. Lu, W., Zhang, C., Zhang, H. & Li, X. Anode for Zinc-Based Batteries: Challenges, Strategies, and Prospects. *ACS Energy Lett.* **6**, 2765–2785 (2021).

204. Liang, Y., Qiu, M., Sun, P. & Mai, W. Comprehensive Review of Electrolyte Modification Strategies for Stabilizing Zn Metal Anodes. *Adv. Funct. Mater.* **33**, 2304878 (2023).

205. Yang, Q. *et al.* Do Zinc Dendrites Exist in Neutral Zinc Batteries: A Developed Electrohealing Strategy to In Situ Rescue In-Service Batteries. *Adv. Mater.* **31**, 1903778 (2019).

206. Liu, W. *et al.* Metallic Particles-Induced Surface Reconstruction Enabling Highly Durable Zinc Metal Anode. *Adv. Funct. Mater.* **33**, 2302661 (2023).

207. Zou, P. *et al.* Polymorph Evolution Mechanisms and Regulation Strategies of Lithium Metal Anode under Multiphysical Fields. *Chem. Rev.* **121**, 5986–6056 (2021).

208. He, P. & Huang, J. Detrimental Effects of Surface Imperfections and Unpolished Edges on the Cycling Stability of a Zinc Foil Anode. *ACS Energy Lett.* **6**, 1990–1995 (2021).

209. Zhou, M. *et al.* Surface-Preferred Crystal Plane for a Stable and Reversible Zinc Anode. *Adv. Mater.* **33**, 2100187 (2021).

210. Chen, Z. *et al.* Texture Control of Commercial Zn Foils Prolongs Their Reversibility as Aqueous Battery Anodes. *ACS Energy Lett.* **7**, 3564–3571 (2022).

211. Pu, S. D. *et al.* Achieving Ultrahigh-Rate Planar and Dendrite-Free Zinc Electroplating for Aqueous Zinc Battery Anodes. *Adv. Mater.* **34**, 2202552 (2022).

212. Bard, A. J. *Electrochemical Methods: Fundamentals and Applications / Allen J. Bard, Larry R. Faulkner, Department of Chemistry and Biochemistry, University of Texas at Austin.* (John Wiley & Sons, Inc., Hoboken, NJ, 2001).

213. Zang, X., Shen, C., Sanghadasa, M. & Lin, L. High-Voltage Supercapacitors Based on Aqueous Electrolytes. *ChemElectroChem* **6**, 976–988 (2019).

214. Li, C., Xie, X., Liang, S. & Zhou, J. Issues and Future Perspective on Zinc Metal Anode for Rechargeable Aqueous Zinc-ion Batteries. *ENERGY Environ. Mater.* **3**, 146–159 (2020).

215. Strmcnik, D., Lopes, P. P., Genorio, B., Stamenkovic, V. R. & Markovic, N. M. Design principles for hydrogen evolution reaction catalyst materials. *Nano Energy* **29**, 29–36 (2016).

216. McBreen, J. Zinc Electrode Shape Change in Secondary Cells. *J. Electrochem. Soc.* **119**, 1620 (1972).

217. Hao, J. *et al.* Deeply understanding the Zn anode behaviour and corresponding improvement strategies in different aqueous Zn-based batteries. *Energy Environ. Sci.* **13**, 3917–3949 (2020).

218. Hao, J. *et al.* Designing Dendrite-Free Zinc Anodes for Advanced Aqueous Zinc Batteries. *Adv. Funct. Mater.* **30**, 2001263 (2020).

219. Wang, D. *et al.* Insight on Organic Molecules in Aqueous Zn-Ion Batteries with an Emphasis on the Zn Anode Regulation. *Adv. Energy Mater.* **12**, 2102707 (2022).

220. Lu, W., Xie, C., Zhang, H. & Li, X. Inhibition of Zinc Dendrite Growth in Zinc-Based Batteries. *ChemSusChem* **11**, 3996–4006 (2018).

221. Li, H. *et al.* Enhancement on Cycle Performance of Zn Anodes by Activated Carbon Modification for Neutral Rechargeable Zinc Ion Batteries. *J. Electrochem. Soc.* **162**, A1439 (2015).

222. Lu, Z., Wu, Y., Ding, L., Wei, Y. & Wang, H. A Lamellar MXene (Ti3C2Tx)/PSS Composite Membrane for Fast and Selective Lithium-Ion Separation. *Angew. Chem.* **133**, 22439–22443 (2021).

223. Cui, Y. *et al.* An Interface-Bridged Organic–Inorganic Layer that Suppresses Dendrite Formation and Side Reactions for Ultra-Long-Life Aqueous Zinc Metal Anodes. *Angew. Chem. Int. Ed.* **59**, 16594–16601 (2020).

224. Yang, Q. *et al.* Hydrogen-Substituted Graphdiyne Ion Tunnels Directing Concentration Redistribution for Commercial-Grade Dendrite-Free Zinc Anodes. *Adv. Mater.* **32**, 2001755 (2020).

225. Kang, L. *et al.* Nanoporous CaCO3 Coatings Enabled Uniform Zn Stripping/Plating for Long-Life Zinc Rechargeable Aqueous Batteries. *Adv. Energy Mater.* **8**, 1801090 (2018).

226. Deng, C. *et al.* A Sieve-Functional and Uniform-Porous Kaolin Layer toward Stable Zinc Metal Anode. *Adv. Funct. Mater.* **30**, 2000599 (2020).

227. Hong, L. *et al.* Boosting the Zn-ion transfer kinetics to stabilize the Zn metal interface for high-performance rechargeable Zn-ion batteries. *J. Mater. Chem. A* **9**, 16814–16823 (2021).

228. Yan, H., Li, S., Nan, Y., Yang, S. & Li, B. Ultrafast Zinc–Ion–Conductor Interface toward High-Rate and Stable Zinc Metal Batteries. *Adv. Energy Mater.* **11**, 2100186 (2021).

229. Yang, Y. *et al.* Redistributing Zn-ion flux by interlayer ion channels in Mg-Al layered double hydroxide-based artificial solid electrolyte interface for ultra-stable and dendrite-free Zn metal anodes. *Energy Storage Mater.* **41**, 230–239 (2021).

230. Zhao, Z. *et al.* Long-life and deeply rechargeable aqueous Zn anodes enabled by a multifunctional brightener-inspired interphase. *Energy Environ. Sci.* **12**, 1938–1949 (2019).

231. Zhu, M. *et al.* A Patternable and In Situ Formed Polymeric Zinc Blanket for a Reversible Zinc Anode in a Skin-Mountable Microbattery. *Adv. Mater.* **33**, 2007497 (2021).

232. Li, Z. *et al.* Uniformizing the electric field distribution and ion migration during zinc plating/stripping via a binary polymer blend artificial interphase. *J. Mater. Chem. A* **8**, 17725–17731 (2020).

233. Cao, Z. *et al.* Eliminating Zn dendrites by commercial cyanoacrylate adhesive for zinc ion battery. *Energy Storage Mater.* **36**, 132–138 (2021).

234. Chen, P. *et al.* An Artificial Polyacrylonitrile Coating Layer Confining Zinc Dendrite Growth for Highly Reversible Aqueous Zinc-Based Batteries. *Adv. Sci.* **8**, 2100309 (2021).

235. Zhang, X. *et al.* Ultra-long-life and highly reversible Zn metal anodes enabled by a desolvation and deanionization interface layer. *Energy Environ. Sci.* **14**, 3120–3129 (2021).

236. Hieu, L. T., So, S., Kim, I. T. & Hur, J. Zn anode with flexible β-PVDF coating for aqueous Zn-ion batteries with long cycle life. *Chem. Eng. J.* **411**, 128584 (2021).

237. Yang, Y. *et al.* Synergistic Manipulation of Zn2+ Ion Flux and Desolvation Effect Enabled by Anodic Growth of a 3D ZnF2 Matrix for Long-Lifespan and Dendrite-Free Zn Metal Anodes. *Adv. Mater.* **33**, 2007388 (2021).

238. Xie, X. *et al.* Manipulating the ion-transfer kinetics and interface stability for high-performance zinc metal anodes. *Energy Environ. Sci.* **13**, 503–510 (2020).

239. Cao, P. *et al.* Fast-Charging and Ultrahigh-Capacity Zinc Metal Anode for High-Performance Aqueous Zinc-Ion Batteries. *Adv. Funct. Mater.* **31**, 2100398 (2021).

240. Hao, J. *et al.* An In-Depth Study of Zn Metal Surface Chemistry for Advanced Aqueous Zn-Ion Batteries. *Adv. Mater.* **32**, 2003021 (2020).

241. Yang, J. *et al.* Zinc Anode for Mild Aqueous Zinc-Ion Batteries: Challenges, Strategies, and Perspectives. *Nano-Micro Lett.* **14**, 42 (2022).

242. Zhang, R. *et al.* Conductive Nanostructured Scaffolds Render Low Local Current Density to Inhibit Lithium Dendrite Growth. *Adv. Mater.* **28**, 2155–2162 (2016).

243. Zhou, Z. *et al.* Graphene oxide-modified zinc anode for rechargeable aqueous batteries. *Chem. Eng. Sci.* **194**, 142–147 (2019).

244. Shen, C. *et al.* Graphene-Boosted, High-Performance Aqueous Zn-Ion Battery. *ACS Appl. Mater. Interfaces* **10**, 25446–25453 (2018).

245. Xia, A., Pu, X., Tao, Y., Liu, H. & Wang, Y. Graphene oxide spontaneous reduction and self-assembly on the zinc metal surface enabling a dendrite-free anode for long-life zinc rechargeable aqueous batteries. *Appl. Surf. Sci.* **481**, 852–859 (2019).

246. Li, Z. *et al.* Pencil Drawing Stable Interface for Reversible and Durable Aqueous Zinc-Ion Batteries. *Adv. Funct. Mater.* **31**, 2006495 (2021).

247. Dong, L. *et al.* Flexible and conductive scaffold-stabilized zinc metal anodes for ultralong-life zinc-ion batteries and zinc-ion hybrid capacitors. *Chem. Eng. J.* **384**, 123355 (2020).

248. Lee, Y., Ma, B. & Bai, P. Concentration polarization and metal dendrite initiation in isolated electrolyte microchannels. *Energy Environ. Sci.* **13**, 3504–3513 (2020).

249. Zhang, N. *et al.* Direct Self-Assembly of MXene on Zn Anodes for Dendrite-Free Aqueous Zinc-Ion Batteries. *Angew. Chem. Int. Ed.* **60**, 2861–2865 (2021).

250. Zhou, J. *et al.* Ultrathin Surface Coating of Nitrogen-Doped Graphene Enables Stable Zinc Anodes for Aqueous Zinc-Ion Batteries. *Adv. Mater.* **33**, 2101649 (2021).

251. Wang, T. *et al.* Planar and dendrite-free zinc deposition enabled by exposed crystal plane optimization of zinc anode. *Energy Storage Mater.* **53**, 273–304 (2022).

252. Cao, J. *et al.* Manipulating Crystallographic Orientation of Zinc Deposition for Dendrite-free Zinc Ion Batteries. *Adv. Energy Mater.* **11**, 2101299 (2021).

253. Li, Q. *et al.* Dendrites issues and advances in Zn anode for aqueous rechargeable Zn-based batteries. *EcoMat* **2**, e12035 (2020).

254. Mackinnon, D. J., Brannen, J. M. & Fenn, P. L. Characterization of impurity effects in zinc electrowinning from industrial acid sulphate electrolyte. *J. Appl. Electrochem.* **17**, 1129–1143 (1987).

255. Zhang, H. *et al.* Inducing the Preferential Growth of Zn (002) Plane for Long Cycle Aqueous Zn-Ion Batteries. *Adv. Energy Mater.* **13**, 2203254 (2023).

256. Yuan, D. *et al.* Anion Texturing Towards Dendrite-Free Zn Anode for Aqueous Rechargeable Batteries. *Angew. Chem.* **133**, 7289–7295 (2021).

257. Shi, X. *et al.* Homogeneous Deposition of Zinc on Three-Dimensional Porous Copper Foam as a Superior Zinc Metal Anode. *ACS Sustain. Chem. Eng.* **7**, 17737–17746 (2019).

258. Kang, Z. *et al.* 3D Porous Copper Skeleton Supported Zinc Anode toward High Capacity and Long Cycle Life Zinc Ion Batteries. *ACS Sustain. Chem. Eng.* **7**, 3364–3371 (2019).

259. Zhang, Q. *et al.* Simultaneously Regulating the Ion Distribution and Electric Field to Achieve Dendrite-Free Zn Anode. *Small* **16**, 2000929 (2020).

260. Zhang, G. *et al.* 3D-Printed Multi-Channel Metal Lattices Enabling Localized Electric-Field Redistribution for Dendrite-Free Aqueous Zn Ion Batteries. *Adv. Energy Mater.* **11**, 2003927 (2021).

261. Guo, W. *et al.* Dendrite-free Zn anode with dual channel 3D porous frameworks for rechargeable Zn batteries. *Energy Storage Mater.* **30**, 104–112 (2020).

262. Xiao, R. *et al.* Localizing concentrated electrolyte in pore geometry for highly reversible aqueous Zn metal batteries. *Chem. Eng. J.* **420**, 129642 (2021).

263. Wang, J. *et al.* A Chemically Polished Zinc Metal Electrode with a Ridge-like Structure for Cycle-Stable Aqueous Batteries. *ACS Appl. Mater. Interfaces* **12**, 23028–23034 (2020).

264. Wang, J. M., Zhang, L., Zhang, C. & Zhang, J. Q. Effects of bismuth ion and tetrabutylammonium bromide on the dendritic growth of zinc in alkaline zincate solutions. *J. Power Sources* **102**, 139–143 (2001).

265. Mansfeld, F. & Gilman, S. The Effect of Lead Ions on the Dissolution and Deposition Characteristics of a Zinc Single Crystal in 6 N KOH. *J. Electrochem. Soc.* **117**, 588 (1970).

266. McBreen, J. & Gannon, E. Bismuth oxide as an additive in pasted zinc electrodes. *J. Power Sources* **15**, 169–177 (1985).

267. Chu, M. G., McBreen, J. & Adzic, G. Substrate Effects on Zinc Deposition from Zincate Solutions: I . Deposition on Cu, Au, Cd and Zn. *J. Electrochem. Soc.* **128**, 2281 (1981).

268. Ding, F. *et al.* Dendrite-Free Lithium Deposition via Self-Healing Electrostatic Shield Mechanism. *J. Am. Chem. Soc.* **135**, 4450–4456 (2013).

269. Hu, P. *et al.* Highly Durable Na2V6O16·1.63H2O Nanowire Cathode for Aqueous Zinc-Ion Battery. *Nano Lett.* **18**, 1758–1763 (2018).

270. Hoang, T. K. A. *et al.* Sustainable gel electrolyte containing Pb2+ as corrosion inhibitor and dendrite suppressor for the zinc anode in the rechargeable hybrid aqueous battery. *Mater. Today Energy* **4**, 34–40 (2017).

271. Mitha, A., Yazdi, A. Z., Ahmed, M. & Chen, P. Surface Adsorption of Polyethylene Glycol to Suppress Dendrite Formation on Zinc Anodes in Rechargeable Aqueous Batteries. *ChemElectroChem* **5**, 2409–2418 (2018).

272. Kakeya, T., Nakata, A., Arai, H. & Ogumi, Z. Enhanced zinc electrode rechargeability in alkaline electrolytes containing hydrophilic organic materials with positive electrode compatibility. *J. Power Sources* **407**, 180–184 (2018).

273. Mor, E. D. & Beccaria, A. M. Inhibitory Action of Acrylonitrile on the Corrosion of Zinc in Sea Water. *Br. Corros. J.* **8**, 25–27 (1973).

274. Chladil, L., Čech, O., Smejkal, J. & Vanýsek, P. Study of zinc deposited in the presence of organic additives for zinc-based secondary batteries. *J. Energy Storage* **21**, 295–300 (2019).

275. Hosseini, S., Han, S. J., Arponwichanop, A., Yonezawa, T. & Kheawhom, S. Ethanol as an electrolyte additive for alkaline zinc-air flow batteries. *Sci. Rep.* **8**, 11273 (2018).

276. Hosseini, S. *et al.* Discharge Performance of Zinc-Air Flow Batteries Under the Effects of Sodium Dodecyl Sulfate and Pluronic F-127. *Sci. Rep.* **8**, 14909 (2018).

277. Hosseini, S. *et al.* The Influence of Dimethyl Sulfoxide as Electrolyte Additive on Anodic Dissolution of Alkaline Zinc-Air Flow Battery. *Sci. Rep.* **9**, 14958 (2019).

278. Hoang, T. K. A. *et al.* Performance of Thixotropic Gel Electrolytes in the Rechargeable Aqueous Zn/LiMn2O4 Battery. *ACS Sustain. Chem. Eng.* **5**, 1804–1811 (2017).

279. Sun, K. E. K. *et al.* Suppression of Dendrite Formation and Corrosion on Zinc Anode of Secondary Aqueous Batteries. *ACS Appl. Mater. Interfaces* **9**, 9681–9687 (2017).

280. Hoang, T. K. A. *et al.* Sustainable Gel Electrolyte Containing Pyrazole as Corrosion Inhibitor and Dendrite Suppressor for Aqueous Zn/LiMn2O4 Battery. *ChemSusChem* **10**, 2816–2822 (2017).

281. Mitha, A. *et al.* Thixotropic gel electrolyte containing poly(ethylene glycol) with high zinc ion concentration for the secondary aqueous Zn/LiMn2O4 battery. *J. Electroanal. Chem.* **836**, 1–6 (2019).

282. Xiong, W. *et al.* Controlling the sustainability and shape change of the zinc anode in rechargeable aqueous Zn/LiMn2O4 battery. *Energy Storage Mater.* **15**, 131–138 (2018).

283. Sun, Q., Cheng, H., Nie, W., Lu, X. & Zhao, H. A Comprehensive Understanding of Interlayer Engineering in Layered Manganese and Vanadium Cathodes for Aqueous Zn-Ion Batteries. *Chem. – Asian J.* **17**, e202200067 (2022).

284. Zhou, T. *et al.* Cathode materials for aqueous zinc-ion batteries: A mini review. *J. Colloid Interface Sci.* **605**, 828–850 (2022).

285. Zhang, Y., Chen, A. & Sun, J. Promise and challenge of vanadium-based cathodes for aqueous zinc-ion batteries. *J. Energy Chem.* **54**, 655–667 (2021).

286. Mao, M. *et al.* Charge storage mechanism of MOF-derived Mn2O3 as high performance cathode of aqueous zinc-ion batteries. *J. Energy Chem.* **52**, 277–283 (2021).

287. Park, J.-S. *et al.* Open-Structured Vanadium Dioxide as an Intercalation Host for Zn Ions: Investigation by First-Principles Calculation and Experiments. *Chem. Mater.* **30**, 6777–6787 (2018).

288. Xia, C. *et al.* Rechargeable Aqueous Zinc-Ion Battery Based on Porous Framework Zinc Pyrovanadate Intercalation Cathode. *Adv. Mater.* **30**, 1705580 (2018).

289. Soundharrajan, V. *et al.* Na2V6O16·3H2O Barnesite Nanorod: An Open Door to Display a Stable and High Energy for Aqueous Rechargeable Zn-Ion Batteries as Cathodes. *Nano Lett.* **18**, 2402–2410 (2018).

290. Yang, Y. *et al.* Li+ intercalated V2O5·nH2O with enlarged layer spacing and fast ion diffusion as an aqueous zinc-ion battery cathode. *Energy Environ. Sci.* **11**, 3157–3162 (2018).

291. Sun, W. *et al.* Zn/MnO2 Battery Chemistry With H+ and Zn2+ Coinsertion. *J. Am. Chem. Soc.* **139**, 9775–9778 (2017).

292. Gao, X. *et al.* H+-Insertion Boosted α-MnO2 for an Aqueous Zn-Ion Battery. *Small* **16**, 1905842 (2020).

293. Zhu, K. *et al.* Synergistic H+/Zn2+ dual ion insertion mechanism in high-capacity and ultra-stable hydrated VO2 cathode for aqueous Zn-ion batteries. *Energy Storage Mater.* **29**, 60–70 (2020).

294. Pang, Q. *et al.* H2V3O8 Nanowire/Graphene Electrodes for Aqueous Rechargeable Zinc Ion Batteries with High Rate Capability and Large Capacity. *Adv. Energy Mater.* **8**, 1800144 (2018).

295. Lai, J., Zhu, H., Zhu, X., Koritala, H. & Wang, Y. Interlayer-Expanded V6O13·nH2O Architecture Constructed for an Advanced Rechargeable Aqueous Zinc-Ion Battery. *ACS Appl. Energy Mater.* **2**, 1988–1996 (2019).

296. Zhu, K., Wu, T. & Huang, K. NaCa0.6V6O16·3H2O as an Ultra-Stable Cathode for Zn-Ion Batteries: The Roles of Pre-Inserted Dual-Cations and Structural Water in V3O8 Layer. *Adv. Energy Mater.* **9**, 1901968 (2019).

297. Chomkhuntod, P., Hantanasirisakul, K., Duangdangchote, S., Phattharasupakun, N. & Sawangphruk, M. The charge density of intercalants inside layered birnessite manganese oxide nanosheets determining Zn-ion storage capability towards rechargeable Zn-ion batteries. *J. Mater. Chem. A* **10**, 5561–5568 (2022).

298. Zhai, X.-Z. *et al.* Layered Birnessite Cathode with a Displacement/Intercalation Mechanism for High-Performance Aqueous Zinc-Ion Batteries. *Nano-Micro Lett.* **12**, 56 (2020).

299. Lee, B. *et al.* Electrochemically-induced reversible transition from the tunneled to layered polymorphs of manganese dioxide. *Sci. Rep.* **4**, 6066 (2014).

300. Alfaruqi, M. H. *et al.* Electrochemically Induced Structural Transformation in a γ-MnO2 Cathode of a High Capacity Zinc-Ion Battery System. *Chem. Mater.* **27**, 3609–3620 (2015).

301. Jin, Y. *et al.* Joint Charge Storage for High-Rate Aqueous Zinc–Manganese Dioxide Batteries. *Adv. Mater.* **31**, 1900567 (2019).

302. Liu, W. *et al.* β-MnO2 with proton conversion mechanism in rechargeable zinc ion battery. *J. Energy Chem.* **56**, 365–373 (2021).

303. Guo, X. *et al.* Zn/MnO2 battery chemistry with dissolution-deposition mechanism. *Mater. Today Energy* **16**, 100396 (2020).

304. Li, H. *et al.* Interface regulated MnO2/Mn2+ redox chemistry in aqueous Zn ion batteries. *Chem. Eng. J.* **446**, 137205 (2022).

305. Conway, B. E. *Electrochemical Supercapacitors*. (Springer US, Boston, MA, 1999). doi:10.1007/978-1-4757-3058-6.

306. *Nanoscience and Technology: A Collection of Reviews from Nature Journals*. (World Scientific ; Nature Pub. Group, Singapore : London, 2010).

307. Augustyn, V., Simon, P. & Dunn, B. Pseudocapacitive oxide materials for high-rate electrochemical energy storage. *Energy Environ. Sci.* **7**, 1597–1614 (2014).

308. Simon, P., Gogotsi, Y. & Dunn, B. Where Do Batteries End and Supercapacitors Begin? *Science* **343**, 1210–1211 (2014).

309. Liu, J. *et al.* Advanced Energy Storage Devices: Basic Principles, Analytical Methods, and Rational Materials Design. *Adv. Sci.* **5**, 1700322 (2018).

310. Brousse, T., Bélanger, D. & Long, J. W. To Be or Not To Be Pseudocapacitive? *J. Electrochem. Soc.* **162**, A5185 (2015).

311. Ribeiro, D. V. & Abrantes, J. C. C. Application of electrochemical impedance spectroscopy (EIS) to monitor the corrosion of reinforced concrete: A new approach. *Constr. Build. Mater.* **111**, 98–104 (2016).

312. Liu, J., Xia, H., Xue, D. & Lu, L. Double-Shelled Nanocapsules of V2O5-Based Composites as High-Performance Anode and Cathode Materials for Li Ion Batteries. *J. Am. Chem. Soc.* **131**, 12086–12087 (2009).

313. Yue, Y. & Liang, H. Micro- and Nano-Structured Vanadium Pentoxide (V2O5) for Electrodes of Lithium-Ion Batteries. *Adv. Energy Mater.* **7**, 1602545 (2017).

314. Yao, J., Li, Y., Massé, R. C., Uchaker, E. & Cao, G. Revitalized interest in vanadium pentoxide as cathode material for lithium-ion batteries and beyond. *Energy Storage Mater.* **11**, 205–259 (2018).

315. Javed, M. S. *et al.* 2D V2O5 nanosheets as a binder-free high-energy cathode for ultrafast aqueous and flexible Zn-ion batteries. *Nano Energy* **70**, 104573 (2020).

316. Chen, S., Li, K., Hui, K. S. & Zhang, J. Regulation of Lamellar Structure of Vanadium Oxide via Polyaniline Intercalation for High-Performance Aqueous Zinc-Ion Battery. *Adv. Funct. Mater.* **30**, 2003890 (2020).

317. Xu, Y. *et al.* Vanadium Oxide Pillared by Interlayer Mg2+ Ions and Water as Ultralong-Life Cathodes for Magnesium-Ion Batteries. *Chem* **5**, 1194–1209 (2019).

318. Yu, W., Shang, W., Zhao, Z., Ma, Y. & Tan, P. Elucidating the performance variations and critical issues of Zn electrodes in different types of aqueous electrolytes for Zn-based rechargeable batteries. *Electrochimica Acta* **425**, 140702 (2022).

319. Yu, W. *et al.* Rechargeable aqueous Zn-LiMn2O4 hybrid batteries with high performance and safety for energy storage. *J. Energy Storage* **45**, 103744 (2022).

320. Wang, Z. *et al.* Simultaneous regulation of cations and anions in an electrolyte for high-capacity, high-stability aqueous zinc–vanadium batteries. *eScience* **2**, 209–218 (2022).

321. Feng, Z. *et al.* Dual ions enable vanadium oxide hydration with superior Zn2+ storage for aqueous zinc-ion batteries. *Chem. Eng. J.* **433**, 133795 (2022).

322. Liu, Y. & Wu, X. Hydrogen and sodium ions co-intercalated vanadium dioxide electrode materials with enhanced zinc ion storage capacity. *Nano Energy* **86**, 106124 (2021).

323. Zhang, N. *et al.* Hydrated Layered Vanadium Oxide as a Highly Reversible Cathode for Rechargeable Aqueous Zinc Batteries. *Adv. Funct. Mater.* **29**, 1807331 (2019).

324. Wang, X. *et al.* A High-Rate and Ultrastable Aqueous Zinc-Ion Battery with a Novel MgV2O6·1.7H2O Nanobelt Cathode. *Small* **17**, 2100318 (2021).

325. Liu, Y. *et al.* Mn2+ Ions Confined by Electrode Microskin for Aqueous Battery beyond Intercalation Capacity. *Adv. Energy Mater.* **10**, 2002578 (2020).

326. Liu, Z., Pulletikurthi, G. & Endres, F. A Prussian Blue/Zinc Secondary Battery with a Bio-Ionic Liquid–Water Mixture as Electrolyte. *ACS Appl. Mater. Interfaces* **8**, 12158–12164 (2016).

327. Cheng, Y. *et al.* Highly Reversible Zinc-Ion Intercalation into Chevrel Phase Mo6S8 Nanocubes and Applications for Advanced Zinc-Ion Batteries. *ACS Appl. Mater. Interfaces* **8**, 13673–13677 (2016).

328. Zhang, B. *et al.* An aqueous rechargeable battery based on zinc anode and Na0.95MnO2. *Chem. Commun.* **50**, 1209–1211 (2014).

329. Zhang, L., Chen, L., Zhou, X. & Liu, Z. Morphology-Dependent Electrochemical Performance of Zinc Hexacyanoferrate Cathode for Zinc-Ion Battery. *Sci. Rep.* **5**, 18263 (2015).

330. Kaveevivitchai, W. & Manthiram, A. High-capacity zinc-ion storage in an open-tunnel oxide for aqueous and nonaqueous Zn-ion batteries. *J. Mater. Chem. A* **4**, 18737–18741 (2016).

331. Liu, X. *et al.* Zeolitic Imidazolate Frameworks as Zn2+ Modulation Layers to Enable Dendrite-Free Zn Anodes. *Adv. Sci.* **7**, 2002173 (2020).

332. Söllinger, D., Berger, T., Redhammer, G. J., Schoiber, J. & Pokrant, S. Chemical Preintercalation of H2V3O8-reduced Graphene Oxide Composites for Improved Na- and Li-ion Battery Cathodes. *ChemElectroChem* **8**, 4223–4232 (2021).

333. Wang, D. *et al.* Flexible additive free H2V3O8 nanowire membrane as cathode for sodium ion batteries. *Phys. Chem. Chem. Phys.* **18**, 12074–12079 (2016).

334. Oka, Y., Tamada, O., Yao, T. & Yamamoto, N. Synthesis and Crystal Structure of σ-Zn0.25V2O5· H2O with a Novel Type of V2O5Layer. *J. Solid State Chem.* **126**, 65–73 (1996).

335. LLOYD, D. & J, G. ALPHA ZINC VANADIUM (IV) DIVANADATE (V), ALPHA -ZNV3O8. *ALPHA ZINC VANADIUM IV DIVANADATE V ALPHA -ZNV3O8* (1973).

336. Meetsma, A. *et al.* Inversion Symmetry in the Spin-Peierls Compound α'-NaV2O5. *Acta Crystallogr. C* **54**, 1558–1561 (1998).

337. Jiang, H. *et al.* Quench-tailored Al-doped V2O5 nanomaterials for efficient aqueous zinc-ion batteries. *J. Energy Chem.* **70**, 52–58 (2022).

338. Zhu, K., Wu, T. & Huang, K. Understanding the Dissolution and Phase Transformation Mechanisms in Aqueous Zn/α-V2O5 Batteries. *Chem. Mater.* **33**, 4089–4098 (2021).

339. Chen, J. *et al.* Sodium Pre-Intercalated Carbon/V2O5 Constructed by Sustainable Sodium Lignosulfonate for Stable Cathodes in Zinc-Ion Batteries: A Comprehensive Study. *ChemSusChem* **15**, e202200732 (2022).

340. Liu, X. *et al.* Operando pH Measurements Decipher H+/Zn2+ Intercalation Chemistry in High-Performance Aqueous Zn/δ-V2O5 Batteries. *ACS Energy Lett.* **5**, 2979–2986 (2020).

341. Simon, P. & Gogotsi, Y. Materials for electrochemical capacitors. in *Nanoscience and Technology* 320–329 (Co-Published with Macmillan Publishers Ltd, UK, 2009). doi:10.1142/9789814287005_0033.

342. Zhang, K. *et al.* Urchin-Like CoSe2 as a High-Performance Anode Material for Sodium-Ion Batteries. *Adv. Funct. Mater.* **26**, 6728–6735 (2016).

343. Chao, D. *et al.* Array of nanosheets render ultrafast and high-capacity Na-ion storage by tunable pseudocapacitance. *Nat. Commun.* **7**, 12122 (2016).

344. Xia, X. *et al.* Generic Synthesis of Carbon Nanotube Branches on Metal Oxide Arrays Exhibiting Stable High-Rate and Long-Cycle Sodium-Ion Storage. *Small* **12**, 3048–3058 (2016).

345. Chao, D. *et al.* Pseudocapacitive Na-Ion Storage Boosts High Rate and Areal Capacity of Self-Branched 2D Layered Metal Chalcogenide Nanoarrays. *ACS Nano* **10**, 10211–10219 (2016).

346. Zhang, N. *et al.* Rechargeable Aqueous Zn–V2O5 Battery with High Energy Density and Long Cycle Life. *ACS Energy Lett.* **3**, 1366–1372 (2018).

347. Wu, T.-H., Lin, Y.-Q., Althouse, Z. D. & Liu, N. Dissolution–Redeposition Mechanism of the MnO2 Cathode in Aqueous Zinc-Ion Batteries. *ACS Appl. Energy Mater.* **4**, 12267–12274 (2021).

348. Zhou, A. *et al.* Manganese-based cathode materials for aqueous rechargeable zinc-ion batteries: recent advance and future prospects. *Mater. Today Chem.* **27**, 101294 (2023).

349. Xie, S., Li, X., Li, Y., Liang, Q. & Dong, L. Material Design and Energy Storage Mechanism of Mn-Based Cathodes for Aqueous Zinc-Ion Batteries. *Chem. Rec.* **22**, e202200201 (2022).

350. Shi, W., Lee, W. S. V. & Xue, J. Recent Development of Mn-based Oxides as Zinc-Ion Battery Cathode. *ChemSusChem* **14**, 1634–1658 (2021).

351. Chu, Y., Ren, L., Hu, Z., Huang, C. & Luo, J. An in-depth understanding of improvement strategies and corresponding characterizations towards Zn anode in aqueous Zn-ions batteries. *Green Energy Environ.* **8**, 1006–1042 (2023).

352. Yuan, Y. *et al.* Understanding intercalation chemistry for sustainable aqueous zinc–manganese dioxide batteries. *Nat. Sustain.* **5**, 890–898 (2022).

353. Chen, H. *et al.* Successive electrochemical conversion reaction to understand the performance of aqueous Zn/MnO2 batteries with Mn2+ additive. *Mater. Today Energy* **20**, 100646 (2021).

354. Guo, X. *et al.* Zn/MnO2 battery chemistry with dissolution-deposition mechanism. *Mater. Today Energy* **16**, 100396 (2020).

355. Zhao, S. *et al.* Unravelling the reaction chemistry and degradation mechanism in aqueous Zn/MnO2 rechargeable batteries. *J. Mater. Chem. A* **6**, 5733–5739 (2018).

356. Yi, Z., Chen, G., Hou, F., Wang, L. & Liang, J. Strategies for the Stabilization of Zn Metal Anodes for Zn-Ion Batteries. *Adv. Energy Mater.* **11**, 2003065 (2021).

357. Yang, Z. *et al.* Revealing the Two-Dimensional Surface Diffusion Mechanism for Zinc Dendrite Formation on Zinc Anode. *Small* **18**, 2104148 (2022).

358. Zheng, J. *et al.* Surface and Interface Engineering of Zn Anodes in Aqueous Rechargeable Zn-Ion Batteries. *Small* **18**, 2200006 (2022).

359. Wu, B. *et al.* Graphene Scroll-Coated α-MnO2 Nanowires as High-Performance Cathode Materials for Aqueous Zn-Ion Battery. *Small* **14**, 1703850 (2018).

360. Shi, M. *et al.* Scalable gas-phase synthesis of 3D microflowers confining MnO2 nanowires for highly-durable aqueous zinc-ion batteries. *J. Power Sources* **463**, 228209 (2020).

361. Huang, J. *et al.* Amphiphilic-molecular templated porous β-MnO2 for high-performance rechargeable aqueous Zn-MnO2 batteries. *Electrochimica Acta* **424**, 140646 (2022).

362. He, B. *et al.* Al doped manganous oxide for high-performance aqueous Zn-ion batteries. *J. Power Sources* **554**, 232353 (2023).

363. Ma, Y. *et al.* Molecular tailoring of MnO2 by bismuth doping to achieve aqueous zinc-ion battery with capacitor-level durability. *Energy Storage Mater.* **48**, 212–222 (2022).

364. Zhao, Y. *et al.* Uncovering sulfur doping effect in MnO2 nanosheets as an efficient cathode for aqueous zinc ion battery. *Energy Storage Mater.* **47**, 424–433 (2022).

365. Qu, W., Cai, Y., Chen, B. & Zhang, M. Heterointerface Engineering-Induced Oxygen Defects for the Manganese Dissolution Inhibition in Aqueous Zinc Ion Batteries. *ENERGY Environ. Mater.* **n/a**, e12645.

366. Zhao, Y. *et al.* Interfacial Designing of MnO2 Half-Wrapped by Aromatic Polymers for High-Performance Aqueous Zinc-Ion Batteries. *Angew. Chem. Int. Ed.* **61**, e202212231 (2022).

367. Deng, W., Xu, Z. & Wang, X. High-donor electrolyte additive enabling stable aqueous zinc-ion batteries. *Energy Storage Mater.* **52**, 52–60 (2022).

368. Feng, D. *et al.* Immunizing Aqueous Zn Batteries against Dendrite Formation and Side Reactions at Various Temperatures via Electrolyte Additives. *Small* **17**, 2103195 (2021).

369. Mu, Y. *et al.* 3D hierarchical graphene matrices enable stable Zn anodes for aqueous Zn batteries. *Nat. Commun.* **14**, 4205 (2023).

370. Liu, B. *et al.* Novel 3D Nanoporous Zn–Cu Alloy as Long-Life Anode toward High-Voltage Double Electrolyte Aqueous Zinc-Ion Batteries. *Small* **16**, 2001323 (2020).

371. Tian, H. *et al.* Three-dimensional Zn-based alloys for dendrite-free aqueous Zn battery in dual-cation electrolytes. *Nat. Commun.* **13**, 7922 (2022).

372. Knehr, K. W. *et al.* Understanding Full-Cell Evolution and Non-chemical Electrode Crosstalk of Li-Ion Batteries. *Joule* **2**, 1146–1159 (2018).

373. Michalak, B., Berkes, B. B., Sommer, H., Brezesinski, T. & Janek, J. Electrochemical Cross-Talk Leading to Gas Evolution and Capacity Fade in LiNi0.5Mn1.5O4/Graphite Full-Cells. *J. Phys. Chem. C* **121**, 211–216 (2017).

374. Song, Y. *et al.* The significance of mitigating crosstalk in lithium-ion batteries: a review. *Energy Environ. Sci.* **16**, 1943–1963 (2023).

375. Kim, M. *et al.* A new mechanism of stabilizing SEI of Si anode driven by crosstalk behavior and its potential for developing high performance Si-based batteries. *Energy Storage Mater.* **55**, 436–444 (2023).

376. Cui, S., Zhang, D., Zhang, G. & Gan, Y. Reaction mechanism for the α-MnO2 cathode in aqueous Zn ion batteries revisited: elucidating the irreversible transformation of α-MnO2 into Zn–vernadite. *J. Mater. Chem. A* **10**, 25620–25632 (2022).

377. Zheng, J. & Archer, L. A. Controlling electrochemical growth of metallic zinc electrodes: Toward affordable rechargeable energy storage systems. *Sci. Adv.* **7**, eabe0219 (2021).

378. Li, H., Guo, S. & Zhou, H. Recent advances in manipulating strategy of aqueous electrolytes for Zn anode stabilization. *Energy Storage Mater.* **56**, 227–257 (2023).

379. Zheng, J. *et al.* Regulating electrodeposition morphology of lithium: towards commercially relevant secondary Li metal batteries. *Chem. Soc. Rev.* **49**, 2701–2750 (2020).

380. Zhang, Q. B. & Hua, Y. Effect of Mn2+ ions on the electrodeposition of zinc from acidic sulphate solutions. *Hydrometallurgy* **99**, 249–254 (2009).

381. Cui, S., Zhang, D., Zhang, G. & Gan, Y. Reaction mechanism for the α-MnO2 cathode in aqueous Zn ion batteries revisited: elucidating the irreversible transformation of α-MnO2 into Zn–vernadite. *J. Mater. Chem. A* **10**, 25620–25632 (2022).

382. Liu, Y. *et al.* Highly efficient dendrite suppressor and corrosion inhibitor based on gelatin/Mn2+ Co-additives for aqueous rechargeable zinc-manganese dioxide battery. *Chem. Eng. J.* **407**, 127189 (2021).

383. Zhang, B. *et al.* Manganese-Based Oxide Cathode Materials for Aqueous Zinc-Ion Batteries: Materials, Mechanism, Challenges, and Strategies. *Chem Bio Eng.* **1**, 113–132 (2024).

384. Zhang, W. & Cheng, C. Y. Manganese metallurgy review. Part III: Manganese control in zinc and copper electrolytes. *Hydrometallurgy* **89**, 178–188 (2007).

385. Zhang, C., Duan, N., Jiang, L. & Xu, F. The impact mechanism of Mn2+ ions on oxygen evolution reaction in zinc sulfate electrolyte. *J. Electroanal. Chem.* **811**, 53–61 (2018).

386. Loukil, N. & Feki, M. Zn–Mn alloy coatings from acidic chloride bath: Effect of deposition conditions on the Zn–Mn electrodeposition-morphological and structural characterization. *Appl. Surf. Sci.* **410**, 574–584 (2017).

387. Pistofidis, N. *et al.* Microstructure of zinc hot-dip galvanized coatings used for corrosion protection. *Mater. Lett.* **60**, 786–789 (2006).

388. Hao, Y. *et al.* Gel Electrolyte Constructing Zn (002) Deposition Crystal Plane Toward Highly Stable Zn Anode. *Adv. Sci.* **9**, 2104832 (2022).

389. Zhang, H. *et al.* Inducing the Preferential Growth of Zn (002) Plane for Long Cycle Aqueous Zn-Ion Batteries. *Adv. Energy Mater.* **13**, 2203254 (2023).

390. Zhang, M. *et al.* Unveiling The Mechanism of The Dendrite Nucleation and Growth in Aqueous Zinc Ion Batteries. *Adv. Energy Mater.* **n/a**, 2303737.

391. Song, G., Li, S., Liu, G., Fu, Q. & Pan, C. Influence of Graphene Oxide Content on the Zn-Gr Composite Layer Prepared by Pulse Reverse Electro-plating. *J. Electrochem. Soc.* **165**, D501 (2018).

392. Jie, J. *et al.* High-performance PVDF-HFP based gel polymer electrolyte with a safe solvent in Li metal polymer battery. *J. Energy Chem.* **49**, 80–88 (2020).

393. Wang, Y., Huang, K., Zhang, P., Li, H. & Mi, H. PVDF-HFP based polymer electrolytes with high Li+ transference number enhancing the cycling performance and rate capability of lithium metal batteries. *Appl. Surf. Sci.* **574**, 151593 (2022).

394. Lu, R. *et al.* PVDF-HFP layer with high porosity and polarity for high-performance lithium metal anodes in both ether and carbonate electrolytes. *Nano Energy* **95**, 107009 (2022).

395. Guo, S. *et al.* PVDF-HFP/LiF Composite Interfacial Film to Enhance the Stability of Li-Metal Anodes. *ACS Appl. Energy Mater.* **3**, 7191–7199 (2020).

396. Pu, W., He, X., Wang, L., Jiang, C. & Wan, C. Preparation of PVDF–HFP microporous membrane for Li-ion batteries by phase inversion. *J. Membr. Sci.* **272**, 11–14 (2006).

397. Miao, R. *et al.* PVDF-HFP-based porous polymer electrolyte membranes for lithium-ion batteries. *J. Power Sources* **184**, 420–426 (2008).

398. Wongchitphimon, S., Wang, R. & Jiraratananon, R. Surface modification of polyvinylidene fluoride-co-hexafluoropropylene (PVDF–HFP) hollow fiber membrane for membrane gas absorption. *J. Membr. Sci.* **381**, 183–191 (2011).

399. Yuan, D. *et al.* Organic-inorganic interlayer enabling the stability of PVDF-HFP modified Li metal for lithium-oxygen batteries. *Appl. Surf. Sci.* **613**, 155863 (2023).

400. Oumghar, K. *et al.* Enhanced piezoelectric properties of PVdF-HFP/PZT nanocomposite for energy harvesting application. *IOP Conf. Ser. Mater. Sci. Eng.* **827**, 012034 (2020).

401. Chakhchaoui, N. *et al.* Improvement of the electroactive β-phase nucleation and piezoelectric properties of PVDF-HFP thin films influenced by TiO2 nanoparticles. *Mater. Today Proc.* **39**, 1148–1152 (2021).

402. Wongchitphimon, S., Wang, R. & Jiraratananon, R. Surface modification of polyvinylidene fluoride-co-hexafluoropropylene (PVDF–HFP) hollow fiber membrane for membrane gas absorption. *J. Membr. Sci.* **381**, 183–191 (2011).

403. Gao, C. *et al.* A high-performance free-standing Zn anode for flexible zinc-ion batteries. *Nanoscale* **13**, 10100–10107 (2021).

404. Yang, C.-C., Lian, Z.-Y., Lin, S. J., Shih, J.-Y. & Chen, W.-H. Preparation and application of PVDF-HFP composite polymer electrolytes in LiNi0.5Co0.2Mn0.3O2 lithium-polymer batteries. *Electrochimica Acta* **134**, 258–265 (2014).

405. Cheng, N. *et al.* Nanosphere-structured hierarchically porous PVDF-HFP fabric for passive daytime radiative cooling via one-step water vapor-induced phase separation. *Chem. Eng. J.* **460**, 141581 (2023).

406. Shen, X. *et al.* Highly Reversible Aqueous Zn-MnO2 Battery by Supplementing Mn2+-Mediated MnO2 Deposition and Dissolution. *Adv. Funct. Mater.* **31**, 2101579 (2021).

407. Wu, F. *et al.* High-Mass-Loading Electrodes for Advanced Secondary Batteries and Supercapacitors. *Electrochem. Energy Rev.* **4**, 382–446 (2021).

408. Wu, X. *et al.* High-Performance, Low-Cost, and Dense-Structure Electrodes with High Mass Loading for Lithium-Ion Batteries. *Adv. Funct. Mater.* **29**, 1903961 (2019).

409. Chen, L. *et al.* Wood-Derived High-Mass-Loading MnO2 Composite Carbon Electrode Enabling High Energy Density and High-Rate Supercapacitor. *Small* **18**, 2201307 (2022).

410. Yu, G., Xie, X., Pan, L., Bao, Z. & Cui, Y. Hybrid nanostructured materials for high-performance electrochemical capacitors. *Nano Energy* **2**, 213–234 (2013).

411. Huang, Z.-H. *et al.* High Mass Loading MnO2 with Hierarchical Nanostructures for Supercapacitors. *ACS Nano* **12**, 3557–3567 (2018).

412. Wang, D. *et al.* Density and porosity optimization of graphene monoliths with high mass-loading for high-volumetric-capacitance electrodes. *Battery Energy* **1**, 20220017 (2022).

413. Zhang, W., Liang, S., Fang, G., Yang, Y. & Zhou, J. Ultra-High Mass-Loading Cathode for Aqueous Zinc-Ion Battery Based on Graphene-Wrapped Aluminum Vanadate Nanobelts. *Nano-Micro Lett.* **11**, 69 (2019).

414. Ma, L., Wang, X. & Sun, J. A strategy associated with conductive binder and 3D current collector for aqueous zinc-ion batteries with high mass loading. *J. Electroanal. Chem.* **873**, 114395 (2020).

415. Wang, N. *et al.* Contribution of Cation Addition to MnO2 Nanosheets on Stable Co3O4 Nanowires for Aqueous Zinc-Ion Battery. *Front. Chem.* **8**, (2020).

416. Rabani, I., Younus, A., Patil, S. & Seo, Y.-S. Fabrication of Fe3O4-incorporated MnO2 nanoflowers as electrodes for enhanced asymmetric supercapacitor performance. *Dalton Trans.* **51**, 14190–14200 (2022).

417. Liu, Y. *et al.* Interfacial Engineering Coupled Valence Tuning of MoO3 Cathode for High-Capacity and High-Rate Fiber-Shaped Zinc-Ion Batteries. *Small* **16**, 1907458 (2020).

418. Gou, L. *et al.* Bi2O3 Induced Ultralong Cycle Lifespan and High Capacity of MnO2 Nanotube Cathodes in Aqueous Zinc-Ion Batteries. *ACS Appl. Energy Mater.* **4**, 7355–7364 (2021).

419. Ma, Y. *et al.* Molecular tailoring of MnO2 by bismuth doping to achieve aqueous zinc-ion battery with capacitor-level durability. *Energy Storage Mater.* **48**, 212–222 (2022).

420. Karaca, E. In situ electrosynthesis of polypyrrole/nano Bi2O4 composite for supercapacitor applications. *J. Mater. Sci. Mater. Electron.* **34**, 1834 (2023).

421. Jiang, M. *et al.* A novel ultrathin single-crystalline Bi2O3 nanosheet wrapped by reduced graphene oxide with improved electron transfer for Li storage. *J. Solid State Electrochem.* **24**, 2487–2497 (2020).

422. Parida, V. K., Srivastava, S. K., Chowdhury, S. & Gupta, A. K. Visible Light-Assisted Degradation of Sulfamethoxazole on 2D/0D Sulfur-Doped Bi2O3/MnO2 Z-Scheme Heterojunction Immobilized Photocatalysts. *Langmuir* **39**, 18846–18865 (2023).

423. Wang, J. *et al.* The role of MnO2 crystal morphological scale and crystal structure in selective catalytic degradation of azo dye. *Environ. Sci. Pollut. Res.* **30**, 15377–15391 (2023).

424. Huang, L., Luo, X., Chen, C. & Jiang, Q. A high specific capacity aqueous zinc-manganese battery with a ε-MnO2 cathode. *Ionics* **27**, 3933–3941 (2021).

425. Singh, S. *et al.* Synthesis of Bi2O3-MnO2 Nanocomposite Electrode for Wide-Potential Window High Performance Supercapacitor. *Energies* **12**, 3320 (2019).

426. Karaca, E., Saka, K., Gökcen, D. & Pekmez, N. Ö. Schottky contact of nano-BiOx thin film synthesized galvanostatically on stainless steel in acetonitrile. *Optik* **285**, 170945 (2023).

427. Zhu, X. *et al.* Ion-intercalation regulation of MXene-derived hydrated vanadates for high-rate and long-life Zn-Ion batteries. *Energy Storage Mater.* **45**, 568–577 (2022).

428. Du, M. *et al.* Calcium ion pinned vanadium oxide cathode for high-capacity and long-life aqueous rechargeable zinc-ion batteries. *Sci. China Chem.* **63**, 1767–1776 (2020).

429. Zhang, Y., Zhao, L., Chen, A. & Sun, J. Cr3+ pre-intercalated hydrated vanadium oxide as an excellent performance cathode for aqueous zinc-ion batteries. *Fundam. Res.* **1**, 418–424 (2021).

430. Huang, L., Luo, X., Chen, C. & Jiang, Q. A high specific capacity aqueous zinc-manganese battery with a ε-MnO2 cathode. *Ionics* **27**, 3933–3941 (2021).

431. Guo, C., Tian, S., Chen, B., Liu, H. & Li, J. Constructing α-MnO2@PPy core-shell nanorods towards enhancing electrochemical behaviors in aqueous zinc ion battery. *Mater. Lett.* **262**, 127180 (2020).

432. Jiang, W. *et al.* Facile plasma treated β-MnO2@C hybrids for durable cycling cathodes in aqueous Zn-ion batteries. *J. Alloys Compd.* **827**, 154273 (2020).

433. Zhang, R. *et al.* Manipulating intercalation-extraction mechanisms in structurally modulated δ-MnO2 nanowires for high-performance aqueous zinc-ion batteries. *Chem. Eng. J.* **433**, 133687 (2022).

434. Xie, Q. *et al.* Alkali ions pre-intercalation of δ-MnO2 nanosheets for high-capacity and stable Zn-ion battery. *Mater. Today Energy* **24**, 100934 (2022).

435. Li, D.-S. *et al.* MnO2 particles grown on the surface of N-doped hollow porous carbon nanospheres for aqueous rechargeable zinc ion batteries. *Appl. Surf. Sci.* **510**, 145458 (2020).

436. Chao, D. *et al.* Atomic Engineering Catalyzed MnO2 Electrolysis Kinetics for a Hybrid Aqueous Battery with High Power and Energy Density. *Adv. Mater.* **32**, 2001894 (2020).

437. Zhu, X. *et al.* Superior-Performance Aqueous Zinc-Ion Batteries Based on the In Situ Growth of MnO2 Nanosheets on V2CTX MXene. *ACS Nano* **15**, 2971–2983 (2021).

438. Tang, F. *et al.* Graphene-Wrapped MnO/C Composites by MOFs-Derived as Cathode Material for Aqueous Zinc ion Batteries. *Electrochimica Acta* **353**, 136570 (2020).

439. Chen, H. *et al.* Porous cube-like Mn3O4@C as an advanced cathode for low-cost neutral zinc-ion battery. *J. Alloys Compd.* **813**, 151812 (2020).

440. Yuan, G., Geng, M., Zhang, P. & Li, B. Hybrids of LiMn2O4 nanoparticles anchored on carbon nanotubes/graphene sheets as long-cycle-life cathode material for rechargeable hybrid aqueous batteries. *J. Solid State Electrochem.* **24**, 601–607 (2020).

441. Wang, S. *et al.* Dual-modification of manganese oxide by heterostructure and cation pre-intercalation for high-rate and stable zinc-ion storage. *J. Energy Chem.* **67**, 82–91 (2022).

442. Zhou, S. *et al.* Dual metal ions and water molecular pre-intercalated δ-MnO2 spherical microflowers for aqueous zinc ion batteries. *J. Colloid Interface Sci.* **623**, 456–466 (2022).

443. Shang, P., Liu, Y., Mei, Y., Wu, L. & Dong, Y. Defective MnO 2 nanosheets based free-standing and high mass loading electrodes for high energy density aqueous zinc ion batteries. *Mater. Chem. Front.* **5**, 8002–8009 (2021).

444. Xie, J. *et al.* g-C3N4-coated MnO2 hollow nanorod cathode for stable aqueous Zn-ion batteries. *Front. Chem. Sci. Eng.* **17**, 217–225 (2023).

445. Zhang, Y. *et al.* MnO2 cathode materials with the improved stability via nitrogen doping for aqueous zinc-ion batteries. *J. Energy Chem.* **64**, 23–32 (2022).

446. Luo, H. *et al.* Stress-release design for high-capacity and long-time lifespan aqueous zinc-ion batteries. *Mater. Today Energy* **21**, 100799 (2021).

447. Liao, Y. *et al.* Unveiling performance evolution mechanisms of MnO2 polymorphs for durable aqueous zinc-ion batteries. *Energy Storage Mater.* **44**, 508–516 (2022).

448. Han, M. *et al.* Oxygen Defects in *β*-MnO2 Enabling High-Performance Rechargeable Aqueous Zinc/Manganese Dioxide Battery. *iScience* **23**, 100797 (2020).

449. Gao, X. *et al.* H+-Insertion Boosted α-MnO2 for an Aqueous Zn-Ion Battery. *Small* **16**, 1905842 (2020).

450. Wang, J. *et al.* A Highly Flexible and Lightweight MnO2/Graphene Membrane for Superior Zinc-Ion Batteries. *Adv. Funct. Mater.* **31**, 2007397 (2021).

451. Li, G. *et al.* Rechargeable Zn-ion batteries with high power and energy densities: a two-electron reaction pathway in birnessite MnO2 cathode materials. *J. Mater. Chem. A* **8**, 1975–1985 (2020).

452. Zhao, Y. *et al.* Uncovering sulfur doping effect in MnO2 nanosheets as an efficient cathode for aqueous zinc ion battery. *Energy Storage Mater.* **47**, 424–433 (2022).

453. Gao, X. *et al.* Three-Dimensional Manganese Oxide@Carbon Networks as Free-Standing, High-Loading Cathodes for High-Performance Zinc-Ion Batteries. *Small Struct.* **4**, 2200316 (2023).

454. Zhao, Y. *et al.* Interfacial Designing of MnO2 Half-Wrapped by Aromatic Polymers for High-Performance Aqueous Zinc-Ion Batteries. *Angew. Chem.* **134**, e202212231 (2022).

455. Zhang, Y. *et al.* In Situ Electrochemically-Bonded Self-Adapting Polymeric Interface for Durable Aqueous Zinc Ion Batteries. *Adv. Funct. Mater.* **34**, 2310995 (2024).

456. Gao, X. *et al.* Co-intercalation strategy for simultaneously boosting two-electron conversion and bulk stabilization of Mn-based cathodes in aqueous zinc-ion batteries. *Energy Environ. Sci.* **17**, 2287–2297 (2024).

457. Shi, M. *et al.* 3D high-density MXene@MnO 2 microflowers for advanced aqueous zinc-ion batteries. *J. Mater. Chem. A* **8**, 24635–24644 (2020).

458. Deng, R. *et al.* “Soggy-Sand” Chemistry for High-Voltage Aqueous Zinc-Ion Batteries. *Adv. Mater.* **36**, 2311153 (2024).

459. Chen, L. *et al.* Adjusting Zn2+ diffusion kinetics and storage capability of MnOOH nanofibers for high-performance cathode of aqueous zinc-ion batteries. *Chem. Eng. J.* **473**, 145046 (2023).

460. Wu, L. *et al.* Interfacial synthesis of strongly-coupled δ-MnO2/MXene heteronanosheets for stable zinc ion batteries with Zn2+-exclusive storage mechanism. *Chem. Eng. J.* **459**, 141662 (2023).

461. Lin, Y. *et al.* Dendrite-free Zn anode enabled by anionic surfactant-induced horizontal growth for highly-stable aqueous Zn-ion pouch cells. *Energy Environ. Sci.* **16**, 687–697 (2023).

462. Li, G. *et al.* A biocompatible electrolyte enables highly reversible Zn anode for zinc ion battery. *Nat. Commun.* **14**, 6526 (2023).

463. Wu, B. *et al.* High Zinc Utilization Aqueous Zinc Ion Batteries Enabled by 3D Printed Graphene Arrays. *Energy Storage Mater.* **54**, 75–84 (2023).

464. Ying, H. *et al.* Freestanding and Flexible Interfacial Layer Enables Bottom-Up Zn Deposition Toward Dendrite-Free Aqueous Zn-Ion Batteries. *Nano-Micro Lett.* **14**, 180 (2022).

465. Zhou, J. *et al.* Establishing Thermal Infusion Method for Stable Zinc Metal Anodes in Aqueous Zinc-Ion Batteries. *Adv. Mater.* **34**, 2200782 (2022).

466. Bai, X. *et al.* Zn Ionophores to Suppress Hydrogen Evolution and Promote Uniform Zn Deposition in Aqueous Zn Batteries. *Adv. Funct. Mater.* **33**, 2307595 (2023).

467. Cao, J. *et al.* Modulating Zn deposition via ceramic-cellulose separator with interfacial polarization effect for durable zinc anode. *Nano Energy* **89**, 106322 (2021).

468. Zhou, J. *et al.* Ultrathin Surface Coating of Nitrogen-Doped Graphene Enables Stable Zinc Anodes for Aqueous Zinc-Ion Batteries. *Adv. Mater.* **33**, 2101649 (2021).

469. Zhang, F. *et al.* Biomineralization-inspired dendrite-free Zn-electrode for long-term stable aqueous Zn-ion battery. *Nano Energy* **103**, 107830 (2022).

470. Shi, S. *et al.* Lightweight Zn-Philic 3D-Cu Scaffold for Customizable Zinc Ion Batteries. *Adv. Funct. Mater.* **n/a**, 2312664.

471. Geng, L. *et al.* Eutectic Electrolyte with Unique Solvation Structure for High-Performance Zinc-Ion Batteries. *Angew. Chem. Int. Ed.* **61**, e202206717 (2022).

472. Woottapanit, P. *et al.* Inhibition of Zinc Dendrite Growth by WC-Cellulose Separators for High-Performance Zinc-Ion Batteries. *ACS Appl. Energy Mater.* **6**, 10578–10584 (2023).

473. Zhang, Q. *et al.* Stable zinc anode with ionic conductive interface layer for high performance aqueous zinc-ion batteries. *Chem. Eng. J.* **474**, 145981 (2023).

474. Yang, N. *et al.* Backside Coating for Stable Zn Anode with High Utilization Rate. *Adv. Mater.* **n/a**, 2312934.

475. Yan, T. *et al.* Refining the inner Helmholtz plane adsorption for achieving a stable solid-electrolyte interphase in reversible aqueous Zn-ion pouch cells. *Energy Storage Mater.* **65**, 103190 (2024).

476. Li, D. *et al.* Self-assembled multilayers direct a buffer interphase for long-life aqueous zinc-ion batteries. *Energy Environ. Sci.* **16**, 3381–3390 (2023).

477. Zhu, X. *et al.* Tailoring the Solvation Environment Enables Dendrite-Free Zn Anodes for Stable Zinc-Ion Batteries. *ACS Sustain. Chem. Eng.* **11**, 16975–16983 (2023).

478. Chen, H. *et al.* Dual-modification of oxygen vacancies and PEDOT coating on MnO2 nanowires for high-performance zinc ion battery. *Appl. Surf. Sci.* **638**, 158057 (2023).

Appendices

Appendix A: Supplementary Information for Chapter 4

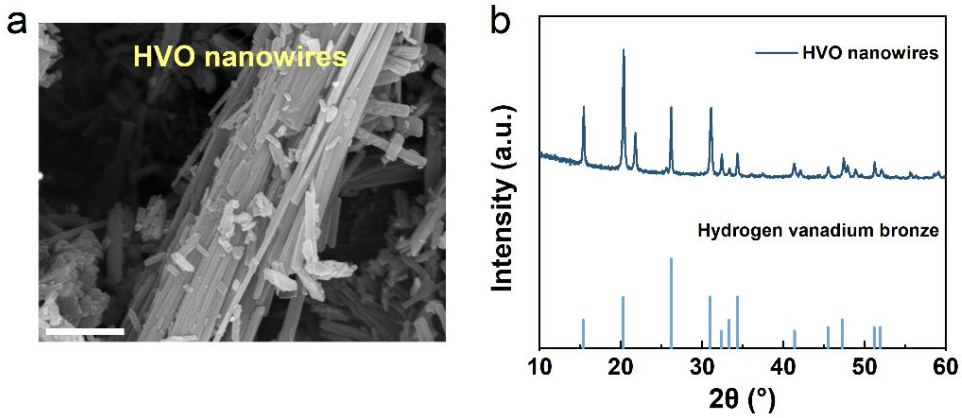


Figure A1. a) Morphology of HVO nanowires. Scale bar: 2 μm. b) XRD pattern of HVO nanowires. Hydrogen vanadium bronze ($H_xV_2O_5$, PDF#45-0429).

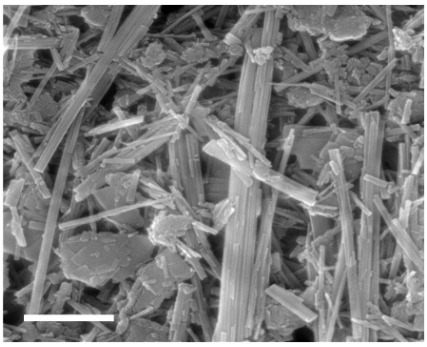


Figure A2. Morphology of ZNVO cathode in $ZnSO_4/Na_2SO_4$ electrolyte at 200th cycles. Scale bar: 1 μm.

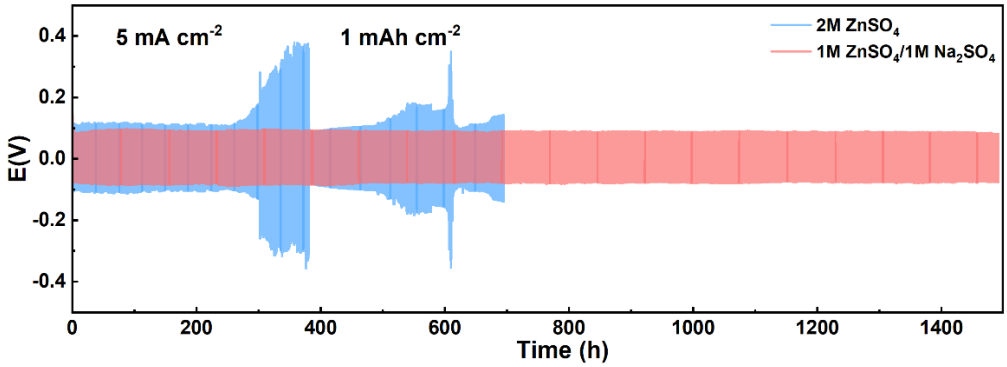


Figure A3. Long-term galvanostatic cycling of Zn-Zn symmetric cells at a current density of 5 mA cm^{-2} with an areal capacity of 1.0 mAh cm^{-2}.

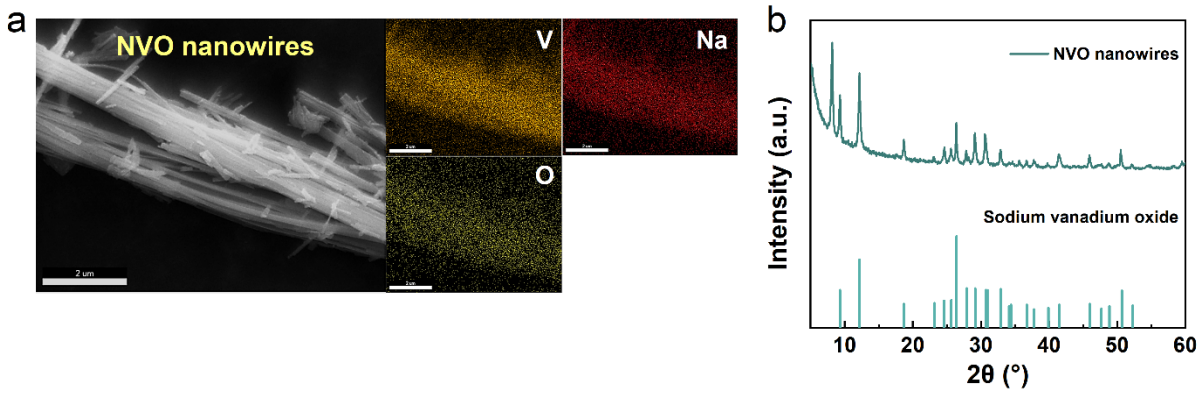


Figure A4. a) Morphology and elemental mapping of NVO nanowires. Scale bar: 2 μm. b) XRD pattern of NVO nanowires. Sodium vanadium oxide ($Na_{0.33}V_2O_5$, PDF#48-0382).

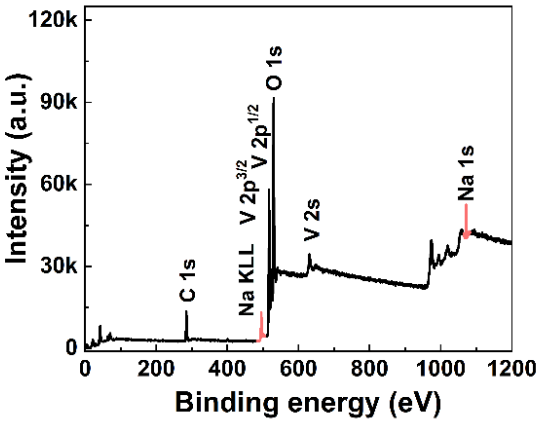


Figure A5. XPS spectra of NVO material.

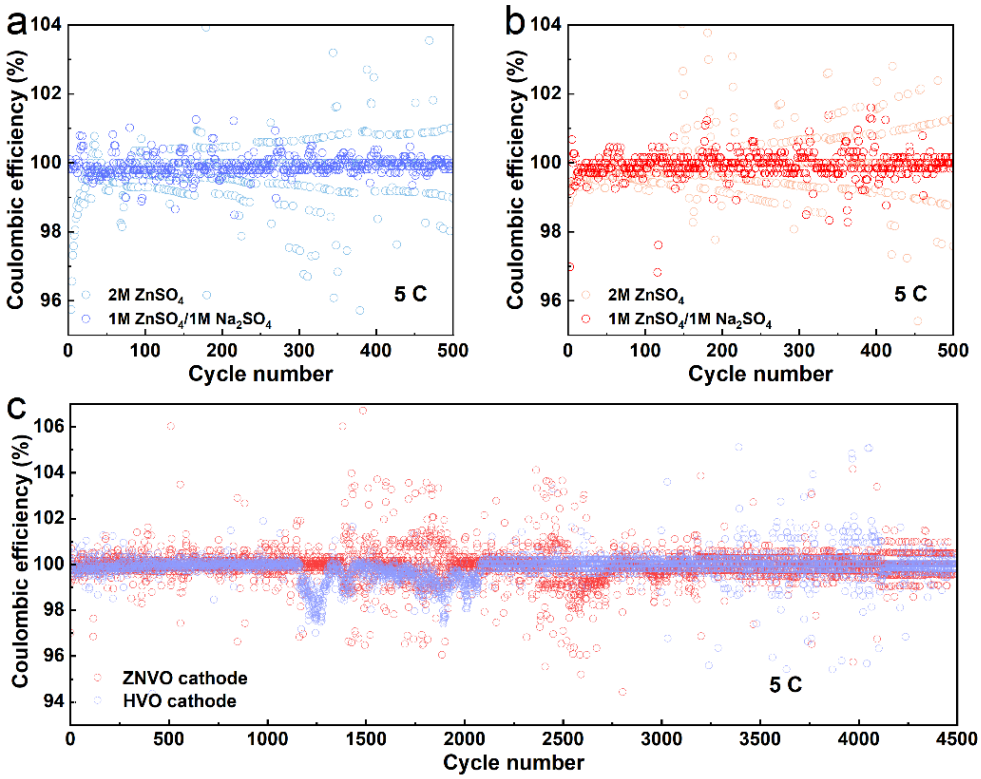


Figure A6. Coulombic efficiency of a) HVO cathode and b) ZNVO cathode in 2 M $ZnSO_4$ and 1 M $ZnSO_4$/1 M Na_2SO_4 electrolytes at 5 C. c) Coulombic efficiency of long-term cycling performance of HVO and ZNVO cathodes in 1 M $ZnSO_4$/1 M Na_2SO_4 electrolytes at 5 C.

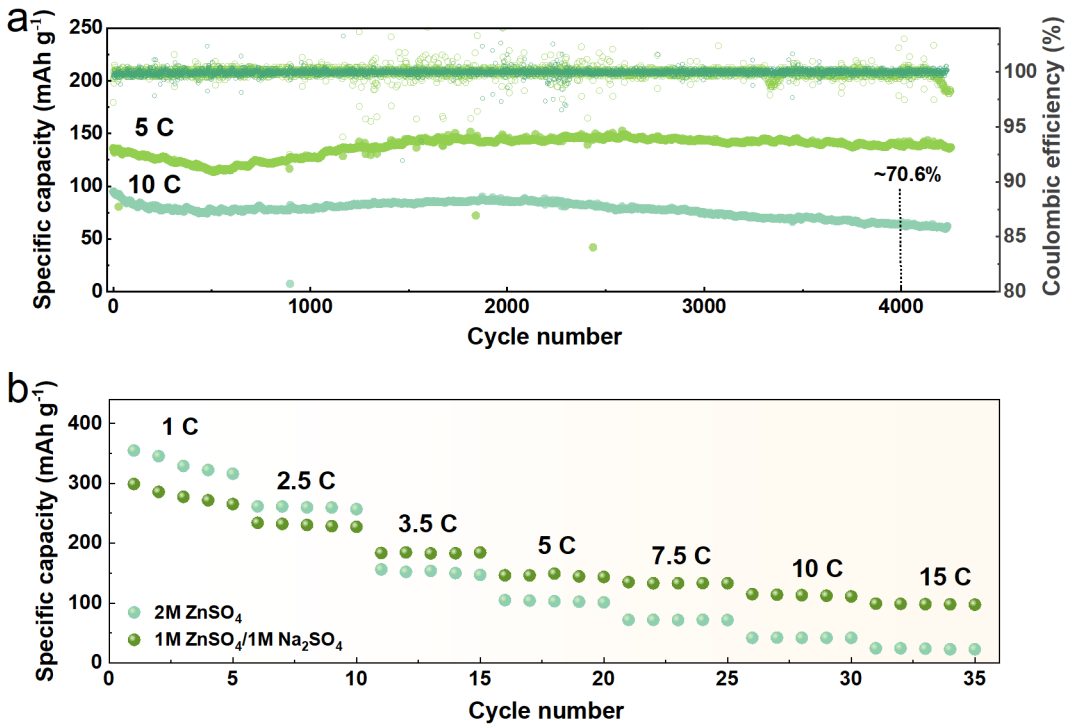


Figure A7. a) Long-term cycling performance of NVO cathode in 1 M $ZnSO_4$/1 M Na_2SO_4 electrolyte at 5 C and 10 C. b) Rate performance of NVO cathode in 2 M $ZnSO_4$ and 1 M $ZnSO_4$/1 M Na_2SO_4 electrolytes.

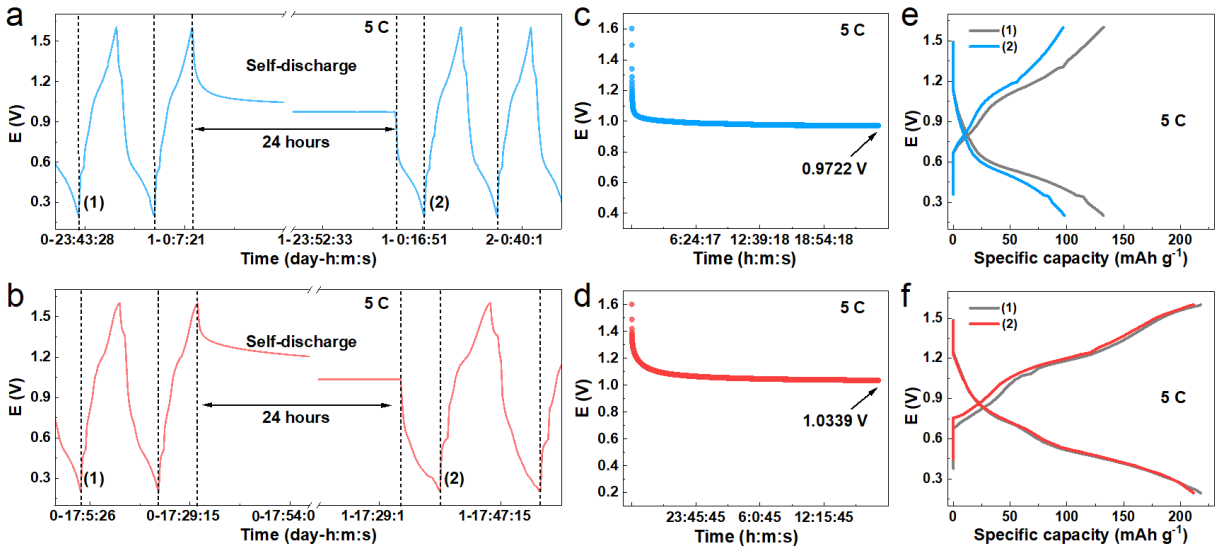


Figure A8. The self-discharge profile of Zn-ZNVO battery in a) 2 M $ZnSO_4$ electrolyte and b) 1 M $ZnSO_4$/1 M Na_2SO_4 electrolyte. The voltage changes of Zn-ZNVO battery after standing for 24 hours in c) 2 M $ZnSO_4$ electrolyte and d) 1 M $ZnSO_4$/1 M Na_2SO_4 electrolyte. The charge/discharge curve of Zn-ZNVO battery in e) 2 M $ZnSO_4$ electrolyte and f) 1 M $ZnSO_4$/1 M Na_2SO_4 electrolyte before and after self-discharge.

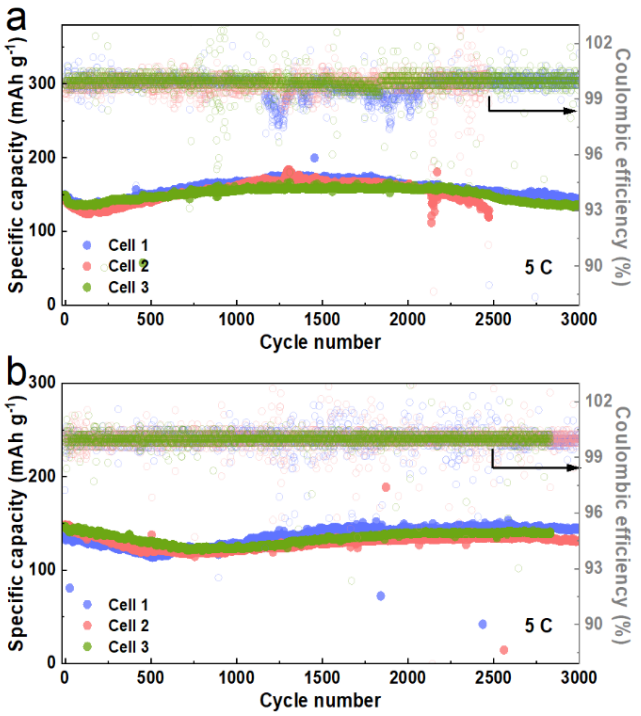


Figure A9. Cycling performance of a) HVO and b) NVO cathodes in 1 M $ZnSO_4$/1 M Na_2SO_4 electrolyte at 5 C.

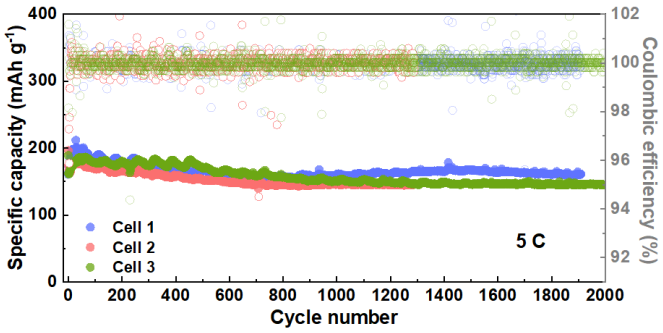


Figure A10. a) External and b) internal composition of the 9 mAh battery. c) Cycling performance of ZNVO cathodes with 1 M $ZnSO_4$/1 M Na_2SO_4 electrolyte in 9 mAh batteries at a current rate of 5 C.

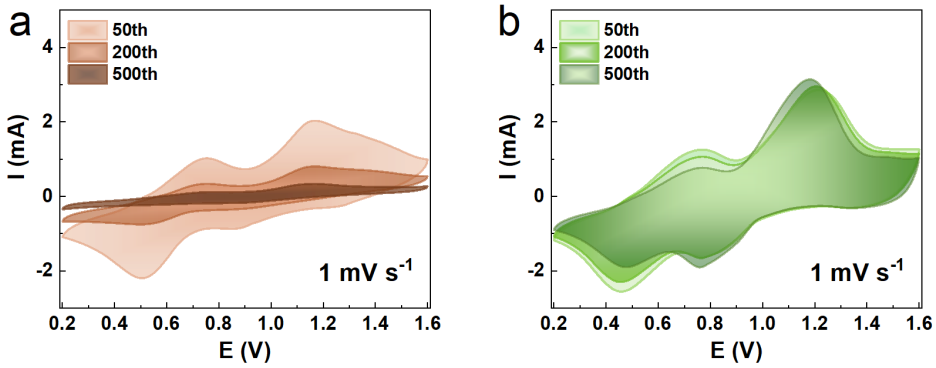


Figure A11. CV profiles of NVO cathode in a) 2 M $ZnSO_4$ and b) 1 M $ZnSO_4$/1 M Na_2SO_4 electrolytes at selected cycle numbers.

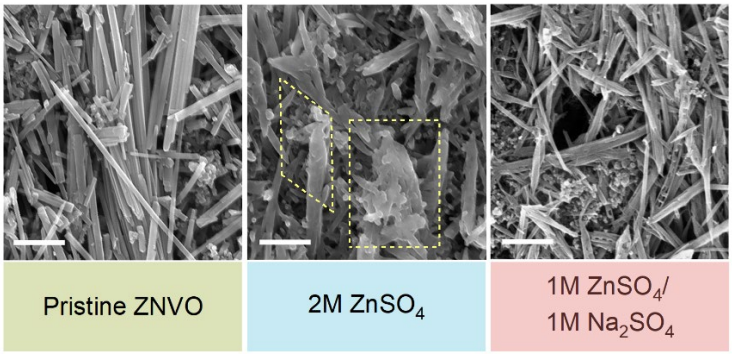


Figure A12. Morphology of cycled HVO cathodes in different electrolytes at 5 C. Scale bar: 1 μm.

Table A1. Electrochemical performances of recently reported vanadium-based cathode materials for zinc-ion battery.

Electrode material	Electrolyte	Current density	Capacity retention	Ref
$Ag_{1.2}V_3O_8$	2 M $ZnSO_4$	1 A g^{-1}	83%/100 cycles	91
$Na_xVO_2 \cdot 0.3H_2O$	2 M $ZnSO_4$	1 A g^{-1}	74%/2000 cycles	322
$K_{1.1}V_3O_8$	3 M $ZnSO_4$	2 A g^{-1}	93.5%/1000 cycles	86
$Zn_{0.25}V_2O_5 \cdot nH_2O$	1 M $ZnSO_4$	2.4 A g^{-1} 4.5 A g^{-1}	81%/1000 cycles 82%/1000 cycles	22
$Sn_{1.5}V_2O_7(OH)_2 \cdot 3.3H_2O$	1 M $ZnSO_4$	1 A g^{-1}	98%/200 cycles	98
$Mn_xV_{10}O_{24} \cdot nH_2O@V_2CT_x$	1 M $Zn(CF_3SO_3)_2$	1 A g^{-1}	93.5%/300 cycles	427
$V_5O_{12} \cdot 6H_2O$	3 M $Zn(CF_3SO_3)_2$	2 A g^{-1}	94%/1000 cycles	323
$Al_{0.2}V_2O_5$	3 M $Zn(CF_3SO_3)_2$	5 A g^{-1}	61.4%/5000 cycles	97
CuV_2O_6 micro-belts	3 M $Zn(CF_3SO_3)_2$	5 A g^{-1}	55.5%/3000 cycles	104
$MgV_2O_6 \cdot 1.7H_2O$	3 M $Zn(CF_3SO_3)_2$	1 A g^{-1}	94%/500 cycles	324
$Ca_{0.04}V_2O_5 \cdot 1.74H_2O$	3 M $Zn(CF_3SO_3)_2$	4 A g^{-1}	100%/1000 cycles	428
Cr-doped $V_2O_5 \cdot nH_2O$	3 M $Zn(CF_3SO_3)_2$	1 A g^{-1} 4 A g^{-1}	82.8%/100 cycles 58.1%/500 cycles	429
$NaCa_{0.6}V_6O_{16} \cdot 3H_2O$	3 M $Zn(CF_3SO_3)_2$	2 A g^{-1}	94%/2000 cycles	296
This work	1 M $ZnSO_4$+1 M Na_2SO_4	1 A g^{-1} (5 C) 2 A g^{-1} (10 C)	90.9%/4000 cycles 85%/3000 cycles	*

Table A2. Cycling performance (within 2000 cycles) of different electrodes in 1 M $ZnSO_4$/1 M Na_2SO_4 electrolyte at 5 C.

Electrodes	Number of cells	Average specific capacity (mAh g^{-1})	Average Coulombic efficiency (%)
HVO	1	154.861±15.008	99.850±0.368
	2	160.268±13.128	99.679±0.619
	3	152.156±7.919	99.997±4.779
ZNVO	1	194.360±4.960	99.992±0.840
	2	191.869±4.589	99.993±2.845
	3	186.748±6.988	99.856±1.334
NVO	1	131.338±9.588	100.331±15.055
	2	126.566±6.906	100.007±1.310
	3	131.151±6.263	99.987±0.415

Appendix B: Supplementary Information for Chapter 5

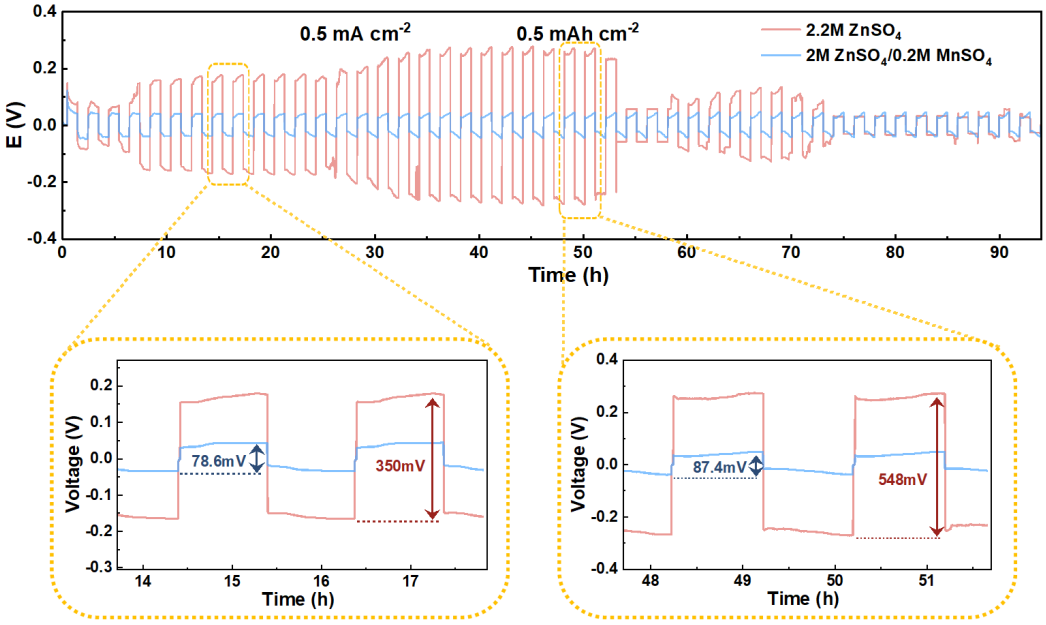


Figure B1. Galvanostatic cycling performance of Zn-Zn symmetric cells in different electrolytes at a current density of 0.5 mA cm^{-2} and an areal capacity of 0.5 mAh cm^{-2}. Enlarged images: detailed voltage profiles at specific cycling times.

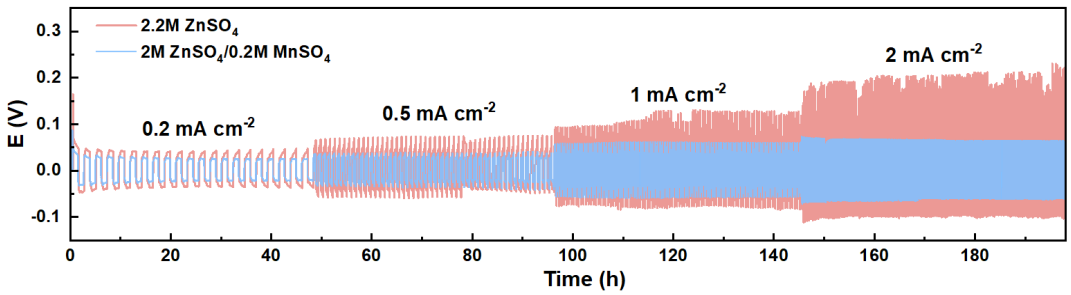


Figure B2. Rate performances for Zn-Zn symmetric cells at various current densities under an areal capacity of 0.5 mAh cm^{-2}.

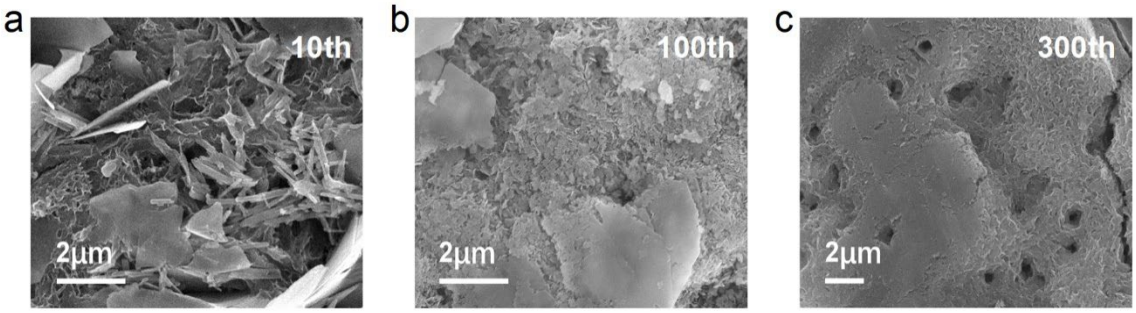


Figure B3. Morphology evolution of the MnO_2 cathode in the discharged state at selected cycle numbers in 2 M $ZnSO_4$/0.2 M $MnSO_4$ electrolyte. Scale bar: 2 μm.

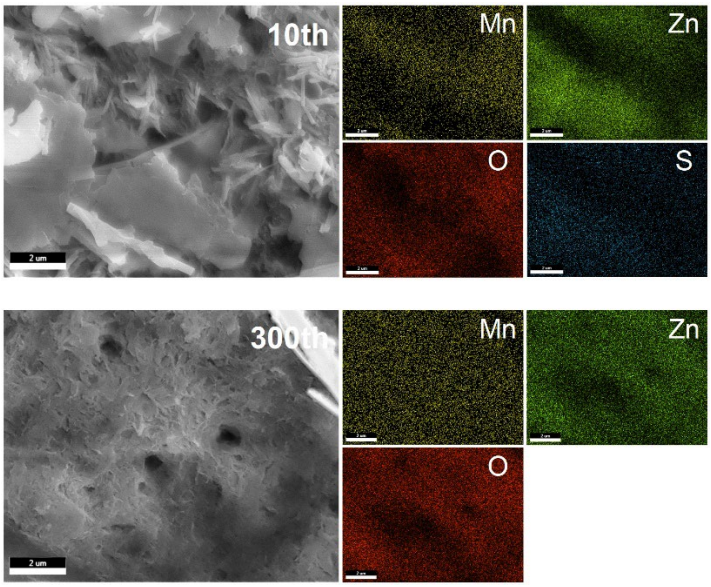


Figure B4. Elemental mapping images of MnO_2 cathode in 2 M $ZnSO_4$/0.2 M $MnSO_4$ electrolyte at 10th discharge and 300th discharge. Scale bar: 2 μm.

Appendix C: Supplementary Information for Chapter 6

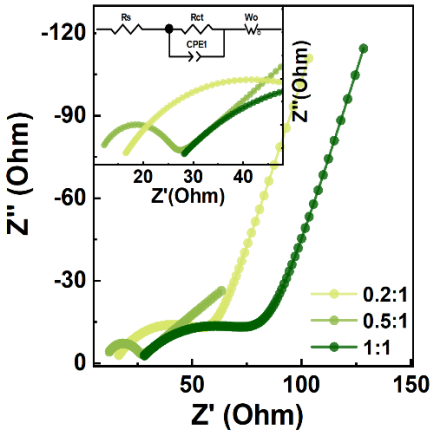


Figure C1. Nyquist plots of MnO_2 cathodes covered by PMs prepared with different solution ratios (0.2:1, 0.5:1 and 1:1) in 2 M $ZnSO_4$/0.2 M $MnSO_4$ electrolyte. Insets are the enlarged profiles and equivalent circuit diagram.

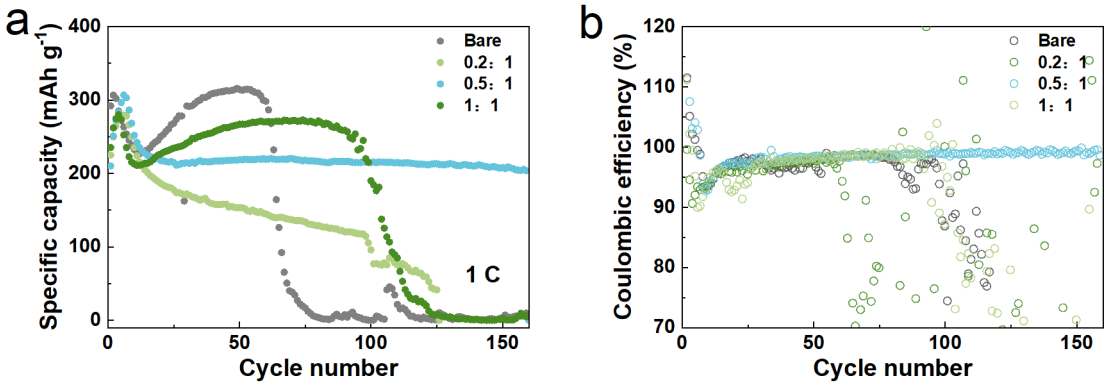


Figure C2. a) Cycling performance and b) Coulombic efficiency of MnO_2 cathodes covered by PMs prepared with different solution ratios (0.2:1, 0.5:1 and 1:1) in 2 M $ZnSO_4$/0.2 M $MnSO_4$ electrolyte. The current density is 1 C.

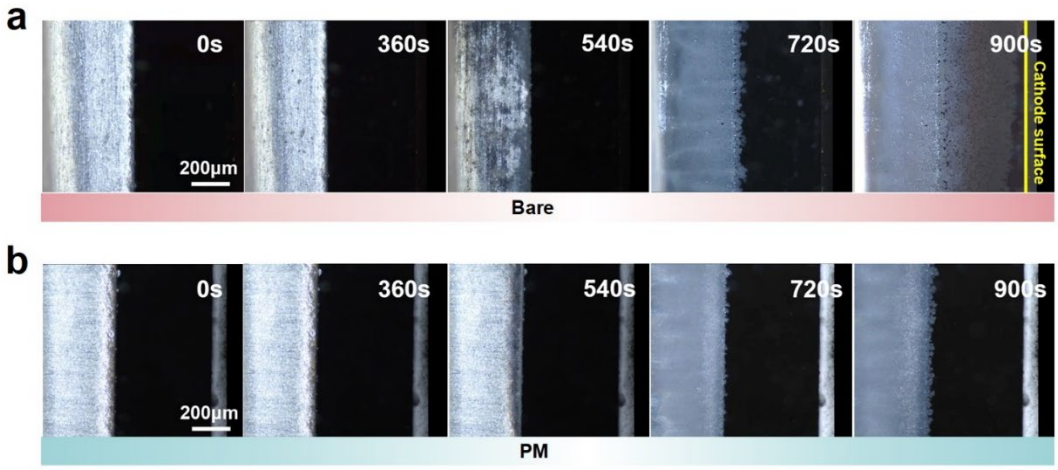


Figure C3. *In situ* optical visualization observations of Zn electrodes paired with a) bare MnO_2 and b) PM-MnO_2 electrodes in 2 M $ZnSO_4$/0.2 M $MnSO_4$ electrolyte within transparent electrochemical cells at various deposition times. Scale bar: 200 μm.

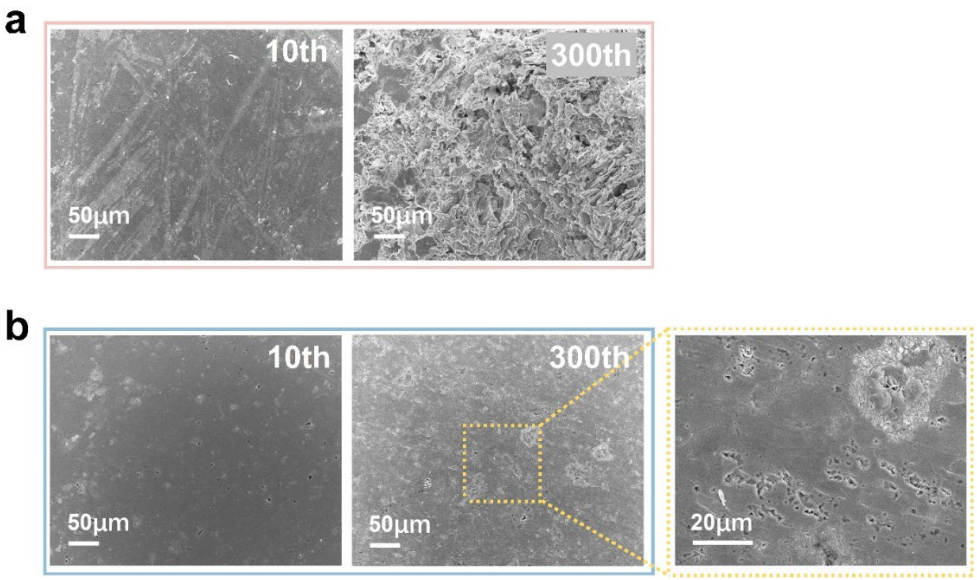


Figure C4. Cycled Zn anode surface paired with a) bare MnO_2 and b) PM-MnO_2 cathodes in 2 M $ZnSO_4$/0.2 M $MnSO_4$ electrolyte. Scale bars: 50 μm and 20 μm.

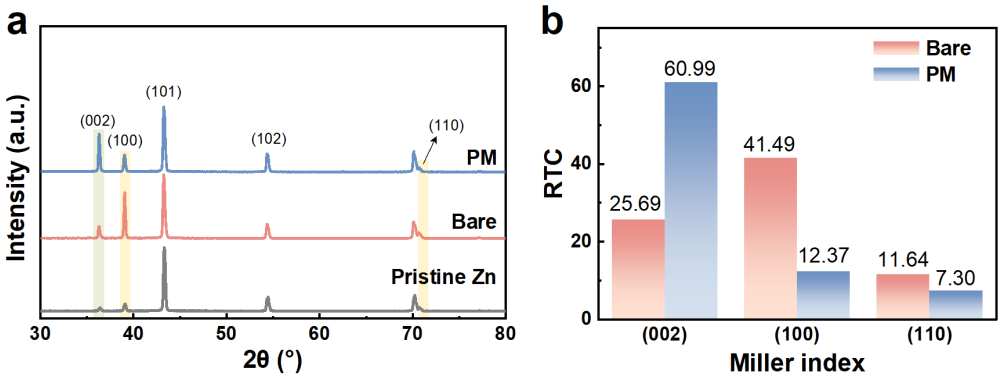


Figure C5. a) *Ex situ* XRD patterns of Zn anodes paired with bare and PM-MnO_2 cathodes after 300 cycles in 2 M $ZnSO_4$/0.2 M $MnSO_4$ electrolyte. b) The RTC of Zn anodes paired with bare and PM-MnO_2 cathodes (300 cycles).

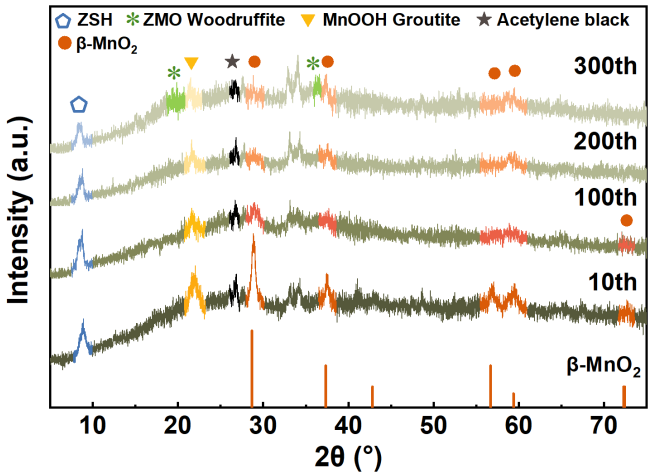


Figure C6. *Ex situ* XRD patterns of PM-MnO_2 cathodes in 2 M $ZnSO_4$/0.2 M $MnSO_4$ electrolyte at selected cycle numbers.

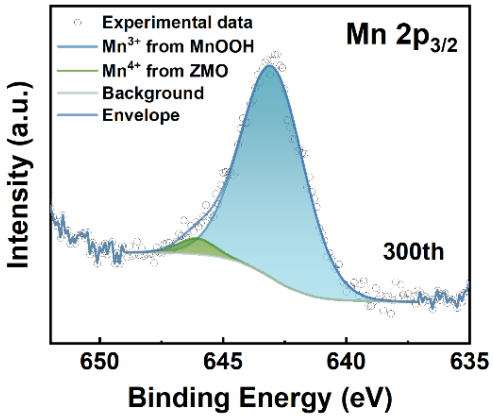


Figure C7. XPS spectra of Mn 2p for PM-MnO_2 cathode at 300th cycle.

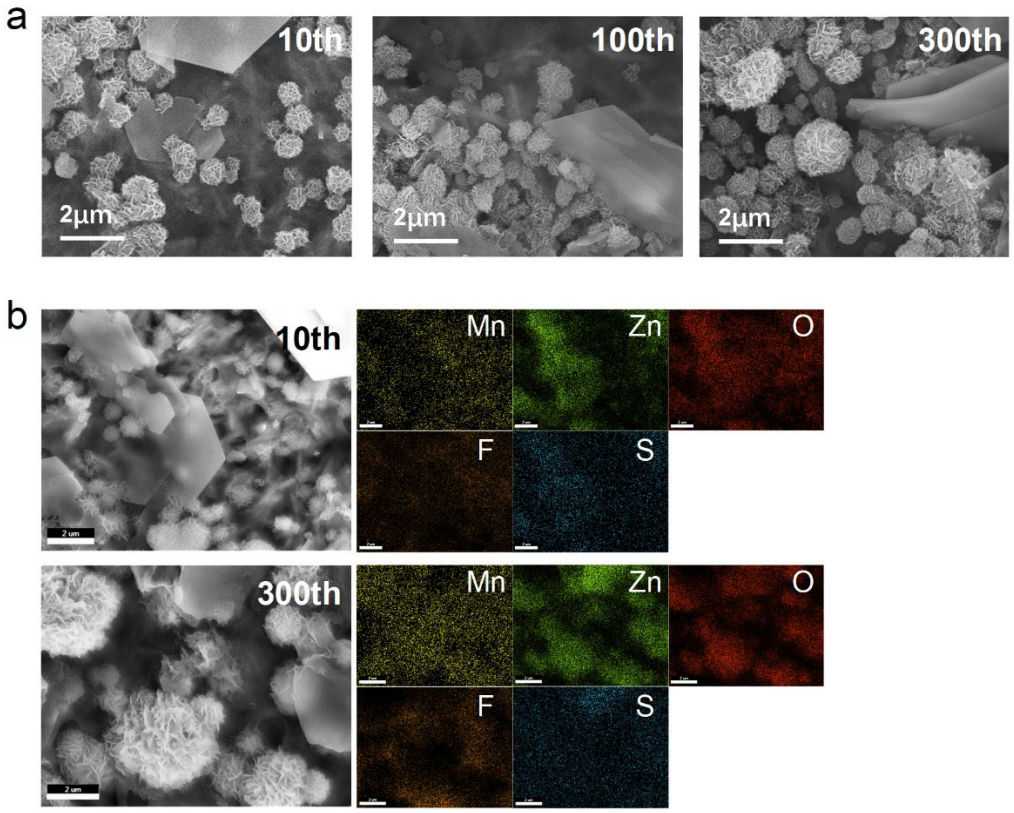


Figure C8. a) Morphology evolution of the PM-MnO_2 cathode in the discharged state at selected cycle numbers in 2 M $ZnSO_4$/0.2 M $MnSO_4$ electrolyte. Scale bar: 2 μm. Elemental mapping images of PM-MnO_2 cathode in 2 M $ZnSO_4$/0.2 M $MnSO_4$ electrolyte at 10th discharge and 300th discharge. Scale bar: 2 μm.

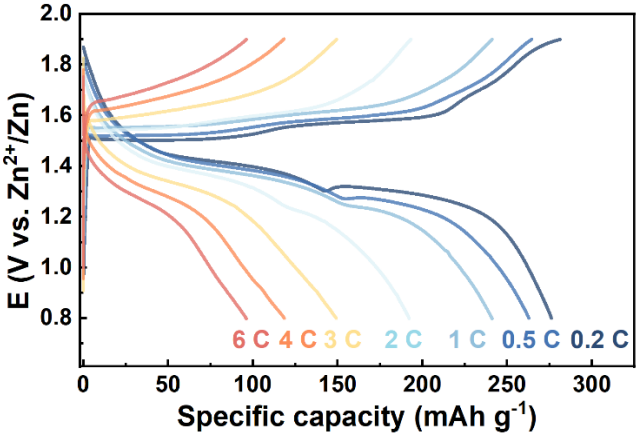


Figure C9. GCD curves PM-MnO_2 cathode in 2 M $ZnSO_4$/0.2 M $MnSO_4$ electrolyte with current density varying from 0.05 to 1.5 A g^{-1}.

Table C1. Electrochemical performances of recently reported manganese-based cathode materials with mild acidic electrolyte for aqueous Zn-ion battery.

Electrode material	Electrolyte	Current density	Cell capacity	Capacity retention	Ref
ε-MnO_2	1 M $ZnSO_4$/0.2 M $MnSO_4$	0.3 A g^{-1} 0.9 A g^{-1}	0.300 mAh	100%/150 cycles 100%/500 cycles	430
α-MnO_2@PPy	2 M $ZnSO_4$/0.1 M $MnSO_4$	0.1 A g^{-1}	0.375 mAh	65%/100 cycles	431
β-MnO_2@C	3 M $Zn(CF_3SO_3)_2$ /0.1 M $MnSO_4$	0.3 A g^{-1}	0.260 mAh	99%/400 cycles	432
Cu^{2+} pre-intercalated δ-MnO_2	2 M $ZnSO_4$/0.2 M $MnSO_4$	0.2 A g^{-1}	0.420 mAh	94%/90 cycles	433
K-δ-MnO_2	2 M $ZnSO_4$/0.1 M $MnSO_4$	0.3 A g^{-1}	0.405 mAh	100%/100 cycles	434
NHCSs@MnO_2	2 M $ZnSO_4$/0.1 M $MnSO_4$	0.5 A g^{-1}	0.103 mAh	98.3%/650 cycles	435
Ni-MnO_2@Carbon felt	3 M $MnSO_4$/0.3 M H_2SO_4/0.06 M $NiSO_4$	0.5 A g^{-1}	0.189 mAh	99%/450 cycles	436
K-V_2C@MnO_2	2 M $ZnSO_4$/0.25 M $MnSO_4$	0.3 A g^{-1}	0.408 mAh	100%/180 cycles	437
MnO/C@rGO	2 M $ZnSO_4$	0.5 A g^{-1}	0.170 mAh	99%/300 cycles	438
Mn_3O_4@C	2 M $ZnSO_4$/0.1 M $MnSO_4$	0.5 A g^{-1}	0.424 mAh	77.1%/200 cycles	439
$LiMn_2O_4$/GN/CNT	0.5 M $Zn(CH_3COO)_2$/0.5 M $LiCH_3COO$	0.24 A g^{-1}	0.232 mAh	82.1%/600 cycles	440
Sn_xMnO_2/SnO_2	2 M $ZnSO_4$/0.1 M $MnSO_4$	0.3 A g^{-1}	0.240 mAh	100%/100cycles	441
Al-KMO	2 M $ZnSO_4$/0.1 M $MnSO_4$	0.5 A g^{-1}	0.325 mAh	91%/300 cycles	442
This work	2 M $ZnSO_4$/0.2 M $MnSO_4$	0.25 A g^{-1} (1 C) 0.5 A g^{-1} (2 C)	0.564 mAh	100%/400 cycles 97%/1000 cycles	*

Table C2. Transference numbers of Zn^{2+} were obtained by analysis of polarization experiments.

	ΔV (mV)	R_0 (Ω)	R_s (Ω)	I_0 (μA)	I_s (μA)	t_{Zn2+}
Bare	10	930	1607	5.14	3.50	0.81
PM	10	13833	14891	0.284	0.189	0.56
PP	10	9689	9945	0.108	0.0133	0.11

Table C3. Transference numbers of Mn^{2+} were obtained by analysis of polarization experiments.

	ΔV (mV)	R_0 (Ω)	R_s (Ω)	I_0 (μA)	I_s (μA)	t_{Mn2+}
Bare	10	2338	2832	3.48	2.06	0.26
PM	10	53803	155802	0.0312	0.0306	0.17

Table C4. Impedance results of bare and PM-MnO_2 cathodes in 2 M $ZnSO_4$/0.2 M $MnSO_4$ electrolyte.

Bare MnO_2

	R_s (Ω)	R_{ct} (Ω)
50th	18.76	21.60
100th	13.51	38.21
200th	29.97	283.5
300th	/	/

PM-MnO_2

	R_s (Ω)	R_{ct} (Ω)
50th	11.45	14.25
100th	9.960	15.57
200th	9.174	17.25
300th	14.24	21.90

Appendix D: Supplementary Information for Chapter 7

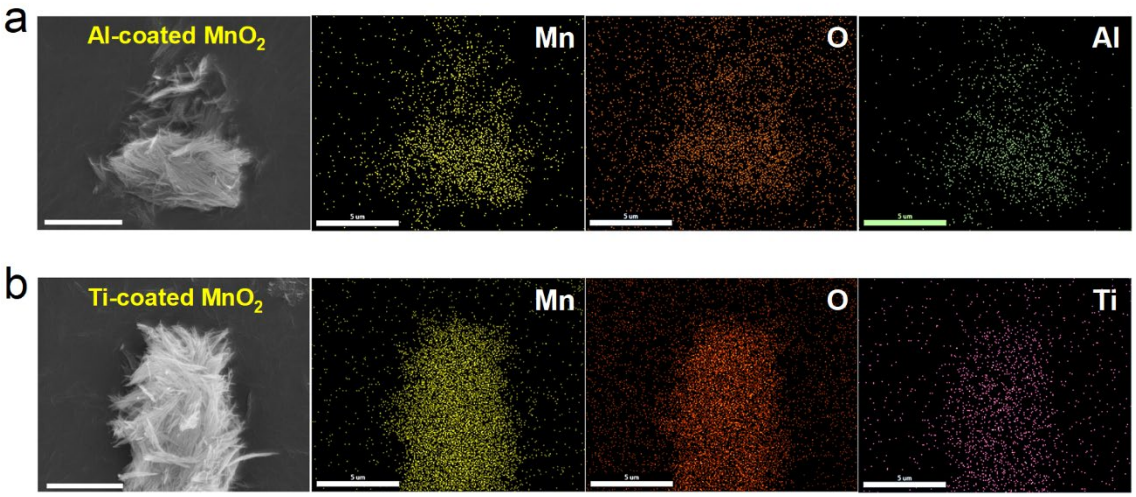


Figure D1. Morphology and elemental mapping of a) Al-coated and b) Ti-coated MnO_2 nanowires. Scale bar: 5 µm.

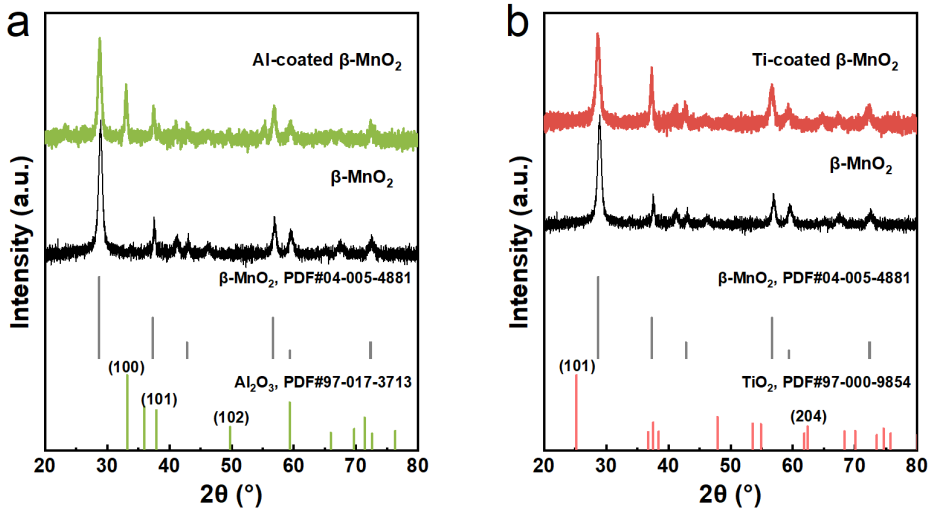


Figure D2. XRD patterns of a) Al-coated and b) Ti-coated MnO_2 nanowires. Aluminum trioxide (Al_2O_3, PDF#97-017-3713), titanium dioxide (TiO_2, PDF#97-000-9854), β-MnO_2 (PDF# 04-005-4881).

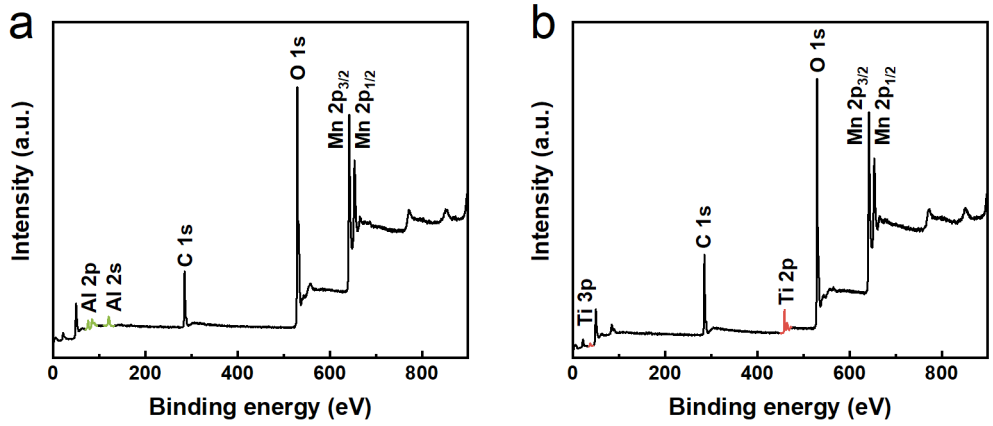


Figure D3. XPS survey spectra of a) AMO sample and b) TMO sample.

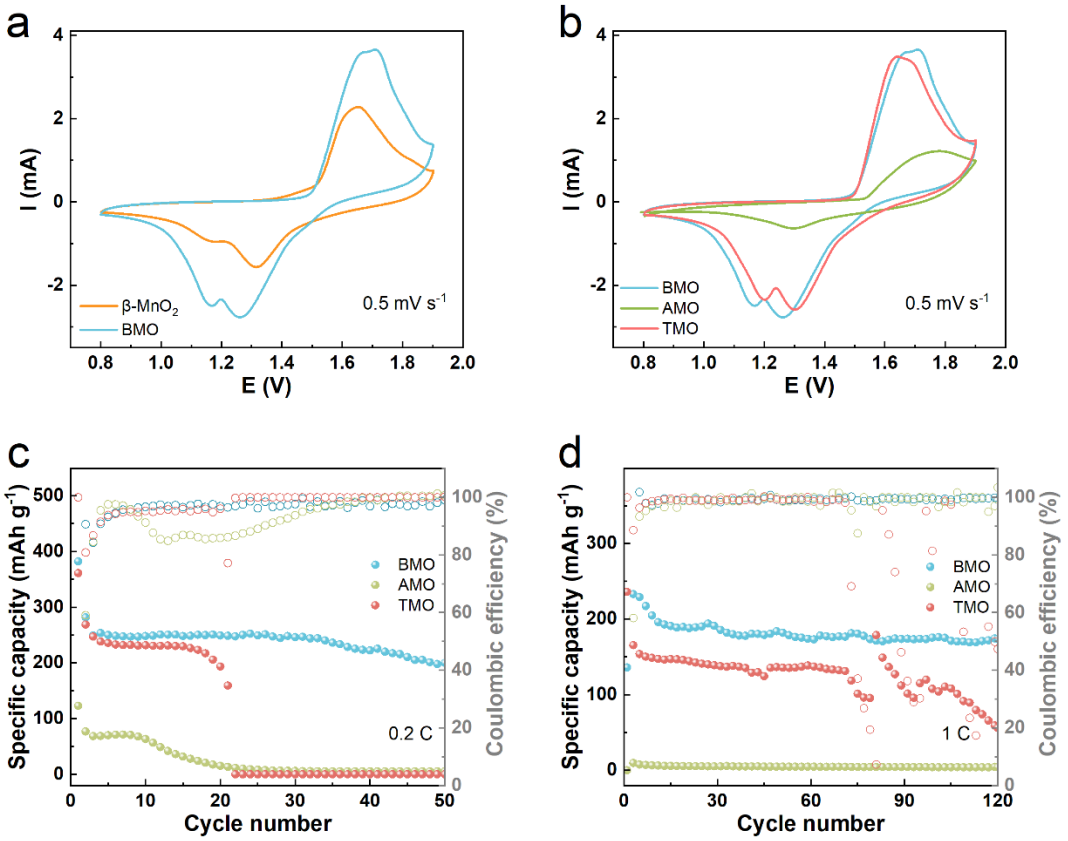


Figure D4. a) CV profiles of β-MnO_2 and BMO cathodes at 3rd cycle, with a scan rate of 0.5 mV s^{-1}. b) CV profiles of BMO, AMO and TMO cathodes at 3rd cycle, with a scan rate of 0.5 mV s^{-1}. Cycling performance of BMO, AMO and TMO cathodes in 2 M $ZnSO_4$/0.2 M $MnSO_4$ electrolyte at the current density of c) 0.2 C and d) 1 C. The active material mass loading is around 9 mg cm^{-2}.

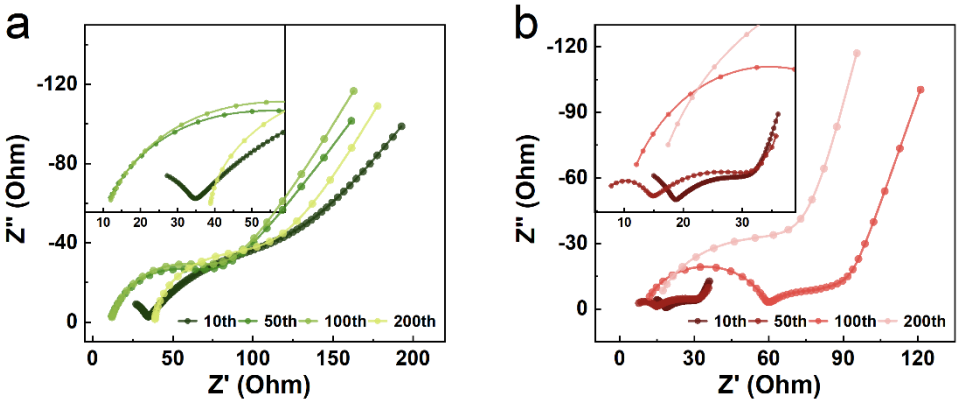


Figure D5. Nyquist plots of a) AMO and b) TMO cathodes in 2 M $ZnSO_4$/0.2 M $MnSO_4$ electrolyte over the frequency range of 100 mHz-1 MHz at selected cycles. Inset is the equivalent circuit diagram.

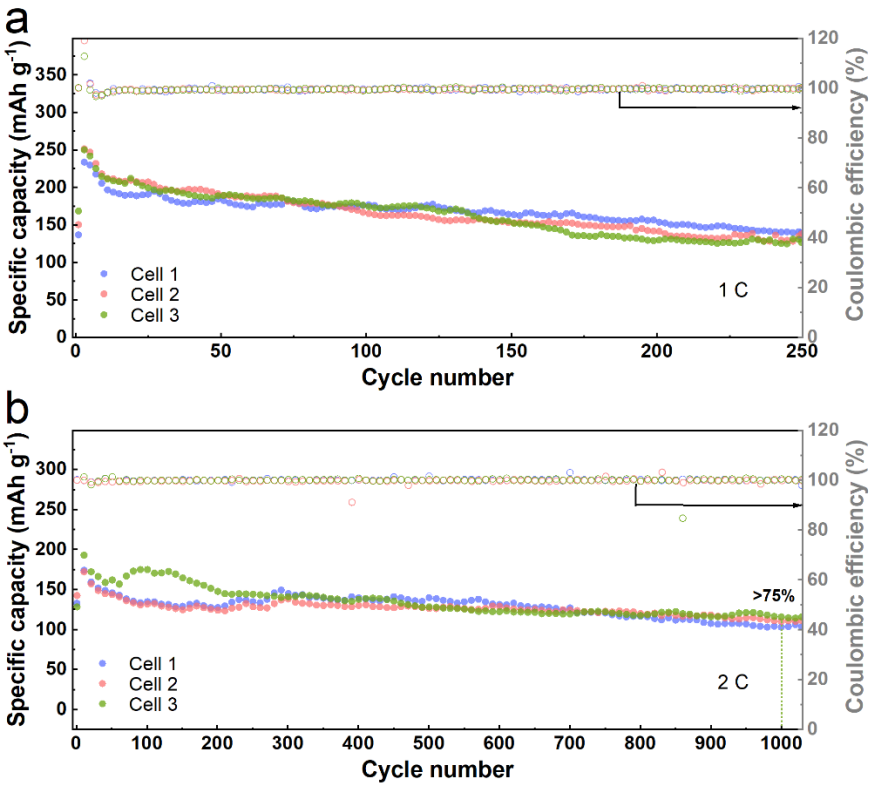


Figure D6. Cycling performance of BMO cathodes in 2 M $ZnSO_4$/0.2 M $MnSO_4$ electrolyte at a) 1 C and b) 2 C.

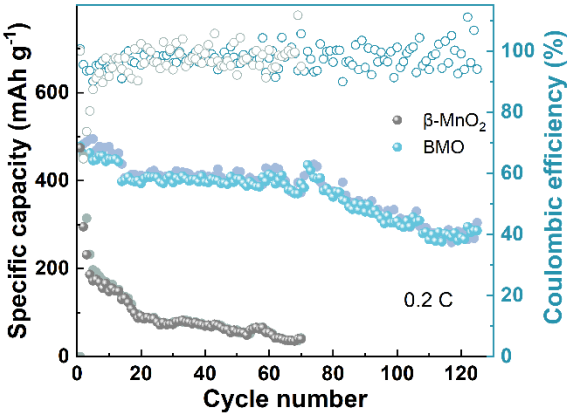


Figure D7. Cycling performance of β-MnO_2 and BMO cathodes in 2 M $ZnSO_4$/0.2 M $MnSO_4$ electrolyte at 0.2 C. The active material mass loading >9 mg cm^{-2}.

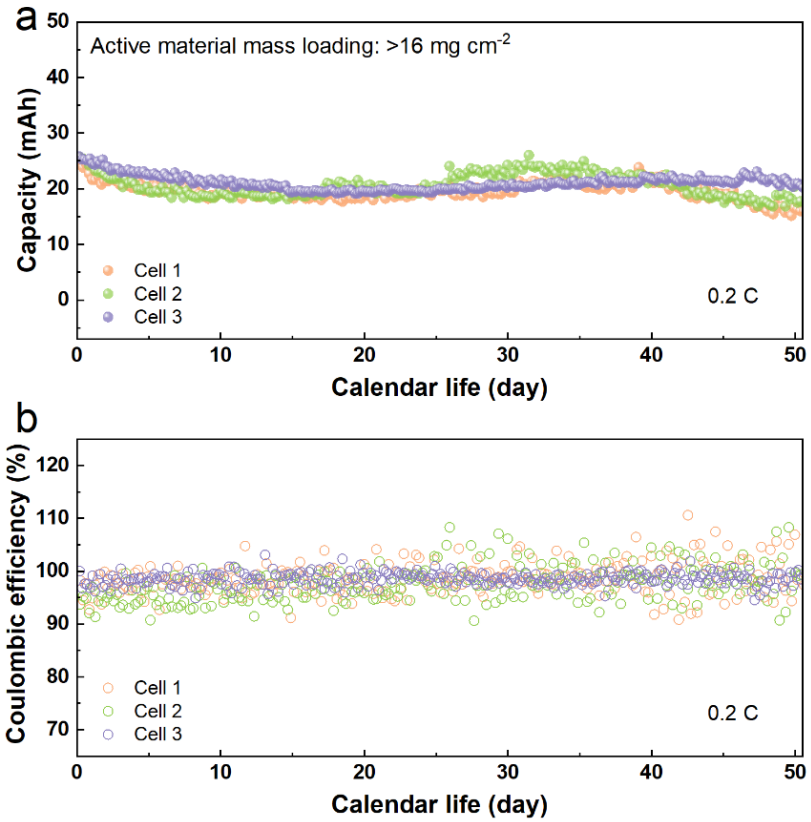


Figure D8. a) Cycling performance of BMO cathodes in 2 M $ZnSO_4$/0.2 M $MnSO_4$ electrolyte at 0.2 C and b) the corresponding Coulombic efficiencies within a narrow y-axis scale.

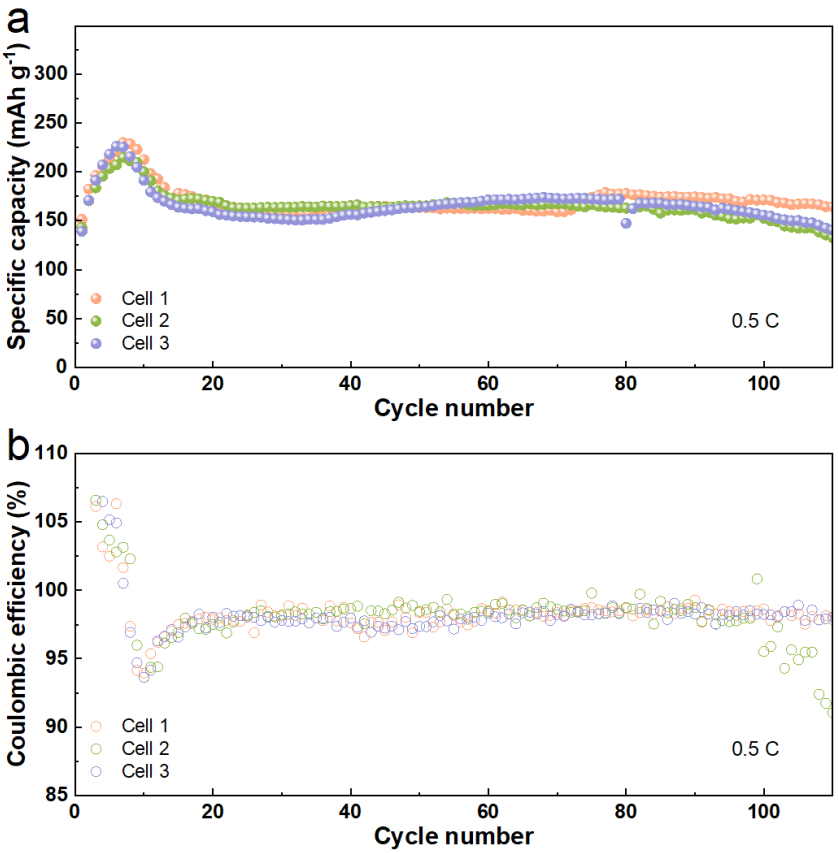


Figure D9. a) Cycling performance of BMO (ε) cathodes with 2 M $ZnSO_4$/0.2 M $MnSO_4$ electrolyte at 0.5 C in coin-type cells, and b) the corresponding Coulombic efficiencies within a narrow y-axis scale.

Table D1. Impedance results of β-MnO_2, BMO, AMO and TMO cathodes in 2 M $ZnSO_4$/0.2 M $MnSO_4$ electrolyte.

β-MnO_2

	R_s (Ω)	R_i (Ω)	R_{ct} (Ω)
10th	7.32	/	16.7
50th	5.00	/	127
100th	6.01	/	129
200th	2.71	/	147

BMO

	R_s (Ω)	R_i (Ω)	R_{ct} (Ω)
10th	12.5	4.15	8.62
50th	6.67	6.94	16.1
100th	7.45	4.51	13.7
200th	8.39	4.86	11.9
400th	17.5	3.28	10.2

AMO

	R_s (Ω)	R_i (Ω)	R_{ct} (Ω)
10th	6.46	27.5	103
50th	10.8	/	66.6
100th	11.1	/	73.1
200th	38.8	/	78.8

TMO

	R_s (Ω)	R_i (Ω)	R_{ct} (Ω)
10th	1.82	16.6	17.5
50th	5.76	8.45	22.4
100th	9.91	49.3	21.0
200th	14.5	/	67.9

Table D2. Cycling performance of BMO electrodes in 2 M $ZnSO_4$/0.2 M $MnSO_4$ electrolyte at different current densities.

Current density	Number of cells	Average specific capacity (mAh g^{-1})	Average Coulombic efficiency (%)
1 C (within 200 cycles)	1	173.955	99.417
	2	173.204	99.487
	3	172.395	99.395
2 C (within 1000 cycles)	1	128.786	99.899
	2	126.196	99.788
	3	134.949	99.974

Table D3. Electrochemical performances of recently reported manganese-based cathode materials for zinc-ion battery.

Electrode material	Electrolyte	Mass loading	Capacity	Current density	Capacity retention	Ref
Sn_xMnO_2/SnO_2	2 M $ZnSO_4$/0.1 M $MnSO_4$	0.8 mg cm^{-2}	0.27 mAh	0.30 A g^{-1}	100%/100 cycles	A[441]
d-MnO_2@CC	2 M $ZnSO_4$/0.1 M $MnSO_4$	1.1 mg cm^{-2}	0.30 mAh	0.25 A g^{-1}	100%/245 cycles	B[443]
K-V_2C@MnO_2	2 M $ZnSO_4$/0.25 M $MnSO_4$	1.2 mg cm^{-2}	0.61 mAh	0.30 A g^{-1}	100%/180 cycles	C[437]
α-MnO_2@g-C_3N_4	2 M $ZnSO_4$/0.1 M $MnSO_4$	1.7 mg cm^{-2}	0.55 mAh	0.50 A g^{-1}	100%/225 cycles	D[444]
K-δ-MnO_2	2 M $ZnSO_4$/0.1 M $MnSO_4$	2.0 mg cm^{-2}	0.63 mAh	0.30 A g^{-1}	100%/100 cycles	E[434]
MnO_2@N	2 M $ZnSO_4$/0.5 M $MnSO_4$	2.0 mg cm^{-2}	0.39 mAh	0.50 A g^{-1}	100%/500 cycles	F[445]
HP-Mn_2O_3-YSMSs	2 M $ZnSO_4$/0.1 M $MnSO_4$	2.0 mg cm^{-2}	0.45 mAh	0.50 A g^{-1}	100%/200 cycles	G[446]
ε-MnO_2	1 M $ZnSO_4$/0.2 M $MnSO_4$	3.0 mg cm^{-2}	0.66 mAh	0.75 A g^{-1}	90.0%/500 cycles	H[430]
β-MnO_2	2 M $ZnSO_4$/0.1 M $MnSO_4$	4.0 mg cm^{-2}	0.79 mAh	0.50 A g^{-1}	45.0%/700 cycles	I[447]
D-β-MnO_2	3 M $ZnSO_4$/0.1 M $MnSO_4$	4.0 mg cm^{-2}	1.10 mAh	0.50 A g^{-1}	100%/300 cycles	J[448]
α-MnO_2	2 M $ZnSO_4$/0.2 M $MnSO_4$	4.0 mg cm^{-2}	0.90 mAh	0.50 A g^{-1}	52.6%/100 cycles	K[449]
MnO_2/rGO	2 M $ZnSO_4$/0.1 M $MnSO_4$	5.0 mg cm^{-2}	1.41 mAh	0.40 A g^{-1}	82.0%/100 cycles	L[450]
MnO_2/C	2 M $ZnSO_4$/0.5 M $MnSO_4$	5.0 mg cm^{-2}	1.64 mAh	0.60 A g^{-1}	100%/250 cycles	M[451]
S-MnO_2	2 M $ZnSO_4$/0.1 M $MnSO_4$	5.0 mg cm^{-2}	1.81 mAh	0.20 A g^{-1}	100%/100 cycles	N[452]
NMO/VTCNTs	2 M $ZnSO_4$/0.2 M $MnSO_4$	5.0 mg cm^{-2}	1.85 mAh	0.20 A g^{-1}	100%/120 cycles	O[453]
C@PODA/MnO_2	2 M $ZnSO_4$/0.1 M $MnSO_4$	6.8 mg cm^{-2}	1.47 mAh	0.50 A g^{-1}	100%/600 cycles	P[454]
$LiMn_2O_4$	1 M $ZnSO_4$/2 M Li_2SO_4	7.2 mg cm^{-2}	0.61 mAh	0.15 A g^{-1}	62.0%/500 cycles	Q[455]

NCMO	2 M $ZnSO_4$/0.2 M $MnSO_4$	7.5 mg cm^{-2}	1.53 mAh	0.75 A g^{-1}	100%/100 cycles	R[456]
3D $Ti_3C_2T_x$@MnO_2	1 M $ZnSO_4$	8.0 mg cm^{-2}	2.35 mAh	0.50 A g^{-1}	71.1%/600 cycles	S[457]
MnO_2/CNT	"soggy-sand"(2 M $ZnSO_4$/0.1 M $MnSO_4$/Al_2O_3/SiO_2)	10 mg cm^{-2}	2.71 mAh	0.50 A g^{-1}	100%/300 cycles	T[458]
S-MnOOH	2 M $ZnSO_4$/0.1 M $MnSO_4$	10 mg cm^{-2}	1.22 mAh	0.50 A g^{-1}	100%/500 cycles	U[459]
MnO_2@MXene	0.5 M $Zn(OTf)_2$/TEP	10.5 mg cm^{-2}	1.93 mAh	0.10 A g^{-1}	100%/100 cycles	V[460]
This work	2 M $ZnSO_4$/0.2 M $MnSO_4$	9.0 mg cm^{-2}	2.54 mAh 1.96 mAh	0.25 A g^{-1} (1 C) 0.50 A g^{-1} (2 C)	80.1%/200 cycles 76.7%/1000 cycles	*

Table D4. Electrochemical performances of recently reported pouch-type Zn-ion batteries.

Battery systems	Active material mass	Current density	Cell capacity	Calendar life	Ref
Zn-ZnVOH	78.8 mg	1 mA cm^{-2}	20.7 mAh	28 day/200 cycles	A[461]
Zn-LMO	100 mg	0.15 A g^{-1}	12.5 mAh	33 day/400 cycles	B[462]
3DGT@Zn-V_2O_5	42.8 mg	4 mA cm^{-2}	20.5 mAh	17 day/150 cycles	C[463]
Zn@MCFs-α-MnO_2	57.6 mg	1 A g^{-1}	11.5 mAh	5.2 day/250 cycles	D[464]
PCu@Zn-LMO	104 mg	0.15 A g^{-1}	10.0 mAh	25 day/300 cycles	E[465]
Zn-V_2O_5	21.0 mg	1 A g^{-1}	5.90 mAh	5.8 day/100 cycles	F[466]
Zn-MnO_2@Graphite	100 mg	2 A g^{-1}	8.50 mAh	4.2 day/50 cycles	G[467]
NGO@Zn-LMO	80.6 mg	0.15 A g^{-1}	10.0 mAh	15 day/180 cycles	H[468]
Zn@C-V_2O_5	25.5 mg	1 A g^{-1}	7.65 mAh	10 day/600 cycles	I[469]
Zn-MnO_2	18.0 mg	0.25 A g^{-1}	3.60 mAh	17 day/200 cycles	J[470]
Zn-PANI	16.48 mg	0.05 A g^{-1}	2.14 mAh	8.5 day/50 cycles	K[471]
Zn-NVO	52.0 mg	0.5 A g^{-1}	6.32 mAh	4.2 day/100 cycles	L[472]
P-Zn-VO_2	5.84 mg	1 A g^{-1}	1.17 mAh	5.5 day/330 cycles	M[473]
ZAP@Zn@Cu-V_2O_5	60.0 mg	0.5 A g^{-1}	12.0 mAh	6.7 day/200 cycles	N[474]
Zn-$NH_4V_4O_{10}$	45.0 mg	1 A g^{-1}	12.2 mAh	17 day/1000 cycles	O[475]
SAM-Zn-$NH_4V_4O_{10}$	48.0 mg	2 A g^{-1}	10.1 mAh	8.3 day/200 cycles	P[476]
Zn-$NH_4V_4O_{10}$	52.5 mg	1 A g^{-1}	10.5 mAh	10 day/600 cycles	Q[477]
Zn-Vö-MnO_2@PEDOT	57.6 mg	0.2 A g^{-1}	17.8 mAh	10 day/120 cycles	R[478]
This work	121 mg	0.05 A g^{-1} (0.2 C)	23.1 mAh	60 day/330 cycles	*